



HAL
open science

Synthèse et hydratation de la phase ye'elimité

Yassine El Khessaimi

► **To cite this version:**

Yassine El Khessaimi. Synthèse et hydratation de la phase ye'elimité. Matériaux. Université de Limoges, 2019. Français. NNT : 2019LIMO0090 . tel-02464853

HAL Id: tel-02464853

<https://theses.hal.science/tel-02464853>

Submitted on 3 Feb 2020

HAL is a multi-disciplinary open access archive for the deposit and dissemination of scientific research documents, whether they are published or not. The documents may come from teaching and research institutions in France or abroad, or from public or private research centers.

L'archive ouverte pluridisciplinaire **HAL**, est destinée au dépôt et à la diffusion de documents scientifiques de niveau recherche, publiés ou non, émanant des établissements d'enseignement et de recherche français ou étrangers, des laboratoires publics ou privés.

Université de Limoges
**École Doctorale Sciences et Ingénierie des Matériaux, Mécanique,
Énergétique (ED 609)**
Institut de Recherche sur les Céramiques (IRCER) - UMR 7315

Thèse pour obtenir le grade de
Docteur de l'Université de Limoges
Matériaux Céramiques et Traitements de Surface

Présentée et soutenue par
Yassine EL KHESSAIMI

Le 11 décembre 2019

Synthesis and hydration of ye'elinite

Thèse dirigée par Agnès SMITH et Youssef EL HAFIANE

JURY :

Présidente du jury

Mme Sylvie FOUCAUD Professeure, IRCER, Université de Limoges, France

Rapporteurs

M. Emmanuel de BILBAO Maître de Conférences, CEMHTI, Université d'Orléans, France

M. Koichiro FUKUDA Professeur, NITech, Nagoya, Japon

Examineurs

M. Jones ALAMI Professeur, MSN, Université UM6P, Maroc

M. Youssef EL HAFIANE Maître de Conférences, IRCER, Université de Limoges, France

Mme Agnès SMITH Professeure, IRCER, Université de Limoges, France

À l'âme de mon père,

à ma famille,

à mes amis.

Acknowledgements

I would like to offer heart full thanks to Prof. Agnès SMITH for her supervision and professional guidance throughout the whole period of study at the University of Limoges. The helpful comments and continued support of Associate Prof. Youssef EL HAFIANE had an essential role in completing my Master and PhD theses.

I would like to thank the members of my thesis Jury, Prof. Sylvie FOUCAUD as president of my PhD defense, Prof. Koichiro FUKUDA (NITech, Nagoya, Japon) and Associate Prof. Emmanuel de BILBAO (CEMHTI, Orléans, France) for reviewing this work. I am also grateful to Prof. Jones ALAMI (MSN, UM6P, Morocco) for the examination of my PhD thesis.

The technical assistance of the IRCER staff at the University of Limoges was greatly appreciated.

Many thanks to Prof. Matias Velázquez at the University of Bordeaux, for his scientific comments and advice during the period of my training in the ICMCB institute.

I am grateful for the useful discussions with Dr Romain Trauchessec, Dr Cécile Diliberto and Prof. André Lecomte (Institut Jean Lamour, University of Lorraine, France).

The sincere fraternity help and encouragement of my colleagues Elmas, Sofien, Jérémie, Siham, Imad, Imane, Marc, Hatim, Halima, Jérémy and Delphine were greatly appreciated.

Droits d'auteurs

Cette création est mise à disposition selon le Contrat :

« **Attribution-Pas d'Utilisation Commerciale-Pas de modification 3.0 France** »

disponible en ligne : <http://creativecommons.org/licenses/by-nc-nd/3.0/fr/>



Notations and Abbreviations

The following list defines the notations and abbreviations used throughout the thesis.

- Cementitious symbols

Cementitious symbol	Chemical formula	Name
A	Al_2O_3	Aluminium oxide
C	CaO	Calcium oxide
\bar{C}	CO_2	Carbon dioxide
F	Fe_2O_3	Iron oxide
H	H_2O	Water
K	K_2O	Potassium oxide
M	MgO	Magnesium oxide
N	Na_2O	Sodium oxide
S	SiO_2	Silicium oxide
\bar{S}	SO_3	Sulfur trioxide
T	TiO_2	Titanium oxide

- Cementitious anhydrous phases

Anhydrous phase	Chemical formula	Name
C_3S	$3\text{CaO}.\text{SiO}_2$	Tricalcium silicate, Alite
C_2S	$2\text{CaO}.\text{SiO}_2$	Dicalcium silicate, Belite
C_3A	$3\text{CaO}.\text{Al}_2\text{O}_3$	Tricalcium aluminate, Celite
C_4AF	$4\text{CaO}.\text{Al}_2\text{O}_3.\text{Fe}_2\text{O}_3$	Tetracalcium aluminoferrite, Ferrite
$\bar{\text{C}}\bar{\text{S}}$	CaSO_4	Anhydrite
$\bar{\text{C}}\bar{\text{S}}\text{H}_{0.5}$	$\text{CaSO}_4.0.5\text{H}_2\text{O}$	Bassanite
$\bar{\text{C}}\bar{\text{S}}\text{H}_2$	$\text{CaSO}_4.2\text{H}_2\text{O}$	Gypsum
CA	$\text{CaO}.\text{Al}_2\text{O}_3$	Calcium Aluminate, Krotite
CA_2	$\text{CaO}.2\text{Al}_2\text{O}_3$	Calcium Dialuminate, Grossite
C_{12}A_7	$12\text{CaO}.7\text{Al}_2\text{O}_3$	Dodecacalcium hepta-aluminate, Mayenite
$\text{C}_4\text{A}_3\bar{\text{S}}$	$4\text{CaO}.3\text{Al}_2\text{O}_3.\bar{\text{S}}\text{O}_3$	Ye'elimitite
$\bar{\text{C}}\bar{\text{C}}$	$\text{CaO}.\text{CO}_2$	Calcium carbonate, Calcite
$\bar{\text{M}}\bar{\text{C}}$	$\text{MgO}.\text{CO}_2$	Magnesium carbonate, Magnesite
C_2MS_2	$2\text{CaO}.\text{MgO}.2\text{SiO}_2$	Akermanite
C_2AS	$2\text{CaO}.\text{Al}_2\text{O}_3.\text{SiO}_2$	Gehlenite

- Hydrates

Hydrates	Chemical formula	Name
AH_3	$\text{Al}_2\text{O}_3.3\text{H}_2\text{O}$	Aluminium hydroxide, Gibbsite
CH	$\text{Ca}(\text{OH})_2$	Calcium hydroxide, Portlandite
CAH_{10}	$\text{CaO}.\text{Al}_2\text{O}_3.10\text{H}_2\text{O}$	Dodeca hydrated calcium aluminate
C_2AH_8	$2\text{CaO}.\text{Al}_2\text{O}_3.8\text{H}_2\text{O}$	Octa hydrated dicalcium aluminate
C_3AH_6	$3\text{CaO}.\text{Al}_2\text{O}_3.6\text{H}_2\text{O}$	Hexa hydrated tricalcium aluminate
		Hydrogrenat, Katoite
C_4AH_{13}	$4\text{CaO}.\text{Al}_2\text{O}_3.13\text{H}_2\text{O}$	Hydrated tetracalcium aluminate
C_2ASH_8	$2\text{CaO}.\text{Al}_2\text{O}_3.\text{SiO}_2.8\text{H}_2\text{O}$	Stratlingite
$\text{C}_4\text{A}\bar{\text{S}}\text{H}_{12}$	$3\text{CaO}.\text{Al}_2\text{O}_3.\text{CaSO}_4.12\text{H}_2\text{O}$	Calcium monosulfoaluminate hydrate
$\text{C}_6\text{A}\bar{\text{S}}_3\text{H}_{32}$	$3\text{CaO}.\text{Al}_2\text{O}_3.3\text{CaSO}_4.32\text{H}_2\text{O}$	Ettringite
MH	$\text{Mg}(\text{OH})_2$	Magnesium hydroxide, Brucite

- Symbols and abbreviations:

ACSA	Alite Calcium Sulfo-Aluminate clinker
ASTM	American Society for Testing and Materials
BCSAA	Aluminum-rich Calcium Sulfo-Aluminate clinker
BCSAF	Iron-rich Belite Calcium Sulfo-Aluminate clinker
BSE	Back-Scattered Electrons
Calcined GEL (T)	Calcination of GEL sample for 1h at T. T: 400-1290°C
CSA cement	Calcium SulfoAluminate cement
CSA-sol-0	Model cement containing ye'elinite blended with gypsum ($Ye/Gy=2$); Ye refers to ye'elinite weight and Gy refers to Gypsum weight
CSA-sol-0.5	Model cement containing ye'elinite blended with gypsum ($Ye/Gy=2$), and 0.5 wt.% citric acid; wt.% refers to weight percentage of citric acid with respect to ye'elinite weight
CSA-sol-1	Model cement containing ye'elinite blended with gypsum ($Ye/Gy=2$), and 1 wt.% citric acid
d_{10}	The diameter at which 10% of the sample's volume is composed of particles with a diameter less than this value
d_{50}	The diameter at which 50% of the sample's volume is composed of particles with a diameter less than this value
d_{90}	The diameter at which 90% of the sample's volume is composed of particles with a diameter less than this value
$D_{Crystallite}$	A measure of the dimension of ye'elinite crystallite determined by Scherrer's equation
$D_{Particle}$	A measure of the dimension of ye'elinite grain size observed by scanning electron microscopy
DTA	Differential Thermal Analysis
EDS	Energy-Dispersive X-ray Spectroscopy
EN	European Norm
FWHM	Full Width at Half Maximum
GEL	Dried gel resulted from Sol-Gel (S-G) method
GOF	Goodness Of Fit
Gy	Gypsum weight
ICSD	Inorganic Crystal Structure Database
LOI	Loss On Ignition
MS	Mass-Spectroscopy
OPC	Ordinary Portland Cement
OSE	Organic Steric Entrapment method
Pech	Pechini method
PSD-IA	Particle Size Distribution determined by Image Analysis of SEM images
PSD-LA	Particle Size Distribution determined by Laser diffraction measurement

PVA	Polyvinyl Alcohol
QRA	Quantitative Rietveld Analysis
Rc	Resin content
Rexp	Expected R-factor
Rwp	Weighted profile R-factor
SEM	Scanning Electron Microscopy
SM	Stoichiometric Mixture
SM(T,t)	Sintered SM samples; T refers to sintering temperature, and t refers to sintering duration. T: 1000 - 1350°C t: 0 - 4h
SPC	Self-Propagating Combustion
SSA _{BET}	Specific Surface Area determined by BET (Brunauer, Emmett et Teller)
TDD	Thermal Differential Dilatometry
TGA	Thermogravimetric Analysis
W	Water weight
XRD	X-Ray Diffraction
XRF	X-Ray Fluorescence
Ye	Ye'elimate weight
Ye-chem	Highly pure ye'elimate powder synthetized by sol-gel (S-G) method
Ye-Sol-0	Highly pure ye'elimate powder synthetized by solid state (S-S) reaction method
Ye-Sol-5	Powder containing ye'elimate and 5 wt.% of citric acid; percentage relative to ye'elimate weight
Ye-Sol-10	Powder containing ye'elimate and 10 wt.% of citric acid; percentage relative to ye'elimate weight

Table of contents

Introduction	1
•Background	1
•Research objectives	4
•Outline of the thesis.....	4
Chapitre I. Literature review	7
I.1. Introduction.....	7
I.2. Calcium Sulfo-Aluminate (CSA) cements.....	7
I.2.1. CO ₂ emission reduction in the manufacturing process of CSA cements.....	7
I.2.2. Mineralogical composition of CSA cements.....	8
I.2.3. Crystallographic structure of ye'elimite.....	16
I.3. Lab-synthesis methods for ye'elimite and other cement phases	19
I.3.1. Solid-state synthesis of ye'elimite.....	19
I.3.2. Sol-gel synthesis of anhydrous cement phases.....	22
I.4. Hydration of ye'elimite phase.....	25
I.4.1. Effect of amount and nature of the added calcium sulfate	25
I.4.2. Effect of ye'elimite crystallographic structure	27
I.5. Parameters influencing cementitious phases hydration at early age	29
I.5.1. Parameters influencing the dissolution of cementitious phases	29
I.5.2. Parameters influencing the crystallization of cementitious hydrates.....	35
I.5.3. A focus on the influence of fineness and citric acid addition.....	38
Chapitre II. Characterization methods.....	41
II.1. X-Ray Diffraction (XRD) and Quantitative Rietveld Analysis (QRA)	41
II.2. Chemical analysis by X-ray fluorescence (XRF)	44
II.3. Thermogravimetric analysis (TGA) coupled to differential thermal analysis (DTA).....	44
II.4. Thermogravimetric analysis (TGA) coupled to Mass-spectroscopy (MS)	45
II.5. Particle Size Distribution by Laser Diffraction (PSD-LD).....	45
II.6. Particle Size Distribution by Image Analysis (PSD-IA).....	45
II.7. BET specific surface area (SSA)	47
II.8. Thermal Differential Dilatometry (TDD).....	47
II.9. Open porosity estimation by Archimedes principle (EN 623-2:1993)	47
II.10. Porosity estimation from backscattered electron image analysis (BSE-IA)	48
II.11. Scanning electron microscopy (SEM)	48
II.12. Ionic conductivity and pH measurements.....	50
II.13. Zeta potential measurement.....	51
II.14. Free-lime determination by volumetric dosage method.....	52
Chapitre III. Synthesis methods and experimental protocols	53
III.1. Raw materials.....	53
III.2. Experimental protocols.....	55
III.2.1. For solid-state synthesis of ye'elimite	55
III.2.2. For sol-gel synthesis of fine ye'elimite.....	57
III.2.3. For the study of solid-state formation mechanisms of ye'elimite.....	65
III.2.4. For suspensions preparation for ye'elimite dissolution experiments (W/C=1000), Figure III-8.....	66
III.2.5. For the hydration of ye'elimite-rich model cements (W/C=2), Figure III-9.....	67
III.3. Samples nomenclature and corresponding characterization techniques	69
Chapitre IV. Solid-state synthesis of ye'elimite.....	71
IV.1. Reactions during C ₄ A ₃ S formation.....	71

IV.2. Optimal synthesis conditions for ye'elimite	74
IV.3. Synthesis of pure orthorhombic ye'elimite	76
IV.4. Microstructural evolution during solid state formation of Ye'elimite.....	78
Chapitre V. Sol-gel synthesis of ye'elimite.....	83
V.1. Thermal analysis of the gel precursor.....	83
V.2. Effect of calcination temperature on ye'elimite phase formation.....	85
V.3. Effect of calcination temperature on crystallite size of the synthesized ye'elimite	89
V.4. Microstructural characterization of ye'elimite synthesized at 1250°C.....	90
Chapitre VI. Examination of ye'elimite formation mechanisms.....	97
VI.1. Mineralogical analysis	97
VI.2. Microstructural observation	99
VI.3. Discussion	105
Chapitre VII. Effect of fineness and citric acid addition on ye'elimite hydration.....	111
VII.1. Description of the anhydrous powders.....	111
VII.2. Effect of fineness and citric acid on ye'elimite dissolution	112
VII.3. Hydration of CSA model cements containing ye'elimite with two different grain sizes	117
VII.4. Influence of citric acid on CSA model cements hydration	120
Conclusions and perspectives	125
References.....	127
Appendixes	141
Appendix 1. EDS point analysis of Figure VI-3 and Figure VI-4.....	142
Appendix 2. Derivative curves of TGA analysis given in Figure VII-4b and Figure VII-5b.....	150
Appendix 3. All mathematical equations mentioned in the present thesis	151
Appendix 4. All chemical reactions mentioned in the present thesis	154
Appendix 5. Publications and communications	155

List of Figures

Figure Intro-1: Embodied carbon (a) and embodied energy (b) of the main construction materials [2].	1
Figure Intro-2: World production of materials in Mt for the years 1981 and 2005 (according to the International Energy Agency (IEA) [3]).	2
Figure Intro-3: Sources of CO ₂ emissions in cement manufacturing and the corresponding quantities for the year 1990 (according to CEMBUREAU [4]).	2
Figure Intro-4: Lokern road bridge rehabilitation project, California (USA) [7].	3
Figure I-1: Energy requirement and CO ₂ released during cement phases formation.	8
Figure I-2: State of the art about CSA composition collected from literature in the ternary system C ₄ A ₃ \bar{S} -C ₂ S-others (Ferrite, Calcium aluminate, ...) [14-24].	10
Figure I-3: State of the art about CSA composition collected from patents in the ternary system C ₄ A ₃ \bar{S} -C ₂ S-others (Ferrite, Calcium aluminate, ...) [25-32].	10
Figure I-4: Crystal structures of (a) cubic-C ₄ A ₃ \bar{S} and (b) orthorhombic-C ₄ A ₃ \bar{S} . Irregular Al-O six membered rings and four-membered rings are highlighted [88].	17
Figure I-5: (a) Calculated ye'elite hydration degree ($\alpha\%$); Formed hydrates quantities relevant to Ettringite (b), Monosulfate (c) and Gibbsite (d); "W/C" refers to water by cement weight ratio; References: Cuesta et al.,2014 [146], Hargis et al.,2014 [149], Jansen et al.,2017 [147], Bullerjahn et al.,2019 [148], ($\alpha\%$) is given by equation (E.0).	27
Figure I-6: Schematic illustration of the thermodynamic concept of over/under saturation to explain dissolution of anhydrous and precipitation of hydrates.	30
Figure I-7: Experimental measurements of dissolution rate of Alite C ₃ S phase as a function of oversaturation logarithm (noted β in the text) (Nicoleau et al. [151]).	32
Figure I-8: The typical S-curve showing dissolution rate as a function of solution saturation state β or difference in Gibbs free energy (ΔG_r) of the corresponding dissolution reaction (adapted from [152,156]).	33
Figure I-9: Calculated Gibbs free energy (ΔG_r) of etch-pit formation as a function of etch-pit size (r) in the case of Quartz surface dissolution, adapted from [157].	34
Figure I-10: Schematic illustration of heterogeneous germination of hydrate.	36
Figure I-11: Germination Gibbs free energy ΔG_{germ} as a function of germ radius (r).	37
Figure II-1: Principle of X-ray diffraction analysis.	41
Figure II-2: Maximum Feret diameter applied to a projection of a 3D schematic nano-particle.	46
Figure II-3: The interaction between electron beam and sample surface, adapted from [190].	48
Figure III-1: Particle size distribution of the SM raw mixture.	56
Figure III-2: Flow diagram showing the processing routes of Pechini method (Rc=70%) Pech70 or (Rc=95%) Pech95. Rc represents the resin content calculated from equation (E.33).	58
Figure III-3: Proposed chemical reactions describing the polymeric process of the Pechini method. The grey spheres represent carbon atoms and the yellow spheres represent sulfur atoms, whereas white, red, pink, purple and green spheres identify hydrogen, oxygen, nitrogen, aluminum and calcium, respectively.	59
Figure III-4: Flow diagram showing the processing route of organic steric entrapment method OSE.	61
Figure III-5: Proposed chemical reactions describing the polymeric process of the OSE method. The grey spheres represent carbon atoms and the yellow spheres represent sulfur atoms, whereas white, red, pink, purple and green spheres identify hydrogen, oxygen, nitrogen, aluminum and calcium, respectively.	62

Figure III-6: Flow diagram showing the processing route of self-propagating combustion SPC method.	64
Figure III-7: Proposed chemical reactions describing the polymeric process of the SPC method. The grey spheres represent carbon atoms and the yellow spheres represent sulfur atoms, whereas white, red, pink, purple and green spheres identify hydrogen, oxygen, nitrogen, aluminum and calcium, respectively.	65
Figure III-8: Preparation protocol for the study of ye'elimite dissolution in dilute suspensions, (a) based on Ye-sol or Ye-chem, (b) based on Ye-sol with different citric acid percentages (0, 5 and 10 wt.%)	67
Figure III-9: Preparation protocol for the study of hydration of CSA model cement pastes, (a) based on Ye-sol or Ye-chem (blended with gypsum), or (b) based on Ye-sol (blended with gypsum) with different citric acid percentages (0, 0.5 and 1 wt.%)	68
Figure IV-1: DTA curves of the SM raw mixture during heating process.	72
Figure IV-2: TGA-Mass spectroscopy of the SM raw mixture during heating from room temperature to 1400 °C.	72
Figure IV-3: XRD patterns of SM sample fired at different temperatures.	73
Figure IV-4: Normalized quantitative phase evolution with sintering temperature of SM sample for 0.5 h (A), 1 h (B), 2h (C), 3h (D) and 4h (E).	75
Figure IV-5: Contour plots showing $C_4A_3\bar{S}$ weight percentage (determined by QRA) versus duration and temperature of the thermal treatment (empty squares indicate measured points).	76
Figure IV-6: Evolution of phase composition (from Rietveld quantitative analysis) according to the sintering strategy. The quantity of $CaSO_4$ is the sum of residual calcium sulfate shown in Figure IV-4, plus 10 wt.% of added $CaSO_4$	76
Figure IV-7: Experimental procedure to compensate sulfate vaporization.	77
Figure IV-8: Rietveld plots and quantitative phase analysis of the SM(1300_3_2) sample.	78
Figure IV-9: Dilatometric curve of the prepared SM raw mixture during heating and cooling.	79
Figure IV-10: Back-scattered SEM micrographs of the SM sample sintered at different temperatures for 3h accompanied with their grey-level threshold segmentation. Magnification of X 50 was used for all images (Bars represent 500 μm and Red area represents pore area fraction of the SEM micrographs).	80
Figure IV-11: Evolution of open porosity fraction and apparent density (grey line) according to sintering temperature of SM fired pellets. Open porosity fraction was obtained from Archimedes principle (dashed black line) and from BSE-image analysis (continuous black line).	81
Figure V-1: DTA-TGA of gel precursor made by the Pech70 method (a), Pech95 method (b), OSE method (c) and SPC method (d).	84
Figure V-2: XRD patterns of the gel precursor, synthesized by the Pech70 method (a), Pech95 method (b), OSE method (c) and SPC method (d), calcined at 400°C, 700°C, 900°C, 1000°C, 1200°C, 1250°C and 1290°C for 1 h (Y= Ye'elimite, G = Grossite, K = Krotite, C = CaO, B = Bassanite, Cc = Calcium carbonate, An = Anhydrite).	87
Figure V-3: Rietveld quantitative analysis plots of ye'elimite powder prepared at 1250°C by the Pech70 method (a), Pech95 method (b), OSE method (c) and SPC method (d).	89
Figure V-4: Effect of calcination temperature on the crystallite size (calculated from (E.24)) of ye'elimite synthesized by the different chemical routes.	90
Figure V-5: SEM micrographs of the gels precursors calcined at 1250°C for 1 h. Zooms show that each agglomerate consists of nanometric particles. Their average diameter, $D_{particle}$, as well as the deviation, determined by PSD-IA, are presented.	92

Figure V-6: PSD-LD analysis (volume % curves) of ye'elinite powder prepared at 1250°C by the Pech method, OSE method and SPC method.	93
Figure V-7: PSD-LD analysis (cumulative volume % curves) of ye'elinite powder prepared at 1250°C by the Pech method, OSE method and SPC method.	93
Figure V-8: Radar chart to summarize all the parameters of ye'elinite powder prepared at 1250°C by the Pech method, OSE method and SPC method (values between brackets represent the maximum value of each parameter).	95
Figure VI-1: X-Ray diffractograms of samples treated from 1000 to 1300°C for 3 h.	98
Figure VI-2: X-Ray diffractograms of samples treated at 1300°C from 0 to 180 min.	99
Figure VI-3: EDS mapping of elements present in the samples treated for 3 h between 1000°C (a), 1100°C (b), 1200°C (c), 1250°C (d) and 1300°C (e). Magnification of x150 was used for all images (Bars represent 250 μ m). The corresponding EDS point analysis are shown in Appendix 1.	100
Figure VI-4: EDS mapping of elements present in the samples treated at 1300°C for different durations: 15 min (a), 30 min (b), 60 min (c), 120 min (d) and 180 min (e). Magnification of x500 was used for all images (Bars represent 50 μ m). The red line of the sample treated at 30 min (Figure VI-4-b) represents EDS line-scan, the results of the line scan are shown in Figure VI-5 and the corresponding EDS point analyses are shown in Appendix 1.	102
Figure VI-5: (a) Composition profile obtained by EDS along the red line for the sample treated at 1300°C for 30 min (The EDS line-scan is represented by the red line in Figure VI-4), (b) Representation of EDS line scan data in ternary atomic percentage diagram of Al-Ca-S (the red square, represents theoretical atomic composition of CA ₂ , the green square represents theoretical atomic composition of CA and the purple square represents theoretical atomic composition of C ₄ A ₃ S̄. The black triangles are associated to the collected EDS data.....	104
Figure VI-6: (a) Schematic representation of solid-state diffusion during ye'elinite formation. (b) Schematic representation of microstructural development of ye'elinite formation according to the sintering temperature. (c) Schematic representation of microstructural development of ye'elinite formation according to the sintering duration.	106
Figure VI-7: Simple schematic model of reaction-product layers forming on alumina grain.	107
Figure VII-1: Ionic conductivity evolution of ye'elinite suspensions Ye-sol-0, Ye-chem, Ye-sol-5 and Ye-sol-10. All suspensions were prepared with W/C = 1000. t = 0 min in the graph's abscissa refers to the time when ye'elinite is added to the citric acid solution.	113
Figure VII-2: SEM micrographs of Ye-sol-0 (a), Ye-sol-10 (b) and Ye-chem (c) suspensions. Observations were carried out after 1 min of hydration and all suspensions were prepared with W/C = 1000.	114
Figure VII-3: (a) Citric acid structure (CHEBI:30769) from the European Bioinformatics Institute Database [228], atoms are represented as spheres and are color coded as: carbon (grey), hydrogen (white) and oxygen (red). (b) Orthorhombic ye'elinite structure from Cuesta et al. [229] showing the (131) crystallographic plane, Ca denoted within dark-green spheres, Al within light blue tetrahedra, S within yellow tetrahedra, and O are red. For clarity CaO bonds are omitted in the represented structure.....	116
Figure VII-4: XRD patterns (a), TGA curves (b), and calculated hydration degree (α) (c), for CSA model cements (CSA-sol-0) and (CSA-Chem) at different hydration ages. E: ettringite; G: Gypsum; M: monosulfate; Y: ye'elinite; A: Gibbsite, (α %) is given by equation (E.0).	120
Figure VII-5: XRD patterns (a), TGA curves (b), and calculated hydration degree (α) (c), for CSA model cements (CSA-sol-0), (CSA-sol-0.5) and (CSA-sol-1) at different hydration ages. E: ettringite; G: Gypsum; M: monosulfate; Y: ye'elinite; A: Gibbsite. (α %) is given by equation (E.0).	123

List of Tables

Table I-1: Classification of calcium sulfoaluminate cements suggested by Aranda et De la Torre (2013) [13]... 11	11
Table I-2: Survey of mineralogical composition of calcium sulfo-aluminate clinkers reported in literature from 1962 to 2019. 11	11
Table I-3: Crystallographic data of ye'elimite published in the literature..... 19	19
Table I-4: Summary of solid-state ye'elimite synthesis protocols used in previous works (S: stoichiometric / NS: non stoichiometric). 21	21
Table I-5: Possible reactions involved during ye'elimite formation in different temperature ranges [9]..... 22	22
Table I-6: Summary of physical and chemical characteristics of some cementitious phases prepared by chemical synthesis routes (Pech=Pechini method; OSE=Organic Steric Entrapment method; SPC=Self-Propagating Combustion)..... 24	24
Table II-1: ICSD collection codes used for XRD-Rietveld quantitative analysis. 43	43
Table II-2: Polishing steps. 50	50
Table III-1: Chemical analysis and physical characteristics of the raw materials used for the synthesis of ye'elimite by solid-state reactions. 54	54
Table III-2: Chemical analysis and physical characteristics of the raw materials used for the synthesis of ye'elimite by sol-gel methods. 55	55
Table III-3: Amounts of raw materials employed for the preparation of SM sample (expressed in grams). 56	56
Table III-4: Temperature and duration of thermal treatment of the samples studied in this work. 56	56
Table III-5: Powder preparation and processing variables. 60	60
Table III-6: Comparison between the principles of the three chemical routes used in the present work for the synthesis of ye'elimite..... 63	63
Table III-7: Presentation of all prepared samples and the corresponding performed characterizations techniques. 69	69
Table V-1: Summary of thermal events shown in Figure V-1 83	83
Table V-2: Quantitative Rietveld analysis of the powders prepared by Pech70, Pech95, OSE and SPC routes after a heat treatment from 1000°C to 1250°C for 1 h. The values in brackets correspond to phase content error from Rietveld quantitative analysis. (*) Rwp is the weighted profile factor (E.25). 88	88
Table VII-1: Physical and chemical characteristics of the ye'elimite powders (Ye-sol and Ye-chem). 112	112
Table VII-2: Zeta potential measurements of the prepared ye'elimite suspensions. 115	115
Table VII-3: Rietveld phase analysis results (wt.%) for model cements (CSA-sol) and (CSA-Chem) at different hydration ages. Rietveld agreement factors are also given (equations E.25, E.26 and E.27). 118	118
Table VII-4: Rietveld phase analysis results (wt.%) for model cements (CSA-sol-0), (CSA-sol-0.5) and (CSA-sol-1) at different hydration ages. Rietveld agreement factors are also given (equations E.25, E.26 and E.27). 121	121

Introduction

- **Background**

To date, concrete is the most commonly used construction material on earth. The hydraulic binder connecting the aggregates contained in the concrete is mainly Ordinary Portland Cement (OPC). Every year, about 1.7 billion tons of OPC are produced worldwide, which corresponds to the amount required to produce annually more than 6 km³ of concrete [1]. OPC cement is a splendid building material not only because of its mechanical properties but also because it is accessible, easy to use and affordable. The concrete embodied energy is lower than that related to the production of other building materials, as shown Figure Intro-1 [2]. However, OPC cement is produced in large quantities in comparison with other building materials (Figure Intro-2) [1,3]. Thereby, OPC cement industry is responsible for almost 5% of total anthropogenic CO₂ emissions. In OPC cement production, the clinkerisation stage (which corresponds to the thermal treatment at high temperature in order to synthesize what is called ‘clinker’) is the most energy-intensive phase, and therefore the largest contributor to CO₂ emissions and costs of energy production (Figure Intro-3) [4]. During the clinkerisation stage, large quantities of emitted CO₂ come mainly from limestone decarbonation, according to the following reaction:

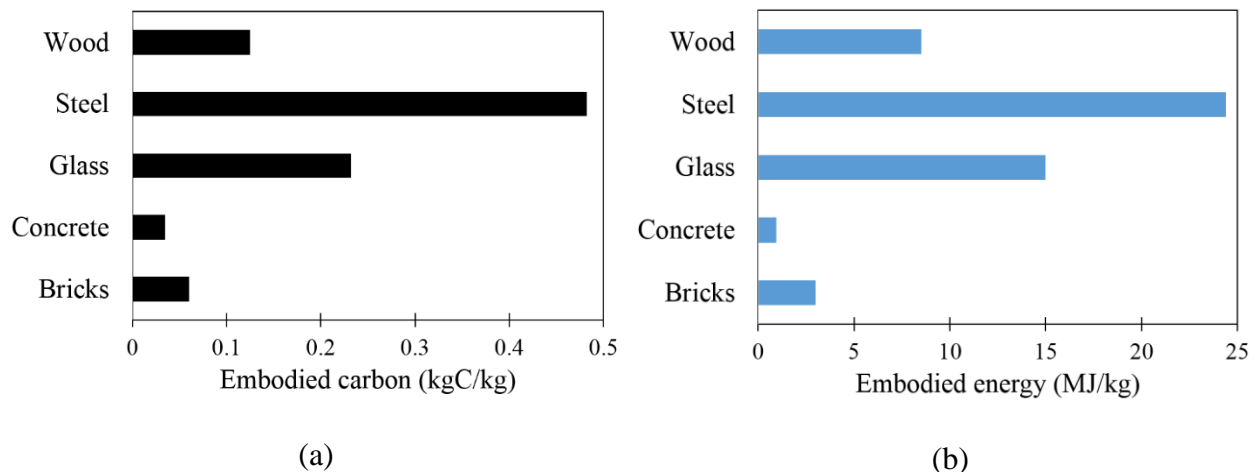
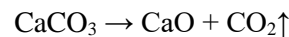


Figure Intro-1: Embodied carbon (a) and embodied energy (b) of the main construction materials [2].

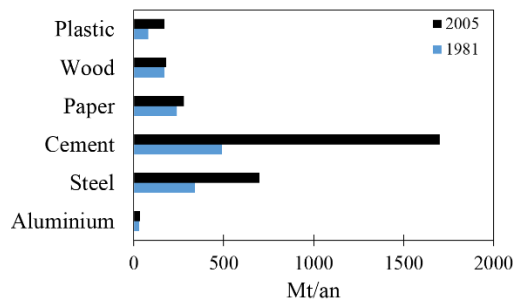


Figure Intro-2: World production of materials in Mt for the years 1981 and 2005 (according to the International Energy Agency (IEA) [3]).

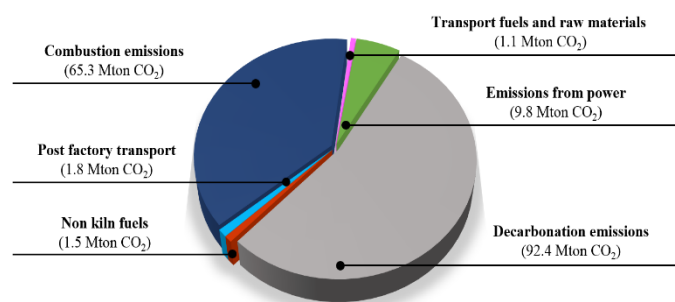


Figure Intro-3: Sources of CO₂ emissions in cement manufacturing and the corresponding quantities for the year 1990 (according to CEMBUREAU [4]).

To reduce CO₂ footprint of OPC cement industry, a great deal of current research projects is focusing on alternative environmental friendly binders. Recently, calcium sulfoaluminate (CSA) cement has been regarded as a sustainable binder to replace OPC cement, since the production of the CSA cement involves less calcium carbonate and a lower clinkering temperature compared to OPC. This entails that the CSA cement is a more sustainable cement than OPC leading to less CO₂ emissions during its production process. In addition, CSA cement can reduce energy consumption during clinker grinding due to its more friable nature [1,5,6]. CSA cements are of interest in applications such as shrinkage-compensating concrete and self-stressing concrete. They exhibit key features including high early strength and rapid setting, which are mainly attributed to the presence of the « ye'elinite ($\text{Ca}_4(\text{AlO}_2)_6\text{SO}_4$ i.e. $\text{C}_4\text{A}_3\bar{\text{S}}$ in cementitious notation) » cementitious phase. CSA cement named (Komponent[®]) was used as a shrinkage-compensating cement additive to minimize or eliminate drying shrinkage cracking of concrete during the rehabilitation project of the Lokern Road Bridge, California, USA (Figure Intro-4) [7].



Figure Intro-4: Lokern road bridge rehabilitation project, California (USA) [7].

The CSA cement contains besides ye'elinite, other phases such as calcium aluminates, belite (dicalcium silicate) and calcium aluminoferrite, and they are generally blended with calcium sulfate [8]. According to recent surveys about the different CSA compositions [9], it is clear there are several types of CSA cements. Because of the chemical and mineralogical nature of the CSA clinkers, it is not possible to standardize under EN 197-1 which only covers Portland compositions. This standardization, which is a necessary condition for the use of these cements in the building sector, will need the development of a completely new standard different from EN 197-1. In this respect, the composition of a cement has to be described precisely and thoroughly, together with its chemical and physical characteristics. At the present time, to our knowledge, CSA cements have not been normalized according to European standardization procedure because neither the composition nor the characteristics have been described precisely. Therefore, there is a need to identify the composition of each phase together with its chemical and physical behaviors. To examine the hydration behavior of calcium sulfoaluminate cements, individual and pure components should be prepared, one being ye'elinite. As commercially available CSA cements are a mix of several phases, it is impossible to separate ye'elinite from the other phases. Therefore, a need exists to synthesize ye'elinite phase in a pure state at the lab scale.

Besides the fundamental comprehension of pure ye'elinite hydration, the investigation of ye'elinite synthesis conditions and the study of its formation mechanisms are of utmost importance. In fact, this is helpful, on one hand, for industrial cement researchers to understand and to optimize the clinkerisation process of CSA cements, and, on the other hand, for academic researchers to synthesis pure ye'elinite

for fundamental hydration studies, crystallographic structure characterization and other investigation experiments.

- **Research objectives**

CSA cement hydration is one subject of interest to cement researchers; the main conclusion is that ye'elimite phase is the main reacting phase at early ages and the silicate phases are contributor to the microstructure development and the durability of CSA cements at later ages [10]. The principal research objectives of our PhD thesis are the following: (i) the synthesis of highly pure ye'elimite powder prepared by two ways consisting in solid-state reaction method and sol-gel routes, (ii) the fundamental comprehension of ye'elimite formation mechanisms during the clinkerisation, and finally, (iii) the hydration study of CSA model cement consisting of the lab-made pure ye'elimite blended with gypsum. In this last part of the work, the influence of an additive, namely citric acid, and ye'elimite finesse on hydration rate will be examined.

- **Outline of the thesis**

This thesis is divided into seven chapters:

Following this introductory chapter, Chapter I shows a literature review relevant to the research presented within the thesis. Especially, a presentation of the environmental advantages of CSA cements, a survey of mineralogical compositions of CSA clinkers reported in literature have also been addressed, a description of ye'elimite crystallographic polymorphs, as well as a review of studies dealing with ye'elimite synthesis methods. Finally, the last part of Chapter I is devoted to the physical and chemical parameters influencing cement hydration at early age, in particular dissolution of anhydrous phases and formation of hydrate phases.

Chapter II describes and justifies the experimental framework of the study. In particular, the experimental techniques of samples characterization used during this work.

Chapter III describes, firstly, the physical and chemical characteristics of the materials used during the present thesis. Then it details the experimental protocols adopted to prepare the different samples. It is worth noting that the synthesis methods described hereafter were originally developed in the present thesis to synthesize highly pure ye'elimite.

Chapter IV deals with the experimental investigation of ye'elimite synthesis by solid-state reaction method. The results obtained are then discussed to identify the optimal synthesis conditions.

Chapter V describes original experimental protocols, based sol-gel method, to synthesize nano-sized ye'elimite grains with small crystallite size. Four different chemical routes were used for the synthesis. The resulting synthesis ye'elimite powders are well characterized and compared.

The main experimental results of Chapter VI were addressed to understand fundamentally the formation mechanisms of ye'elimite during a thermal treatment. Mineralogical composition and microstructural development were identified at each stage of ye'elimite formation.

The last chapter of this thesis, Chapter VII, presents the effect of two basic factors influencing the hydration of ye'elimite-rich cements. The chapter starts by discussing the effect of finesse and citric acid addition on ye'elimite powder dissolution. The role of ye'elimite powder finesse was examined by comparing the hydration of ye'elimite powder synthesized by solid-state reactions with that synthesized originally by sol-gel method. The last part of this chapter continues with studying the influence of the said factors on CSA model cement hydration.

Finally, the conclusion part covers the main results that emerge throughout this study and future perspectives are also suggested in this part.

Note: part of the work presented in this manuscript has been published (3 published articles, 3 submitted publications) and presented in conferences (5 conferences; one got the best poster award). The complete list is given in appendix 5.

Chapitre I. Literature review

I.1. Introduction

This literature review contains a presentation of the environmental advantages of CSA cements (I.2). A survey of mineralogical compositions of CSA clinkers reported in literature (I.3) has also been addressed, together with a description of ye'elimite crystallographic polymorphs (I.4), as well as a review of studies dealing with ye'elimite synthesis (I.5). Finally, the last part of Chapter I is devoted to the physical and chemical parameters influencing cement hydration at early age (I.6), particularly, dissolution of anhydrous phases and formation of hydrate phases.

I.2. Calcium Sulfo-Aluminate (CSA) cements

CSA cements have been developed since the end of the 1950s, when Professor Alexander Klein studied the addition of CSA based clinkers to OPC cements for shrinkage compensation, which contributed to the invention of ASTM Type K¹ cement (ASTM C845). CSA cement has been used as a binder in specific concretes for bridges, airport runways, freeway pavement, and many other applications where a fast setting is needed. Under the name, « the third cement series », CSA cements were industrially produced and standardized in China for the first time in 1970. To date, CSA cements are produced and commercialized in Europe and USA to make fast-setting mortars, shrinkage compensation and expansive concretes [11].

Recently, the interest of the international cement research community toward CSA cements has been due not only to their expansive behaviour, but also to environmentally friendly characteristics associated to their production, which includes reduced CO₂ footprint [1,5]. This reduction depends on the cement composition, but CSA manufacturing process can release up to 40% less CO₂ than that of OPC cement. This is detailed in the next chapter part.

I.2.1. CO₂ emission reduction in the manufacturing process of CSA cements

CSA clinkers are produced at temperature ranges between 1250 and 1300 °C, which is ~200 °C lower than that of OPC clinker production. Moreover, the amount of limestone needed is much less. Limestone calcination is one of the main emitters of CO₂ in the clinkering process. Figure I-1 shows the energy requirements (calculated from standard enthalpies) and CO₂ quantities released during formation of pure

¹ Type-K cement is a mix of OPC cement, ye'elimite, gypsum and lime.

anhydrous cement phases made from stoichiometric mixtures $\text{CaCO}_3, \text{SiO}_2, \text{Al}_2\text{O}_3$ or CaSO_4 depending on the cement phase [11]. The formation of ye'elimite, which is the main phase in CSA cements, requires only 800 kJ/kg, which represents 43%, 60% and 77% of the specific energy needed to form C_3S (Ca_3SiO_5), C_2S (Ca_2SiO_4) and CA (CaAl_2O_4), respectively. The reduced amounts of formation energy and limestone amounts involved during CSA production enable a reduction of at least 40 % of CO_2 emissions. In addition, thanks to their high porosity, CSA clinkers are easier to grind than OPC clinkers. However, SO_2 gas emission during their clinkering stage is still significantly higher.

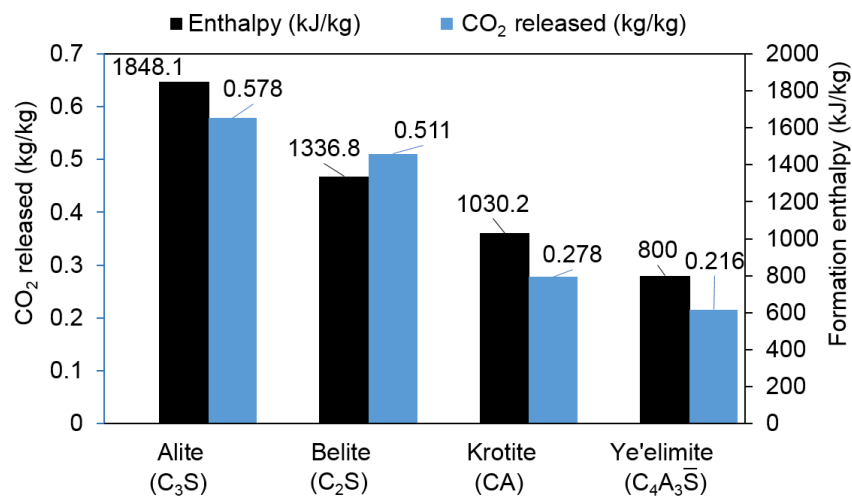


Figure I-1 : Energy requirement and CO_2 released during cement phases formation.

Despite these environmental advantages, the production and commercialization of CSA cements are still somewhat limited by the expensive cost of alumina source like bauxite, which is less abundant than other raw materials like clay and limestone. Nevertheless, several industrial by-products and wastes could be valorized as raw materials to produce CSA cements. We mention as examples bauxite wastes, fly ashes, granulated blast furnace slag, phosphogypsum and dams sludge [12]. So far, it is unlikely that CSA cements will be produced on a large scale until the cost of emitting CO_2 becomes significantly higher than it currently is [6].

I.2.2. Mineralogical composition of CSA cements

Depending on raw materials composition, CSA clinker contains different cementitious phases such as ye'elimite ($\text{C}_4\text{A}_3\bar{\text{S}}$) as characteristic and main phase, belite (C_2S), krotite (CA), grossite (CA_2), tricalcium aluminate C_3A , brownmillerite (C_4AF), mayenite (C_{12}A_7), and sometimes it contains also

small quantities of gehlenite (C_2AS), perovskite (CT) and periclase (M). CSA clinker is generally blended either with gypsum or with anhydrite to obtain CSA cement. The quantity of the added $CaSO_4$ generally ranges between 15 and 25 wt.% [12].

Since durability and hydration properties of CSA cements depend primarily on their mineralogical composition, Aranda et al. [13] suggest a classification of CSA cements into 4 categories: Calcium Sulfo-Aluminate clinker (CSA), Iron-rich Belite Calcium Sulfo-Aluminate clinker (BCSAF), Aluminum-rich Calcium Sulfo-Aluminate clinker (BCSAA) and Alite Calcium Sulfo-Aluminate clinker (ACSA). Table I-1 summarizes this classification.

The clinker labeled CSA refers to ye'elimite-rich clinker, which contains between 50 and 80 wt.% of ye'elimite. This type of cement contains belite (C_2S) as a secondary cementitious phase and small amounts of C_4AF , $C\bar{S}$ and CT. Under the name of « the third cement series », CSA cement was the first type of calcium sulfo-aluminate cement produced in China since 1970. It is characterized by its dimensional expansive behavior at early age of hydration.

Several authors studied BCSA clinker in order to develop an environment friendly binder, which can replace OPC cement. BCSA cement shows somewhat similar hydration properties to those of OPC cement, and its production requires lower quantities of bauxite compared to CSA clinker. BCSA clinkers are belite-rich cements and contain ye'elimite as a secondary cementitious phase. They contain more than 50 wt.% of β - C_2S and from 20 to 30 wt.% of $C_4A_3\bar{S}$. The most common formulation of BCSA clinker is the iron-rich one called Iron-rich Belite Calcium Sulfo-Aluminate clinker (BCSAF), which contains primarily β - C_2S , $C_4A_3\bar{S}$ and C_4AF . Its clinkering temperature is almost 1250°C. To improve the mechanical properties of BCSAF cement at early age of hydration, C_4AF could be substituted by calcium aluminate phases such as krotite CA or mayenite $C_{12}A_7$. This recent formulation is named Aluminum-rich Calcium Sulfo-Aluminate clinker (BCSAA).

The presence of ye'elimite ($C_4A_3\bar{S}$) and alite (C_3S) as major phases simultaneously in one formulation of calcium sulfo-aluminate clinker is possible. In fact, this type of clinker is named Alite Calcium Sulfo-Aluminate clinker (ACSA). C_2S , C_4AF and C_3A constitute the minor cementitious phases of this type of clinker.

Referring to the Aranda et al. [13] suggested classification shown in Table I-1, we report in Table I-2 a survey of mineralogical composition of calcium sulfo-aluminate clinkers reported in literature from 1962 to 2019. Some examples of these composition were reported in Figure I-2 and Figure I-3. It is clear that calcium sulfo-aluminate clinkers show a very large range of composition that need to be clarified.

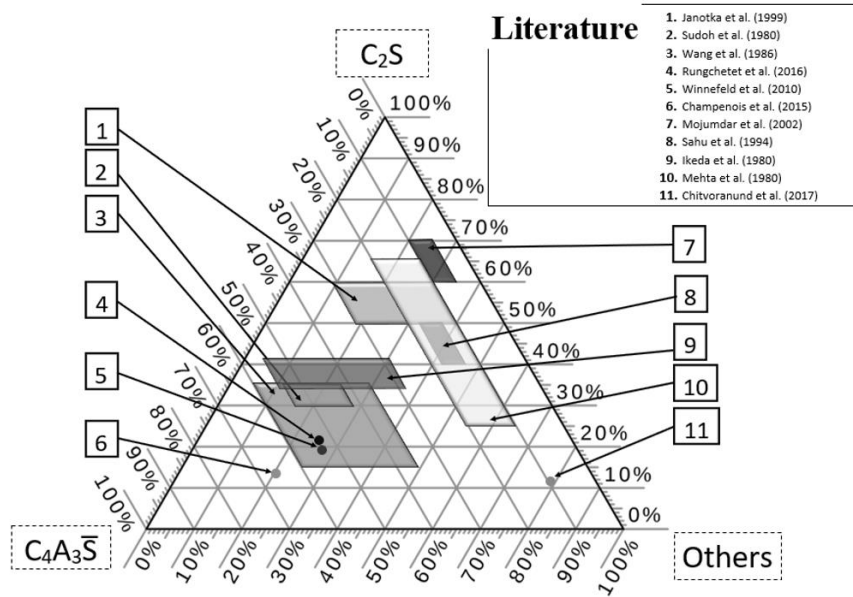


Figure I-2: State of the art about CSA composition collected from literature in the ternary system $C_4A_3\bar{S}$ - C_2S -others (Ferrite, Calcium aluminate, ...) [14-24].

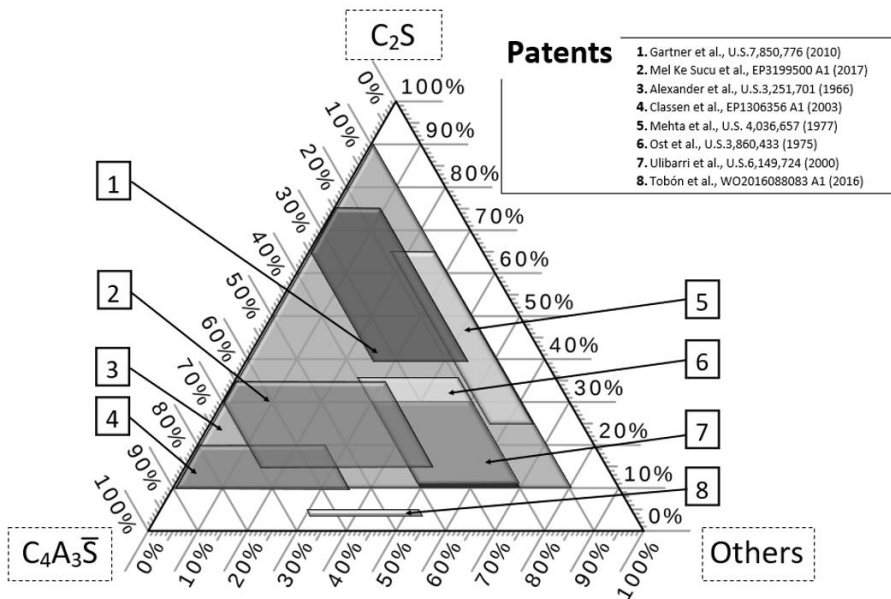


Figure I-3: State of the art about CSA composition collected from patents in the ternary system $C_4A_3\bar{S}$ - C_2S -others (Ferrite, Calcium aluminate, ...) [25-32].

Table I-1: Classification of calcium sulfoaluminate cements suggested by Aranda et De la Torre (2013) [13].

Acronym	Nomenclature	Major phase	Secondary phases	Minor phases
CSA	Calcium sulfo-aluminate	$C_4A_3\bar{S}$	C_2S	$C_4AF, C\bar{S}, CT$
BCSAF	Iron-rich belite calcium sulfo-aluminate cement	C_2S	$C_4A_3\bar{S}$	C_4AF, CT
BCSAA	Aluminum-rich calcium sulfo-aluminate cement	C_2S	$C_4A_3\bar{S}$	$CA, C_{12}A_7$
ACSA	Alite calcium sulfo-aluminate cement	$C_4A_3\bar{S}$	C_3S	C_2S

Table I-2: Survey of mineralogical composition of calcium sulfo-aluminate clinkers reported in literature from 1962 to 2019.

Year	Type	Major phase	Secondary phases	Minor phases	Document	Réf.
1962	CSA	$C_4A_3\bar{S}$ (55%)	C (19%)	C_3A	Article	[33]
1965	CSA	$C_4A_3\bar{S}$ (20-100%)	-	$C\bar{S}-C$	Article	[34]
1966	BCSAF	C_2S (23.7-44.4%)	$C_4A_3\bar{S}$ (16.7-19.3%)	$C_4AF-C\bar{S}-C$	Patent	[27]
1975	BCSAF	C_2S (45.0%)	$C_4A_3\bar{S}$ (26.5%)	$C\bar{S}-C-C_4AF$	Patent	[30]
1977	BCSAF	C_4AF (15-65%)	$C_4A_3\bar{S}$ (10-20%)	$C_2S-C\bar{S}$	Patent	[29]
1981	BCSAF	C_2S (63%)	$C_4A_3\bar{S}$ (23%)	$C-C_4AF$	Article	[35]
1982	CSA	$C_4A_3\bar{S}$ (29.7%)	C_2S (23.87%)	$C\bar{S}-C_4AF-C_3S$	Article	[36]
1983	BCSAF	C_2S (44.6%)	$C_4A_3\bar{S}$ (16.1%)	$C_4AF-C_3S-C\bar{S}$	Article	[37]
1985	BCSAF	C_2S (65.4%)	$C_4A_3\bar{S}$ (18.5%)	$C_4AF-C\bar{S}-C$	Article	[38]

1991	BCSAF	C_2S (67%)	$C_4A_3\bar{S}$ (19%)	$C_4AF-C\bar{S}-C$	Article	[39]
1994	BCSAF	C_2S (43.2-58.2%)	$C_4A_3\bar{S}$ (13.3-18.4%)	$C_2AS-C\bar{S}-C_4AF-C$	Article	[21]
1995	BCSAF	C_2S (47.1%)	$C_4A_3\bar{S}$ (20.1%)	$C\bar{S}-C_4AF$	Article	[40]
1996	CSA	$C_4A_3\bar{S}-C\bar{S}-C$	-	-	Article	[41]
1996	CSA	$C_4A_3\bar{S}$ (54.5%)	$C_5S_2\bar{S}$ (18.2%)	$C\bar{S}$	Article	[42]
1999	BCSAF	C_2S (51.7%)	$C_4A_3\bar{S}$ (23.4%)	$C_3S-C_4AF-C_3A-C\bar{S}$	Article	[14]
1999	BCSAF	C_2S (49.07%)	C_4AF (19.16%)- $C_4A_3\bar{S}$ (10.15%)	$C\bar{S}-C$	Article	[43]
2000	CSA	$C_4A_3\bar{S}$ (20-40%)	C_2S (10-30%)	$C_3S-C\bar{S}-C$	Patent	[31]
2000	BCSAF	C_2S (53.2%)	$C_4A_3\bar{S}$ (33.9%)	$C\bar{S}-C_4AF$	Article	[44]
2002	BCSAF	C_2S (67.1%)	C_4AF (19%)	$C_4A_3\bar{S}-C\bar{S}$	Article	[20]
2003	CSA	$C_4A_3\bar{S}$ (>55%)	C_2S (>10%)	$C\bar{S}$	Patent	[28]
2003	BCSAF	C_2S (61%)	$C_4A_3\bar{S}$ (11%)	C_4AF-C_3S	Article	[45]
2006	BCSAF	C_2S (40-75%)	$C_4A_3\bar{S}$ (15-35%)	$C_2A_xF_{1-x}$ ($0.2 < x < 0.8$)- $C\bar{S}$	Patent	[46]
2006	CSA	$C_4A_3\bar{S}$ (53.0%)	C_2S (13.2%)	$C\bar{S}-C_{12}A_7$	Article	[47]
2006	CSA	$C_4A_3\bar{S}$ (57%)	CA (15%)- C_2AS (16%)	$C\bar{S}-C_{12}A_7-C_4AF-$ $CT-C$	« Rockfast450® » Lafarge	[48]
2007	BCSAF	C_2S (51%)	$C_4A_3\bar{S}$ (29%)	C_4AF	Article	[49]
2007	BCSAF	C_2S (50.3%)	$C_4A_3\bar{S}$ (20.2%)	$C\bar{S}-C_4AF$	Article	[50]

2008	CSA	$C_4A_3\bar{S}$ (43%)	C_2S (12%)	$C_4AF-C_3A-C\bar{S}$ - CT- $C_5S_2\bar{S}$	Article	[51]
2009	CSA	$C_4A_3\bar{S}$ (53.5%)	C_2S (21.2%)	C_4AF -CT	« TS [®] » Belitex	[52]
2010	CSA	$C_4A_3\bar{S}$ (55-75%)	C_2S (15-30%)	$C_4AF-C\bar{S}$ -MgO- CT- C_2AS	Patent	[53]
2010	CSA	$C_4A_3\bar{S}$ (54%)	C_2S (19%)	$C\bar{S}$	Article	[12]
2010	CSA	$C_4A_3\bar{S}$ (68.1%)	C_2AS (14.8%)	$C_3A-CA-CA_2$ -CT- C	Article	[54]
2010	BCSAF	C_2S (52%)	$C_4A_3\bar{S}$ (33%)	C_4AF	Article	[55]
2011	CSA	$C_4A_3\bar{S}$ (68.5%)	C_2S (15.9%)	$C\bar{S}-C_{12}A_7$ -CT-M-S	Article	[56]
2011	CSA	$C_4A_3\bar{S}$ (62.8%)	C_2AS (18.3%)	CA- CA_2 -CT-MA	Article	[57]
2011	CSA	$C_4A_3\bar{S}$ (65%)	C_2S (22%)	$C\bar{S}-C_4AF$ -C	Article	[58]
2011	CSA	$C_4A_3\bar{S}$ (68.5%)	C_2S (15.9%)	$C\bar{S}-C_{12}A_7$ -M-CT-S	« KTS100 [®] » Belitex	[59]
2011	BCSAF	C_2S (48.3%)	$C_4A_3\bar{S}$ (28.2%)	$C_4AF-C\bar{S}$	« Aether [®] » Lafarge	[60]
2011	CSA	$C_4A_3\bar{S}$ (57.37%)	C_2S (25.55%)	$C_4AF-C\bar{S}$	« R.SAC 42.5 » Tangshan Polar Bear Building Materials Co- China	[61]
2012	CSA	$C_4A_3\bar{S}$ (65.3%)	C_2S (22.4%)	$C\bar{S}-C_4AF$	Article	[62]
2012	BCSAF	C_2S (56.7%)	$C_4A_3\bar{S}$ (31.1%)	C_4AF -CT	Article	[63]
2013	BCSAA	C_2S (56.2%)	$C_4A_3\bar{S}$ (34.4%)	C_3A	Article	[64]
2013	CSA	$C_4A_3\bar{S}$ (40.3%)	CSH_2 (26.1%) - C_2S (9.4%)	CT-M- $K\bar{S}$ - C_4AF	« CS10 [®] » BELITH	[65]
2014	BCSAF	C_2S (58.8%)	$C_4A_3\bar{S}$ (26.5%)	$C_4AF-C_2AS-K\bar{S}$	Article	[66]

2015	CSA	$C_4A_3\bar{S}$ (66.2%)	C_2S (13.5%)	$C_{12}A_7$ -CT-MgO	Article	[19]
2015	CSA	$C_4A_3\bar{S}$ (63.7%)	C_2S (21.7%)	C_4AF -C-M- $C\bar{S}$ - $K\bar{S}$ - $C_2K\bar{S}_3$	Article	[67]
2015	CSA	$C_4A_3\bar{S}$ (65%)	C_2S (9%)	$C_{10}S_3\bar{S}_3F_2$ - $C_{12}A_7$ -CT-M- $C\bar{S}$	Article	[68]
2016	CSA	$C_4A_3\bar{S}$ (48.43%)	C_2S (30.27%)	C_4AF -C- $C\bar{S}$	Article	[17]
2016	CSA	$C_4A_3\bar{S}$ (65.5%)	C_2S (4.6%)	C_3S - C_3A - $C\bar{S}$ - $C\bar{S}H_2$ -C-S	Patent	[32]
2016	CSA	$C_4A_3\bar{S}$ (24.8%)	C_2S (52.4%)	C_4AF - C_2F -CA- $C\bar{C}$ - $C\bar{S}$ - $K\bar{S}$	Article	[69]
2016	BCSAF	C_2S (43.6%)	$C_4A_3\bar{S}$ (22.3%)	C_4AF - $C\bar{S}$ -C	Article	[70]
2017	ACSA	C_3S (48.3%)	C_4AF (12.9%)	$C_4A_3\bar{S}$ - $C\bar{S}$ - C_2AS - $C_5S_2\bar{S}$	Article	[24]
2017	CSA	$C_4A_3\bar{S}$ (35-70%)	C_2S (15-35%)	C_4AF - $C\bar{S}$ - $C_{12}A_7$	Patent	[26]
2017	CSA	$C_4A_3\bar{S}$ (20-70%)	C_2S (40-60%)	C_4AF - $C_5S_2\bar{S}$	Patent	[71]
2017	CSA	$C_4A_3\bar{S}$ (20-40%)	C_2S (10-30%)	$C\bar{S}$ - C_3S -C	« CSA » Cemex	[71]
2017	BCSAF	C_4AF (30-40%)	$C_4A_3\bar{S}$ (15-25%) - CH (20-35%)	C	« Denka® » CSA	[71]
2017	CSA	$C_4A_3\bar{S}$ (60-70%)	C_2S (10-25%)	C_4AF - $C_5S_2\bar{S}$	« Type II et III CSA » » China	[71]
2017	CSA	$C_4A_3\bar{S}$ (60%)	C_2S (22%)	C_4AF - $C_{12}A_7$ - C_3S	« Barnstone CSA »	[71]
2017	CSA	$C_4A_3\bar{S}$ (48.4%)	C_2S (30.3%)	C_4AF -C- $C\bar{S}$	Article	[72]
2017	CSA	$C_4A_3\bar{S}$ (54.3%)	C_2S (29.1%)	C_3MS_2 -C- $C\bar{S}$ - C_3FT	« Alpenat® » Vicat	[73]

2018	CSA	$C_4A_3\bar{S}$ (64%)	C_2S (30%)	C_4AF	Article	[74]
2018	CSA	$C_4A_3\bar{S}$ (64.4%)	C_2S (7.7%)	$C_9S_3\bar{S}_3, CaF_2-M-C_2AS-C\bar{S}$	Article	[75]
2018	CSA	$C_4A_3\bar{S}$ (15.85%)	$C_5S_2\bar{S}$ (12.60%)	$C_2S-C\bar{S}-S$	Article	[76]
2018	BCSAF	C_2S (45-75%)	$C_4A_3\bar{S}$ (20-45%)	$C_4AF-C\bar{S}-C_3S-C_3A-CA-CA_2-C_{12}A_7-C_5S_2\bar{S}$	« Ternocem® » HeidelbergCement	[77]
2019	CSA	$C_4A_3\bar{S}$ (87.9%)	$C\bar{S}$ (6.7%)	$CA-C\bar{S}-CA_2$	Article	[78]
-	CSA	$C_4A_3\bar{S}$ (>58%)	C_2S (<25%)	$C\bar{S}$	« ALIPRE GREEN® » Italcementi	[79]
-	CSA	-	-	-	« BluCem® » Bluey Technologies Pty Ltd.	[80]
-	CSA	-	-	-	« Rapid Set CTS 24/6® » CTS Cement	[7]
-	BCSAF	C_2S	$C_4A_3\bar{S}$	-	« Calumex BeliCem® » Caltra Nederland BV	[81]
-	CSA	$C_4A_3\bar{S}$ (50%)	$C\bar{S}$ (18%)	-	« Next base » Buzzi Unicem	[82]
2019	CSA	$C_4A_3\bar{S}$ (87.9%)	$C\bar{S}$ (6.7%)- CA (5.1%)	CA_2	Article	[83]
2019	CSA	$C_4A_3\bar{S}$ (71.2%)	C_2S (25.9%)	$C_3A-C_{12}A_7-C\bar{S}-S-C_3AS_3$	Article	[84]

Important points to remember:

Calcium sulfo-aluminate were developed for the first time in China with the production of CSA cement, which is a ye'elinite-rich cement. CSA cements show expansive behavior at early age of hydration. This characteristic makes CSA cements interesting candidates to be used for specific applications such as shrinkage compensation concrete or rapid-setting concrete. Recently, a new composition of calcium sulfo-aluminate clinkers, called Iron-rich Belite Calcium Sulfo-Aluminate clinker (BCSAF), was patented and well studied by several authors. BCSAF clinker contains, beside ye'elinite, high amounts of belite and ferrite. It shows hydration behaviour somewhat similar to that of OPC cement, and its manufacturing process releases less CO₂. That is why it is considered as an environmental friendly binder and thereby a sustainable alternative to OPC cement. In this respect, different research projects dealing with BCSAF clinker were developed especially in Europe.

From Aranda et al. [13] suggested classification, a survey of mineralogical composition of calcium sulfo-aluminate clinkers reported in literature from 1962 to 2019 has been reported. It shows a very large range of compositions, this can be a major obstacle for the standardization of CSA calcium sulfo-aluminate cements under the European norm. Meanwhile, it is noted that ye'elinite is the common cementitious phase present in all reported compositions. Thereby, hydration study and fundamental comprehension of its formation could be very helpful for the urgent need of CSA cement standardization under the European norm.

I.2.3. Crystallographic structure of ye'elinite

Ye'elinite phase ($\text{Ca}_4\text{Al}_6\text{O}_{12}\text{SO}_4$ or $\text{C}_4\text{A}_3\bar{\text{S}}$) is the main reacting phase of CSA cements, and many hydration characteristics depends on its reaction with water. Ye'elinite is also called « Klein's salt », because in the 1960s, Alexandre Klein studied the use of ye'elinite-rich clinker as expansive binder to compensate the OPC cement shrinkage [27]. The name of the mineral « Ye'elinite » originally refers to the geographic region « Hill Har Ye'elim » in Israel, where it was discovered in its natural form for the first time [85]. Recently, several authors got interested in lab-synthesis and structural characterization of this mineral to demystify its special hydration characteristics. In this part of Chapter I, a literature review of ye'elinite crystallographic structures as well as the current understanding in ye'elinite phase hydration are presented.

Ye'elinite phase belongs to the Sodalite mineral family. The general formula of sodalite structure is $\text{M}_4(\text{T}_6\text{O}_{12})\text{X}$, where T occupies tetrahedral sites and is often Si or Al, M is a low-charge cation (e.g., Na⁺, K⁺, Ca²⁺, Sr²⁺, ...) and X a charge-balancing anion (e.g., Cl⁻, SO₄²⁻, WO₄²⁻, CrO₄²⁻). However,

crystallographic structure of ye'elimite is complex and difficult to resolve precisely. For this reason there is no crystallographic structure resolved on ye'elimite single crystal up to now [86]. According to the powder X-ray diffraction data, ye'elimite was reported in literature as cubic, tetragonal and orthorhombic. However, it was noted recently that only cubic ($I\bar{4}3m$) and orthorhombic (Pcc2) structures exist. These two crystallographic polymorphs show different physical and chemical properties, such as reactivity with water. According to theoretical calculations based on density functional theory (DFT) [87], the ye'elimite orthorhombic structure is energetically more stable than the cubic structure. This is the reason why the cubic structure is not stable at ambient temperature and it exists only at high temperatures. The phase transition from Pcc2 to $I\bar{4}3m$ is reversible and it occurs at $\sim 470^\circ\text{C}$ showing a thermal hysteresis of $10\text{-}30^\circ\text{C}$. Table I-3 summarizes crystallographic data on ye'elimite polymorphs published in literature.

The cubic and orthorhombic polymorphs of ye'elimite are somewhat similar (Figure I-4) [88]. In fact, the two structures framework contain AlO_4 tetrahedra forming two different types of tetrahedral rings. The first one contains 6 connected AlO_4 tetrahedra and the second one contains 4 connected AlO_4 tetrahedra. Ca and S atoms are located inside the tetrahedral rings forming CaO_n polyhedra and SO_4 tetrahedra, respectively.

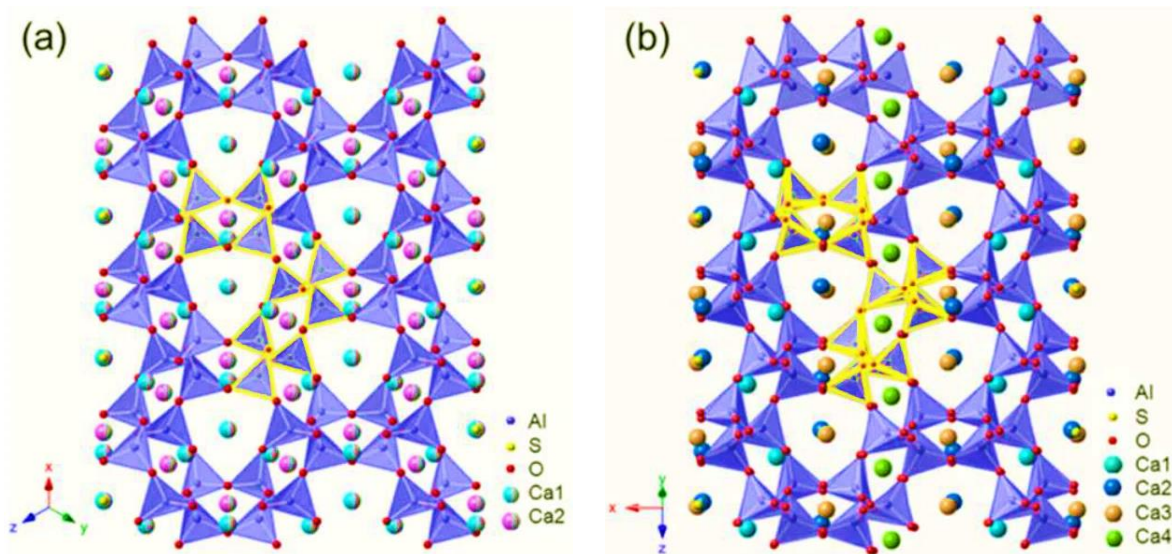


Figure I-4: Crystal structures of (a) cubic- $C_4A_3\bar{S}$ and (b) orthorhombic- $C_4A_3\bar{S}$. Irregular Al-O six membered rings and four-membered rings are highlighted [88].

In the case of ye'elimite cubic structure ($I\bar{4}3m$), there is one crystallographic site occupied by Al atoms and two crystallographic sites occupied by Ca atoms, their Wyckoff positions are 12d and 8c, respectively. The occupation ratio of 2 CaO_n ($n = 7$ and 9) polyhedron is 0.5. However, ye'elimite orthorhombic structure shows the lowest symmetry (Pcc2), and it contains 8 sites occupied by Al (2a, 2b, 2c, 2d, 4e) and 4 sites occupied by Ca (4e). The difference between the coordination environment of AlO_4 tetrahedra and CaO_n ($n = 7$ et 8) polyhedra explains the structural distortion of the ye'elimite orthorhombic lattice [86].

The thermal quenching, at temperature higher than structural transition temperature, and/or the addition of atoms forming solid-solution are usually two efficient techniques to stabilize high-temperature polymorph. In the case of ye'elimite, the high-temperature polymorph is cubic. It is stabilized by Ca^{2+} and Al^{3+} substitution with ions showing higher atomic radii to extend the structure to a stable state. For example, Al^{3+} substitution by Fe^{3+} ions allows the stabilization of the cubic phase ($I\bar{4}3m$). Iron contents up to 4.3 mol% (8.8 wt.%) were found in the $C_4A_3\bar{S}$ phase coexisting with melt and ferrite [89]. As well as, other solid solutions of ye'elimite were studied by addition of Na^+ , Si^{4+} , and Fe^{3+} [66,67,90]. In fact, Na^+ ions substitute partially Ca^{2+} ions, and Fe^{3+} , Si^{4+} substitute Al^{3+} ions to obtain a cubic structure of ye'elimite with formula $Ca_{3.8}Na_{0.2}Al_{5.6}Fe_{0.2}Si_{0.2}O_{12}SO_4$. Other authors confirm that Ba^{2+} and Sr^{2+} ions addition allows the stabilization of the ye'elimite cubic phase.

Kurokawa et al. [91] investigated the orthorhombic to cubic transformation of ye'elimite. The starting temperature of the orthorhombic-to-cubic transformation during heating was $438^\circ C$ and that of the reverse transformation during cooling was $469^\circ C$. The thermal hysteresis was negative ($-31^\circ C$), suggesting the thermoelasticity of the transformation. They found that the orthorhombic to cubic phase transformation would be principally accompanied by the statistical disordering in orientation of the SO_4 tetrahedra. These results were well confirmed by the change in Raman band corresponding to the ν_1 mode (SO_4 internal stretching mode) during heating.

Recently, the structure of $Sr_4[Al_6O_{12}]SO_4$ phase was studied by Banno et al. [92]. It was found that its structure is isomorphous with that of $Ca_4[Al_6O_{12}]SO_4$ (space group Pcc2). The structural model at $300^\circ C$ (space group I23 and $Z = 2$) was characterized by the positional disordering of oxygen atoms that form $[SO_4]$ tetrahedra.

Table I-3: Crystallographic data of ye'elimite published in the literature.

Year	Crystallographic polymorph	Space group	Crystallographic lattice parameters				ICSD Code	Réf.
			a (Å)	b (Å)	c (Å)	$\alpha; \beta; \gamma$ (°)		
1962	Cubic	I4 ₁ 32	18.390	18.390	18.390	90	-	Halstead et al. [33]
1965	Cubic	I23	9.190	9.190	9.190	90	28480	Kondo et al. [93]
1972	Cubic	I4 ₃ m	9.205	9.205	9.205	90	9560	Saalfeld et al. [94]
1992	Cubic	I4 ₃ m	9.022	9.022	9.022	90	67589	Brenchley et al. [95]
1992	Tetragonal	P4 ₁ 22	13.030	13.030	9.161	90	-	Krstanović et al. [96]
1995	Orthorhombic	Pcc2	13.028	13.037	9.161	90	80361	Calos et al. [97]
2013	Orthorhombic	Pcc2	13.025	13.025	9.155	90	237892	Cuesta et al. [87]
2014	Cubic	I4 ₃ m	9.243	9.243	9.243	90	194482	Kurokawa et al. [91]
2014	Cubic	I4 ₃ m	9.197	9.197	9.197	90	248572	Cuesta et al. [90]
2017	Orthorhombic	Pcc2	13.323	13.324	9.379	90	-	Banno et al. [92]

I.3. Lab-synthesis methods for ye'elimite and other cement phases

I.3.1. Solid-state synthesis of ye'elimite

To examine the hydration behaviour of calcium sulfoaluminate cements, individual and pure components should be prepared, one being ye'elimite. As commercially available CSA cements are a mix of several phases, it is impossible to separate ye'elimite from the other phases. Therefore, a need exists to synthesize $C_4A_3\bar{S}$ phase in a pure state at the lab scale. Table I-4 summarizes various protocols described in the literature for the synthesis of ye'elimite by solid-state reaction [18,33,87,90,91,94,96,98–103]. It can be prepared from a mixture of different raw materials such as limestone ($C\bar{C}$), gypsum ($C\bar{S}H_2$) and bauxite blended with water (or ethanol) in agate mortars. Some authors also pre-fired the raw materials in order to convert gypsum into anhydrite ($C\bar{S}$) whereas limestone is decarbonated inducing the formation of lime (C) and carbon dioxide ($C\bar{C}$). Nevertheless, none of the protocols describe completely the experimental conditions, there is always one piece of information missing, especially the quantity of material prepared. The tricky point with the synthesis is the instability at high temperature of ye'elimite [104] and anhydrite [101] leading to their decomposition. 10-20 wt.% of calcium sulfate can be decomposed during the thermal treatment [89,101]. Peixing et al. [98] mentioned the used of non-stoichiometric blends to compensate sulfur

evaporation. Therefore, it is difficult to produce pure ye'elimite and the synthesis induces the formation of minor phases (C, $C_{12}A_7$, CA, CA_2).

Ye'elimite is a significant component in BCSAF and CSA cements [105]. The detailed understanding of ye'elimite solid-state formation during the thermal treatment may be the key for solving burnability² encountered during the production of CSA type clinkers. Table I-2 shows the cement phases present in CSA clinkers compositions given in the literature. It is absolutely clear that on top of ye'elimite CSA clinker products contain various calcium aluminate phases as minor phases. Similar observations were made during pure ye'elimite powder preparation by solid-state reaction methods [9,63,106–111] or by low temperature chemical routes [100,112], where the final product contained CaO, $CaAl_2O_4$ and $CaAl_4O_7$ as main impurities when the sintering temperature was below 1300°C. Hence, successful preparation of highly pure ye'elimite powder by solid-state reactions required multiple milling, pelleting and firing cycles at 1300°C. However, the question of how these successive processing steps increased the ye'elimite content was not raised. Table I-5 represents the possible reactions involved during ye'elimite formation in different temperature ranges [9]. Solid-state formation of ye'elimite from pure raw materials starts at 1000°C and it continues until 1300°C through reactions between calcium aluminate phases (CA, CA_2) and $CaSO_4$ until 1300°C. In this temperature range, CA and CA_2 can be qualified as 'intermediate' compounds since they form between 1000 and 1100°C. From 1300°C, ye'elimite can decompose into calcium aluminate phases (CA and $C_{12}A_7$), O_2 gas and SO_2 gas. Li et al. [113] studied the formation of ye'elimite from C_3A and gypsum; they reported that the optimal conditions for $C_4A_3\bar{S}$ formation were 1150 to 1350°C for 1 h to 6 h. Ca^{2+} and SO_4^{2-} were the diffusive species in both the different reactions. Nonetheless, there is no suitable study at microstructural scale involving ye'elimite formation from pure Al_2O_3 , CaO and $CaSO_4 \cdot 2H_2O$ phases.

As shown by reactions R3 and R5 (Table I-5), calcium aluminate phases (CA and CA_2) can form during the thermal treatment. The microstructural changes happening during the formation of calcium aluminates are well described in the literature (which is not the case for ye'elimite). For example, Iftekhar et al. [114] studied the formation of CA from a mixture of $CaCO_3$ - Al_2O_3 powders in a temperature range between 1300 and 1500°C. The authors noted that Ca^{2+} ions diffuse through calcium aluminates and react with alumina, the dense layer of CA_2 formed around the A/ CA_2 contact region acts then as a diffusion barrier. The high calcium concentration observed at the pore surface may be an indication that Ca^{2+} diffusion during phase formation occurs at the grain surface. Other authors do not confirm this last hypothesis about the formation of phases in the direction of the interface but confirm the fact that Ca^{2+} diffuse through the calcium aluminates, from calcium-rich aluminates to calcium-poor aluminates [115] [116]. De Bilbao et al. [117] studied the corrosion kinetics of high-alumina refractories

² Burnability is the facility with which the components of CSA cements raw mixture are combined.

by a binary slag (Al_2O_3 50 wt.% CaO 50 wt.%) at 1650°C for 30 min. It was observed via scanning electron microscopy that CA_6/CA_2 layers formed around the alumina aggregates. The formation of these layers was explained by the diffusion of Ca^{2+} and O^{2-} ions, and the existence of each layer depends on the temperature. Mercury et al. [118] studied the formation of CA phase from a mixture of Al_2O_3 and CaCO_3 milled by attrition and from a $\text{Al}(\text{OH})_3$ and CaCO_3 powder mix. From 900°C , the formation of mayenite C_{12}A_7 occurs at the contact between the CaO grains and the alumina particles. At higher temperatures, Ca^{2+} ions of calcium-rich phases diffuse through the C_{12}A_7 phase layer to then form the CA phase and so on for the formation of the CA_2 phase. Once these reactions are complete, the densification starts from 1250°C onwards. Scian et al. [119] also studied the formation of the calcium aluminate phase CA, and identified two steps in the process of its formation. During the first stage (short duration and low temperature), the reaction between CaO and Al_2O_3 produces a layer of calcium aluminate at a controlled rate by an interface process (chemical reaction, nucleation and product growth). Then, inside this interface of reaction, separating the two reagents, the calcium (free or combined), diffuses to react with the alumina rich phases and diffusion was identified as the limiting step of the reactions [120].

Table I-4: Summary of solid-state ye'elinite synthesis protocols used in previous works (S: stoichiometric / NS: non stoichiometric).

Ref.	Raw materials	Preparation/Mix	Ratio	Burning conditions				Ye'elinite purity
				Temperature	sintering (h)	Fired	Quenching	
Halstead and Moore, 1962 [33]	$\text{C}\bar{\text{S}}\text{H}_2 / \text{A} / \text{C}\bar{\text{C}}$	Prefired (1000°C)	S and NS	1350°C	4-12	-	-	-
Saalfeld and Depmeier, 1972 [94]	-	Prefired (1000°C) + Pellets	S	800 - 1400°C	12-14	Many times	-	-
Hanic et al, 1989 [121]	$\text{Ca}(\text{NO}_3)_2$, $(\text{NH}_4)_2\text{SO}_4$ et $\text{Al}(\text{NO}_3)_3$	Mix in water + Prefired (597°C) + Pellets	-	1100 - 1125 - $1150 - 1175^\circ\text{C}$	0.25 / 0.5 / 1 / 2 / 4	-	-	-
	$\text{C}\bar{\text{S}} / \text{CA}$	Pellets	-	1160 - 1180 - $1190 - 1200^\circ\text{C}$	0.25 / 0.5 / 1 / 2 / 4	-	-	-
Krstanović et al, 1992 [96]	$\text{C}\bar{\text{S}}\text{H}_2 / \text{A} / \text{C}\bar{\text{C}}$	Crushed and mixed	-	1350°C	3	-	-	-
Peixing et al, 1992 [98]	$\text{C}\bar{\text{S}}\text{H}_2 / \text{AH}_3 / \text{C}\bar{\text{C}}$ 158 g	-	NS	1320°C	1	-	-	-
Ali et al, 1994 [102]	$\text{C}\bar{\text{S}} / \text{A} / \text{C}\bar{\text{C}}$	Crushed < $63\mu\text{m}$ + Pellets	S	1100-1200- $1250-1300-1325^\circ\text{C}$	0.5 -4	-	-	Ye'elinite with CA
Andac et Glasser,	$\text{C}\bar{\text{S}} / \text{A} / \text{C}\bar{\text{C}}$	Predry	S	6h at 800°C then 4h at	-	-	-	-

1994 [103]				900°C and then 1300°C				
Ikeda et al, 1996 [102]	$C\bar{S}H_2 / A / C\bar{C}$ Quantity for 10 g of ye'elimite	Gypsum prefired at 1000°C mixe in ethanol during 10h	S	1300°C	9	-	-	Ye'elimite single phase by XRD
Song et Young, 2002 [122]	$C\bar{S}H_2 / A / C\bar{C}$ Ca(NO ₃) ₂ , 4H ₂ O / Al(NO ₃) ₂ .9H ₂ O / et Al ₂ (SO ₄) ₃ ,14-18H ₂ O	- Mixed in poly(vinyl alcohol)	- S	1350°C 12h at 105°C - 1h at 1300°C	1 -	-	-	Ye'elimite with CA Ye'elimite with CA
Winnefeld et Barlag, 2010 [18]	$C\bar{S}H_2 / A / C\bar{C}$	Mix in water + Pellets	S	1300°C	4	-	-	-
Cuesta et al, 2013 [87]	$C\bar{S}H_2 / A / C\bar{C}$	Mix in ethanol + Pellets	S	1300°C	4	-	slow	Ye'elimite with CA, C ₃ A and C ₁₂ A ₇
Cuesta et al, 2014 [90]	Quantity for 8 g of ye'elimite							
Kurokawa et al, 2014 [91]	$C\bar{S} / A / C\bar{C}$	-	S	1300°C	2	-	slow	Ye'elimite with CA

Table I-5: Possible reactions involved during ye'elimite formation in different temperature ranges [9].

Solid-state reaction		Temperature range
$C\bar{S}H_2 \rightarrow C\bar{S} + 2 H$	(R1)	T < 1000°C
$C\bar{C} \rightarrow C + \bar{C}$	(R2)	
$C + A \rightarrow CA$	(R3)	1000°C < T < 1100°C
$3C + 3A + 1C\bar{S} \rightarrow C_4A_3\bar{S}$	(R4)	
$CA + A \rightarrow CA_2$	(R5)	
$3CA + 1C\bar{S} \rightarrow C_4A_3\bar{S}$	(R6)	1100°C < T < 1300°C
$3C + 3CA_2 + 2 C\bar{S} \rightarrow 2C_4A_3\bar{S}$	(R7)	
$C\bar{S} \rightarrow C + \bar{S} \rightarrow C + SO_2^\uparrow + \frac{1}{2}O_2^\uparrow$	(R8)	T > 1300°C
$C_4A_3\bar{S} \rightarrow 1/5 C_{12}A_7 + 8/5 CA + SO_2^\uparrow + 1/2 O_2^\uparrow$	(R9)	

I.3.2. Sol-gel synthesis of anhydrous cement phases

When ye'elimite is prepared by solid-state reactions, the final product contains phases like krotite (CA), grossite (CA₂) and mayenite (C₁₂A₇) as secondary phases below 1300°C. Hence, successful preparation of C₄A₃ \bar{S} by solid state reaction required intermediate grinding steps and high-temperature firings (at or above 1300°C) [9,106,107,110,111,123].

Nowadays, it is possible to bypass the grinding and refiring steps and to decrease the synthesis temperature of cementitious pure phases through chemical routes starting from a solution. According to

the literature, different polymer precursor methods were used in this case. Polymer precursor methods such as Pechini method (Pech), Organic Steric Entrapment method (OSE) and Self-Propagating Combustion (SPC) are well known for the synthesis of calcium aluminates and calcium silicates [124]. These chemical methods are based on the mixing of salts with a polymer precursor (citric acid, ethylene glycol or polyvinyl alcohol). The polymerization reaction progresses by increasing the temperature. The solution was heated until the formation of a viscous gel was achieved. The gel was dried and a foam was formed. The foam was crushed and used as a precursor material for the subsequent sintering process [124].

Table I-6 summarizes the physical and chemical characteristics of some cementitious phases prepared by chemical synthesis routes [125–137]. Ye'elimite was prepared by Song et al. [125] using chemical synthesis from calcium nitrate, aluminium nitrate and aluminium sulfate. The specific surface area of the synthesized ye'elimite after calcination at 1300°C was 1 m²/g. Lee and Kriven [126] were able to produce C₃S, C₂S, C₃A and C₄AF by an organic steric entrapment method. The cement components synthesized by chemical routes have sub-micronic or nanometric crystallites, high specific surface area and extremely high reactivity at relatively low calcination and crystallization temperatures. Raab and Pöllmann [127] synthesized pure phases of Portland and Calcium Aluminate Cements (CAC), with particle sizes around 50 nm, using the Pechini or the combustion method. Thomas et al. [128] managed to prepare highly reactive forms of β-C₂S with specific surface areas of 8.3 m²/g and 26.5 m²/g using the Pechini method. There is also other work [129–131] on reactive forms of β-C₂S synthesis by the Pechini process. Use of the self-propagating combustion method for preparation of clinker phases was reported by Zapata and Bosch [132], who synthesized C₃S phase at low temperature, and by Fumo et al. [133], Tas [134] and Yi et al. [135], who synthesized calcium aluminate cementitious phases.

Referring to Table I-6, there is only one work in literature which deals with ye'elimite synthesis by a chemical route [125]. The multiscale size characterization and the effect of organic precursors on ye'elimite synthesis were not investigated. The purity of the synthesized ye'elimite [125] was not confirmed by accurate methods like Rietveld analysis when examination of pure cement phases requires knowledge of the purity. Detailed characterization of the microstructure is also important [138,139].

Table I-6: Summary of physical and chemical characteristics of some cementitious phases prepared by chemical synthesis routes (Pech=Pechini method; OSE=Organic Steric Entrapment method; SPC=Self-Propagating Combustion).

Ref.	Cementitious phases													
	C ₄ A ₃ S̄	C ₃ S	C ₃ S	C ₃ S	C ₂ S	C ₂ S	C ₂ S	C ₂ S	C ₂ S	CA	CA	CA	CA	CA
Ref.	[125]	[126]	[132]	[136]	[126]	[128]	[129]	[130]	[131]	[133]	[127]	[137]	[134]	[135]
Chem. method	OSE	OSE	SPC	Sol-gel	OSE	Pech	Pech	Pech	Pech	SPC	Pech or SPC	Pech	SPC	SPC
Grain size (nm)	-	200-300	-	-	80-90	-	-	-	-	45	50	-	-	-
Specific surface area (m ² /g)	1-2.5	50	-	-	22.1	8.3	1-30	0.8-3.1	1-22	-	-	10	-	-
Purity	Pure	-	Not pure	Pure	-	Pure	Pure	Pure	Pure	Pure	Pure	Pure	Pure	Not pure
Purity checking method	XRD pattern	XRD pattern	XRD pattern	XRD pattern	XRD pattern	XRD pattern	XRD pattern	XRD pattern	XRD pattern	XRD pattern	XRD pattern	XRD pattern	XRD pattern	Rietveld method

Important points to remember:

Various protocols described in the literature for the synthesis of ye'elimite by solid-state reaction. It can be prepared from a mixture of different raw materials such as limestone, gypsum and bauxite blended with water (or ethanol) in agate mortars. Some authors also pre-fired the raw materials in order to convert gypsum into anhydrite whereas limestone is decarbonated inducing the formation of lime and carbon dioxide. Nevertheless, none of the protocols describe completely the experimental conditions, there is always one piece of information missing, especially the quantity of material prepared. The tricky point with the synthesis is the instability at high temperature of ye'elimite and anhydrite leading to their decomposition. 10–20 wt.% of calcium sulfate can be decomposed during the thermal treatment. Therefore, it's difficult to produce pure ye'elimite and the synthesis induces the formation of minor phases (C, C₁₂A₇, CA, CA₂).

According to the literature, different polymer precursor methods were used in this case. Polymer precursor methods such as Pechini method (Pech), Organic Steric Entrapment method (OSE) and Self-Propagating Combustion (SPC) are well known for the synthesis of calcium aluminates and calcium silicates. These chemical methods are based on the mixing of salts with a polymer precursor (citric acid, ethylene glycol or polyvinyl alcohol). The polymerization reaction progresses by

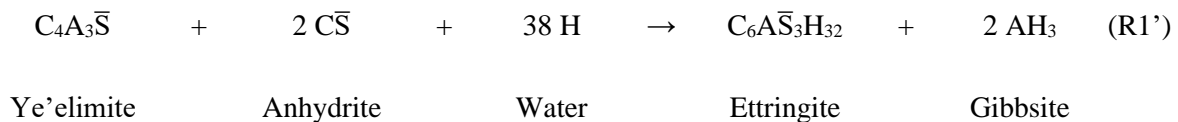
increasing temperature. The solution was heated until the formation of a viscous gel was achieved. The gel was dried and a foam was formed. The foam was crushed and used as a precursor material for the subsequent sintering process. The multiscale size characterization and the effect of organic precursors on ye'elimite synthesis were not investigated. The purity of the synthesized ye'elimite was not confirmed by accurate methods like Rietveld analysis when examination of pure cement phases requires knowledge of the purity. Detailed characterization of the microstructure is also important.

I.4. Hydration of ye'elimite phase

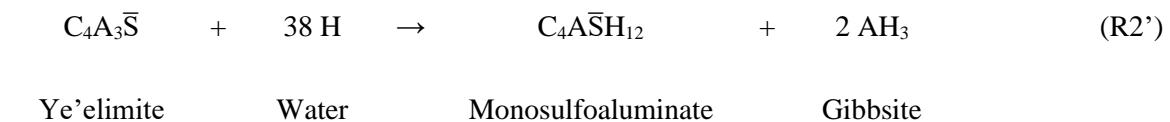
Several research works addressed ye'elimite hydration study. It was shown that ye'elimite hydration depends on the amount and the nature of the added calcium sulfate, and also on the crystallographic structure of ye'elimite. Referring to previous works concerning ye'elimite hydration, a literature review about the influence of each said factor on ye'elimite hydration is now presented.

I.4.1. Effect of amount and nature of the added calcium sulfate

The expansive behaviour of CSA cements is mainly controlled by ettringite $C_6A_3\bar{S}_3H_{32}$ ³ amount, produced upon hydration of their key-phase, ye'elimite $C_4A_3\bar{S}$ [140,141]. In fact, ye'elimite hydration proceeds through dissolution and precipitation [142], leading to the precipitation of various hydrates. In the presence of anhydrite (calcium sulfate), ye'elimite hydrates to form ettringite as well as gibbsite (Reaction R1') [18,107,143,144]:



In the absence of calcium sulfate, the hydration of ye'elimite can lead to the formation of monosulfoaluminate and gibbsite (Reaction R2') [18,107,143,144]:



Recently, significant work has been carried out on ye'elimite single phase hydration, pioneered by Hanic et al. [121]. Ye'elimite hydration was shown to occur through a two-step reaction. The reaction product

³The cement phase notations are used in this work (C = CaO, A = Al₂O₃, \bar{S} = SO₃, \bar{C} = CO₂, H = H₂O)

in the first step was ettringite, whereas monosulfoaluminate $C_4A\bar{S}H_x$ was the hydration product in the second step of hydration reaction. Suspensions of synthetic ye'elimite in a saturated gypsum solution were also investigated [109]. The most voluminous hydration product observed was ettringite. During the hydration of orthorhombic ye'elimite in dilute suspensions with a water over binder mass ratio equal to 40 and 100, Bullerjahn et al. [83] identified five stages of hydration: stage I (initial period), stage II (dormant period), stage III (acceleration period), stage IV (main hydration period) and stage V (final period). The duration of each stage was directly linked to the evolution of the solution concentrations and the type hydration reaction [145]. Other authors were interested in the hydration behavior of orthorhombic and pseudo-cubic ye'elimite [146–148]. It was shown that in the absence of additional sulfate sources, orthorhombic-ye'elimite reacts slower than pseudo-cubic-ye'elimite, and monosulfoaluminate phases are the main hydrated crystalline phases (see reaction R2'). However, in the presence of additional sulfates, orthorhombic-ye'elimite reacts faster than pseudo-cubic-ye'elimite, and the main hydrated crystalline phase is ettringite (see reaction R1'). The published data on ye'elimite single phase hydration [146–149] are summarized in Figure I-5, which shows the degree of ye'elimite hydration (α) (Figure I-5a) and the amount of the formed hydrates (Figure I-5b, Figure I-5c and Figure I-5d). The degree of ye'elimite hydration, α , is calculated as follows:

$$\alpha(\%) = \frac{\text{wt}\%_{\text{ye'elimite}}(t_0) - \text{wt}\%_{\text{ye'elimite}}(t)}{\text{wt}\%_{\text{ye'elimite}}(t_0)} \times 100 \quad \text{E.0}$$

where $(\text{wt}\%_{\text{ye'elimite}})$ refers to the weight percentage of ye'elimite, (t_0) is the starting hydration time and (t) is the final hydration time, the hydration duration corresponds to $(t-t_0)$. The amounts of formed hydrates (see Figure I-5b to Figure I-5d), namely ettringite, monosulfate and gibbsite, are directly extracted from the literature data. The plots show that depending on the authors, a large range of hydration degrees, α , can be found in the literature. Besides, ye'elimite hydration degree influences upon the amount of the formed hydrates, especially ettringite hydrate, and it depends on parameters, such as the presence of minor elements (iron, sodium) and the initial water over cement mass ratio. Thereby, physical and chemical characteristics of ye'elimite play a significant role on ettringite formation, and consequently, it could influence the interesting expansion behavior of CSA cements.

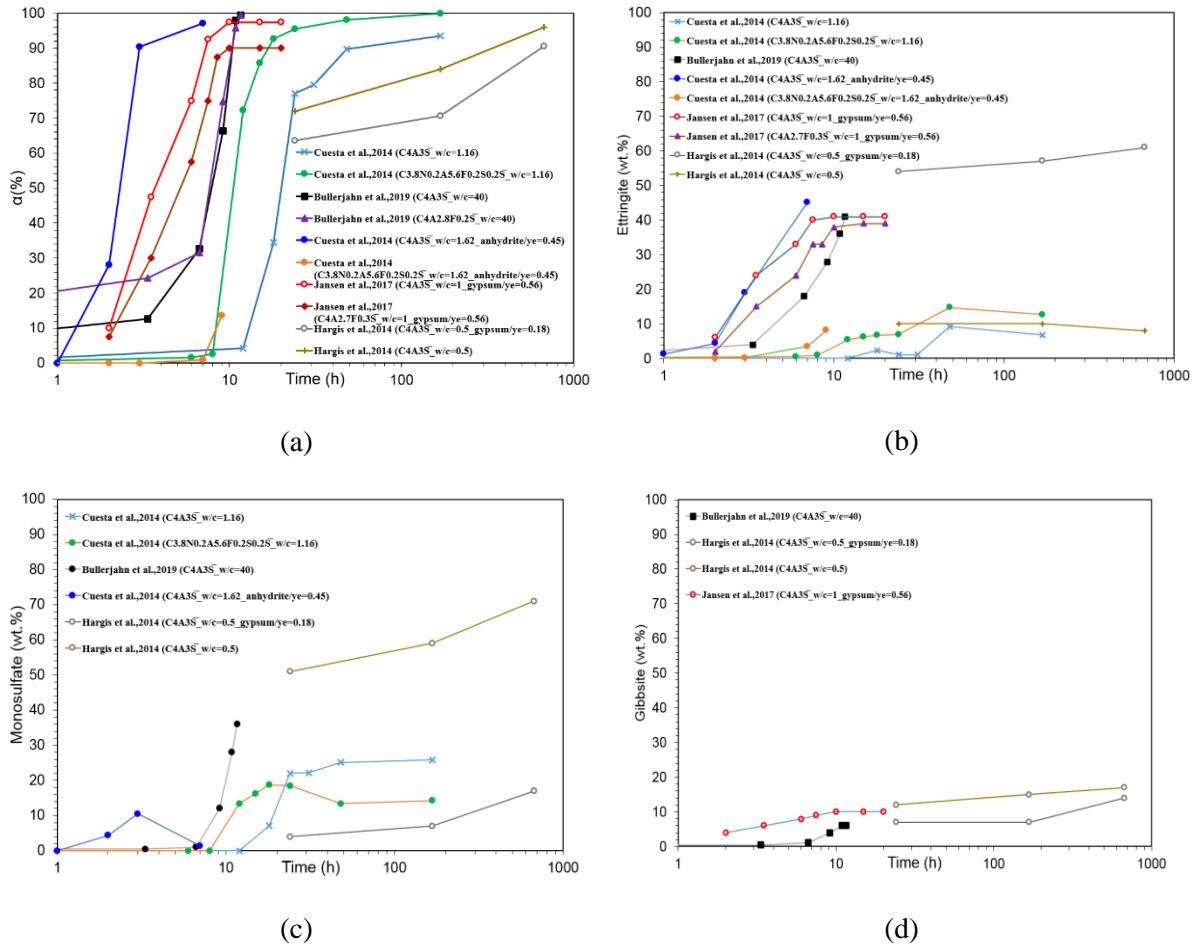


Figure I-5: (a) Calculated ye'elimite hydration degree (α %); Formed hydrates quantities relevant to Etringite (b), Monosulfate (c) and Gibbsite (d); “W/C” refers to water by cement weight ratio; References: Cuesta et al.,2014 [146], Hargis et al.,2014 [149], Jansen et al.,2017 [147], Bullerjahn et al.,2019 [148], (α %) is given by equation (E.0).

I.4.2. Effect of ye'elimite crystallographic structure

The influence of the crystallographic structure on ye'elimite hydration was discussed for the first time by Cuesta et al. [146]. They compared orthorhombic ye'elimite (C₄A₃S̄) with cubic ye'elimite (C_{3,8}Na_{0,2}Al_{5,6}Fe_{0,2}Si_{0,2}O₁₂SO₄). It was shown that, in the case of no calcium sulfate source addition, orthorhombic ye'elimite reacts more slowly than cubic ye'elimite, and the major hydrate product is monosulfoaluminate. In addition, cubic ye'elimite hydration produces more ettringite. However, by the addition of gypsum, the hydration rate of orthorhombic ye'elimite becomes higher.

Jansen et al. [150] studied the hydration of orthorhombic ye'elimite (C₄A₃S̄) and cubic iron-rich ye'elimite (C₄A_{2,7}F_{0,3}S̄). In the presence of gypsum and for both structures, ettringite forms in two stages. During the first stage, ye'elimite and gypsum dissolve to precipitate ettringite and aluminium hydroxide

(AH_x) gel, while during the second stage, ettringite crystallization was supplied only by ye'elimite dissolution. In the absence of gypsum, the cubic ye'elimite is less reactive than the orthorhombic one at early age of hydration. These results are in accordance with Cuesta et al. [146] results.

Other authors were interested in the hydration behavior of orthorhombic and pseudo-cubic ye'elimite [146–148]. It was shown that in the absence of additional sulfate sources, orthorhombic-ye'elimite reacts slower than pseudo-cubic-ye'elimite, and monosulfoaluminate phases are the main hydrated crystalline phases, as expected. Moreover, pseudo-cubic-ye'elimite produces higher amounts of ettringite than orthorhombic-ye'elimite. However, in the presence of additional sulfates, orthorhombic-ye'elimite reacts faster than pseudo-cubic-ye'elimite.

Important points to remember:

The ye'elimite ($C_4A_3\bar{S}$) structure belongs to the sodalite group. The crystal structure of ye'elimite is complex to resolve, it has been suggested to exhibit cubic ($I\bar{4}3m$) and orthorhombic (Pcc2) structures. The cubic ye'elimite polymorph is usually an impure solid-solution including generally Si, Na and Fe atoms. Besides, orthorhombic ye'elimite polymorph includes stoichiometric quantities of only Ca, Al, S and O atoms. It was shown theoretically and experimentally that the orthorhombic structure is the most stable.

Ye'elimite hydration produces mainly ettringite ($C_6A\bar{S}_3H_{32}$) and monosulfoaluminate ($C_4A\bar{S}H_{12}$) with a quantity of gibbsite (AH₃) (in either crystalline or amorphous form). Ye'elimite-rich cements are usually blended with 10 to 25 wt.% of calcium sulfate, in the form of anhydrite, hemihydrate or gypsum. The nature and the amount of calcium sulfate influence upon hydration. In fact, the mass ratio of ye'elimite to calcium sulfate determines the mass ratio of ettringite to monosulfoaluminate produced during hydration. Furthermore, the addition of soluble calcium sulfate like gypsum increases the dissolution rate of ye'elimite, whereas this effect does not occur in the case of addition of less soluble calcium sulfate like anhydrite.

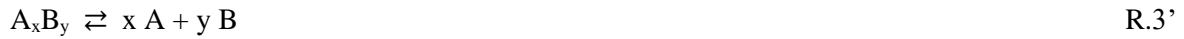
The crystallographic structure affects also its hydration. In fact, pseudo-cubic-ye'elimite produces higher amounts of ettringite than orthorhombic-ye'elimite, in the presence of gypsum. However, in the presence of additional sulfates, orthorhombic-ye'elimite reacts faster than pseudo-cubic-ye'elimite.

I.5. Parameters influencing cementitious phases hydration at early age

According to Le Châtelier's works (1904) [142], the hydration process of an hydraulic binder starts by the dissolution of cementitious phases followed by the crystallization of hydrated phases. In this last part of Chapter I, we will present the parameters influencing the dissolution of cementitious phases, then those influence the crystallization of hydrates.

I.5.1. Parameters influencing the dissolution of cementitious phases

Let us consider the following dissolution reaction of a solid, A_xB_y :



Gibbs free energy of dissolution reaction can be written as:

$$\Delta G_r = \Delta G_r^0 + RT \ln[(a_A)^x (a_B)^y] \quad \text{E.1}$$

a_A and a_B are the activities of A and B, respectively, ΔG_r^0 is Gibbs free energy of dissolution reaction under standard state, R is gas constant, et T refers to the temperature.

At thermodynamic equilibrium, ΔG_r value becomes 0:

$$\Delta G_r = \Delta G_r^0 + RT \ln[(a_A)^x (a_B)^y] = 0 \quad \text{E.2}$$

$$\Delta G_r^0 = -RT \ln[(a_A)^x (a_B)^y]_{\text{éq}} = -RT \ln(k_{sp}) \quad \text{E.3}$$

k_{sp} is the solubility product at equilibrium.

The β ratio is defined by:

$$\beta = \frac{[(a_A)^x (a_B)^y]}{[(a_A)^x (a_B)^y]_{\text{éq}}} = \frac{[(a_A)^x (a_B)^y]}{k_{sp}} \quad \text{E.4}$$

We therefore deduce that:

$$\Delta G_r = -RT \ln(k_{sp}) + RT \ln[(a_A)^x (a_B)^y] = RT \ln(\beta) \quad \text{E.5}$$

When β is lower (resp. greater) than 1, the solution is under (resp. over) saturated with respect to the equilibrium situation.

Figure I-6 illustrates the concept of under/over-saturation applied on cement dissolution-crystallization process. When an anhydrous phase dissolves in water, ions are released in solution (white arrow in Figure I-6). When the solution becomes oversaturated with respect to the corresponding hydrate, its crystallization becomes possible (pink arrow in Figure I-6). The concept of under/over-saturation explains why cementitious phase dissolves first before hydrate phase crystallization, and not the opposite. Therefore, the under/over-saturation is the main driving force for dissolution and crystallization during cement hydration.

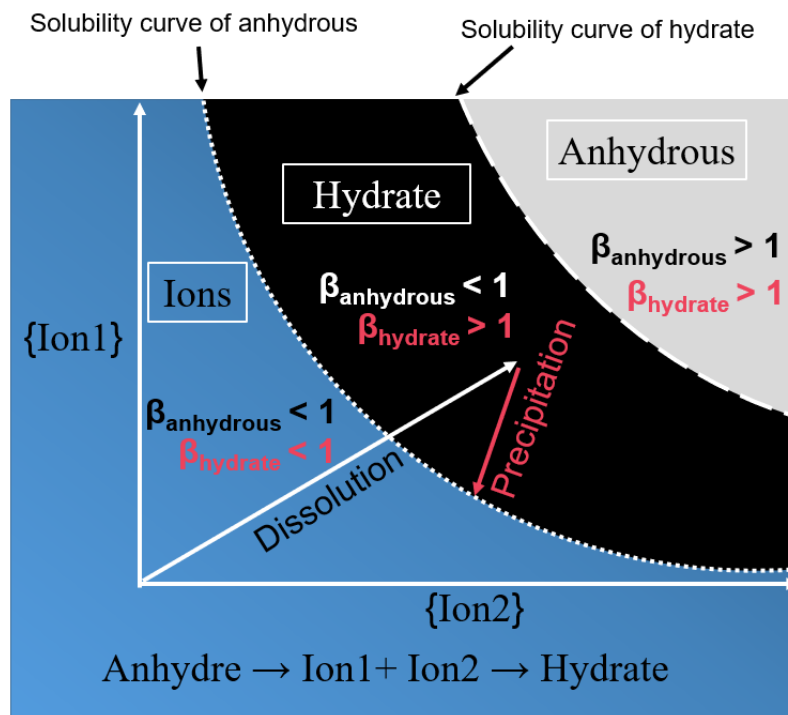


Figure I-6: Schematic illustration of the thermodynamic concept of over/under saturation to explain dissolution of anhydrous and precipitation of hydrates.

In the case of ye'elinite hydration, the anhydrous cementitious phase is ye'elinite powder, and the dissolved ions are Ca^{2+} , $\text{Al}(\text{OH})_4^-$, OH^- , and SO_4^{2-} . Finally, the precipitated hydrate phases are ettringite, monosulfoaluminate and gibbsite.

Cement grain dissolution occurs when water diffuses to the grain surface where dissolution reactions occur [151]. Lasaga [152,153] suggests a general equation to describe mineral dissolution rate (E.6):

$$R_{\text{diss}} = k_0 \times S_{\text{reac}} \times e^{-E_a/RT} \times a_{\text{H}^+}^{\text{mH}^+} \times \prod_i a_i^{\text{mi}} \times g(I) \times f(\Delta G_r) \quad \text{E.6}$$

R_{diss} ($\text{mol m}^{-2} \text{s}^{-1}$): dissolution rate, k_0 : rate constant ($\text{mol m}^{-2} \text{s}^{-1}$), S_{reac} : mineral **reactive surface**, $e^{-E_a/RT}$: exponential term which describes temperature dependence (T refers to temperature, E_a refers to activation energy of dissolution reaction, and R is the gas constant), $a_{\text{H}^+}^{\text{mH}^+}$: H^+ activity in the solution which reflects **pH** effect on dissolution, mH^+ : reaction order with respect to H^+ , a_i^{mi} : is the activity of the compound i which reflects the effect of **catalyst** or **organic additive** on dissolution reaction, mi : reaction order with respect to compound i, $g(I)$: ionic force function which reflects the effect of **solution ionic force** (I) on dissolution, and $f(\Delta G_r)$: is a function relating dissolution rate to the **Gibbs free energy of dissolution** ΔG_r .

Based on theoretical works of Lasaga [153–155] concerning mineral dissolution, Juilland et al. [152] applied a geochemical approach to study the dissolution of « Alite C_3S », the major cementitious phase in OPC cements. The dissolution of Alite grain at early age of hydration was explained by the saturation state of the solution and by the crystallographic defects density of anhydrous Alite grain. In fact, the first stage of dissolution is controlled by the formation of etch-pits at the surface of Alite grains, as it was previously observed on other minerals such as Quartz and CaCO_3 , by Lasaga [153–155]. Then when the solution becomes oversaturated, the dissolution rate is controlled by step-retreat mechanism. Nicoleau et al. [151] confirmed the discussions of Juilland et al. [152] by measuring the dissolution rate of Alite according to the solution saturation state.

The curve shape showing dissolution rate as a function of logarithmic solution saturation state (Figure I-7, [151]), is usually a sigmoidal curve or S-curve. The curve presents three different kinetic domains (I, II and III).

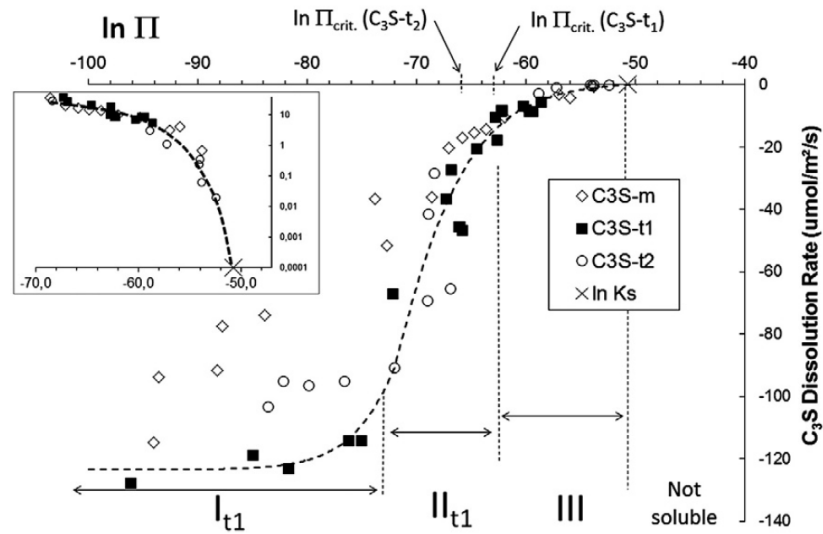


Figure I-7: Experimental measurements of dissolution rate of Alite C_3S phase as a function of oversaturation logarithm (noted β in the text) (Nicoleau et al. [151]).

Domain I (Figure I-7): it is far from equilibrium where alite dissolution proceeds by etch-pits formation formed on grain surface especially on surface defects (e.g. dislocations). The dissolution rate is very high and does not depend on solution saturation.

Domain II (Figure I-7): it is the curve region where alite dissolution rate depends considerably on solution saturation. The dissolution continues by opening the initially formed etch-pits.

Domain III (Figure I-7): it is close to equilibrium where alite dissolution rate becomes very slow. Dissolution continues by step-retreat mechanism of initially opened etch-pits.

Figure I-8 proposes a simple schematic description of dissolution mechanism in each domain.

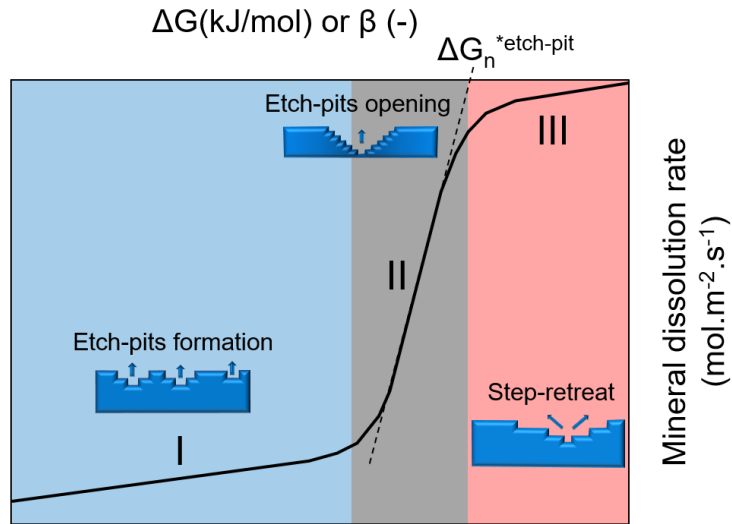


Figure I-8: The typical S-curve showing dissolution rate as a function of solution saturation state β or difference in Gibbs free energy (ΔG_r) of the corresponding dissolution reaction (adapted from [152,156]).

Gibbs free energy $\Delta G_n^{\text{etch-pit}}(r)$ related to the formation of an etch-pit with a radius (r) is given by the following expression [151,157]:

$$\Delta G_n^{\text{etch-pit}}(r) = \frac{\pi r^2 h}{V_m} [\Delta G_r] + 2\pi r h \sigma \quad \text{E.7}$$

where h is the depth of the formed etch-pit, σ is the surface energy of the dissolved mineral, and V_m refers to its molar volume.

The etch-pit formation occurs spontaneously on the mineral surface when $r > r^*$, where r^* is the critical radii to form an etch-pit. The radius when $r = r^*$ corresponds to a maximum value for $\Delta G_n^{\text{etch-pit}}(r)$ (Figure I-9, [157]), that means:

$$\frac{d\Delta G_n^{\text{etch-pit}}(r)}{dr} = 0 \quad \text{E.8}$$

$$\frac{d\Delta G_n^{\text{etch-pit}}(r=r^*)}{dr} = \frac{2\pi r^* h}{V_m} [\Delta G_r] + 2\pi h \sigma = 0 \quad \text{E.9}$$

$$r^* = -\frac{\sigma \times V_m}{[\Delta G_r]} \quad \text{E.10}$$

The critical radii (r^*) is proportional to the surface energy (σ), and when the dissolution reaction is close to equilibrium (Domain III, Figure I-8), r^* becomes large, thereby it becomes difficult to form spontaneously new etch-pits in this domain.

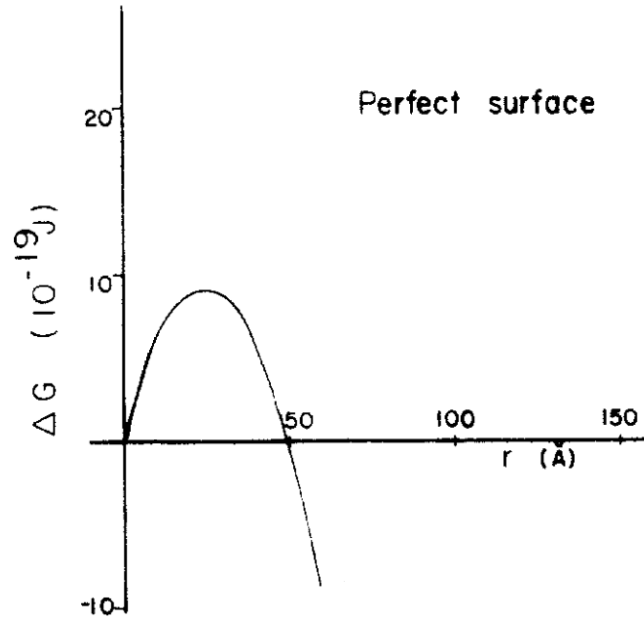


Figure I-9: Calculated Gibbs free energy (ΔG_r) of etch-pit formation as a function of etch-pit size (r) in the case of Quartz surface dissolution, adapted from [157].

Critical Gibbs free energy $\Delta G_n^{* \text{etch-pit}}(r = r^*)$ related to the formation of an etch-pit, could be deduced from expressions (E.7 and E.10):

$$\Delta G_n^{* \text{etch-pit}}(r = r^*) = \frac{-3\pi h V_m \sigma^2}{[\Delta G_r]} \quad \text{E.11}$$

Mineral surface defects such as dislocations could influence $\Delta G_n^{* \text{etch-pit}}(r = r^*)$ value, this can be illustrated by the term $\sqrt{1 - \omega}$:

$$\Delta G_n^{* \text{etch-pit}}(r = r^*) = \frac{3\pi h V_m \sigma^2}{[\Delta G_r]} \times \sqrt{1 - \omega} \quad \text{E.12}$$

The coefficient ω is given by the expression (E.13):

$$\omega = \frac{N_a \times S \times b^2}{2\pi \sigma^2 V_m} \Delta G_r \quad \text{E.13}$$

with S is the mineral shear modulus, b is the Burgers' vector which characterizes dislocations of the mineral.

Critical free energy $\Delta G_n^{* \text{etch-pit}}(r = r^*)$ can be estimated experimentally, by plotting the tangent of the dissolution rate curve in domain III (Figure I-8).

Close to equilibrium, $\Delta G_n^{\text{etch-pit}}$ exceeds the critical energy ($\Delta G_n^{\text{etch-pit}} > \Delta G_n^{* \text{etch-pit}}$), consequently etch-pit formation does not occur spontaneously, and the dissolution rate becomes slower and controlled by step-retreat mechanism.

Since the 1980s, researchers suggest kinetic models to discuss mineral dissolution rate [153–155,158,159]. The majority of these models are based on the Transition State Theory (TST) developed by Eyring in 1935 [160]. It includes all elementary steps controlling the detachment of constituents from solid surface to the solution. It is based on the assumption that, the reagents must exceed some energy barrier called activated complex before converting into reaction products. The TST predicts an exponential dependence of dissolution rate with the free energy of dissolution (E.14):

$$f(\Delta G_r) = (1 - e^{-\Delta G_r/RT}) \quad \text{E.14}$$

Many research works concerning mineral dissolution shows that TST theory explains dissolution experimental results only close to equilibrium, where the dissolution rate curve is linear (domain III, Figure I-8). Close to equilibrium, ΔG_r becomes much smaller than the term (RT) . By applying the Taylor expansion on terme $e^{-\Delta G_r/RT}$, Dissolution rate function $f(\Delta G_r)$ becomes linearly dependent on ΔG_r as expressed in (E.15):

$$f(\Delta G_r) = \frac{\Delta G_r}{RT} \quad \text{E.15}$$

TST theory is only valid for domain III (Figure I-8), and it does not seem to be valid far from equilibrium (domains I and II, Figure I-8), because the dissolution mechanism changes in these domains [151].

I.5.2. Parameters influencing the crystallization of cementitious hydrates

Cementitious hydrates crystallization obeys to the germination-growth law [151]. Germination corresponds to the formation of primary hydrate germ in hydration solution. There are two types of germination process: homogeneous germination and heterogeneous germination. In the case of homogeneous germination, primary germs can form anywhere in the hydration solution. However, heterogeneous germination occurs in a privileged way on a solid support (Figure I-10). The solid support

includes undissolved cement grain, walls of the hydration solution container, or any other solid impurity present in the hydration solution. In the case of cementitious hydrates crystallization, the heterogeneous germination process is the most common [151].

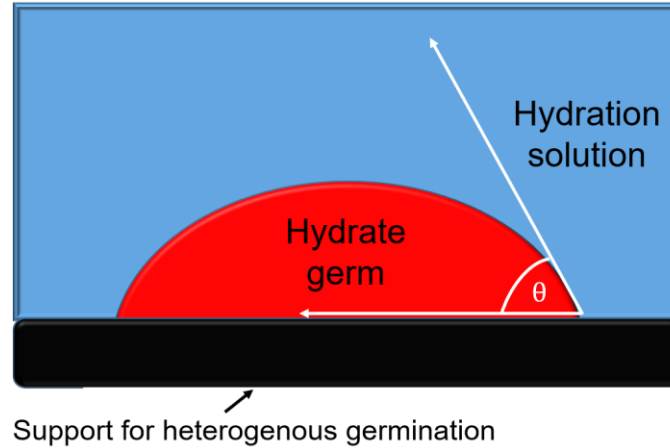


Figure I-10: Schematic illustration of heterogeneous germination of hydrate.

From a thermodynamical perspective, Gibbs free energy of heterogeneous germination can be expressed by (E.16):

$$\Delta G_{\text{germ}} = \left\{ -\frac{4}{3} \pi r^3 \Delta G_v + 4 \pi r^2 \gamma \right\} \left\{ \frac{1}{4} (2 + \cos \theta) (1 - \cos \theta)^2 \right\} \quad \text{E.16}$$

with r is the primary germ radii, assuming that this latter has a spherical form (classical theory of germination), ΔG_v is the volume free energy of the primary germ, γ refers to its mean surface energy related to the interface germ-solution and θ is the wetting angle reflecting the germ affinity for the support of heterogeneous germination (Figure I-10).

The volume free energy of the primary germ (ΔG_v) can be expressed as a function of solution oversaturation (β) by (E.17) [161]:

$$\Delta G_v = \frac{kT \ln \beta}{\Omega} \quad \text{E.17}$$

with k is the Boltzmann constant, T is temperature, and Ω is molar volume of the germ.

Thereby (E.16) can be written as:

$$\Delta G_{\text{germ}} = \left\{ -\frac{4}{3} \pi r^3 \frac{kT \ln \beta}{\Omega} + 4 \pi r^2 \gamma \right\} \left\{ \frac{1}{4} (2 + \cos \theta) (1 - \cos \theta)^2 \right\} \quad \text{E.18}$$

The plot of Gibbs free energy of germination (ΔG_{germ}) according to the primary germ radius (r) highlights the contribution of the two terms, volume energy ($-\frac{4}{3}\pi r^3 \frac{kT \ln \beta}{\Omega}$) and surface energy ($4\pi r^2 \gamma$) (Figure I-11). When the primary germ reaches a critical radius (r^*), the $\Delta G_{\text{germ}}(r)$ function reaches its maximum value noted ΔG_{germ}^* . Thus, when ($r < r^*$), primary germ dissolves. However, if some atoms are added to exceeds (r^*) value, i.e., ($r > r^*$), the germ will growth.

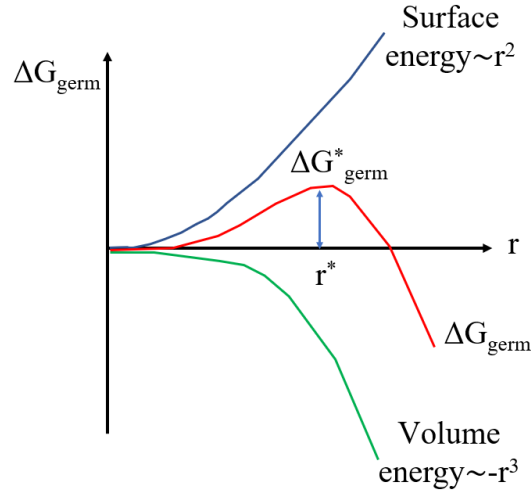


Figure I-11: Germination Gibbs free energy ΔG_{germ} as a function of germ radius (r).

The critical radii (r^*) and the critical energy (ΔG_{germ}^*) can be determined by developing the equation

$\frac{d\Delta G_{\text{germ}}}{dr}(r = r^*) = 0$ as following:

$$\frac{d\Delta G_{\text{germ}}}{dr}(r = r^*) = \left\{ -4\pi r^{*2} \frac{kT \ln \beta}{\Omega} + 8\pi r^* \gamma \right\} \left\{ \frac{1}{4} (2 + \cos \theta)(1 - \cos \theta)^2 \right\} = 0 \quad \text{E.19}$$

$$r^* = \frac{2\gamma\Omega}{kT \ln \beta} \quad \text{E.20}$$

$$\Delta G_{\text{germ}}^*(r = r^*) = \left(\frac{16\pi\Omega^2\gamma^3}{3(kT \ln \beta)^2} \right) \left\{ \frac{1}{4} (2 + \cos \theta)(1 - \cos \theta)^2 \right\} \quad \text{E.21}$$

$$\Delta G_{\text{germ}}^*(r = r^*) = \left(\frac{4}{3} \pi \gamma r^{*2} \right) \left\{ \frac{1}{4} (2 + \cos \theta)(1 - \cos \theta)^2 \right\} \quad \text{E.22}$$

According to E.20, the critical radius of the primary germ decreases when the temperature and the solution oversaturation increase, and when the surface energy of the formed solid is low.

I.5.3. A focus on the influence of fineness and citric acid addition

In the literature on cementitious materials and specifically Portland cements, different authors mention the effect of fineness on hydration [122,128,129,133,162,163]. Thomas [128] examined the hydration of the β polymorph of belite. He observed that if this polymorph had a specific surface area similar to a Portland cement, it was less reactive with water than a β -belite prepared by a chemical route (Pechini process). Pollman [162] and Hong [129] indicated that the interest in using chemical synthesis methods was to be able to study the hydration behaviour of pure belite and in particular fine particles. Hong's research focussed on the role of the specific surface area and the particle size on belite hydration. The interplay between fineness and chemical composition of fillers (limestone, alumina, silica) on Portland mortars hydration was studied by [164]. Whatever the type of filler, the finer it is, the more accelerated the early hydration of the mortar is. Fineness can also influence Portland concrete properties such as self-compactibility, shrinkage, durability or reduction of product cost. The role of ye'elimite fineness on hydration has not been as much studied as in Portland cements (see part. I.4). This first observation is one motivation for the present work.

For industrial applications, cement pastes always contain admixtures since they permit to tune the workability and the setting time of CSA cements on a building site. The choice of the appropriate admixture to lengthen the setting time of CSA cements at the same time as controlling the nature of the formed hydrates, the expansion behaviour and the preservation of the long-term mechanical performances of the set material are a concern for industry. In this respect, citric acid is currently the primary set retarding agent recommended for use with CSA cements [165]. The first authors who worked on the influence of citric acid on hydration reactions in the $3\text{CaO}\cdot\text{Al}_2\text{O}_3\text{-CaSO}_4\cdot 2\text{H}_2\text{O}\text{-CaO-H}_2\text{O}$ system were Tinnea and Young [166]. They found that hydration reactions are retarded by the addition of citric acid. Ettringite and monosulfoaluminate were all detected as early hydration products. The influence of citric acid as a retarder for ternary binders based on Ordinary Portland Cements (OPC), CSA and anhydrite was investigated by Winnefeld et al [167]. Their main conclusions were that the addition of citric acid retarded the early ettringite formation, lengthened the workability time, and reduced significantly the compressive strength even after 28 days. Zhang et al. [168] studied the effect of citric acid on the fluidity and strength of CSA commercial cements. They found that the initial fluidity of paste admixed with superplasticizers would be decreased by the presence of citric acid. Moreover, both early and late strengths of cement were decreased by the addition of citric acid. In a recent study about the effect of citric acid on hydration properties of commercial CSA, Burriss et al. [165] found that citric acid successfully retarded initial set by 120 min for CSA cement. Despite the reported studies about the effect of citric acid on CSA cements hydration, there is a lack of understanding on how citric acid influences early age hydration.

Important points to remember:

To recapitulate, many endogenous and exogenous parameters can influence cement hydration, both cement dissolution and hydrate formation, these parameters are:

- Cement fineness;
- Solution oversaturation state;
- Temperature and pH;
- Ionic strength of hydration solution;
- Presence of solid supports for hydrate germination;
- Presence of organic or inorganic additive in hydration solution.

Chapitre II. Characterization methods

Chapter II details the various experimental techniques and apparatus used to characterize the raw materials and the prepared samples of the present work.

II.1. X-Ray Diffraction (XRD) and Quantitative Rietveld Analysis (QRA)

X-ray diffraction (XRD) is the elastic scattering of x-ray photons by atoms in a periodic lattice. The scattered monochromatic x-rays that are in phase give constructive interference [169]. XRD by crystal planes allows one to derive lattice spacings by using the Bragg's law:

$$n\lambda = 2d \sin \theta \quad (\text{E.23})$$

where n is an integer called the order of reflection, λ is the wavelength of X-rays, d is the distance between the crystal planes and θ is the angle between the incident beam and the reflecting lattice plane. By measuring the angles, θ , under which the constructively interfering X-rays leave the crystal, the interplanar spacings, d_{hkl} , of every single crystallographic phase can be determined. The schema showing the principle of X-ray diffraction analysis is given in Figure II-1.

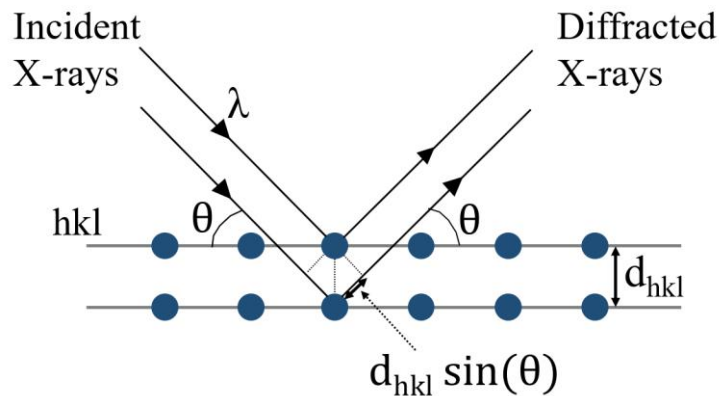


Figure II-1: Principle of X-ray diffraction analysis

Before the qualitative exploitation of the acquired diffractograms, two pre-treatments are made:

- Subtraction of $K_{Cu\alpha 2}$ contribution;
- Subtraction of background.

For crystallite sizes below 100 nm, line broadening occurs due to incomplete destructive interference in scattering directions where the X-rays are out of phase [169]. Scherrer's equation relates the crystal size to the line width:

$$D_{\text{crystallite}} = \frac{K \times \lambda}{\text{FWHM} \times \cos \theta} \quad (\text{E.24})$$

where $D_{\text{crystallite}}$ is a measure of the dimension of a crystallite in the direction perpendicular to the reflecting plane, λ is the x-ray wavelength, FWHM is the peak full width at half maximum, θ is the angle between the beam and the normal on the reflection plane, and K is a constant which is often taken as 0.89. It is worth noting that X-ray line broadening provides a quick, but not always reliable estimate of the particle size.

XRD is a direct method for qualitative and quantitative characterization of polyphasic materials. It becomes also an indispensable tool to analyze clinker and cement. Each phase of cement produces a unique diffraction pattern independent of others with the intensity of each pattern being related to the concentration of the phase in a mixture.

The possibility of quantifying the phase composition of a clinker by the Rietveld method (QRA) was shown by many investigations. To carry out QRA analysis, crystal structure of phases present in the sample should be known. Table II-1 shows the ICSD (Inorganic Crystal Structure Database) codes of the crystal structures used in the present work. For QRA analysis on anhydrous cement, the accuracy error can reach 2%, but it can be more than 2% for hydrated samples [63,170]. In the present thesis, all the QRA errors are the mathematical errors from the Rietveld fits, not the standard deviations derived from multiple measurements.

Table II-1: ICSD collection codes used for XRD-Rietveld quantitative analysis.

Phase name	Formula	ICSD codes	Ref.
Orthorhombic ye'elimite	$C_4A_3\bar{S}$	80361	[97]
Krotite	CA	260	[41]
Grossite	CA_2	34487	[42]
Alumina	A	73725	[173]
Lime	C	52783	[43]
Anhydrite	$C\bar{S}$	15876	[44]
Mayenite	$C_{12}A_7$	241003	[176]
Tricalcium aluminate	C_3A	151369	[177]
Ettringite	$C_6A\bar{S}_3H_{32}$	155395	[178]
Monosulfoaluminate	$C_4A\bar{S}H_{12}$	100138	[179]
Gibbsite	AH_3	6162	[180]
Gypsum	$C\bar{S}H_2$	151692	[181]

To check the Rietveld fitting quality between measured and calculated diffractograms, reliability factors should be given as, Rwp (weighted profile R-factor), Rexp (expected R-factor) and GOF (goodness of fit) [182]. These reliability factors reflect the deviation between measured intensities (I_{iM}) and calculated intensities (I_{iC}) at any given measurement point (i) as follows:

$$R_{wp} = \sqrt{\frac{\sum_i w_i (I_{iM} - I_{iC})^2}{\sum_i w_i (I_{iM})^2}} \quad (E.25)$$

$$R_{exp} = \sqrt{\frac{N-P}{\sum_i w_i (I_{iM})^2}} \quad (E.26)$$

$$GOF = \left(\frac{R_{wp}}{R_{exp}} \right)^2 \quad (E.27)$$

where w_i is the attributed weight, N is the number of data points and P is the number of the refined parameters.

Since cement pastes and set cements contain a complex mix of different crystalline and appreciable amorphous hydrates, an accurate quantification by Rietveld analysis is sometimes difficult due to peaks overlapping [63,183]. Therefore, we will consider our data as semi-quantitative in the case of quantification of hydration products.

In the present work, XRD technique was applied on sample powders. In order to achieve an isotropic distribution of the crystals in the samples in all directions, the particle size is brought down to less than 100 μm by grinding then sieving. XRD data were collected at room temperature in the Bragg-Brentano geometry using a Bruker D8 Advance X-ray diffractometer with $\text{CuK}\alpha$ radiation ($\lambda_{\text{Cu}}=1.54056 \text{ \AA}$, without monochromator) at a step scan of 0.02° with a time counting per step of 0.45 s operated at a voltage 40 kV and an electric current 40 mA. The sample was rotated during data collection at 15 rpm in order to increase particle statistics. The diffractometer was equipped with energy-dispersive LYNXEYE XE-T detector for filtration of fluorescence and $\text{K}\beta$ radiation. Mineral phases of the synthesized samples were quantified by using the Rietveld method as implemented in the TOPAS 4.2 software. The fitting parameters were the background coefficients, the phase scales, the zero-shift error, the cell parameters, and the phase shape parameters. The peak shapes were fitted by using the pseudo-Voigt function.

II.2. Chemical analysis by X-ray fluorescence (XRF)

XRF spectrometry is an elemental analysis technique to identify and quantify most of the chemical elements present in a sample. This technique can be used for a wide variety of materials. The analyzed sample is irradiated by X-rays. Under the effect of this irradiation, the atoms of the sample move from their fundamental state to an excited state. The excited state is unstable, the atoms tend thus to return to the fundamental state by emitting energy, especially in the form of X-photons. This is the X-ray fluorescence phenomenon that is a secondary emission of X-rays. Analysis of this secondary emitted X-rays gives the nature and the concentration of the chemical elements present in the sample.

Chemical analyses of the raw materials were carried out using X-ray fluorescence spectrometer, PANalytical, Zetium model. Samples were prepared as fused beads using glass discs prepared by melting about $1 \pm 0.001 \text{ g}$ of sample powder with $10 \pm 0.001 \text{ g}$ of lithium tetra borate flux. The Loss on Ignition (LOI) was calculated for samples treated at 1050°C for 1 h. The oxide contents are expressed in weight percent (wt.%).

II.3. Thermogravimetric analysis (TGA) coupled to differential thermal analysis (DTA)

TGA coupled to DTA, measures weight difference and temperature of a sample, in comparison with a reference, during increasing or decreasing temperature. Weight and temperature variations refer to physicochemical processes such as, dehydration, decarbonation and crystallization. TGA coupled with DTA, allows the identification and the semi-quantification of some cement hydrates, because they are considerably unstable during a temperature increase.

In the present work, the thermal behavior of the mixtures prepared for studying ye'elimite synthesis was followed using DTA on a Setaram SETSYS 24 apparatus. 50 mg of the sample was introduced into a platinum crucible and analyzed with a heating ramp of 10 °C/min from 30 to 1300°C. α -Al₂O₃ previously calcined was used as a reference.

TGA analysis of hydrated cement samples was carried out in N₂ atmosphere on 30 mg of sample using a SETARAM Labsys TG-DTA/DSC thermal analyser with a heating ramp of 10 °C/min up to 1100°C.

II.4. Thermogravimetric analysis (TGA) coupled to Mass-spectroscopy (MS)

The use of MS in the identification of released gaseous species in TGA experiments is well established. The mass spectrometer can be attached directly to the outgas port of the thermogravimetric instrument. Mass spectrometers have the ability to detect species to 1 ppm or better, and the detection is done in real time as the thermogravimetric analysis (TGA) scans [184].

In the present thesis work, the thermal behavior was studied using a thermogravimetric analyzer (STA 449F3 graphite - Netzsch 1750, argon flow: 20 ml/min, heating rate 10 °C/min) coupled with a Mass Spectrometer (Omnistar, Balzers Instrument).

II.5. Particle Size Distribution by Laser Diffraction (PSD-LD)

Particle-size distribution is one of the most fundamental physical properties of a powder. PSD-LD technique is based on the forward diffraction of a laser beam by particles. The angle of diffraction is inversely proportional to particle size, and the intensity of diffracted beam at any angle is a measure of the number of particles with a specific cross-sectional area in the beam's path. Two optical models are commonly used to calculate PSD, the Fraunhofer diffraction model and the Mie theory [185].

PSD-LD of the sample powders were obtained using a Mastersizer 2000 laser size analyzer (Malvern). The Fraunhofer model was selected for the analysis. Prior to this measurement, the powder (approximately 50 mg) was mixed in 40 ml of absolute ethanol and the suspension was agitated for 1 min with the help of a Vibracell 75041-Bioblock scientific ultrasonic apparatus in order to break the weakest agglomerates.

II.6. Particle Size Distribution by Image Analysis (PSD-IA)

In many studies of the properties of nanoparticles a detailed knowledge of the size distribution is important for the interpretation of experimental results. PSD-IA technique seems to be very useful for

this purpose. In particular, it can easily handle a large number of particles and it is much faster and less subjective than commonly used manual techniques. The technique has, of course, limitations, especially if the particles overlap and if the particle shape is not well represented by the used template. Uncertainties in the estimated volume distributions can also be expected because one observes 2D images of 3D objects [186].

The particle size distribution of the synthesized nano-sized ye'elinite powders was examined by PSD-IA technique of the SEM micrographs which gave information at nanometric scale, using imageJ V1.51 software. A statistical analysis of the data was made using OriginPro V9.2 software. The particle size, D_{particle} , corresponds to the mean Feret maximum diameter estimated from a total of 160 ye'elinite particles ($N_{\text{total}} = 160$). The standard deviation, σ , is estimated for each analyzed image. The mean particle diameter of the distribution D_{particle} is calculated as follows:

$$D_{\text{particle}} = \frac{1}{N_{\text{total}}} \sum_{i=1}^{N_{\text{total}}} D_F \quad (\text{E.28})$$

where D_F refers to the maximum Feret diameter which can be defined as the distance between the most distant points on the projection of the particle (Figure II-2). Lastly, the standard deviation of the particle size distribution is calculated:

$$\sigma = \sqrt{\frac{1}{N_{\text{total}} - 1} \sum_{i=1}^{N_{\text{total}}} (D_F - D_{\text{particle}})^2} \quad (\text{E.29})$$

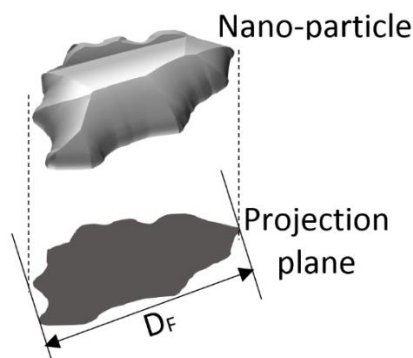


Figure II-2: Maximum Feret diameter applied to a projection of a 3D schematic nano-particle.

II.7. BET specific surface area (SSA)

The BET theory was originally elaborated by Brunauer, Emmett and Teller, the determination of specific surface by means of the BET theory is based upon the phenomenon of physical adsorption of gases on the external and internal surfaces of a porous material. Such a material which is surrounded by and in equilibrium with a certain gas (N₂ for example) which has a certain temperature and relative vapour pressure, adsorbs physically a certain amount of gas. The amount of adsorbed gas is dependent on its relative vapour pressure and is proportional to the total external and internal surface of the material. The connection between relative vapour pressure and amount of adsorbed gas at a constant temperature is called an adsorption isotherm [187].

The BET specific surface area was estimated from N₂ adsorption experiments using a Micromeritics model TristarII® 3020 analyzer. Prior to measurements, a degassing step of the sample powder was carried out at 80°C overnight in order to achieve a pressure equal to 60 mTorr.

II.8. Thermal Differential Dilatometry (TDD)

Differential dilatometry is a powerful technique for precise measurements of the thermal dilatation behavior as a function of temperature/time during application of a specific heat-treatment cycle [188].

The dilatometric analysis was performed using a NETZSCH DIL402 C apparatus, which records the sample expansion and/or shrinkage of the powder compact as a function of temperature. This experiment was carried out at the heating ramp of 10 °C/min.

II.9. Open porosity estimation by Archimedes principle (EN 623-2:1993)

The principle of the method is to determine by weighing, the weight of the dry sample (m_1), its apparent weight (m_3) after vacuum impregnation in a liquid with known density (ρ_L), and the weight of the sample, in-situ, immersed in the liquid (m_2). From these weight values, bulk density (ρ_s) and open porosity (P_o) could be calculated using the following equations:

$$\rho_s = \frac{m_1}{m_1 - m_2} \times \rho_L \quad (\text{E.30})$$

$$P_o = \frac{m_3 - m_1}{m_3 - m_2} \times 100 \quad (\text{E.31})$$

Bulk densities and open porosities of the fired specimens were determined according to Archimedes principle, following the European norm (EN 623-2:1993), and using ethanol as the immersion liquid.

The measured open porosity fraction is compared with the porosity estimated from backscattered electron image analysis (BSE-IA) using ImageJ version 1.51.

II.10. Porosity estimation from backscattered electron image analysis (BSE-IA)

The specimens were first impregnated with a resin and polished before BSE image analysis. The threshold grey level between porosity and solid phases was selected by a technique based on the shape of the histogram. A single threshold value was made to every image, brightness and contrast were held constant. For statistical significance, magnification of $\times 50$ was used for all images and five image analyses were carried out for each sample. The volume fractions of anhydrous material and porosity derived from BSE image analysis are compared with those obtained by other techniques and good correlation was found.

II.11. Scanning electron microscopy (SEM)

When a beam of primary electrons strikes a bulk solid, the electrons are either reflected (scattered) or absorbed, producing various signals. The incident electrons disperse into a “pear shaped” volume in the solid. Besides secondary electrons, backscattered electrons (BSE), X-rays, Auger electrons, and other responses, are also produced. Figure II-3 shows the interaction between electron beam and sample surface. Different modes of observation and/or microanalysis can thus be employed on the object under examination. The most frequent modes in the SEM involve the capture of secondary and backscattered electrons, while the most commonly used microanalytical techniques, based on the detection of x-rays, are energy dispersive x-ray analysis and wavelength dispersive (WD) analysis. Modern SEMs are usually equipped with the EDX detector while the WD analyzer unit remains an option for the expensive models [189].

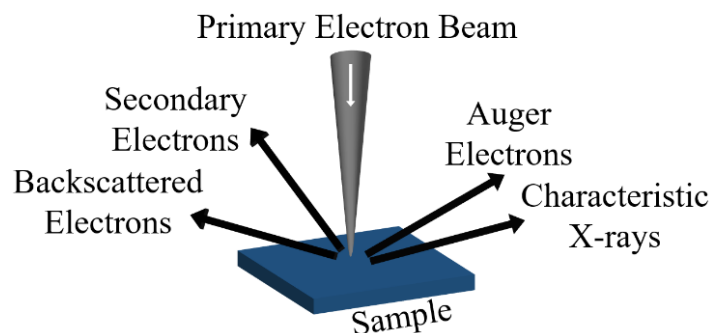


Figure II-3: The interaction between electron beam and sample surface, adapted from [190].

- *SEM sample preparation for the study of solid-state synthesis of ye'elinite*

The scanning electron microscope (SEM) used for this study was a FEI Quanta 450 with EDS detector. The microscope was operated at 15 kV accelerating voltage. Prior to any observation, a 15 nm Au-Pd layer was deposited in order to ensure suitable electronic conduction at the surface of samples. The specimens are stored in desiccators with silica gel prior to and after examinations to prevent hydration or carbonation. The microscope was set up to take a backscattered electron image (BSE) and to carry out EDS element analysis. Specimens for BSE-IA were prepared from polished epoxy-impregnated samples. The samples were impregnated with epoxy in plastic container. Epoxy consists of 10 ml resin (IP, PRESI France) and 1 ml hardener (Catalyst, PRESI France), was injected into the plastic container in a vacuum chamber until the surface of samples was covered. The epoxy-impregnated samples were solidified at 25 °C for 24 h, then smoothed by grinding until the surface is flat, using abrasive SiC papers of P500 and P1000 rotated at 70 and 100 rpm, respectively. Next, the sample is rinsed for a few minutes with ethanol in an ultrasonic bath. After epoxy impregnation, the 3 and 1 μm diamond suspensions were consecutively used for polishing during 2 h. The applied contacting force between the epoxy-impregnated sample surface and the rotating disks was carried out manually.

- *SEM sample preparation for the study of sol-gel synthesis of ye'elinite*

Powder morphology was examined by LEO 1530 VP field emission scanning electron microscopy (SEM) equipped with an EDS detector (Oxford INCA 250). The microscope was operated at a 1 kV accelerating voltage. This low voltage is necessary in order to avoid spoiling the sample. SEM samples were prepared by dispersing the powder in absolute ethanol. One drop of the suspension was then deposited on an aluminum support and dried in air. The specimens are stored in desiccators with silica gel prior to and after examination to prevent hydration or carbonation. The SEM observations were carried out without using a deposited conducting layer.

- *SEM sample preparation for the study of ye'elinite formation mechanisms*

The scanning electron microscope (SEM, JSM-IT300, JEOL, Japan) used for this study was equipped with an Energy Dispersive Spectrometer (EDS, Oxford, UK). The microscope was operated at 15 kV accelerating voltage. Prior to any observation, a 15 nm Au-Pd or Carbone coating was deposited in order to ensure suitable electronic conduction at the surface of samples. The specimens were stored in desiccators filled with silica gel prior to and after examinations to prevent hydration or carbonation. Colored Backscattered Electron (BSE) images reveal the different phases because of the atomic number contrast. EDS mapping and compositional profile along a line were made to localize each formed phase. For reliable observations, the essential prerequisite is a well-polished sample. Polished sections can provide representative images of a cross section of the sample microstructure. In this respect, the

impregnation of the sample (under the form of a pellet) is done with a low-viscosity epoxy resin (IP, PRESI France). The hardening time of the resin is about 24 h at room temperature. Once the sample is removed from the mold, the top side of the embedded sample is polished using SiC paper and absolute ethanol as a lubricant. Water should not be used at any time as it could lead to hydration of anhydrous grains. Regular observation of the surface under a light microscope is essential to check the surface aspect after each polishing step. Polishing was performed using Minitech 233 type machine (Presi, France). Details of the polishing protocol are given in Table II-2.

Table II-2: Polishing steps.

Polishing Steps	SiC paper	Lubricant	Polishing time (s)	Force (daN)	Rotation speed of the polishing disc (rpm)
1	P240	Ethanol (*)	30	0.25	150
2	P600	Ethanol	180	0.25	150
3	P1200	Ethanol	270	0.25	150
4	P2400	Ethanol	360	0.25	150
5	P4000	Ethanol	450	0.25	150

(*) Absolute ethanol was used as polishing lubricant to avoid sample hydration reactions.

- *SEM sample preparation for the study of ye'elimite-rich cement hydration*

The prepared samples were examined by LEO 1530 VP field emission scanning electron microscopy (SEM) equipped with an EDS detector (Oxford INCA 250). The microscope was operated at a 1 kV accelerating voltage. This low voltage is necessary in order to avoid spoiling the sample. The samples are stored in desiccators with silica gel prior to and after examination to prevent hydration or carbonation. SEM observations were carried out without using a deposited conducting layer. For ye'elimite dissolution experiments, ye'elimite powder was mixed with demineralized water at 500 rpm using magnetic agitator for the desired time. Hydration was stopped by the solvent exchange method using acetone, then filtered by vacuum aspiration and the samples could then be observed under the SEM.

II.12. Ionic conductivity and pH measurements

Ionic conductivity of a solution is measured by the application of a tension between two electrodes in the conductivity measurement cell. Anions migrate to the cathode and cations migrate to anode. The inverse of the solution electrical resistance is the conductance, this latter is measured in Siemens (S). Ionic conductivity of a solution is measured in a standard cell with electrodes whose surface is equal to 1 cm² and separated by 1 cm. The unit of ionic conductivity is traditionally in (mS/cm) [191].

For very diluted solutions, ionic conductivity obeys to Kohlrausch's law:

$$\sigma = \sum_i \lambda_i \times C_i \quad (\text{E.32})$$

where σ is the ionic conductivity (mS/cm), λ_i is the molar conductivity (mS.cm²/mol), and C_i is the molar concentration of the involved ions (mol/cm³). Ionic conductivity is thus directly proportional to the concentration of ions present in the solution.

The ionic conductivity variations with time of ye'elimite suspensions was performed using a CDM210 Conductivity Meter. The water over ye'elimite mass ratio, W/Ye, is equal to 1000. This high dilution has been chosen to avoid the formation of hydrates and in order to have specifically information about ye'elimite dissolution. During the measurement, the suspension was stirred at 500 rpm. The volume of the measurement cell is about 150 ml. The temperature was controlled by a thermostatic bath with external water circulation at 25 °C.

II.13. Zeta potential measurement

Adsorption of particles in an aqueous medium is a very general phenomenon. It includes physical adsorption, ion exchange, and surface complexation at the surfaces of metal oxides, hydroxides, and hydrous oxides, etc. The measurement of particle surface charge is highly interesting to examine adsorption phenomena [192].

In a colloidal medium, the identification of the particle surface charge is approached by the measurement of zeta potential (ζ), which corresponds to the potential at the slipping plane between the Stern layer and diffuse layer. The zeta potential is a key indicator of the stability of colloidal dispersions. The value of the (ζ) indicates the degree of electrostatic repulsion between adjacent, similarly charged particles in a dispersion. The most known and exploited phenomena to measure zeta potential is electrophoresis, i.e. the motion of charged particles under an electrical field in a liquid suspension. In the present case, the applied electrical field was an alternative to avoid electrode polarization [193].

The interaction between the added citric acid and ye'elimite powder was evaluated by measuring the zeta potential of ye'elimite particles as a function of the citric acid concentration. Suspensions of 0.1 wt.% were prepared by mixing, during about 24 h, ye'elimite powder with deionized water containing different dosages of citric acid (0, 5 and 10 wt.% relative to ye'elimite powder weight), the pH of the corresponding acidic suspensions were 11.79, 10.84 and 10.80, respectively. Citric acid is normally considered to be a tribasic acid, with pKa values at 25 °C, extrapolated to zero ionic strength, of 2.92, 4.28, and 5.21 [194]. Thereby, citrate is the dominant form of citric acid present in the prepared

suspensions. The zeta potential was measured using a Malvern ZetaSizer Nano ZS, which works on the basis of the electrophoresis method.

II.14. Free-lime determination by volumetric dosage method

For free-lime determination, a sample of 2.00 ± 0.01 g of ground clinker was weighed into a 50 ml Erlenmeyer. About 25 ml of ethylene glycol was added to the flask and stirred for 10 min using a magnetic stirrer, then the suspension was heated in a lab oven at 110 °C for 10 min. The hot suspension was filtered in a Buchner under vacuum. The filtrate solution was poured into a glass beaker, which contained beforehand 200 ml of demineralized water and 5 ml of concentrate HCl. Before titration 4 ml of ammonia solution and 15 ml of ethanolamine were added, then NaOH solution (2N) was added to maintain a pH=13. A few drops of Patton-Reeder reagent as a color indicator were added. Titration was carried out to a blue color endpoint with a solution of Ethylene diamine tetra acetic acid EDTA (0.05 M).

Chapitre III. Synthesis methods and experimental protocols

Chapter III describes, firstly, the physical and chemical characteristics of the materials used during the present thesis. Then it details the experimental protocols adopted to prepare the different samples. It is worth noting that the synthesis methods described hereafter were originally developed in the present thesis to synthesis highly pure ye'elinite.

III.1. Raw materials

The synthesis of high pure ye'elinite powder requires the utilization of reactants with high purity and reactivity. The physical and chemical characteristics of the raw materials used for the synthesis of ye'elinite are summarized in Table III-1 and Table III-2. The used reactants for ye'elinite solid-state synthesis were alumina, calcium sulfate dihydrate (or gypsum) and calcium carbonate. These reactants are in the form of fine white powders, where the d_{50} are 5.62, 23.08, and 10.83 μm for alumina, calcium sulfate dihydrate and calcium carbonate, respectively. They show reagent purity grade ($> 99.0 \text{ wt.}\%$), their purity was checked using XRD and XRF analyses. Their specific surface BET is somehow acceptable to solid-state synthesis. It is equal to 0.58, 4.19 and 0.22 m^2/g for alumina, calcium sulfate dihydrate and calcium carbonate, respectively. The apparatus and techniques are described in chapter II.

In the case of ye'elinite sol-gel synthesis, the used precursors were in form of salts powders, calcium nitrate, aluminium nitrate and aluminium sulfate. The choice of salts as precursors is justified by their high solubility in water giving immediately the required ionic precursors. For the polymerization reactions, citric acid, ethylene glycol and polyvinyl alcohol were used. The reactants show a high purity grade that is required for the synthesis of highly pure ye'elinite powder.

Table III-1: Chemical analysis and physical characteristics of the raw materials used for the synthesis of ye'elinite by solid-state reactions.

Raw material	Alumina	Calcium sulfate dihydrate	Calcium carbonate	
CAS number and Supplier name	1344-28-1, Acros-Organics	10101-41-4, Sigma-Aldrich	471-34-1, Sigma-Aldrich	
Composition ^(a)	α -Al ₂ O ₃	CaSO ₄ .2H ₂ O	CaCO ₃	
Purity (wt.%)	> 99.7	> 99.0	> 99.9	
Real density ^(b) (g/cm ³)	3.08	2.30	2.67	
Specific surface BET ^(c) (m ² /g)	0.58	4.19	0.22	
Particle size ^(d)	d ₁₀ (μm)	3.11	9.92	4.70
	d ₅₀ (μm)	5.62	23.08	10.83
	d ₉₀ (μm)	11.38	45.32	24.16
Chemical analysis (wt.%) ^(e)	Al ₂ O ₃	99.869	0.030	-
	Fe ₂ O ₃	0.046	-	0.057
	SiO ₂	-	0.042	0.039
	SO ₃	-	46.504	0.062
	CaO	-	33.777	56.029
	SrO	-	0.017	0.033
	Ga ₂ O ₃	0.011	-	-
	Loss on Ignition (LOI)	0.07	19.63	43.78
Physical form	Powder	Powder	Powder	

^(a) XRD phase identification
^(b) Helium pycnometry

^(c) BET analysis
^(d) Particle size distribution by laser diffraction

^(e) XRF analysis

Table III-2: Chemical analysis and physical characteristics of the raw materials used for the synthesis of ye'elimité by sol-gel methods.

Raw material	Calcium nitrate	Aluminum nitrate	Aluminum sulfate	Citric acid	Ethylene glycol	Polyvinyl alcohol 22000
CAS number and Supplier name	13477-34-4, Fisher Scientific	7784-27-2, Fisher Scientific	17927-65-0, Fisher Scientific	77-92-9, Sigma-Aldrich	107-21-1, Fisher Scientific	9002-89-5, VWR Chemicals
Composition	Ca(NO ₃) ₂ ·4H ₂ O	Al(NO ₃) ₃ ·9H ₂ O	Al ₂ (SO ₄) ₃ ·16H ₂ O	HOC(CH ₂ CO ₂ H) ₂ CO ₂ H	HOCH ₂ CH ₂ OH	[-CH ₂ CH(OH)-] _n
Purity (wt.%)	> 99.0	> 99.0	> 99.0	> 99.5	> 99.0	-
Physical form	Powder	Powder	Powder	Powder	Viscous liquid	Powder

III.2. Experimental protocols

III.2.1. For solid-state synthesis of ye'elimité

Stoichiometric mixture samples (SM) corresponding to $C_4A_3\bar{S}$ were prepared from high purity (> 99.9 wt.%) CaCO₃, Al₂O₃ and CaSO₄·2H₂O all from Sigma-Aldrich. Table III-3 shows the amounts of raw materials used for the preparation. Each mixture (102 g) was first homogenized in a Turbula[®] shaker mixer for 15 min. Then it was crushed and homogenized again at 120 rpm for 1 h in planetary ball mills, using a 250 ml corundum jar and fifty corundum balls of 10 mm diameter. Particle size distribution of SM raw mixture is shown in Figure III-1 where d₅₀ is 14.6 μm. The homogenized mixture was uniaxially pressed under a load of 1 ton into pellets using a 20 mm cylindrical die. The compacted green body was subsequently placed in a platinum crucible and thermally treated in an elevator furnace (internal volume 13.8 l) under air atmosphere at temperatures ranging from 1000 to 1350°C (heating ramp: 5 °C/min, dwell duration: 0.5 to 4 h; air quenching). The sintered product was ground into a fine powder in an agate mortar and sieved (< 100 μm). For each thermal cycle, three 2 g pellets were placed in the same crucible. The samples are referenced as shown: SM(temperature_duration_1 or 2), where (temperature) is the sintering temperature in °C, (duration) is the sintering duration in hours, 1 refers to samples fired once and 2 refers to samples fired twice. Table III-4 shows temperature and duration of sintering of the samples studied in this work.

Table III-3: Amounts of raw materials employed for the preparation of SM sample (expressed in grams).

Raw materials	CaCO ₃	Al ₂ O ₃	CaSO ₄ .2H ₂ O	Total
Weights (g)	39.34	40.13	22.56	102.03

Table III-4: Temperature and duration of thermal treatment of the samples studied in this work.

Temperature (°C)	Sintering duration (hours)				
	0.5	1	2	3	4
1000	SM(1000_0.5_1)	SM(1000_1_1)	SM(1000_2_1)	SM(1000_3_1)	SM(1000_4_1)
1200	SM(1200_0.5_1)	SM(1200_1_1)	SM(1200_2_1)	SM(1200_3_1)	SM(1200_4_1)
1250	SM(1250_0.5_1)	SM(1250_1_1)	SM(1250_2_1)	SM(1250_3_1)	SM(1250_4_1)
1300	SM(1300_0.5_1)	SM(1300_1_1)	SM(1300_2_1)	SM(1300_3_1) SM(1300_3_2)	SM(1300_4_1)
1350	SM(1350_0.5_1)	SM(1350_1_1)	SM(1350_2_1)	SM(1350_3_1)	SM(1350_4_1)

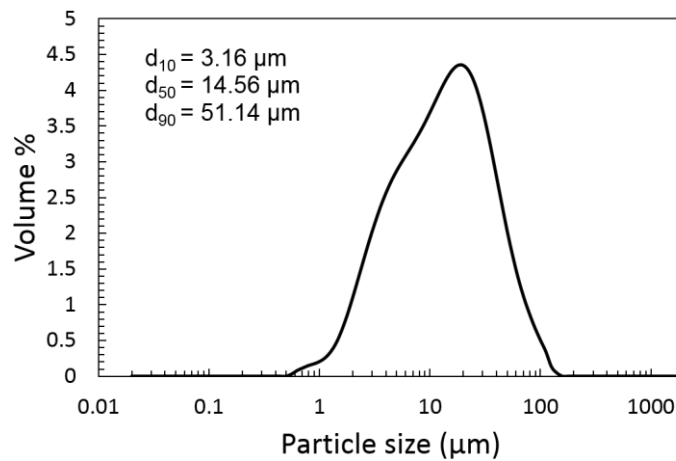


Figure III-1: Particle size distribution of the SM raw mixture.

III.2.2. For sol-gel synthesis of fine ye'elinite

$\text{Ca}(\text{NO}_3)_2 \cdot 4\text{H}_2\text{O}$ (N°CAS: 13477-34-4, Fisher Scientific), $\text{Al}(\text{NO}_3)_3 \cdot 9\text{H}_2\text{O}$ (N°CAS: 7784-27-2, Fisher Scientific) and $\text{Al}_2(\text{SO}_4)_3 \cdot 16\text{H}_2\text{O}$ (N°CAS: 17927-65-0, Fisher Scientific) were used as starting materials and mixed in stoichiometric amounts corresponding to ye'elinite.

The steps and the amounts of raw materials for the synthesis of ye'elinite through the different chemical routes are presented in Figure III-2, Figure III-4, Figure III-6 and Table III-5, respectively. Each method is described below. For each route, a schematic representation of the reactants and products at the molecular scale is proposed in Figure III-3, Figure III-5, and Figure III-7.

- Pechini method (Pech), Figure III-2 and Figure III-3

30 years ago, Pechini [195] proposed a method to synthesize pure oxides based on the ability of α -hydroxy acids, such as citric acid, to form chelates (citric acid-metal) with different cations (Figure III-3). The cation precursors (nitrates and sulfates) and citric acid are dissolved in distilled water and then mixed with polyhydroxy alcohol, such as ethylene glycol [196]. By heating this mixture, water evaporates and polyesterification takes place, which leads to the formation of a metal-polymer network (Figure III-3). The major aim of this synthesis route is to achieve a random distribution of cations within the resin. The advantage is that the viscosity and the molecular mass of the polymer can be controlled by varying the resin content [197]. The resin content noted Rc is given by equation (E.33):

$$\%Rc = \frac{m_{\text{resin}}}{m_{\text{resin}} + m_{\text{oxide}}} \times 100 \quad (\text{E.33})$$

where m_{oxide} is the mass of the final oxide to be produced (ye'elinite in the present case), calculated from the known masses of the precursors, and m_{resin} is the mass of the organic part. In the Pech method, m_{resin} is the mass of citric acid and ethylene glycol in the mixture. For the other two methods described and used in this study, namely the OSE and the SPC methods, m_{resin} corresponds respectively to the mass of polyvinyl alcohol and the mass of citric acid in the mixture.

The salts corresponding to a final mass of 2 g of ye'elinite were dissolved in 30 ml of deionized water. The resin was composed of 60 wt.% of citric acid $\text{HOC}(\text{CH}_2\text{CO}_2\text{H})_2\text{CO}_2\text{H}$ (N°CAS: 177-92-9, Fisher Scientific) and 40 wt.% of ethylene glycol $\text{HOCH}_2\text{CH}_2\text{OH}$ (N°CAS: 107-21-1, Fisher Scientific). Rc was fixed at 70% and 95%. The choice of Rc is based on work by Nettleship et al. [131]. The masses of each chemical reactant for Rc=70% and Rc=95% are presented in Table III-5. The corresponding products are noted Pech70 and Pech95.

Citric acid was introduced according to the following sequence: dissolution in deionized water with a 1:3 molar ratio, addition to the solution of salts, mixing within a solution of ethylene glycol in order to promote polyesterification reactions. The mixture was then stirred at 80°C for 8 h on a hot plate to evaporate water and to favor polymerization. The resulting viscous gel was completely dried at 150°C for 2 h to become a crisp aerated gel (Figure III-2). The crispy gel was calcined in a platinum crucible with a heating ramp of 5 °C/min, up to a temperature ranging between 400 and 1290°C for 1 h. After cooling the furnace to room temperature, the samples were collected and stored in airtight plastic containers.

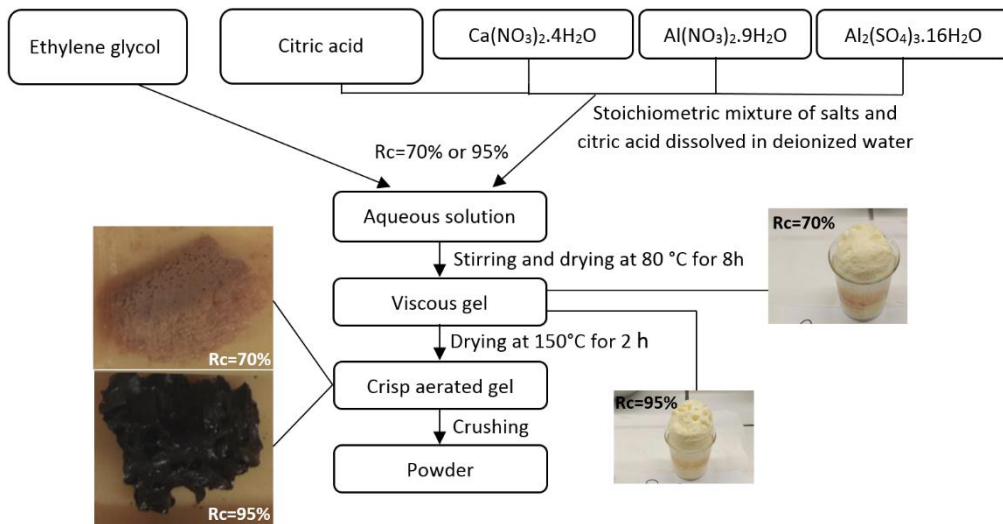


Figure III-2: Flow diagram showing the processing routes of Pechini method (Rc=70%) Pech70 or (Rc=95%) Pech95. Rc represents the resin content calculated from equation (E.33).

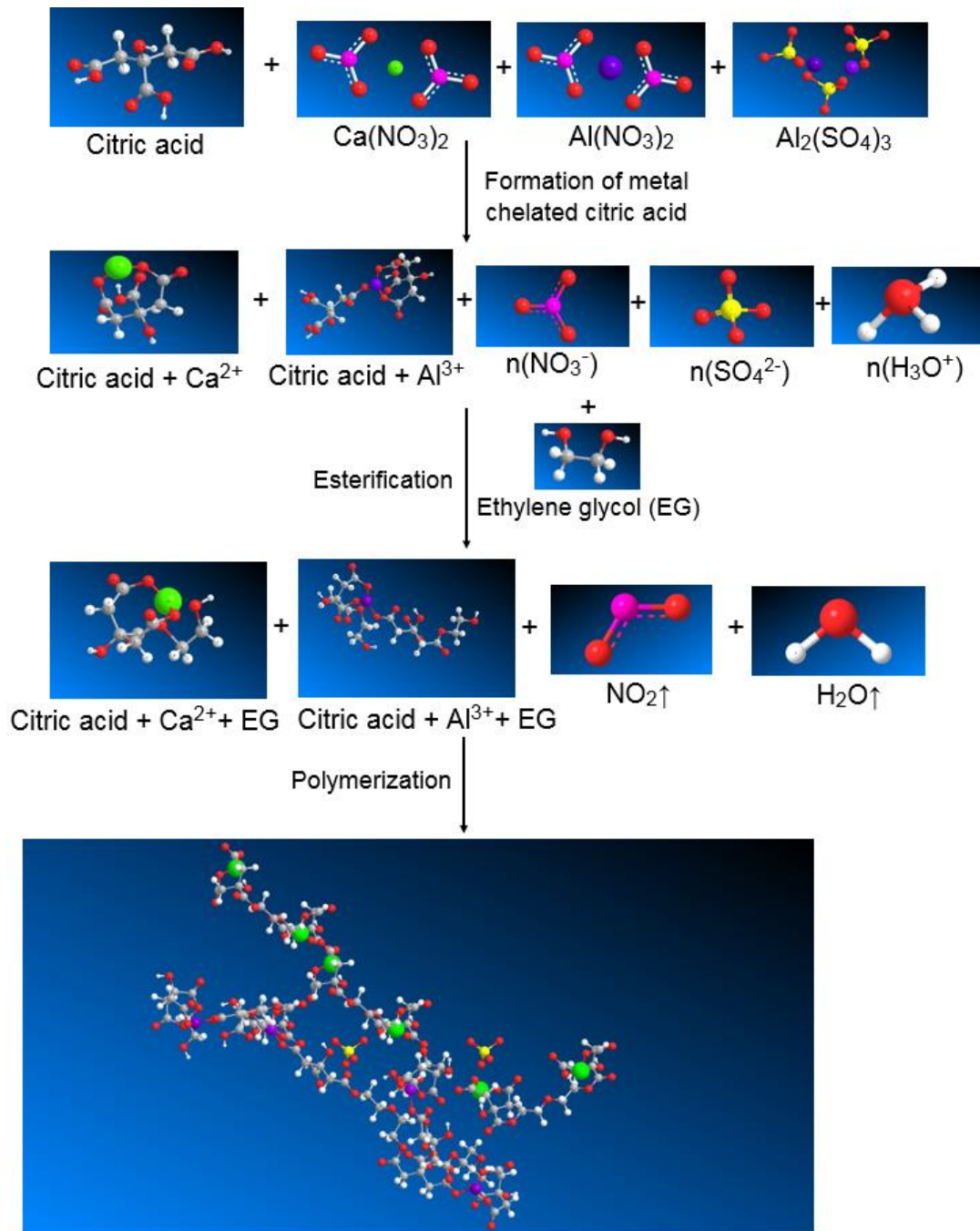


Figure III-3: Proposed chemical reactions describing the polymeric process of the Pechini method. The grey spheres represent carbon atoms and the yellow spheres represent sulfur atoms, whereas white, red, pink, purple and green spheres identify hydrogen, oxygen, nitrogen, aluminum and calcium, respectively.

Table III-5: Powder preparation and processing variables.

Chemical synthesis route	Chemical reactants	Content (g or ml)	pH of the solution	Solution color	Visual aspect of the dried gel (Figure III-2, Figure III-4, Figure III-6)
Pechini method (Rc70%)	Ca(NO ₃) ₂ .4H ₂ O	3.095 g	4.13	Transparent	Brown gel, fairly coarse texture
	Al(NO ₃) ₂ .9H ₂ O	6.557 g			
	Al ₂ (SO ₄) ₃ .16H ₂ O	0.688 g			
	Deionized H ₂ O	30 ml			
	Citric acid	2.8 g			
	Ethylene glycol	1.68 ml			
Pechini method (Rc95%)	Ca(NO ₃) ₂ .4H ₂ O	3.095 g	1.93	Transparent	Black gel, soft and porous texture
	Al(NO ₃) ₂ .9H ₂ O	6.557 g			
	Al ₂ (SO ₄) ₃ .16H ₂ O	0.688 g			
	Deionized H ₂ O	30 ml			
	Citric acid	22.8 g			
	Ethylene glycol	13.69 ml			
Organic steric entrapment method	Ca(NO ₃) ₂ .4H ₂ O	3.095 g	5.8	Transparent	White gel, coarse texture
	Al(NO ₃) ₂ .9H ₂ O	6.557 g			
	Al ₂ (SO ₄) ₃ .16H ₂ O	0.688 g			
	Deionized H ₂ O	30 ml			
	PVA 22000 (5 mass% aqueous sol.)	1.11 g			
Self-propagating combustion method	Ca(NO ₃) ₂ .4H ₂ O	3.095 g	3.62	Transparent	Dark brown gel, soft and porous texture
	Al(NO ₃) ₂ .9H ₂ O	6.557 g			
	Al ₂ (SO ₄) ₃ .16H ₂ O	0.688 g			
	Deionized H ₂ O	30 ml			
	Citric acid	10 g			

- Organic steric entrapment method (OSE), Figure III-4 and Figure III-5

More recently, a new processing route has been developed. Unlike the Pechini-resin process, which involves chelation and polymerization, the OSE process consists of primarily steric entrapment of cations in the polymer network, namely Polyvinyl Alcohol (PVA). PVA ensures the homogenous distribution of the ions in its polymer network structure and prevents further agglomeration and/or precipitation from the solution (Figure III-5) [125,126].

The starting salts were the same as for the Pechini process. The salts were dissolved in stoichiometric proportions in deionized water. Once the salts were completely dissolved, water containing 5 wt.% of dissolved PVA (N^oCAS: 9002-89-5, VWR Chemicals) was added. The molecular weight of PVA was 22000 g/mol with a degree of polymerization of 500 (monomers/polymer). The mass ratio of the PVA to cation sources was chosen in such a way that there were 4 times more positively charged valence ions from the cations than from the potentially charged $-(OH)$ functional groups of the polymers [198]. In one PVA monomer, there is one hydroxyl $-(OH)$ functional group. In the case of the 4:1 $C_4A_3\bar{S}$ cations

to PVA hydroxyl ratio, the total positively charged valency of ions is 32 ($4\text{Ca}^{2+}+6\text{Al}^{3+}+1\text{S}^{6+}$). Thus 8 PVA monomers are used per 1 $\text{C}_4\text{A}_3\bar{\text{S}}$ molecule. The results of weight calculations are listed in Table III-5.

After PVA addition to the initial mixture, water was evaporated by continuous stirring during heating at 80°C on a hot plate. The resulting viscous gel was completely dried after several hours at 150°C (Figure III-4) and then thermally treated at different temperatures ($400\text{-}1290^\circ\text{C}$) in a muffle furnace with a heating rate of $5^\circ\text{C}/\text{min}$. After cooling the furnace to room temperature, the samples were stored in airtight plastic containers.

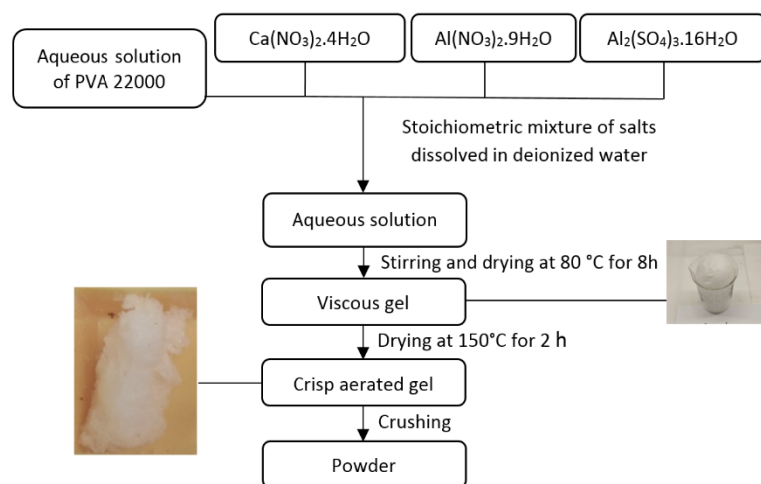


Figure III-4: Flow diagram showing the processing route of organic steric entrapment method OSE.

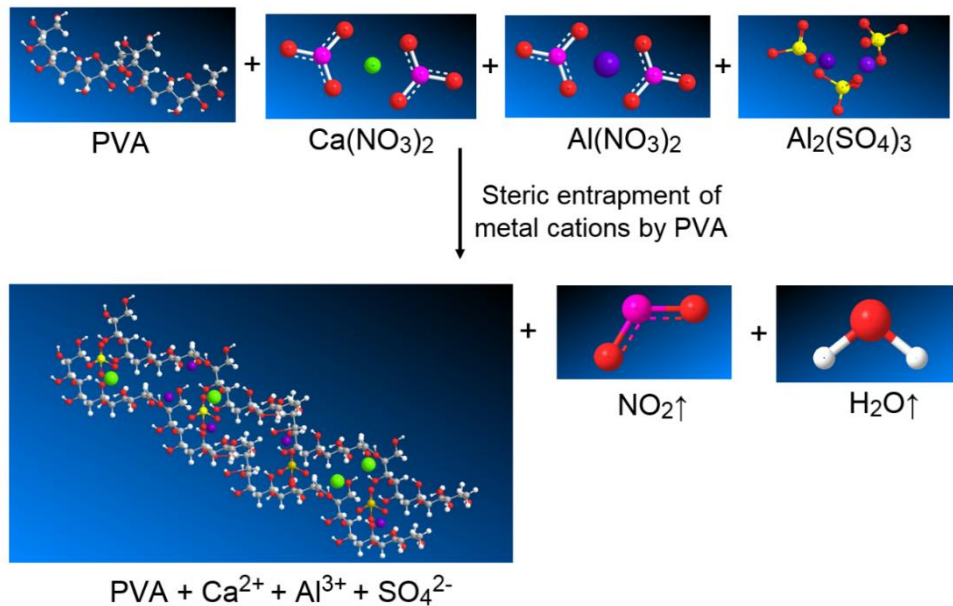


Figure III-5: Proposed chemical reactions describing the polymeric process of the OSE method. The grey spheres represent carbon atoms and the yellow spheres represent sulfur atoms, whereas white, red, pink, purple and green spheres identify hydrogen, oxygen, nitrogen, aluminum and calcium, respectively.

- Self-propagating combustion synthesis (SPC), Figure III-6 and Figure III-7

Among the techniques of chemical synthesis, combustion synthesis is a novel route with a unique combination of the chemical sol-gel process and the combustion process. The success of the method is due to an intimate blending that is achieved among the constituents by using a suitable fuel or complexing agent, such as citric acid, in an aqueous media and an exothermic redox reaction between the fuel and an oxidizer (i.e. nitrates and sulfates) (Figure III-7) [199]. The SPC method is characterized by the fact that once the initial exothermic reaction mixture is ignited by means of an external thermal source, a rapid (typically from 0.1 to 10 cm/s) high-temperature (1000-3000°C) reaction wave propagates through the mixture in a self-sustained manner [200].

Combustion in a mixture of the salts with citric acid in an aqueous solution was carried out to synthesize a fine powder of ye'elimite. The citric acid was added to chelate Ca^{2+} and Al^{3+} in the solution (Figure III-7) and as a suitable fuel for the combustion reaction. The molar ratio of citric acid to total moles of nitrate and sulfates ions was adjusted to 1:1 [201].

The aqueous solution was evaporated to a dry state by heating at 80°C on a hot plate with continuous stirring. As the water evaporated, the solution became viscous and finally formed a very viscous gel (Figure III-6). Increasing the temperature up to 150°C led to the ignition of the gel. The reaction was initiated locally and the dried gel burnt in a self-propagating combustion manner until all of it was completely burnt out to form a loose powder (Figure III-6) [202]. Finally, the as-burnt powders were calcined in air at different temperatures 400-1290°C for 1 h with a heating rate of 5 °C/min.

A comparison between the major steps of the three used chemical routes for ye'elimite synthesis at low temperature is given in Table III-6. In the following, the term 'dried gel' will refer to the gels treated at 150°C as explained in these three protocols. It should be kept in mind that during this step, the gel prepared by the SPC method could be exposed in some points to a temperature higher than 150°C [24].

Table III-6: Comparison between the principles of the three chemical routes used in the present work for the synthesis of ye'elimite.

Chemical route	Pechini synthesis	Organic steric entrapment	Self-propagating combustion
Symbol	Pech	OSE	SPC
Raw materials	Citric acid + ethylene glycol + dissolved salts	Polyvinyl alcohol + dissolved salts	Citric acid + dissolved salts
Organic medium	Polyester	PVA chain	Citric acid
Resin content Rc %	Rc (Pech70) = 70 % Rc (Pech95) = 95 %	Rc (OSE) = 35 %	Rc (SPC) = 83 %

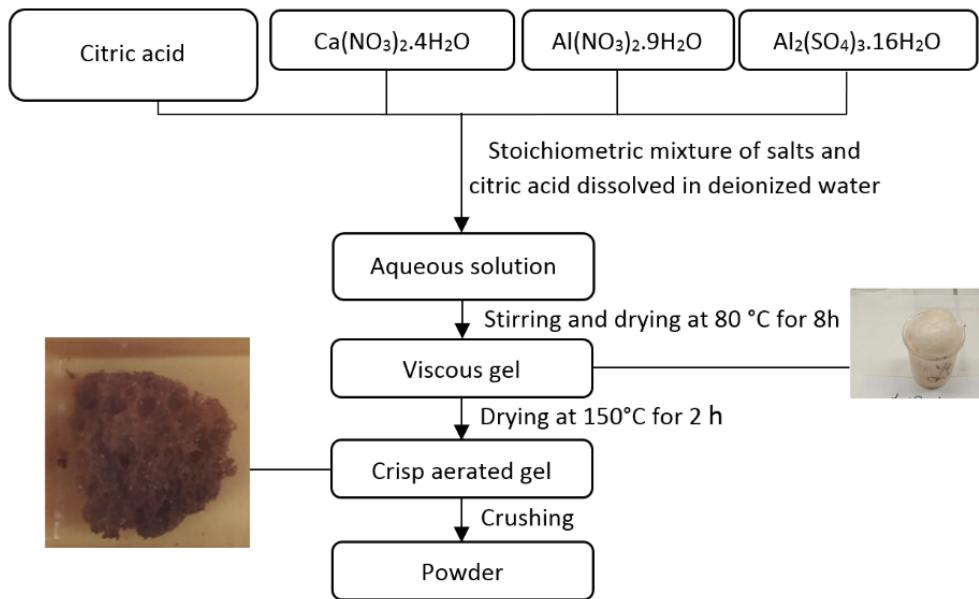


Figure III-6: Flow diagram showing the processing route of self-propagating combustion SPC method.

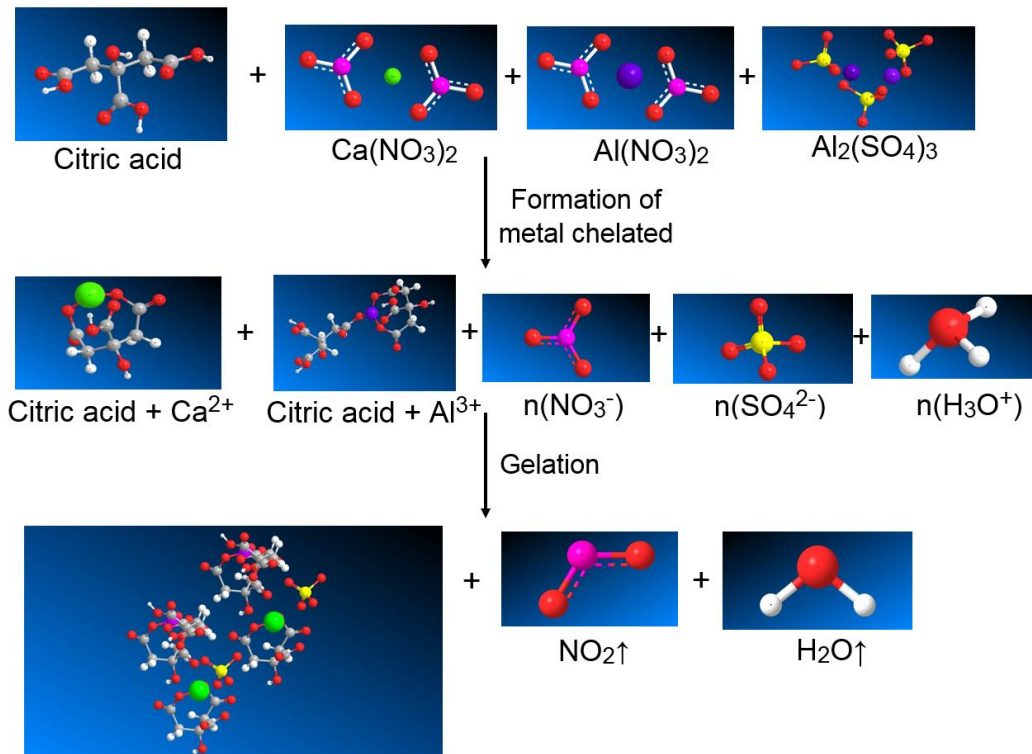


Figure III-7: Proposed chemical reactions describing the polymeric process of the SPC method. The grey spheres represent carbon atoms and the yellow spheres represent sulfur atoms, whereas white, red, pink, purple and green spheres identify hydrogen, oxygen, nitrogen, aluminum and calcium, respectively.

III.2.3. For the study of solid-state formation mechanisms of ye'elinite

The starting materials used in this work were high purity CaCO_3 , Al_2O_3 and $\text{CaSO}_4 \cdot 2\text{H}_2\text{O}$ all from Sigma-Aldrich. Table III-1 shows the chemical analysis and physical characteristics of these raw materials. The samples were prepared in the form of pellets from stoichiometric mixtures (SM) according to the protocol mentioned in [9]. Each mixture (102 g) was first homogenized in a Turbula[®] shaker for 15 min. Then it was crushed and homogenized again at 120 rpm for 1 h in planetary ball mills, using a 250 ml corundum jar and fifty corundum balls of 10 mm diameter. The homogenized mixture was uniaxially pressed under a load of 1 ton into pellets using a 20 mm cylindrical die. The compacted green body was subsequently placed in a platinum crucible and thermally treated. The choice of 1300°C for isothermal study is based on the results of our previous work [9] on pure ye'elinite synthesis since we found that 1300°C was the optimal ye'elinite synthesis temperature. The heat

treatment from 1100 to 1300°C were performed in a platinum crucible and in an elevator-furnace to ensure air quenching. To avoid the degradation of the elevator-furnace heating elements, experiments at 1000°C were carried out in muffle furnace without air quenching.

**III.2.4. For suspensions preparation for ye'elinite dissolution experiments (W/C=1000),
Figure III-8**

All suspensions were made by adding the ye'elinite powder to the demineralized water with a water to ye'elinite mass ratio, W/Ye, equal to 1000. The suspension was stirred at 500 rpm for different dissolution times. To examine the influence of citric acid on ye'elinite dissolution, three different concentrations of citric acid were pre-dissolved in the demineralized water, equivalent to 0, 5 and 10 wt.% of the ye'elinite powder, labelled Ye-Sol-0, Ye-Sol-5 and Ye-Sol-10, respectively. The chosen citric acid dosages are much higher than the common concentrations range generally used to retard CSA cements [15, 18, 29–31]. These dosages were chosen in order to allow us to highlight clearly the effect of citric acid addition. To gain information on the effect of ye'elinite fineness on the dissolution kinetics, two suspensions were compared; the first one contained ye'elinite powder synthesized by solid-state reactions (Ye-sol), and the second one contained ye'elinite powder synthesized by sol-gel method (Ye-chem).

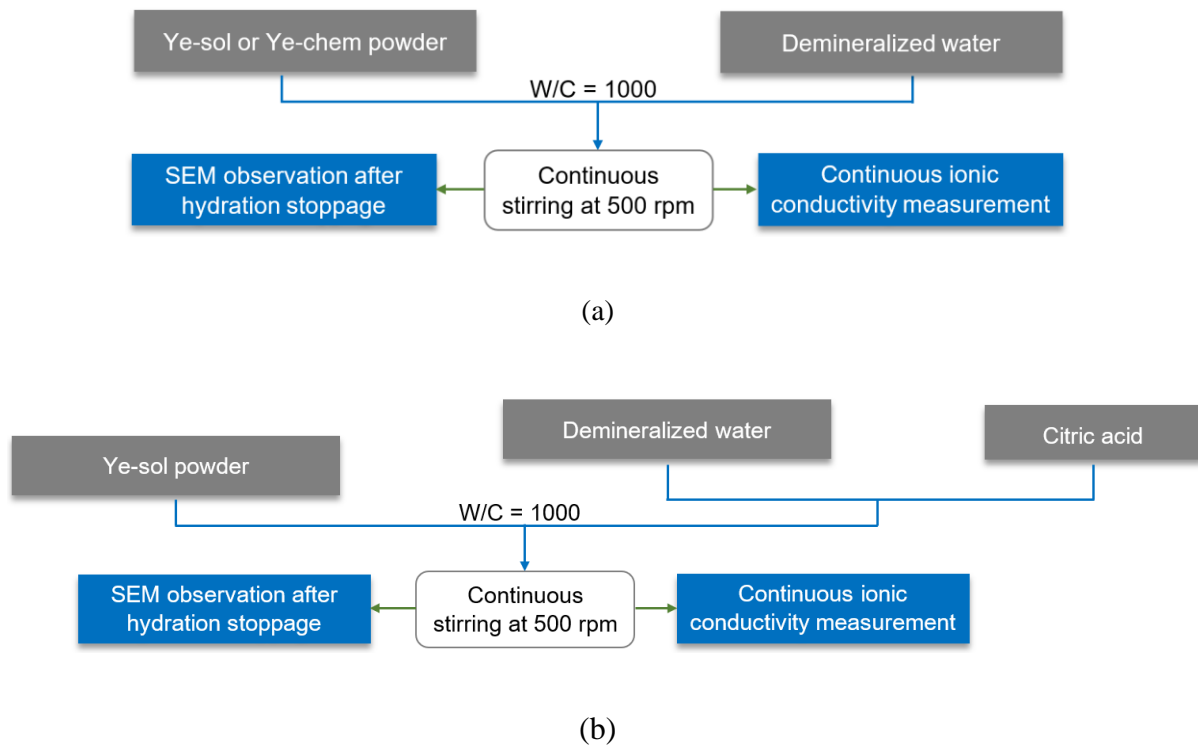
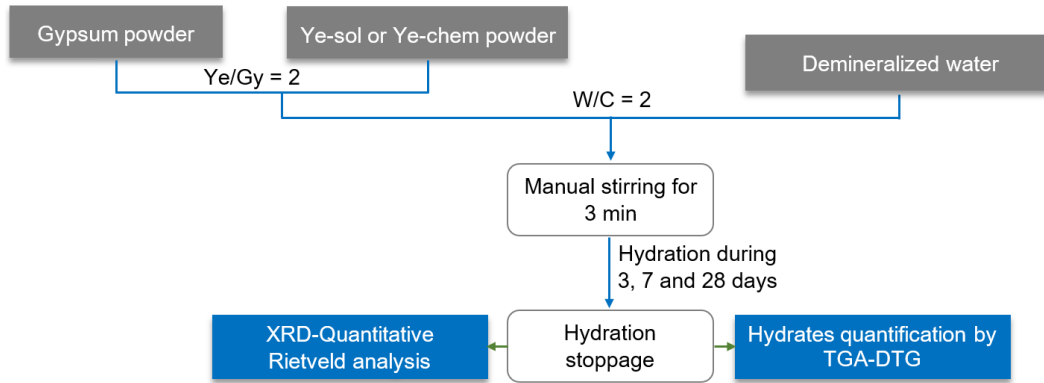


Figure III-8: Preparation protocol for the study of ye'elinite dissolution in dilute suspensions, (a) based on Ye-sol or Ye-chem, (b) based on Ye-sol with different citric acid percentages (0, 5 and 10 wt.%).

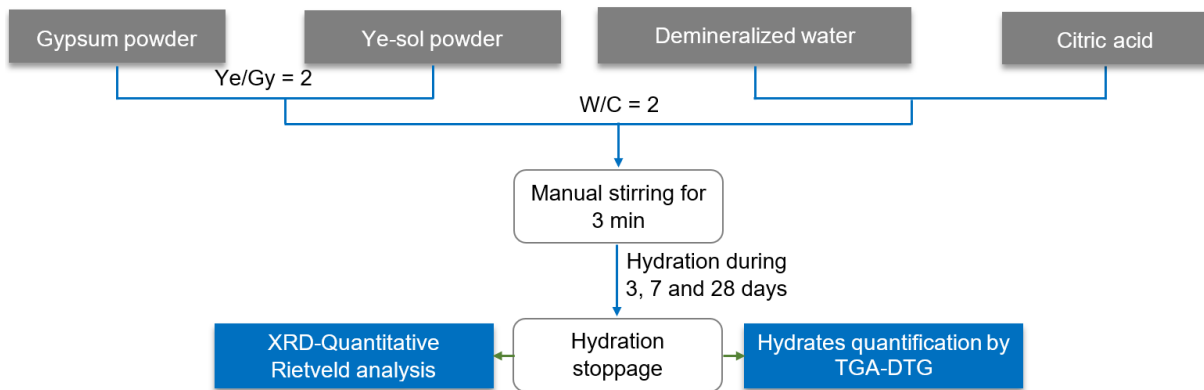
III.2.5. For the hydration of ye'elinite-rich model cements (W/C=2), Figure III-9

All experiments were carried out using a CSA model cement. It was prepared by dry mixing gypsum with ye'elinite powder either synthesized by solid-state reaction (labelled: CSA-sol) or synthesized by sol-gel method (labelled: CSA-chem). Cement pastes were prepared by adding this cement powder to demineralised water. The cement powders were prepared with a ye'elinite (Ye) to gypsum (Gy) mass ratio of 2 ($Ye/Gy = 2$) and experiments were conducted with a water to cement mass ratio, W/C, of 2. Performing the hydration study at these chosen Ye/Gy and W/C ratios should allow full ettringite precipitation [4]. The pastes were mixed manually for 3 min, sealed in polyethylene containers and stored at 20°C for 3, 7 and 28 days. These durations correspond to typical storage conditions for testing various properties of set cements. To study the influence of citric acid on ye'elinite hydration, three different concentrations of citric acid were pre-dissolved in the mixing water, equivalent to 0, 0.5 and 1 wt.% relative to ye'elinite powder weight, labelled CSA-sol-0, CSA-sol-0.5 and CSA-sol-1, respectively. The chosen citric acid dosages are within the common concentrations range generally used

to retard CSA cements [15, 18, 29–31]. After the different hydration times, the hydration was stopped by washing the samples with ketone, and samples were kept in a desiccator until analysis.



(a)



(b)

Figure III-9: Preparation protocol for the study of hydration of CSA model cement pastes, (a) based on Ye-sol or Ye-chem (blended with gypsum), or (b) based on Ye-sol (blended with gypsum) with different citric acid percentages (0, 0.5 and 1 wt.%).

III.3. Samples nomenclature and corresponding characterization techniques

The different prepared samples and the corresponding characterization that have undertaken on these samples are summarized in Table III-7.

Table III-7: Presentation of all prepared samples and the corresponding performed characterizations techniques.

Sample name	Description	Characterization technique ^(§)	
SM	Stoichiometric mixture of raw materials	TGA-MS	DA
SM(T,t)	Sintered SM samples, T refers to sintering temperature, and t refers to sintering duration. T: 1000 - 1350°C t: 0 - 4h	XRD-Quantitative Rietveld analysis	
Gel precursor	Dried gel resulted from Sol-gel method	TGA-DTA	XRD
Calcined gel (T)	Calcination of Gel precursor sample for 1h at T. T: 400-1290°C	XRD-Quantitative Rietveld analysis	
Ye-Sol-0	Highly pure ye'elimite powder synthesized by solid state reaction method	SEM BET	PSD IC
Ye-Sol-5	Powder containing ye'elimite and 5 wt.% of citric acid; percentage relative to ye'elimite weight	IC	
Ye-Sol-10	Powder containing ye'elimite and 10 wt.% of citric acid	IC	
Ye-chem	Highly pure ye'elimite powder synthesized by sol-gel method	SEM BET	PSD IC
CSA-sol-0	Model cement containing ye'elimite blended with gypsum (Ye/Gy=2); Ye refers to ye'elimite weight and Gy refers to Gypsum weight	XRD TGA	
CSA-sol-0.5	Model cement containing ye'elimite blended with gypsum (Ye/Gy=2), and 0.5 wt.% citric acid; wt.% refers to weight percentage of citric acid with respect to ye'elimite weight	XRD TGA	
CSA-sol-1	Model cement containing ye'elimite blended with gypsum (Ye/Gy=2), and 1 wt.% citric acid;	XRD TGA	

^(§) TGA-MS: thermogravimetric analysis coupled to mass spectroscopy, DA: dilatometric analysis, XRD: X-ray diffraction, TGA-DTA: thermogravimetric analysis coupled to differential thermal analysis, SEM: Scanning electronic microscopy, BET: BET surface area, PSD: particle size distribution by Laser diffraction, IC: continuous ionic conductivity.

Chapitre IV. Solid-state synthesis of ye'elimite

The aim of this chapter is to describe thoroughly the protocol to prepare ye'elimite. It is important to know each step and experimental procedure because these pieces of information are often missing in the literature, which lead to results that cannot always be understood. It also presents the influence of sintering duration and temperature on the ye'elimite proportion and the minor phases formed. It describes the phase assemblage at various temperatures and proposes a protocol to form pure ye'elimite. It also details a protocol to compensate the sulfate decomposition. During ye'elimite synthesis, the microstructure evolution and phase assemblage determination are investigated in order to better understand ye'elimite phase formation, since it can contribute to the comprehension of CSA cement clinkering. Synthesis products are identified by X-Ray diffraction and quantified by Rietveld analysis. Ye'elimite formation is also studied by dilatometer analysis, thermogravimetric analysis and electronic microscope observations.

IV.1. Reactions during $C_4A_3\bar{S}$ formation

Differential thermal analysis (DTA) and thermal gravimetric analysis coupled with mass spectrometry (TGA-MS) were conducted on SM sample to identify thermal phenomena during sintering. The DTA curves and TGA-MS are presented in Figure IV-1 and Figure IV-2, respectively. The first two endothermic peaks, at 150 °C and 240 °C (Figure IV-1) accompanied with a weight loss of 3% and released gas at $m/z = 18$ (H_2O), correspond to the partial dehydration of gypsum according to reaction (R10) and reaction (R12), respectively. The strong endothermic effect at 840 °C (Figure IV-1), with a considerable associated weight loss and released gas at $m/z = 44$ (CO_2) (Figure IV-2), is due to the decarbonation of $CaCO_3$ according to reaction (R12) [203]. Between 930 and 1200°C, there is almost no weight loss and no gas released but some minor exothermic thermal effects can be observed, that may correspond to the crystallization of some phases. Beyond 1200 °C, Figure IV-2 shows a weight loss of around 7.5 wt.% accompanied with an off-gassing at $m/z = 64$ (SO_2) and $m/z = 16$ (O_2). It can be explained by the decomposition of the unreacted $CaSO_4$ [204–207]. Yan et al. [205] reported that the presence of Al_2O_3 decreases the initial decomposition temperature of $CaSO_4$ and led to different effects on desulfurization, depending on the kind of aluminate mineral products. The formation of CA and CA_2 reduces the departure of sulfates, while the formation of $C_4A_3\bar{S}$ improves the desulfurization efficiency. At temperatures above 1300°C, another weight loss starts to take place immediately after the end of the previous weight loss accompanied with a significant off-gassing (SO_2 and O_2) (Figure IV-2). It is probably related to the partial decomposition of $C_4A_3\bar{S}$ [49,104]. The thermal stability of $C_4A_3\bar{S}$ was studied by Halstead and Moore [33]. According to these authors, SO_3 in $C_4A_3\bar{S}$ is more strongly fixed

than in CaSO_4 . Choi et al. [208] reported that $\text{C}_4\text{A}_3\bar{\text{S}}$ vapor pressure is lower than CaSO_4 one. These reports may explain the decomposition of CaSO_4 at temperature lower than that for $\text{C}_4\text{A}_3\bar{\text{S}}$.

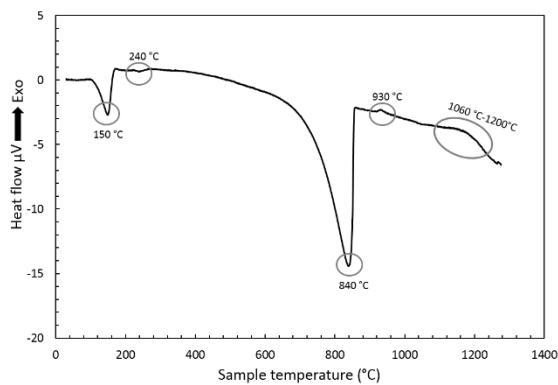
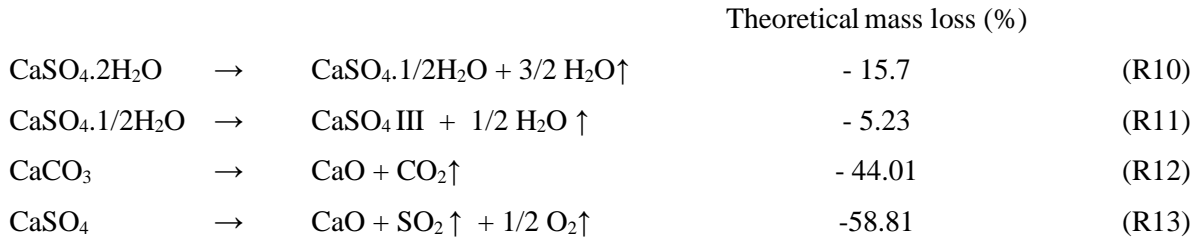


Figure IV-1: DTA curves of the SM raw mixture during heating process.

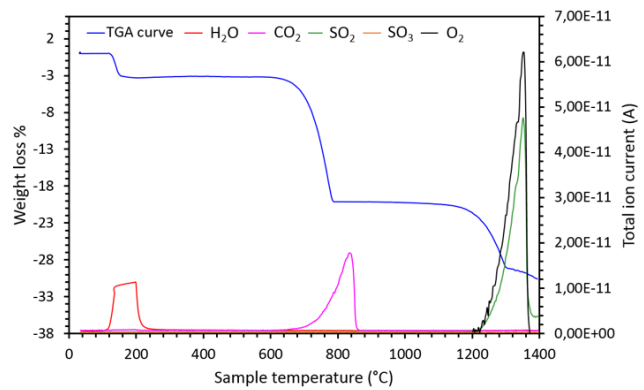


Figure IV-2: TGA-Mass spectroscopy of the SM raw mixture during heating from room temperature to 1400 °C.

In order to obtain more information about ye'elimité formation and decomposition mechanisms, X-ray diffraction was performed. The XRD patterns of SM sample after dry pressing and firing for 3 hours at 1100, 1200, 1250, 1300 and 1350 °C are shown in Figure IV-3.

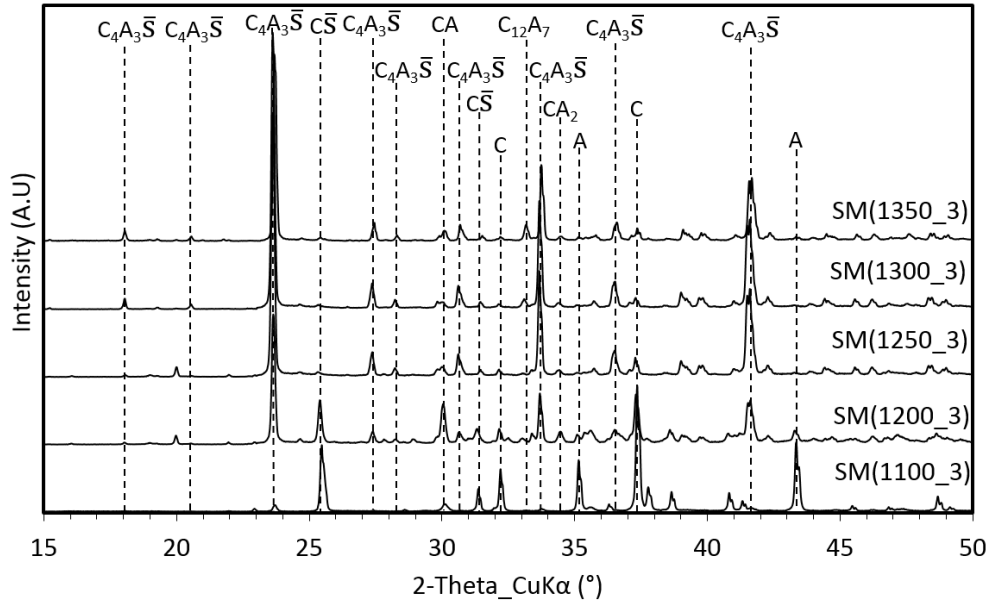


Figure IV-3: XRD patterns of SM sample fired at different temperatures.

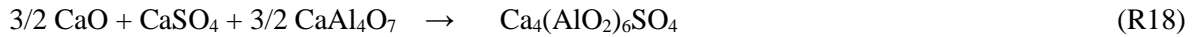
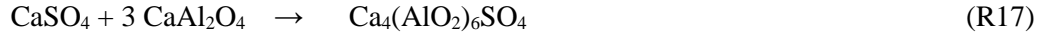
At 1100 °C, the main phases are CaO, Al₂O₃ and CaSO₄ with a small amount of orthorhombic ye'elimite and krotite (CA). The appearance of CaO and CaSO₄ phases is attributed to the decomposition of CaCO₃ and gypsum as shown in reactions (R10), (R11), (R12) and (R13), which confirms the results shown in Figure IV-1 and Figure IV-2. The formation of ye'elimite and krotite may be attributed to the solid-state reactions (R14) and (R15), respectively.



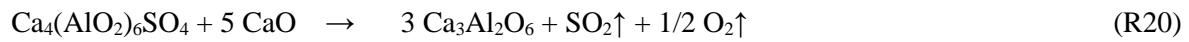
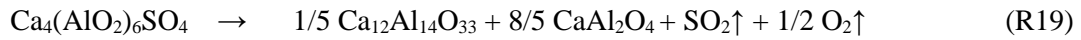
At 1200 °C, diffraction peaks attributable to CA₂ begin to appear, while those of CaO and Al₂O₃ are attenuated. Grossite (CA₂) forms by the solid-state reaction (R16):



From 1200 to 1300°C, the diffraction intensities of CA, CA₂, CaO, Al₂O₃ and CaSO₄ peaks are strongly attenuated, indicating that these phases are consumed for the ye'elimite formation through the solid-state reactions (R14), (R17) and (R18):



After a heat treatment at 1300 or 1350°C, reflections attributable to C_{12}A_7 appear, while those corresponding to $\text{C}_4\text{A}_3\bar{\text{S}}$ are attenuated. When the temperature is sufficiently high (as high as 1350°C) the decomposition of $\text{C}_4\text{A}_3\bar{\text{S}}$ occurs through reaction (R19) [113]. Other authors [209] suggest that $\text{C}_4\text{A}_3\bar{\text{S}}$ could be also decomposed to C_3A according to reaction (R20):



IV.2. Optimal synthesis conditions for ye'elimite formation

The effect of temperature and sintering duration on the quantity of crystalline phases was determined by Rietveld analysis. $\text{C}_4\text{A}_3\bar{\text{S}}$ is in the orthorhombic form. The results are shown in Figure IV-4. First of all, even at 1100°C after half an hour (Figure IV-4(a)), the formation of $\text{C}_4\text{A}_3\bar{\text{S}}$ and CA occurred according to reactions (R14) and (R15), respectively. With increasing temperature to 1200°C (Figure IV-4), $\text{C}_4\text{A}_3\bar{\text{S}}$ continues slowly to form from Al_2O_3 , CaSO_4 and CaO (reaction R14) together with calcium aluminates phases (CA, CA_2 and C_{12}A_7) from Al_2O_3 and CaO . From 1100 to 1200°C, the percentages of $\text{C}_4\text{A}_3\bar{\text{S}}$ increase with the sintering duration (Figure IV-4). Moreover, no further formation of CA and CA_2 was observed above 1200°C, because higher temperatures (from 1200 to 1300°C) combined to prolonged sintering duration (from 2 to 3h) accelerated the formation of $\text{C}_4\text{A}_3\bar{\text{S}}$ at the expense of calcium aluminate phases. During 4 h of firing at temperatures higher than 1200 °C (Figure IV-4 (e)), C_3A starts to appear in the synthesized stoichiometric samples. The presence of C_3A phase is suggested to be mainly due to $\text{C}_4\text{A}_3\bar{\text{S}}$ decomposition according to reaction (R20). Cuberos et al. [210] found the presence of about 1 wt.% of C_3A in belite sulfoaluminate clinker synthesized at 1300 °C for 15 min. They suggested that the formation of C_3A phase could depend on many kinetic parameters such as firing duration, firing temperature and the presence or not of impurities. Furthermore, the activation energy of solid-state formation of C_3A (224 kJ/mol) [120] is higher than that of C_{12}A_7 (182 kJ/mol) [211].

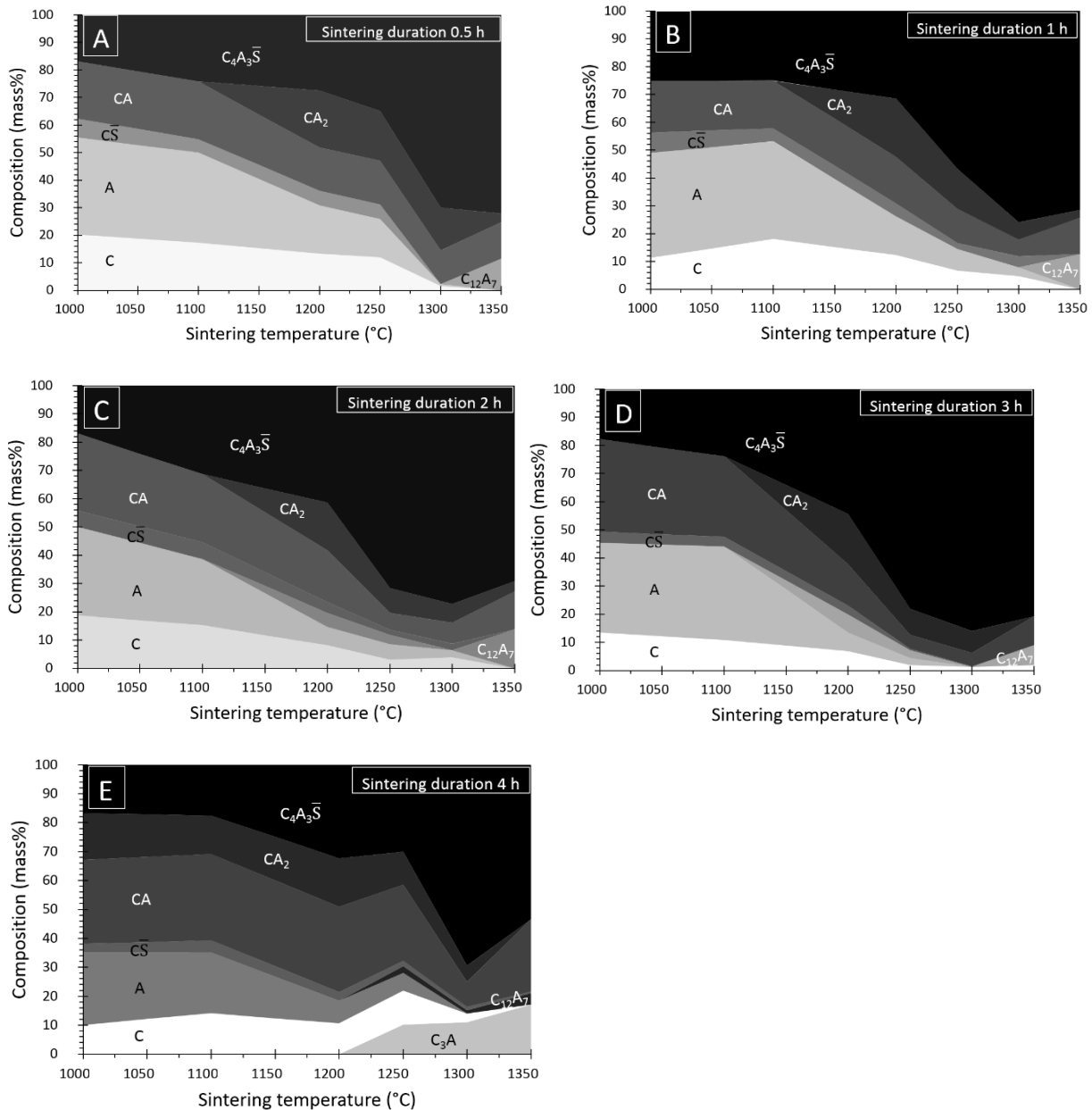


Figure IV-4: Normalized quantitative phase evolution with sintering temperature of SM sample for 0.5 h (A), 1 h (B), 2h (C), 3h (D) and 4h (E).

Contour plots of the $C_4A_3\bar{S}$ content versus the sintering duration and temperature, shown in Figure IV-5, highlight the optimal formation conditions of $C_4A_3\bar{S}$ (red area in Figure IV-5). In our study, the orthorhombic- $C_4A_3\bar{S}$ content reached its maximum (84.5 ± 1.5 wt.%) within approximately 3 h at 1300°C (red area in Figure IV-5). The standard deviation of the mass percentage was calculated from the result obtained on three samples. Making reference to Figure IV-3 and Figure IV-4, CA, CA₂ and C₁₂A₇ are the main impurities.

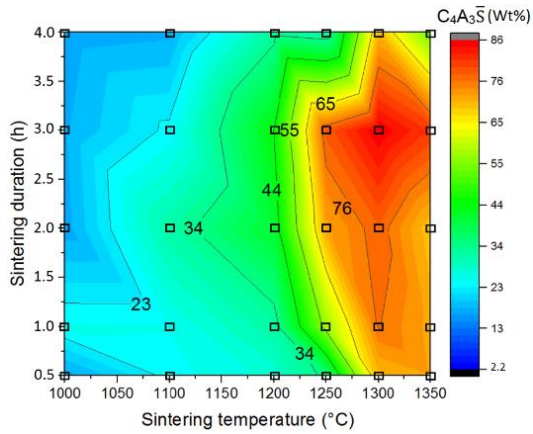


Figure IV-5: Contour plots showing $C_4A_3\bar{S}$ weight percentage (determined by QRA) versus duration and temperature of the thermal treatment (empty squares indicate measured points).

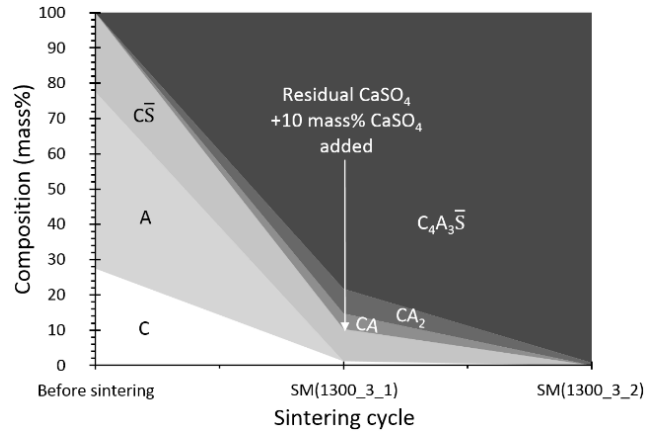


Figure IV-6: Evolution of phase composition (from Rietveld quantitative analysis) according to the sintering strategy. The quantity of $CaSO_4$ is the sum of residual calcium sulfate shown in Figure IV-4, plus 10 wt.% of added $CaSO_4$.

IV.3. Synthesis of pure orthorhombic ye'elinite

From section IV.1 of the present work, we have found that $CaSO_4$ is present in all reactions leading to form ye'elinite (see reactions (R14), (R17) and (R18)) and sulfate decomposition, which occurs at temperatures above $1200^\circ C$, limits the formation of a pure $C_4A_3\bar{S}$. Moreover, from section IV.2, we reported that maximum of $C_4A_3\bar{S}$ (84.5 ± 1.5 wt.%) was achieved at $1300^\circ C$ for 3 h with one sintering cycle (SM(1300_3_1) sample).

In order to improve the $C_4A_3\bar{S}$ content, SM(1300_3_1) sample (20.00 g) was ground using an agate mortar and 10 wt.% of $CaSO_4 \cdot 2H_2O$ was thoroughly added. The resultant powder was pelletized and ten 2g-pellets are fired in the optimal conditions ($1300^\circ C$ for 3h). After cooling, the material was finely ground ($S_{BET} = 0.74$ m²/g) before analysis (SM(1300_3_2) sample). Figure IV-7 shows the used experimental procedure to compensate sulfate vaporization.

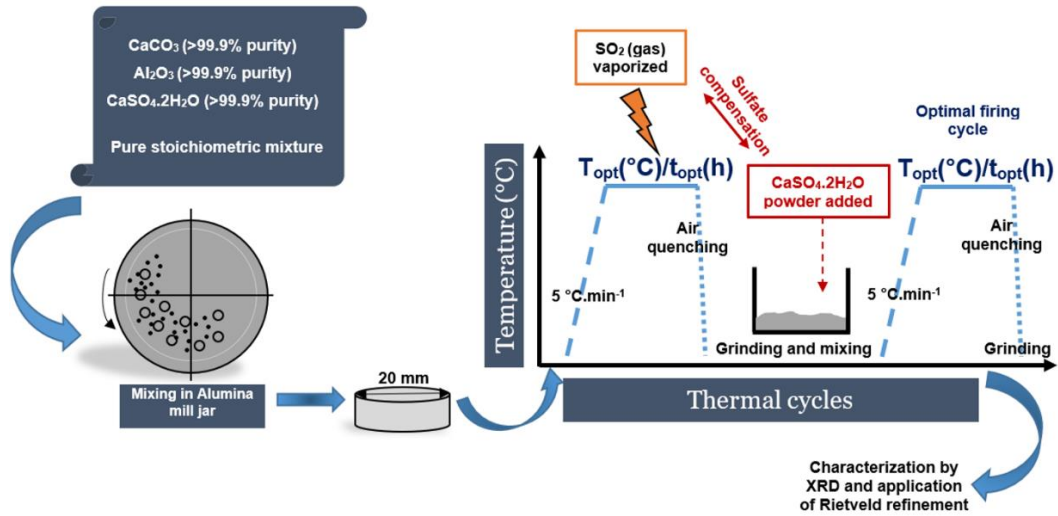


Figure IV-7: Experimental procedure to compensate sulfate vaporization.

Evolution of phase composition (from Rietveld quantitative analysis) according to the sintering strategy is shown in Figure IV-6. The SM(1300_3_2) sample presents a higher purity than SM(1300_3_1) sample. It means that the addition of a slight excess of CaSO_4 compensates the SO_2 loss during firing. The purity of SM(1300_3_2) sample is estimated by Rietveld quantitative analysis. For statistical significance, three samples are fired and each of them is analyzed. As an example, the Rietveld plots and quantitative analysis of the first fired and analyzed SM(1300_3_2) sample is shown in Figure IV-8. The quantity of orthorhombic- $\text{C}_4\text{A}_3\bar{\text{S}}$ is about 98 wt.% with a standard deviation of 1.3 wt.%, the quantity of CA_2 is about 1.7 with a standard deviation of 1.3 wt.% and negligible amounts of amorphous phases. The standard deviation was estimated from the results of Rietveld quantitative analysis of the three fired and analyzed SM(1300_3_2) samples.

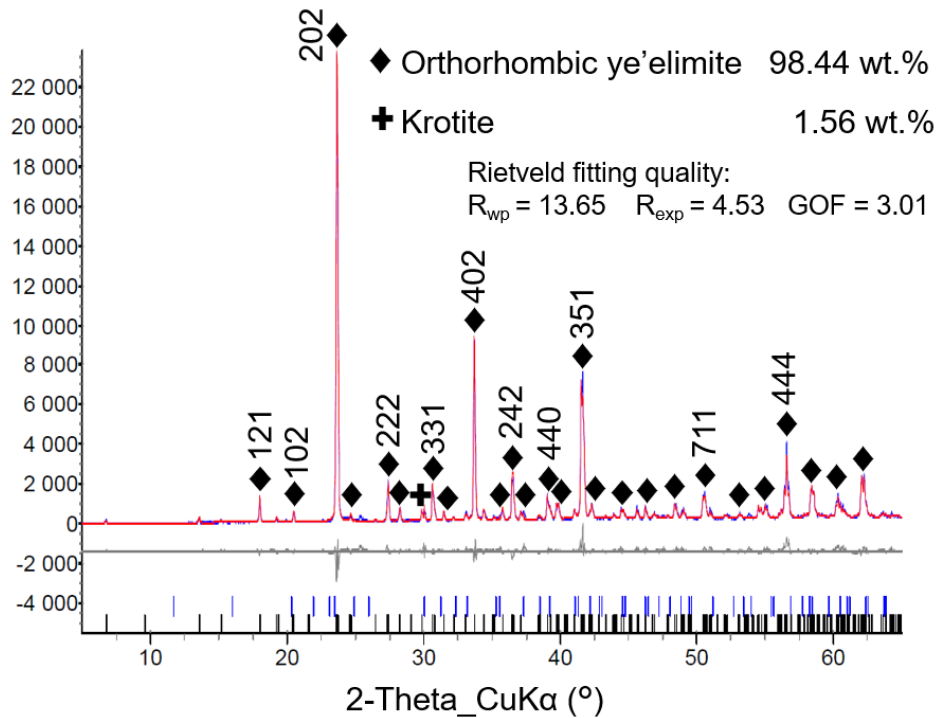


Figure IV-8: Rietveld plots and quantitative phase analysis of the SM(1300_3_2) sample.

The free-lime quantity f-CaO wt.% of the SM(1300_3_1) sample, measured by the EDTA method, is 2.9 wt.% and for the SM(1300_3_2) is 0.9 wt.%. The excess of CaO coming from the added $\text{CaSO}_4 \cdot 2\text{H}_2\text{O}$ could explain the presence of f-CaO (0.9 wt.%) and CA_2 (1.7 wt.%) in the SM(1300_3_2) product.

IV.4. Microstructural evolution during solid state formation of ye'elimite

The sintering behavior of SM sample was obtained using the dilatometer analysis. During the solid state reaction, the variation of percentage of linear change of the sample with an increase in the sintering temperature is shown in Figure IV-9. The sample SM shows a significant expansion between 30 and 760°C (point 1 in Figure IV-9), related to the normal thermal expansion of raw materials, which reaches the maximum at 760°C. Beyond this temperature, the sample starts to shrink with a slower rate between 760 and 860°C (point 2 in Figure IV-9), than between 860 and 960°C (point 2' in Figure IV-9), which can be associated with the decomposition of CaCO_3 . The shrinkage keeps on increasing at a slower rate when the temperature varies from 960 °C to 1100°C (point 2 in Figure IV-9). It is associated with the closure of the green porosity during the solid state sintering process. The SM raw mixture shows a slight expansion from 1100 to 1250°C (point 3 in Figure IV-9), attributed to the formation of calcium aluminates and ye'elimite (Figure IV-3). Above 1250°C, a significant linear expansion (11%) takes

place, which is due to the decomposition of unreacted CaSO_4 and $\text{C}_4\text{A}_3\bar{\text{S}}$ with the release of SO_2 and O_2 gases [212].

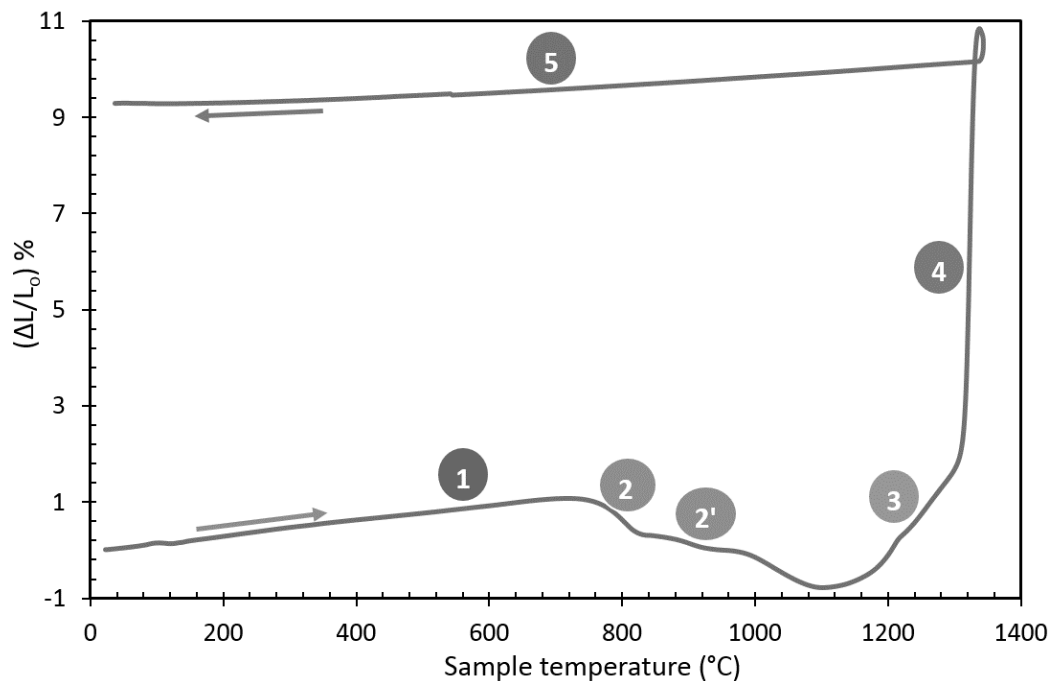


Figure IV-9: Dilatometric curve of the prepared SM raw mixture during heating and cooling.

To investigate the evolution of SM sample microstructure during sintering, Figure IV-10 gives original SEM micrographs of SM samples sintered at different temperatures for 3 hours. In order to identify the porous region of the fired samples, the grey-level threshold is also given (Black area represents pore area fraction of the SEM micrographs). These images evidence a significant change of porosity produced with increasing sintering temperature. The significant tortuosity of the porous media is also evident in the samples sintered at temperatures up to 1000 °C.

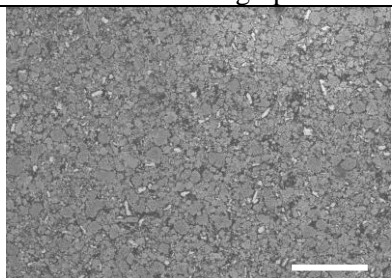
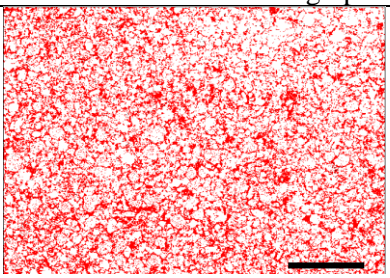
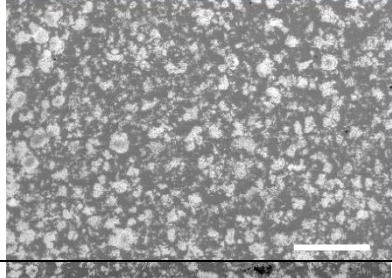
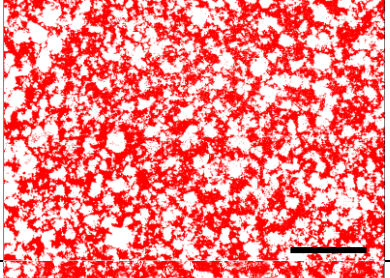
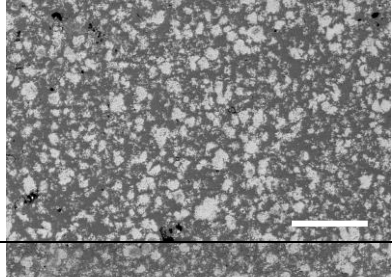
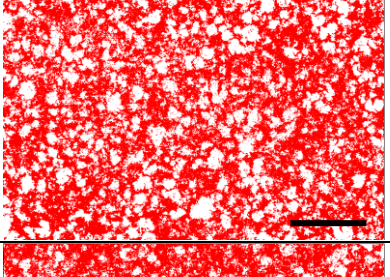
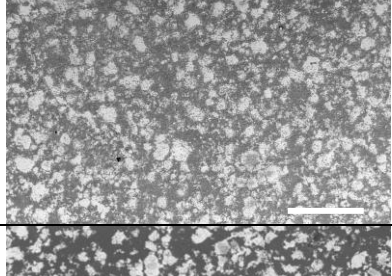
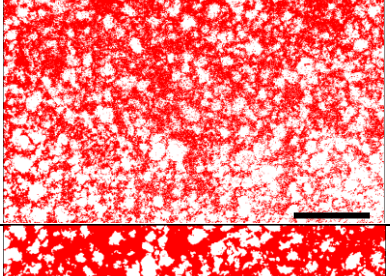
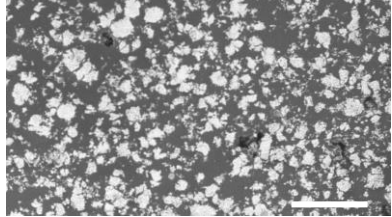
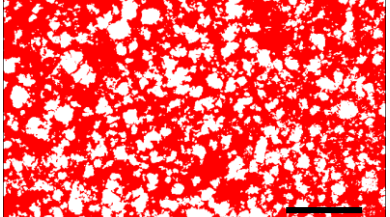
Sample name	SEM micrograph	Thresholded SEM micrograph
SM_1000_3_1		
SM_1100_3_1		
SM_1200_3_1		
SM_1250_3_1		
SM_1300_3_1		

Figure IV-10: Back-scattered SEM micrographs of the SM sample sintered at different temperatures for 3h accompanied with their grey-level threshold segmentation. Magnification of X 50 was used of all images (Bars represent 500 μm and Red area represents pore area fraction of the SEM micrographs).

Open porosity fraction estimated from the image analysis of SM pellets on sintering temperature is compared to the experimental values measured by the Archimedes principle method and results are illustrated in Figure IV-11. First of all, the values of open porosity estimated from image analysis or that obtained from experimental measurement follow the same trend. It was determined that the average error of the 7 compared values of open porosity (Figure IV-11) is 7.4 %, a margin of error that is reasonably small and acceptable [213]. From 1000°C up to 1350°C (Figure IV-11), the open porosity increases almost linearly with rising the sintering temperature to attain 75.5 % at 1350°C and the apparent density decreases. In particular, between 1100 and 1300°C (Figure IV-11), the open porosity increases rapidly with increasing sintering temperature and the apparent density also decreases rapidly. The rapid increasing of open porosity between 1100 and 1300°C can be explained by the strong SO₂ and O₂ gas release at this range of temperature as shown in Figure IV-2 and Figure IV-9. The high porosity of the synthesized samples shows the difficulty to have dense sintered ye'elinite. This drawback, from a ceramist point of view, can be an advantage for a cement producer since a porous material implies an ease for grinding the clinker into a cement.

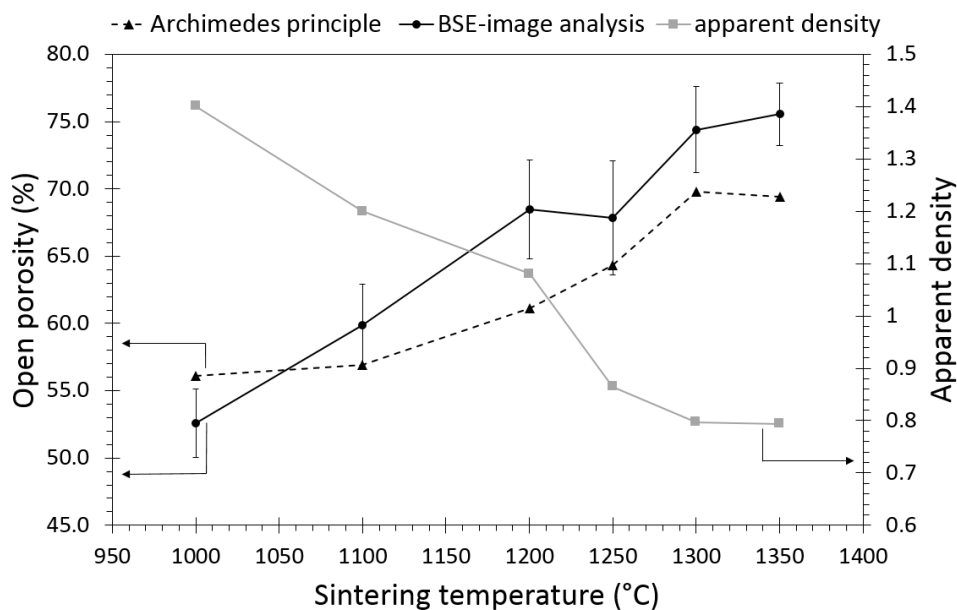


Figure IV-11: Evolution of open porosity fraction and apparent density (grey line) according to sintering temperature of SM fired pellets. Open porosity fraction was obtained from Archimedes principle (dashed black line) and from BSE-image analysis (continuous black line).

Important points to remember:

The results of the present study have allowed us to clarify the effect of sintering conditions (temperature and duration) on the ye'elimite formation and microstructure of stoichiometric mixtures produced from pure commercial powders and with a thoroughly described protocol. Solid-state formation of ye'elimite from the raw materials starts at 1000°C and continues to form from the reaction between minor calcium aluminate phases ($C_{12}A_7$, CA, CA_2) and $CaSO_4$ until 1300°C. The optimal sintering condition to maximize the ye'elimite formation is about 1300 °C for sintering temperature and 3 hours for sintering duration. Above 1300°C ye'elimite decomposes into calcium aluminate phases and SO_2 gas. Gas releases (CO_2 from calcite decomposition and SO_2 from unreacted anhydrite) are also observed during the ye'elimite formation which promotes the dilatation and the formation of an open porosity of the fired pellets. It should also be noticed that to our knowledge, this is the first time a dilatometric study has been carried out on pure ye'elimite.

Moreover, it is difficult to achieve dense sintered ye'elimite because of the gas releases during the firing process and the sintering of pure oxide ceramic requires relatively long time and high temperature because the diffusion proceeds in solid state. In order to have denser sintered ye'elimite as a perspective idea, an impurity (sintering aid) could be added to help in the bonding process and/or finding a way to limit sulfates decomposition before the melting point of ye'elimite.

Based on the present work, it emerges that a key strategy for forming ye'elimite in laboratory with a high purity is to compensate sulfate decomposition. Sulfate compensation can be achieved by the addition of a slight excess of $CaSO_4$ (10 wt.%) before repeating the firing cycle at optimal conditions. It is then possible to have a pure product that can be used for further studies (hydration behavior, mechanical characteristics of the hydrated product, durability) in order to be able to comply with the requirements for European normalization of these cements and finally their wide commercialization.

Chapitre V. Sol-gel synthesis of ye'elinite

The present chapter deals with the synthesis of pure orthorhombic ye'elinite using three low temperature chemical routes: Pech method, OSE method and SPC synthesis. The different synthesized products were compared in terms of purity and physical characteristics. The purity was deduced from Rietveld quantitative analysis. The physical characteristics were studied by Scanning Electron Microscopy, particle size analysis and X-Ray Diffraction. Finally, the dried gels were characterized by thermal analysis.

V.1. Thermal analysis of the gel precursor

The thermal events that occur when heating the dried gels are shown in Figure V-1. The thermal events can be divided into four stages according to the temperature ranges. The phenomena associated with each temperature range are summarized in Table V-1.

Table V-1: Summary of thermal events shown in Figure V-1

Chemical route	Stage	Temperature range	Thermal event		Possible phenomena
			TGA	TDA	
Pech70	I	30 - 200°C	-1 %	Endo.	Evaporation of residual water
	II	370 - 750°C	-8 %	Exo.	Organic phase combustion
	III	860 - 950°C	~ 0 %	Exo.	Phase crystallization
	IV	950 - 1000°C	-0.7 %	Exo.	Residual carbon combustion
Pech95	I	30 - 200°C	-0.9 %	Endo.	Evaporation of residual water
	II	300 - 700°C	-7.5 %	Exo.	Organic phase combustion
	III	850 - 940°C	~ 0 %	Exo.	Phase crystallization
	IV	940 - 1000°C	-0.1 %	Exo.	Residual carbon combustion
OSE	I	30 - 200°C	-0.3 %	Endo.	Evaporation of residual water
	II	400 - 650°C	-2.1 %	Endo.	Breakdown of the polymer chains
	III	850 - 950°C	-0.4 %	Exo.	Residual carbon combustion
	IV	950 - 1000°C	~ 0 %	Exo.	Phase crystallization
SPC	I	30 - 200°C	-1.6 %	Endo.	Evaporation of residual water
	II	400 - 750°C	-7.4 %	Exo.	Organic phase combustion
	III	750 - 855°C	~ 0 %	Exo.	Phase crystallization
	IV	900 - 1000°C	-1 %	Exo.	Residual carbon combustion

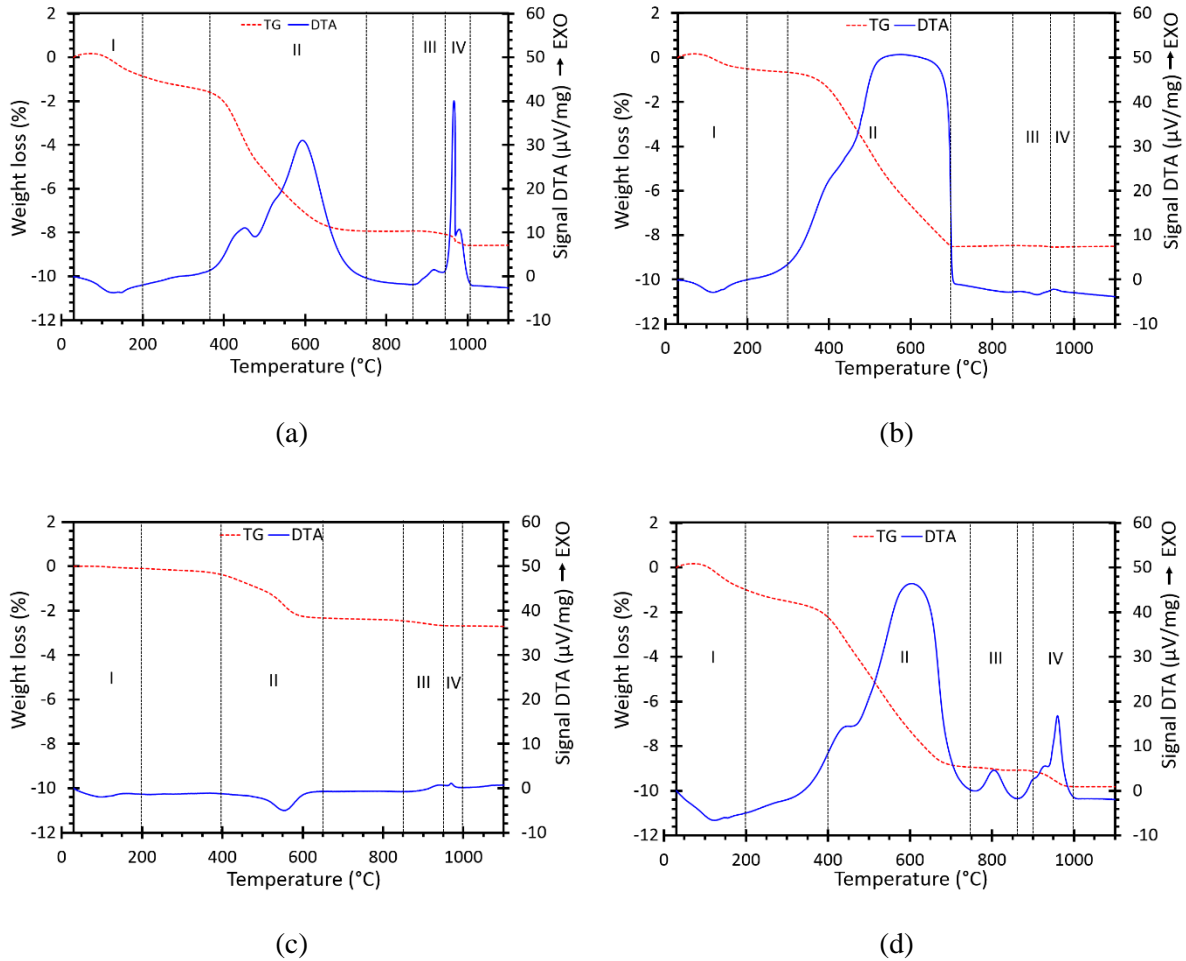


Figure V-1: DTA-TGA of gel precursor made by the Pech70 method (a), Pech95 method (b), OSE method (c) and SPC method (d).

During the first stage between 30 and 200°C, Pech70, Pech95, OSE and SPC lose respectively around 1, 0.9, 0.3 and 1.6 wt.%. The mass losses are combined with a small endothermic signal. These events are attributed to the loss of residual water which is weakly physisorbed in the dried gels. The second stage for dried gels prepared by Pech70 method (Figure V-1 (a)), Pech95 method (Figure V-4 (b)), and SPC method (Figure V-4 (d)), is in the range 370-750 °C, 300-700 °C, and 400-750 °C, respectively. The thermal analysis curves reveal the decomposition (burning) of organic bearing compounds (between 2 to 8 wt.% loss), with a clear exothermic effect. The exothermic peak is the biggest for the dried gel prepared by the Pech95 method (Figure V-4 (b)). It could be due to the high resin content. The second stage for the dried gel prepared by the OSE method occurs between 400 and 650°C (Figure V-4 (c)). It corresponds to the partial dehydration of PVA and its transformation into polyene, as suggested by the endothermic event at 556.8°C accompanied with 2.1 % mass loss [214–216].

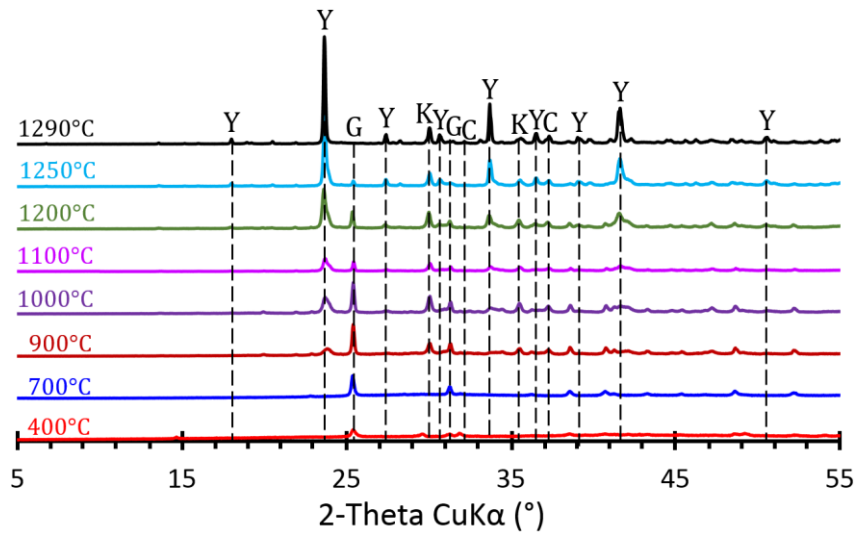
The third stage is between 850-860 and 950°C for the dried gels prepared by Pech70, Pech95 and OSE method. In this temperature range, DTA curves show a small exothermic peak around 920.1°C, 875.4°C and 940.6°C, respectively, with no significant mass loss. It could be related to a crystallization process and may indicate the possible formation of the $C_4A_3\bar{S}$ phase. In the case of the dried gel prepared by the SPC method, the temperature range of stage III is between 750 and 855°C (Figure V-1 (d)). The exothermic peak at 800°C with about 0.4 wt.% loss is due to combustion of residual carbon [135].

Lastly, stage IV is between 900 and 1000°C for the dried gels prepared by the SPC method, whereas it is from 940-950 to 1000°C for the other dried gels. For dried gel prepared by OSE, a small exothermic peak appeared at 971.2°C with no mass loss which could be attributed to ye'elimite crystal formation. For the other three dried gels, the exothermic peaks accompanied with small mass losses (0.1 to 1 wt.%), are probably due to residual organic matter decomposition.

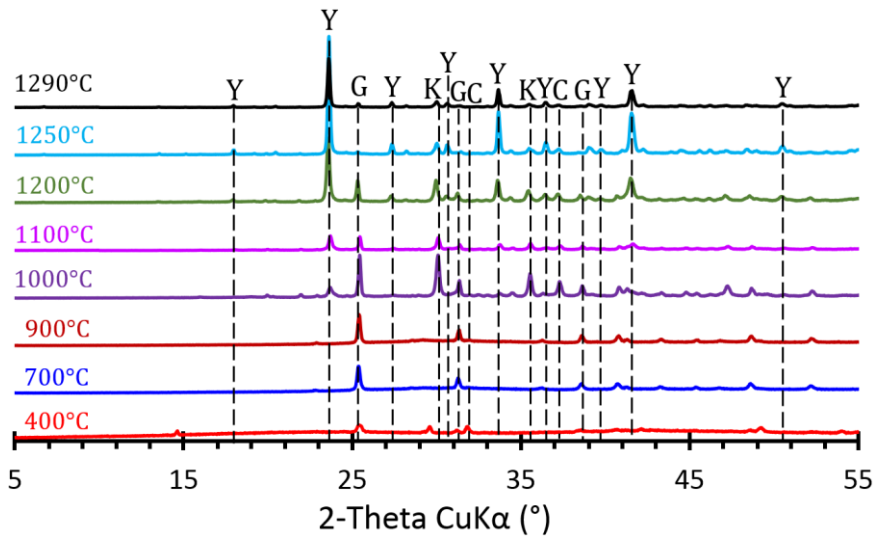
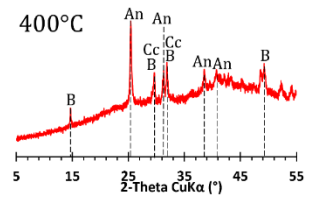
The main conclusions from the thermal analysis are the following: (i) the decomposition of organic products occurs mostly below 700 – 750°C, (ii) the crystallization of ye'elimite could start in the range 900°C to 1000°C.

V.2. Effect of calcination temperature on ye'elimite phase formation

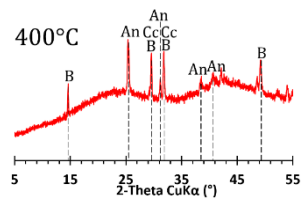
Figure V-2 shows the XRD patterns of the four synthesized gels calcined at different temperatures in the range of 400-1290°C. When the initial dried gels are calcined at 400°C, the X-ray pattern presents a wide dome at low angles, indicating that amorphous phases are still present, and also crystalline peaks belonging to bassanite, anhydrite and calcium carbonate. The presence of $C\bar{C}$ could be explained by the presence of CO_2 generated from the combustion reaction of organic precursors. As the calcination temperature increases to 1000°C, the Grossite, CA_2 , peak (noted G on Figure V-2) increases to a maximum, and then above this temperature decreases to a trace amount. Krotite, CA, (noted K on Figure V-2) peaks appear at 900°C with an intensity that can be low (Figure V-2a and Figure V-2b) to very low (Figure V-2c) as the temperature increases. Concomitantly, ye'elimite ($C_4A_3\bar{S}$) first appears at 900°C and its peak intensity increases as the CA and CA_2 peaks decrease in intensity. As the calcination temperature increases to 1250°C, the corresponding diffraction pattern peak intensities of $C_4A_3\bar{S}$ are significantly increased, which indicates a good crystallinity of the ye'elimite powders. At 1250°C, all the diffraction peaks of the synthesized $C_4A_3\bar{S}$ are attributed to the pure orthorhombic crystal phase of ye'elimite with a space group of Pcc2 and are in good agreement with the available standard ICSD#80361 [97]. By increasing the calcination temperature to 1290°C, peaks related to CA can be slightly enhanced due to the decomposition of ye'elimite [9,104]. Thus, we confirm that 1250°C is an optimum temperature for pure phase formation of the ye'elimite synthesized by chemical routes.



(a)



(b)



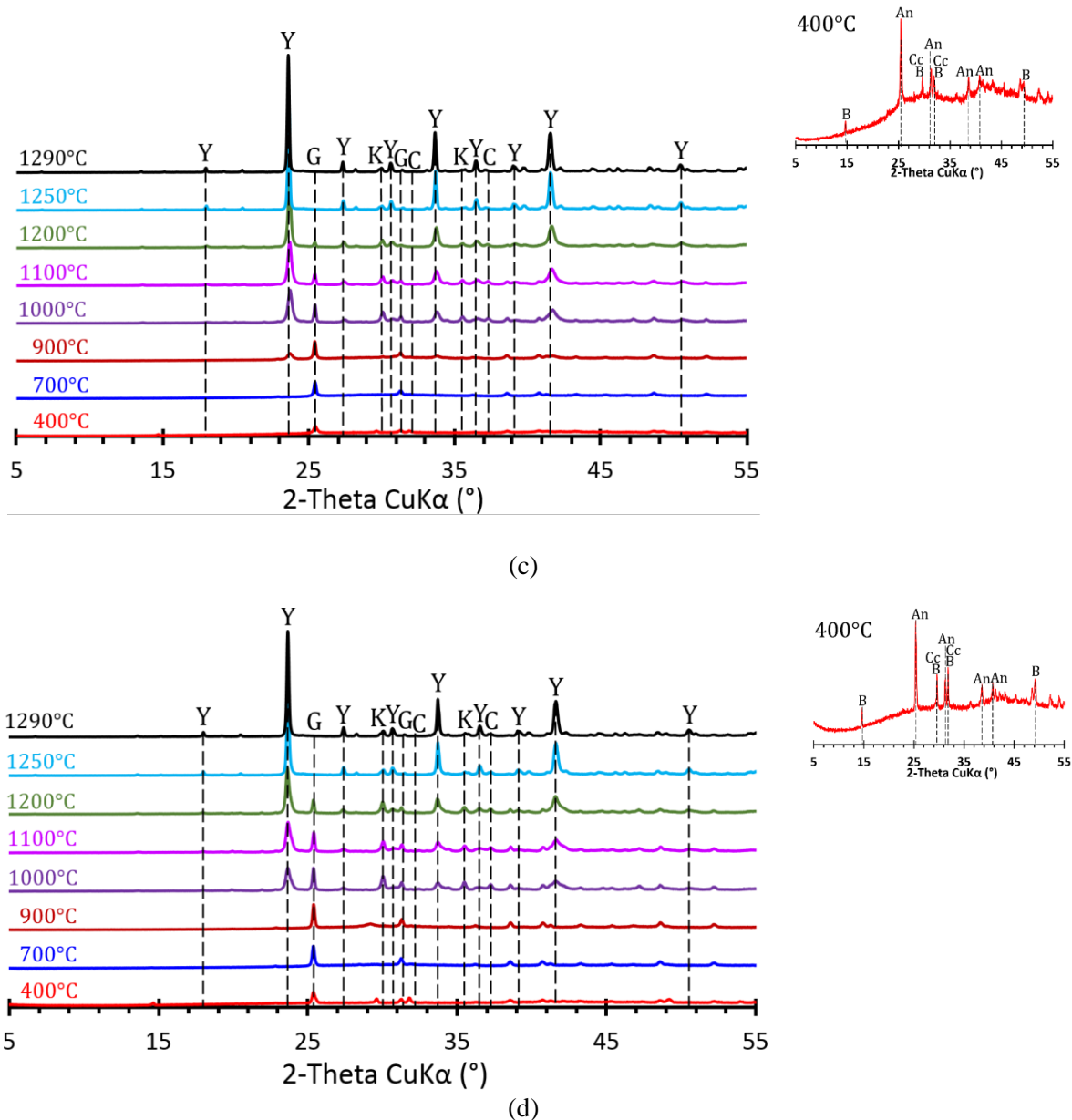


Figure V-2: XRD patterns of the gel precursor, synthesized by the Pech70 method (a), Pech95 method (b), OSE method (c) and SPC method (d), calcined at 400°C, 700°C, 900°C, 1000°C, 1200°C, 1250°C and 1290°C for 1 h (Y= Ye'elimeite, G = Grossite, K = Krotite, C = CaO, B = Bassanite, Cc = Calcium carbonate, An = Anhydrite).

The purity of ye'elimeite powders, synthesized by the Pech70, Pech95, OSE and SPC methods and calcined between 1000 and 1290°C for 1 h, are presented in Table V-2. To check the quality of the analysis fitting, the Rwp values are given in Table V-2. The Rwp values are of the same order of magnitude as values found in literature [113,123], the corresponding Rietveld plots are given in Figure V-3. The highest purity is obtained after calcination at 1250°C for 1 h. The powder prepared by the OSE and SPC methods exhibit a high purity of ye'elimeite (about 98 wt.%), whereas powders prepared by the

Pech70 and Pech95 methods show ye'elinite purity of 79.4 wt.% and 95.8 wt.%, respectively. The differences on ye'elinite purity between the four methods could be explained by several factors such as the polymerization reaction, the changing viscosity of the precursor solution during the reaction and the chelation ability of the complexing agent. In our case, the formation of a polyester (reaction between citric acid and ethylene glycol) during the Pechini process is less beneficial for obtaining pure ye'elinite than when there is only one alcohol (PVA in the OSE route) or one acid (citric acid in the SPC route). Other parameters could play a role in the purity of the final powder. The influence of the polymer-to-cation ratio on the polymerization reaction was well discussed by Petrykin et Kakihana [217]. It was also noted in previous work that the amount of polymer and its molecular length could affect the distribution of the cations and hence the purity of the product [126,198,218].

Table V-2: Quantitative Rietveld analysis of the powders prepared by Pech70, Pech95, OSE and SPC routes after a heat treatment from 1000°C to 1250°C for 1 h. The values in brackets correspond to phase content error from Rietveld quantitative analysis. (*) Rwp is the weighted profile factor (E.25).

Temperature of heat treatment (°C)	Synthesis method	Crystalline phases			Fitting parameters of Rietveld analysis
		Orth-C ₄ A ₃ S̄ (wt.%)	CA (wt.%)	CA ₂ (wt.%)	Rwp ^(*)
1000	Pech70 method	55.2 (1.5)	17.9 (1.2)	26.9 (1.1)	12.52
	Pech95 method	37.1 (1.3)	41.1 (1.2)	21.7 (1.1)	13.54
	OSE method	64.9 (1.2)	22.5 (1.1)	12.6 (0.7)	8.65
	SPC method	58.1 (1.6)	24.9 (1.4)	16.9 (1.0)	9.77
1100	Pech70 method	63.7 (1.4)	21.2 (1.3)	15.1 (0.8)	13.04
	Pech95 method	48.9 (1.0)	32.2 (0.9)	18.9 (0.8)	12.11
	OSE method	68.4 (1.1)	17.3 (0.9)	14.3 (0.8)	8.79
	SPC method	59.6 (1.8)	21.3 (1.6)	19.0 (0.9)	10.52
1200	Pech70 method	62.1 (1.2)	23.2 (1.1)	14.7 (0.8)	12.62
	Pech95 method	57.3 (1.0)	26.6 (0.8)	16.2 (0.9)	10.96
	OSE method	78.7 (0.9)	12.2 (0.7)	9.0 (0.8)	7.85
	SPC method	57.3 (1.2)	26.4 (0.9)	16.2 (0.9)	10.96
1250	Pech70 method	79.4 (0.5)	18.4 (0.3)	2.2 (0.3)	12.63
	Pech95 method	95.8 (0.4)	4.2 (0.3)	0 (0.3)	10.65
	OSE method	98.3 (0.3)	1.7 (0.2)	0 (0.2)	11.45
	SPC method	97.9 (0.2)	2.1 (0.1)	0 (0.1)	12.02
1290	Pech70 method	78.9 (0.5)	18.2 (0.3)	2.9 (0.4)	18.14
	Pech95 method	92.6 (0.4)	7.4 (0.3)	0 (0.3)	17.01
	OSE method	97.5 (0.3)	2.4 (0.2)	0 (0.2)	15.28
	SPC method	96.9 (0.2)	3.1 (0.1)	0 (0.2)	13.80

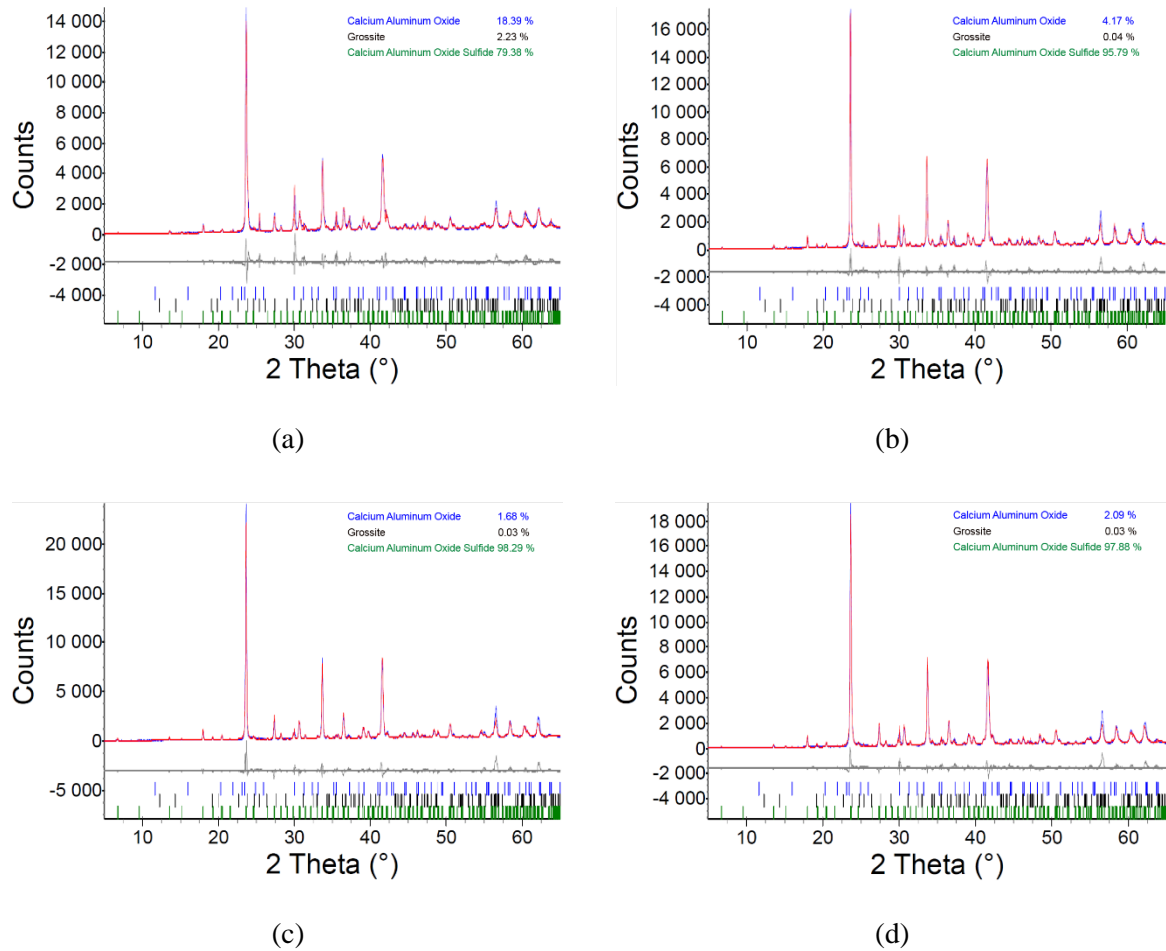


Figure V-3: Rietveld quantitative analysis plots of ye'elimitite powder prepared at 1250°C by the Pech70 method (a), Pech95 method (b), OSE method (c) and SPC method (d).

V.3. Effect of calcination temperature on crystallite size of the synthesized ye'elimitite

Figure V-4 presents the effect of calcination temperature on the crystallite size (calculated using Scherrer's equation E.24) of ye'elimitite synthesized by the different chemical routes. The crystallite size increases with the calcination temperature, especially in the range from 1200 to 1250°C. At 1250°C, temperature at which the highest percentage of pure ye'elimitite is obtained (Figure V-3), the crystallite size, $D_{\text{crystallite}}$, of powders prepared by the Pech70, Pech95, OSE and SPC methods are 50.2 nm, 53.6 nm, 57.5 nm and 50.9 nm, respectively. According to Quinelato et al. [42], increasing the distance

between chelated cations leads to weak interactions among primary particles during crystallization, which yields small particles.

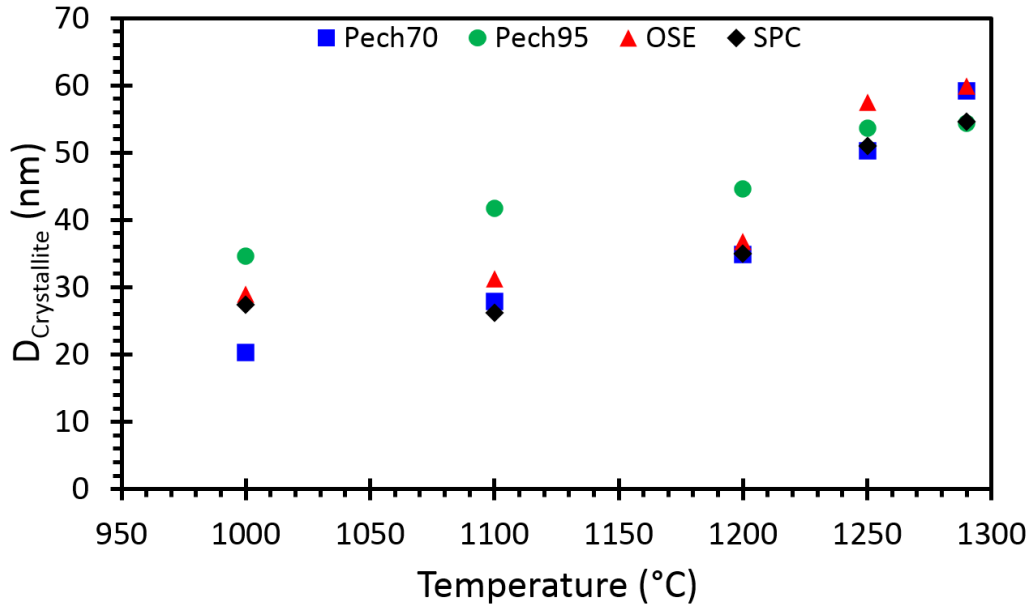
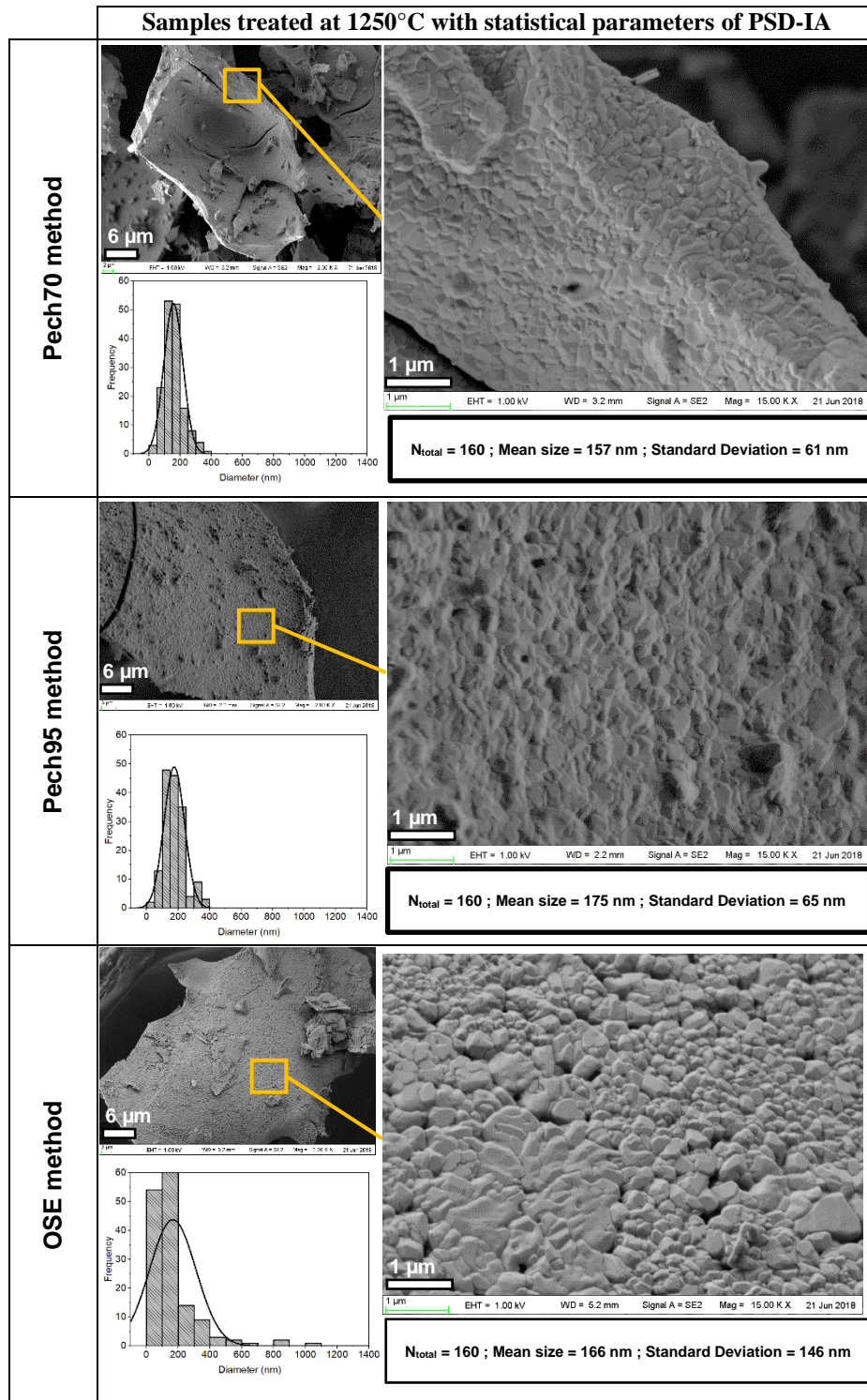


Figure V-4: Effect of calcination temperature on the crystallite size (calculated from (E.24)) of ye'elinite synthesized by the different chemical routes.

V.4. Microstructural characterization of ye'elinite synthesized at 1250°C

By referring to XRD diffractograms (Figure V-2) and Rietveld quantitative Rietveld analysis (Table V-2 and Figure V-3), we noted that the maximum of ye'elinite was obtained at 1250°C. Consequently, microstructural characterization has been carried out only for samples treated at 1250°C (Figure V-5).



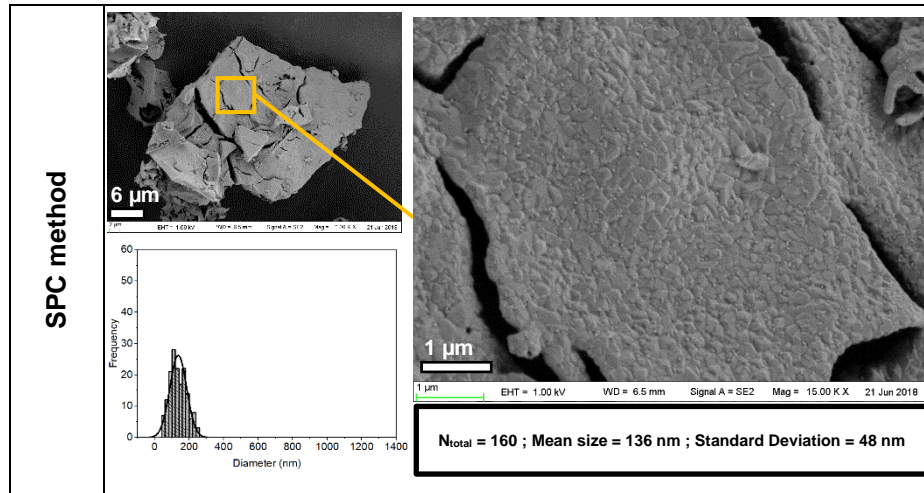


Figure V-5: SEM micrographs of the gels precursors calcined at 1250°C for 1 h. Zooms show that each agglomerate consists of nanometric particles. Their average diameter, D_{particle} , as well as the deviation, determined by PSD-IA, are presented.

Heat treatment at 1250°C for 1 h shows the presence of nanometric particles that can form large agglomerates (Figure V-5). It could be the signature of the beginning of sintering of ye'elinite crystallites at 1250°C. D_{particle} , determined by PSD-IA as explained in the experimental section, are 157 nm, 175 nm, 166 nm and 136 nm, respectively for the Pech70, Pech95, OSE and SPC methods (Figure V-5). A standard deviation, σ , of 146 nm was obtained using PVA (poly vinyl alcohol) as a polymer agent for organic steric entrapment. A relatively narrow size distribution was observed for particles prepared by SPC ($\sigma = 48$ nm), Pech70 ($\sigma = 61$ nm) and Pech95 ($\sigma = 65$ nm). These distributions are dependent on the amount and the nature of the organic part and hence are probably dependent on the amount of heat generated by the combustion reaction, which is a function of the starting resin [202]. Raab and Pöllmann [124] reported that the type and amount of the polymer govern its decomposition and influences the phase formation and the particle size of the synthesized product.

To conclude, the chemical routes permit to synthesize crystalline ye'elinite at 1250°C instead of 1300°C for the powder prepared by solid state synthesis [9,106,107,110,111,123]. Data at the nanometric scale show that the particles (around 136-175 nm) are about 3 times larger than the crystallites (51 to 57 nm). It could be the signature of the beginning of sintering of ye'elinite crystallites at 1250°C.

Laser size analysis (volume % curves) of ye'elinite powder prepared at 1250°C by the Pech method, OSE method and SPC method is presented in Figure V-6. The samples prepared by Pech95 method, OSE method and SPC method have a bimodal grain size distribution, where the maximum vol.% of the first grain size population is between 20 and 30 μm . The second grain size population represents some residual agglomerates whose size ranges between 300 and 800 μm for the sample prepared by Pech95 method, between 100 and 400 μm for the sample prepared by OSE method and between 200 and 700

μm for the sample prepared by SPC method. The powder prepared by Pech70 is slightly coarser than the other three powders and it presents a monomodal grain size distribution, where the maximum vol.% corresponds to a particle size of $39 \mu\text{m}$.

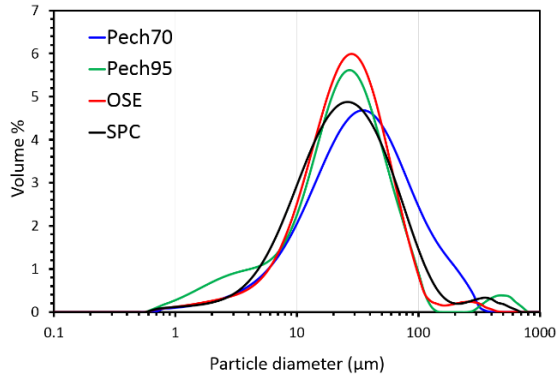


Figure V-6: PSD-LD analysis (volume % curves) of ye'elimite powder prepared at 1250°C by the Pech method, OSE method and SPC method.

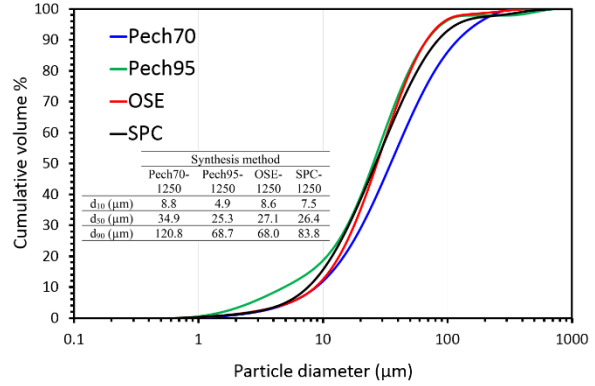


Figure V-7: PSD-LD analysis (cumulative volume % curves) of ye'elimite powder prepared at 1250°C by the Pech method, OSE method and SPC method.

The particles form hard agglomerates (Figure V-5) whose size range between 1 to $100 \mu\text{m}$ as shown by the LSA curves (Figure V-7). The distribution is typical of what is required for a Portland cement and usually obtained after grinding the clinker [219]. In the present case, it is interesting to point out that this distribution is obtained directly after the sintering of the powders prepared by a chemical route and without the necessity of a grinding step.

Important points to remember:

This main conclusions of this work illustrated in Figure V-8 are:

Fairly pure and fine ye'elimité particles were successfully obtained at 1250°C for 1 hour by means of three chemical routes: the Pechini-method (with resin content 95%), the self-propagating combustion synthesis method and the organic steric entrapment method. The ye'elimité purity is respectively equal to 95.8 wt.%, 97.9 wt.% and 98.3 wt.%.

The application of quantitative Rietveld analysis to X-ray diffraction data indicates that ye'elimité with high purity (close to 98 wt.%) was achieved by the organic steric entrapment method and by the self-propagating combustion synthesis. The formation of a polyester (reaction between citric acid and ethylene glycol) during the Pechini process inhibits the yield of pure ye'elimité. It is not the case when there is only one alcohol (PVA in the OSE route) or one acid (citric acid in the SPC route) involved.

Referring to X-ray diffraction results, CA and CA₂ are the only intermediate crystalline phases detected. Upon increasing the heat treatment temperature, the amount of CA and CA₂ decreased being gradually transformed into the C₄A₃ \bar{S} phase.

After a heat treatment at 1250°C for 1 h, the nanosized crystallites (51 to 57 nm) form particles about 3 times larger (average size, D_{particle} , between 136 and 175 nm) which could result from the sintering of the crystallites.

The particles form hard agglomerates whose size range between 1 to 100 μm as shown by the laser size analysis curves (Figure V-6, Figure V-7). The distribution, which is typical of a ground Portland clinker or cement, is obtained directly after sintering and without the necessity of a grinding step.

Thus, the present work provides an original protocol, using chemical routes, to synthesis nano-size ye'elimité particles showing small crystallite sizes and high purity. Moreover, the synthesized ye'elimité powders have the particle size distribution of a clinker. This could be usefully exploited for studying the kinetics and thermodynamics of ye'elimité hydration. In order to contribute to the understanding of ye'elimité hydration (the main phase of CSA cements), a thorough and exhaustive study about the hydration of the synthesized ye'elimité powders constitutes the main perspective of the present work.

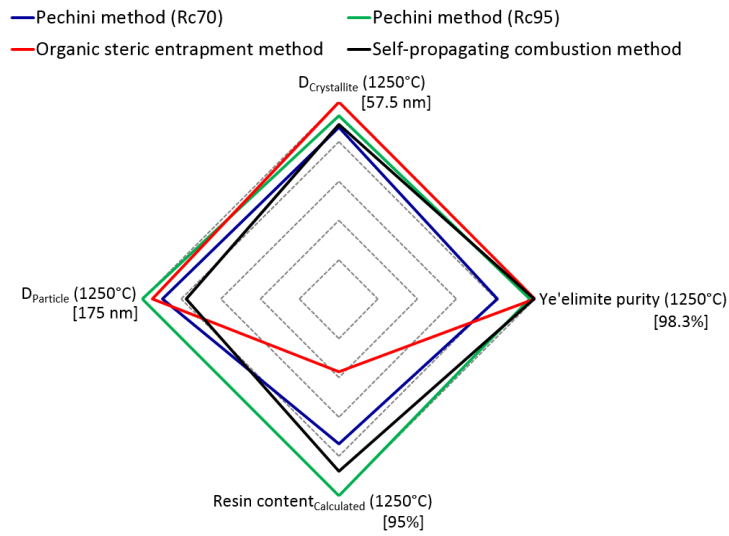


Figure V-8: Radar chart to summarize all the parameters of ye'elinite powder prepared at 1250°C by the Pech method, OSE method and SPC method (values between brackets represent the maximum value of each parameter).

Chapitre VI. Examination of ye'elimite formation mechanisms

The purpose of the current chapter is to investigate the ye'elimite formation mechanisms by solid-state reactions from pure raw materials calcium carbonate, alumina and gypsum. This study was conducted using X-ray diffraction and scanning electron microscopy to get information about mineralogical and microstructural assemblages at different synthesis temperatures. Avrami's model was suggested to highlight the effect of synthesis conditions on ye'elimite kinetic formation.

VI.1. Mineralogical analysis

Figure VI-1 represents X-Ray diffractograms of the samples heated between 1000 to 1300°C for 3 h. For temperatures ranging from 1000 to 1200°C, the diffraction peaks with the main intensities correspond to CaO (C), Al₂O₃ (A) and CaSO₄ (C \bar{S}). The peaks for ye'elimite (C₄A_{3 \bar{S}) and krotite (CA) are much smaller. The appearance of CaSO₄ and CaO phases is attributed to the decomposition of gypsum and CaCO₃, respectively (reactions R1 and R2 in Table I-5). At 1100°C, CA₂ diffraction peaks appear, while those related to CaO and Al₂O₃ are attenuated. Grossite (CA₂) forms by the solid-state reaction between CaO and Al₂O₃ (reaction R5, Table I-5) [118]. From 1100 to 1200°C, the diffraction intensities of CaO and Al₂O₃ are attenuated while those of CA and CA₂ peaks are slightly more intense; this variations in peak intensities can be related to the crystallisation of calcium aluminates (reactions R3 and R5, Table I-5) [118]. Beyond 1200°C, the peak intensities of CA and CA₂ decrease while the peak intensities of ye'elimite increase; this last phase can form through solid-state reaction between calcium aluminates and calcium sulphate reactions R6 and R7 (Table I-5) [9]. Hence, the reaction of ye'elimite formation is well activated by increasing the sintering temperature, especially from 1200 to 1300°C.}

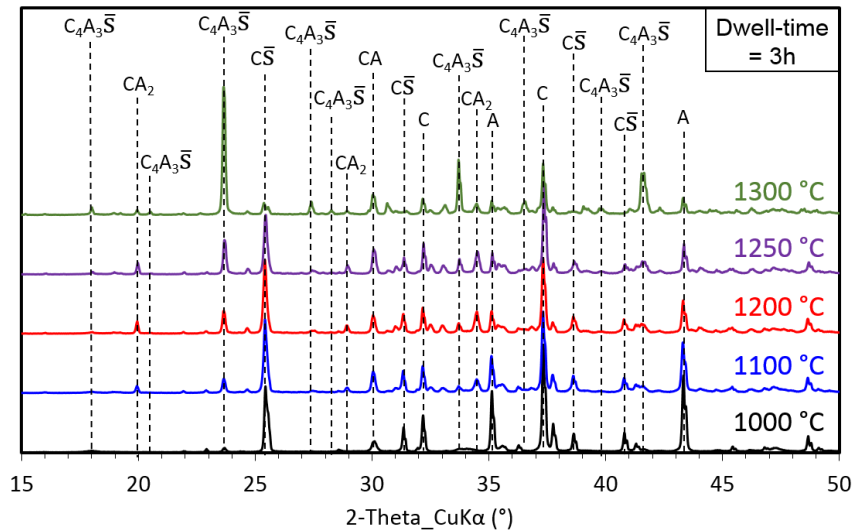


Figure VI-1: X-Ray diffractograms of samples treated from 1000 to 1300°C for 3 h.

Figure VI-2 shows the XRD patterns of the samples heated at 1300°C for various durations, from 15 to 180 min. CaO, CaSO₄, Al₂O₃, CA, CA₂ and ye'elimite were identified in the sample heated at 1300°C and immediately quenched (dwell time at 1300°C : 0 min). By increasing the dwell time from 0 to 180 min, CA diffraction peaks become more intense, while those related to CaO, Al₂O₃ and CaSO₄ are attenuated. Simultaneously, the intensity of the peaks related to ye'elimite phase increases with increasing the dwell time with a simultaneous decrease in calcium aluminate peak intensities. This confirms the conversion of calcium aluminate phases to ye'elimite phase according to the reactions R6 and R7 (Table I-5). Hence, the reaction of ye'elimite formation is well activated by increasing the dwell time at 1300°C.

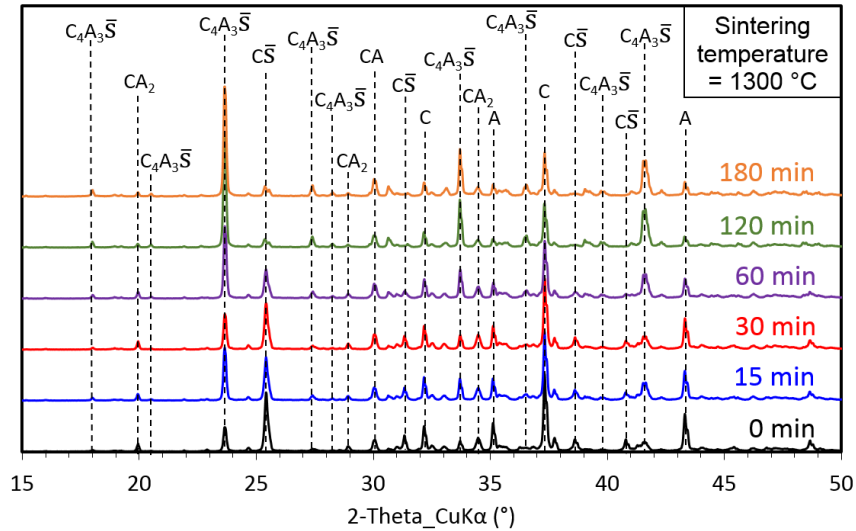


Figure VI-2: X-Ray diffractograms of samples treated at 1300°C from 0 to 180 min.

The XRD results can be summarized as follows: (i) ye'elimite starts forming at 1000°C; (ii) CA and CA₂ are intermediate phases formed between 1000 and 1100°C; (iii) above 1100°C, CA (resp. CA₂) progressively react with C̄S through R6 (Table I-5), (resp. C and C̄S through R7, Table I-5) to convert into ye'elimite.

VI.2. Microstructural observation

The observed microstructural changes during ye'elimite formation are shown in Figure VI-3 and Figure VI-4. The colored EDS mapping of back-scattered electron images for the samples sintered at different temperatures (from 1000 to 1300°C) for 3 hours are shown in Figure VI-3. The following descriptions can be made: samples treated at 1000°C present a heterogeneous microstructure with the presence of three compounds, namely Al₂O₃, CaO and CaSO₄. CaO and CaSO₄ come respectively from CaCO₃ decarbonation and CaSO₄·2H₂O dehydration. After sintering at 1100°C, small amounts of CA and CA₂ are formed around fine alumina grains. Similar observations can be made for the sample sintered at 1200°C. By increasing the temperature to 1250°C, the CA layer around alumina aggregates thickens while alumina grains decrease in size. We also see C₄A₃S̄ grains formed thanks to the reaction between CA and CaSO₄ grains. As the temperature increases to 1300°C, the CA phase almost totally surrounds alumina grains whose size reduces considerably. These observations are in accordance with the XRD results shown in Figure VI-1.

EDS mapping of BSE images (x150)

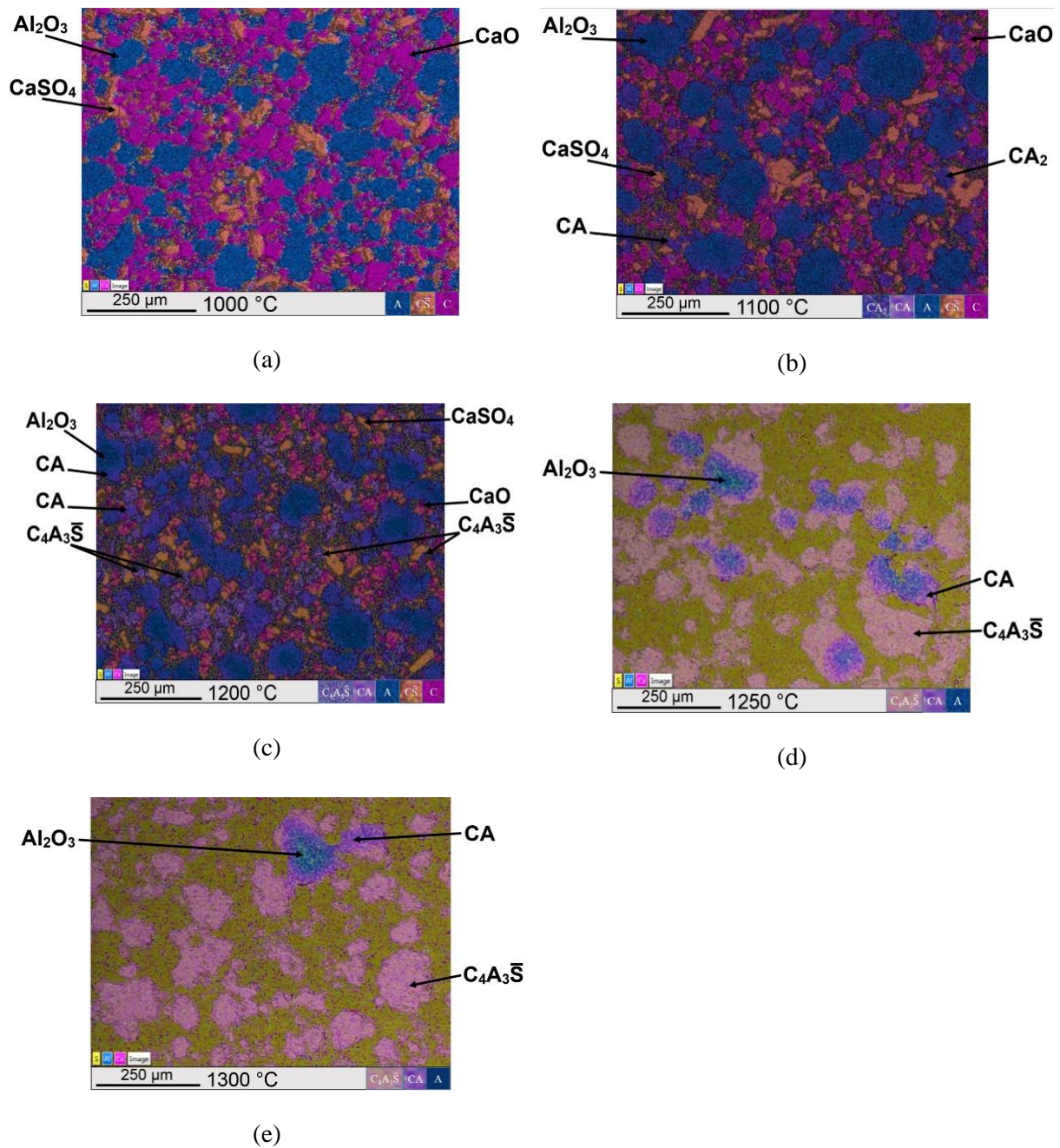


Figure VI-3: EDS mapping of elements present in the samples treated for 3 h between 1000°C (a), 1100°C (b), 1200°C (c), 1250°C (d) and 1300°C (e). Magnification of x150 was used for all images (Bars represent 250 μm). The corresponding EDS point analysis are shown in Appendix 1.

After the examination of the microstructural changes as a function of heating temperature, it is interesting to look at the microstructural changes as a function of dwell time for a given temperature. Colored EDS mapping of back-scattered electron images for the samples sintered at 1300°C from 15 to 180 min are shown in Figure VI-5. After 15 min heat treatment at 1300°C, ye'elimite surrounds CA and CA itself surrounds Al₂O₃ grains (Figure VI-4 a). Some lime grains are present. For the sample sintered for 30 min, we notice the presence of a core of Al₂O₃ grains surrounded by CA₂, CA and an external layer of C₄A₃ \bar{S} (Figure VI-4 b). For the sample sintered for longer time (60 and 120 min, Figure VI-4 c and Figure VI-4 d), C₄A₃ \bar{S} becomes dominant compared to CA and Al₂O₃. Lastly, after 180 min, large C₄A₃ \bar{S} grains are formed and no Al₂O₃, CaO and CaSO₄ are left (Figure VI-4 e). It clearly shows that the formation of ye'elimite is almost complete for sintering duration above 120 min.

EDS mapping of BSE images (x500)

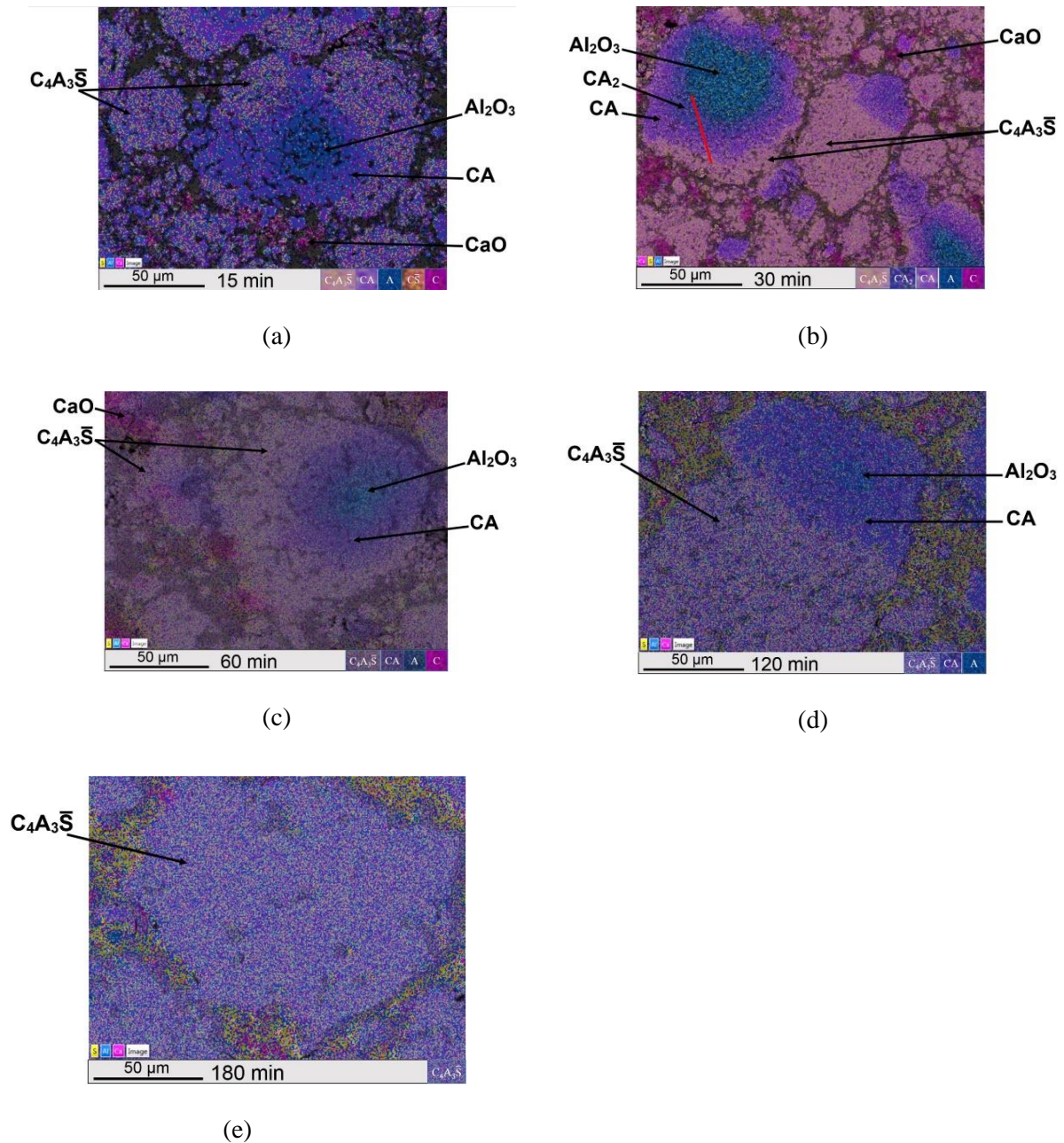
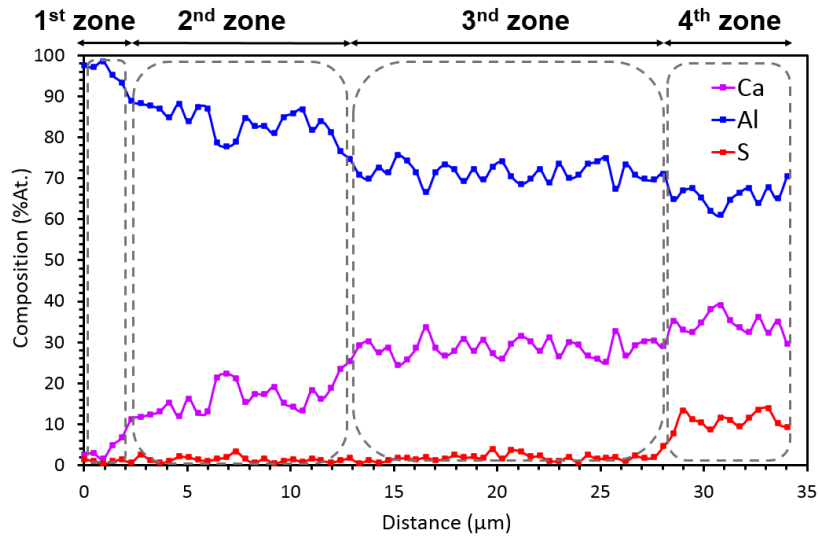
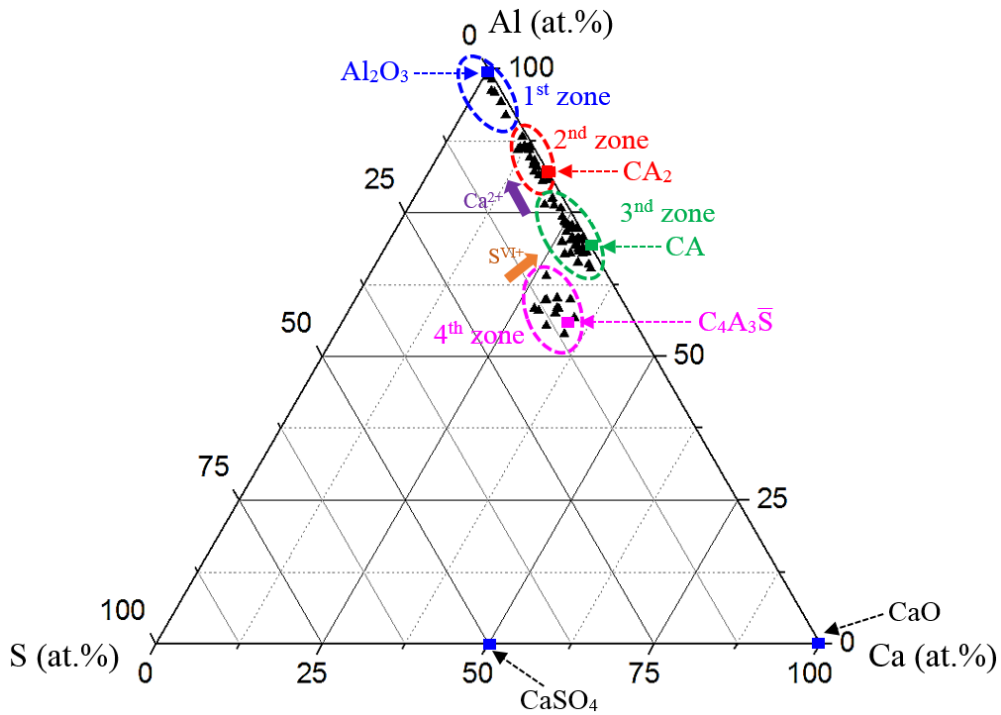


Figure VI-4: EDS mapping of elements present in the samples treated at 1300°C for different durations: 15 min (a), 30 min (b), 60 min (c), 120 min (d) and 180 min (e). Magnification of x500 was used for all images (Bars represent 50 μm). The red line of the sample treated at 30 min (Figure VI-4-b) represents EDS line-scan, the results of the line scan are shown in Figure VI-5 and the corresponding EDS point analyses are shown in Appendix 1.

Figure VI-5 a corresponds to EDS data of atomic percentage for calcium, aluminum and sulfur elements as a function of the position on the scan line for the sample heated at 1300°C for 30 min (see the red line on Figure VI-4 b). We can obviously identify four zones in Figure VI-5 a. To identify the compositions corresponding to each zone, the data are plotted in atomic percentage in the ternary composition diagram Al-Ca-S (Figure VI-5 b). Four regions can be distinguished: the first is Al_2O_3 rich (blue ellipse), the second is close to CA_2 (red ellipse), the third is close to CA (green ellipse) and the last one is close to $\text{C}_4\text{A}_3\bar{\text{S}}$ (pink ellipse). Thus, CA_2 phase tends to form on Al_2O_3 grains, then CA phase tends to form on CA_2 grains and $\text{C}_4\text{A}_3\bar{\text{S}}$ forms on CA grains according to solid-state reaction R5 (Table I-5).



(a)



(b)

Figure VI-5: (a) Composition profile obtained by EDS along the red line for the sample treated at 1300°C for 30 min (The EDS line-scan is represented by the red line in Figure VI-4), (b) Representation of EDS line scan data in ternary atomic percentage diagram of Al-Ca-S (the red square, represents theoretical atomic composition of CA_2 , the green square represents theoretical atomic composition of CA and the purple square represents theoretical atomic composition of $C_4A_3\bar{S}$. The black triangles are associated to the collected EDS data.

VI.3. Discussion

Based on the XRD analysis and the microstructural observations, ye'elimite amount increases as the sintering temperature goes from 1000 to 1300°C for 3 h. However, it is still not pure at 1300°C since some CA, CA₂, CaO, Al₂O₃ and CaSO₄ remain. The presence of these phases could be explained by an incomplete solid-state reaction between the different reactants.

Figure VI-6a summarizes the possible solid-state diffusion during ye'elimite formation Figure VI-6b and Figure VI-6c give a schematic representation of the microstructure transformations as a function of temperature for a given duration (Figure VI-6b) and as a function of dwell time at 1300°C (Figure VI-6c). Based on the literature [113], we assume that the diffusive species are Ca²⁺ and SO₄²⁻. Ca²⁺ ions coming from CaO can reach the CA/CA₂ interface and react with CA₂ to produce CA (reaction (a), Figure VI-6a); the consequence is a growth of CA grain and a consumption of CA₂ (the displacement of the CA/CA₂ interface is schematized by arrow 1, Figure VI-6a). Alternatively, CA can decompose into CaO – thus producing Ca²⁺ ions – and CA₂ (reaction (b), Figure VI-6a); the result is a growth of CA₂ grain and a decrease of CA (the displacement of the CA/CA₂ interface is schematized by arrow 2, Figure VI-6a). The Ca²⁺ ions can also reach the next interface CA₂/Al₂O₃ and consume alumina to form CA₂ (reaction (c) with a growth of CA₂ and a decrease in size of Al₂O₃, arrow 3). For the outer layer which contains C₄A₃ \bar{S} phase, its growth depends upon the contact between CA phase and CaSO₄ phase. Ca²⁺ and S^{VI+} may diffuse from CaSO₄ grains to C₄A₃ \bar{S} /CA and/or to C₄A₃ \bar{S} /CA₂ to form C₄A₃ \bar{S} (reactions R6 and R7, Table I-5). Figure VI-6b and Figure VI-6c give a schematic representation of the microstructural evolutions. As the temperature increases (Figure VI-6b), the Al₂O₃ grains progressively disappear and are replaced by CA and CA₂. These two compounds themselves eventually transform into ye'elimite. From microstructural observations of samples treated at 1300°C for different durations (Figure VI-4), the schematic representation on Figure VI-6 represents what happens: Al₂O₃ grains then calcium aluminate phases present at 1300°C are progressively consumed to give C₄A₃ \bar{S} -rich regions.

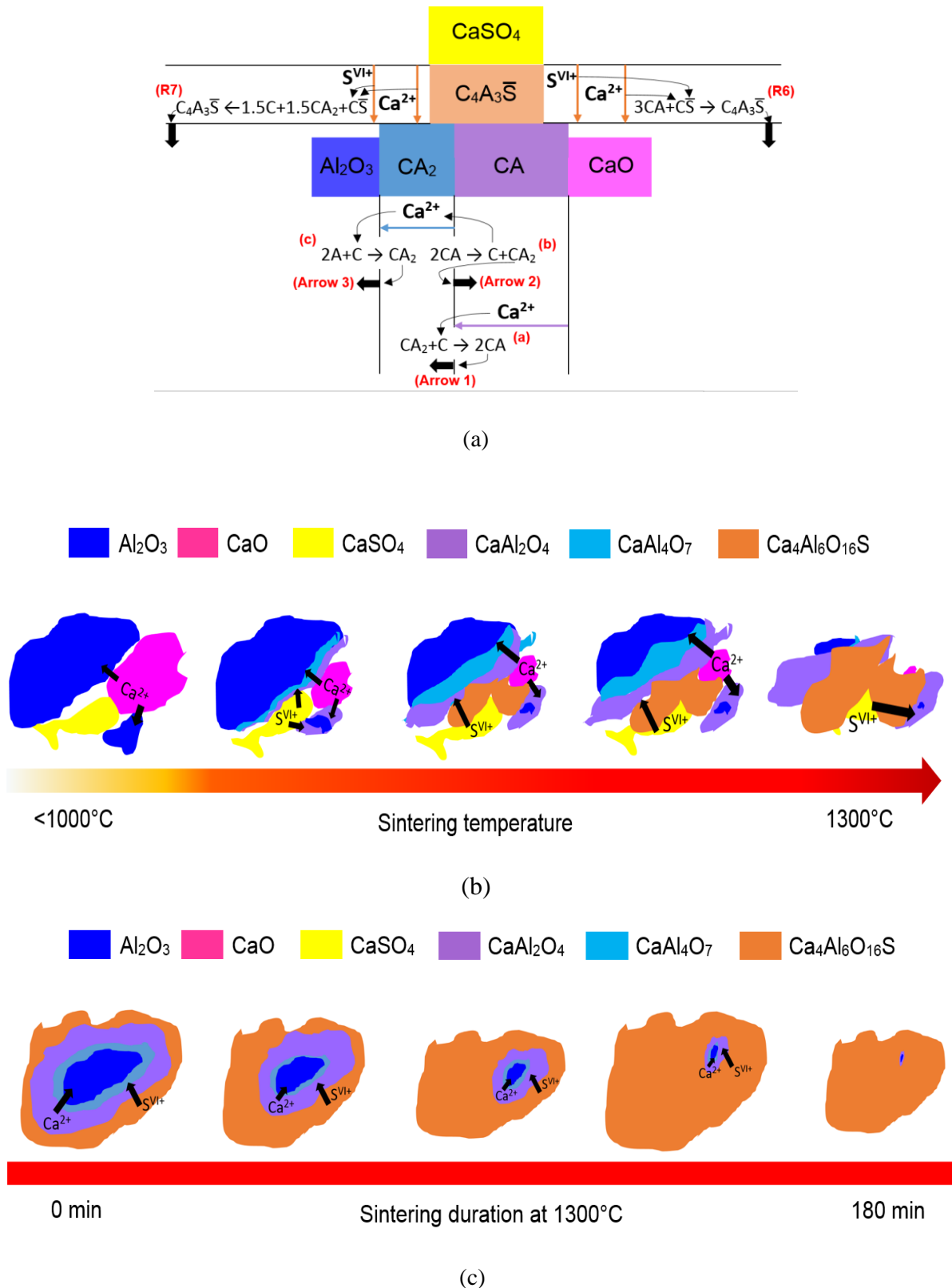


Figure VI-6: (a) Schematic representation of solid-state diffusion during ye'elimite formation. (b) Schematic representation of microstructural development of ye'elimite formation according to the sintering temperature. (c) Schematic representation of microstructural development of ye'elimite formation according to the sintering duration.

Avrami's kinetic model based on geometrical contraction of reactant grains, can be qualitatively applied to our case. The rate of a solid-state reaction is described by equation (E.34) [220]:

$$\frac{d\sigma}{dt} = k f(\sigma) \quad (\text{E.34})$$

where σ is the conversion fraction given by equation (E.35), $f(\sigma)$ is the function of the reaction model and k is the reaction rate constant, k is usually given by the Arrhenius equation (equation E.36) [221]:

$$\sigma = \frac{m_0 - m_t}{m_0 - m_\infty} \quad (\text{E.35})$$

m_0 is the initial reactant weight, m_t is the reactant weight at sintering time t , and m_∞ is the final weight which is generally approximated to be equal to 0 (complete reaction).

$$k = A. e^{-E_a/RT} \quad (\text{E.36})$$

A is the frequency factor, R is the gas constant, T is the sintering temperature and E_a is the activation energy.

Figure VI-7 is a schematic representation of the successive layers formed on the surface of Al_2O_3 grains. In the present case, the rate of Al_2O_3 grain consumption is supposed to be controlled by the progress of the interface reaction towards the middle of the grain.

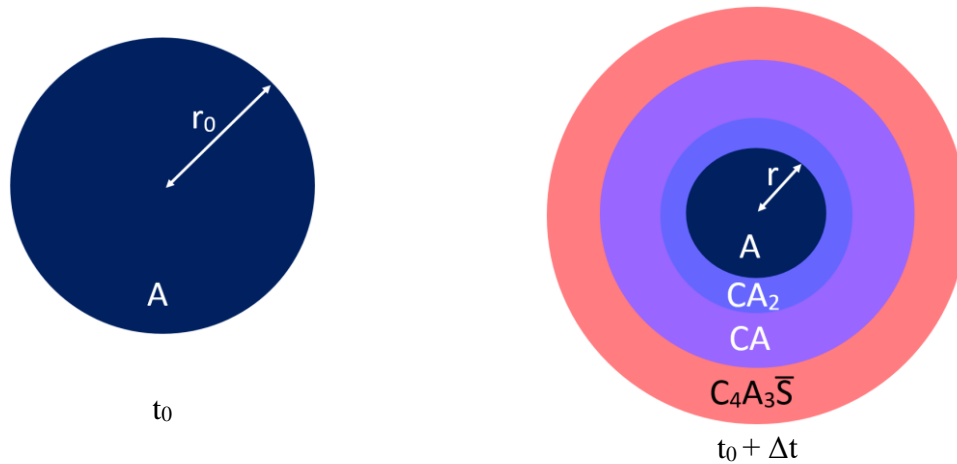


Figure VI-7: Simple schematic model of reaction-product layers forming on alumina grain.

The radius (r) at sintering time t is given by equation (E.37) [220]:

$$r = r_0 - kt \quad (\text{E.37})$$

where r_0 is the radius at time t_0 and t is the solid-state reaction time.

If we make a simple assumption that Al_2O_3 grains are spherical with a volume of $\frac{4\pi r^3}{3}$ and a density ρ , equation (E.35) becomes:

$$\sigma = \frac{\frac{4}{3}\pi\rho r_0^3 - \frac{4}{3}\pi\rho r^3}{\frac{4}{3}\pi\rho r_0^3} \quad (\text{E.38})$$

which reduces to equation (E.39):

$$1 - \sigma = \frac{r^3}{r_0^3} \quad (\text{E.39})$$

By combining equation (E.37) with equation (E.39) we have:

$$1 - (1 - \sigma)^{1/3} = \frac{k}{r_0} t = g(\sigma) \quad (\text{E.40})$$

$g(\sigma)$ is the integral form of the $f(\sigma)$ function.

The proposed sequence is the following: Al_2O_3 converts into CA_2 which in turn transforms into CA . Then CA reacts with CaSO_4 to form $\text{C}_4\text{A}_3\bar{\text{S}}$. So ye'elimite formation depends on Al_2O_3 consumption. Al_2O_3 conversion rate increases with increasing the sintering temperature (T), increasing the sintering time (t) and/or reducing the size of the starting Al_2O_3 grains (r_0). This could explain qualitatively the high thickness of $\text{C}_4\text{A}_3\bar{\text{S}}$ -rich and CA -rich regions around the smallest Al_2O_3 grains. It should be noted that there is some extreme values for T and t that should not be exceeded due to the sulfate instability above 1300°C as synthesis temperature and/or 4 h duration [9].

Important points to remember:

The reaction sequence by which ye'elimite forms through solid-state reactions from pure raw materials (alumina, lime and gypsum) was studied. First, mineralogical development during ye'elimite formation from 1000 to 1300°C for 3 hours and from 15 to 180 min at 1300°C, shows that ye'elimite content increases with increasing sintering temperature and duration. These results were confirmed by microstructural observations using colored EDS mapping of BSE micrographs. The formation of thick ye'elimite region and the remanence of small alumina grains is explained qualitatively by the dependence of diffusion rate with sintering temperature, sintering duration and Al_2O_3 grains size. The microstructure forms in different layers going from Al_2O_3 -rich region to $\text{C}_4\text{A}_3\bar{\text{S}}$ -rich region, where Ca^{2+} diffuses from CaO to Al_2O_3 through CA and CA_2 , and S^{VI} diffuse through $\text{C}_4\text{A}_3\bar{\text{S}}$ to calcium aluminate phases to form ye'elimite. It was concluded that CA and CA_2 are the mean intermediate products during ye'elimite formation. Finally, the formation rate of ye'elimite could be simply described by the geometrical contracted Avrami model. This model provides an insight about the relation between alumina consumption grains during clinking and ye'elimite formation.

The results reported herein deepen the understanding of the phenomenological description of ye'elimite solid-state formation, which could help cement producers to improve the burnability of raw materials during the clinkering process of calcium sulfoaluminate cements (ye'elimite-rich cements) and to minimize the presence of secondary phases like calcium aluminate phases. Lastly, the present study could also help academic researchers to synthesize lab-made calcium sulfoaluminate cements for crystallographic characterizations and hydration studies.

Chapitre VII. Effect of fineness and citric acid addition on ye'elimite hydration

Since CSA expansion behaviour depends on ettringite formation rate, which mainly relies on ye'elimite hydration [140,141], it would be of high scientific as well as industrial relevance to study the influence of ye'elimite powder fineness, on one hand, and citric acid addition, on the other hand, on controlling the nature and the amount of hydrate phases formation. This would also contribute to a better understanding of industrial expansive CSA cement early hydration [10]. In this context, the present data concern the effect of these two factors, namely fineness and citric acid addition, on the hydration of ye'elimite-rich cements. The present chapter starts by discussing the effect of fineness and citric acid addition on the dissolution of lab-made and pure ye'elimite powder alone. The role of ye'elimite powder fineness on hydration was examined by comparing the hydration of two model CSA cements. These model cements contain gypsum and lab-made ye'elimite powders, either synthesized by a sol-gel method and or by a solid-state reaction. The discussion carries on with the hydration in the presence of citric acid of one CSA model cement prepared by mixing gypsum and one lab-made ye'elimite by solid state reaction. The studied model systems show a schematic picture of the early behaviour of CSA cements [10]. Despite the fact that model cements do not reflect the whole complexity of commercial products, it helps to give a basic understanding of the hydration by focussing on the major hydration reactions [10].

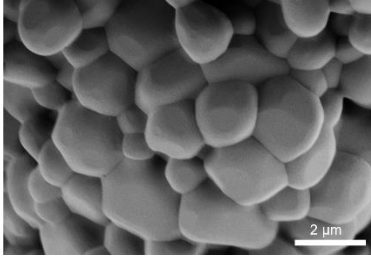
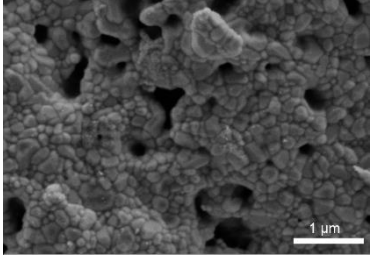
The experimental approach of the present chapter focuses on determining the nature and the amount of the hydration products using Rietveld analysis coupled to TGA analysis and on monitoring the ye'elimite dissolution using continuous ionic conductivity measurement. Zeta potential measurements were also carried out to examine mechanisms by which citric acid acts on ye'elimite-rich cement hydration.

VII.1. Description of the anhydrous powders

In our previous works concerning ye'elimite synthesis [222,223], the mineralogical composition determined by XRD-quantitative Rietveld analysis, particle size distribution (PSD), powder microstructure and BET specific surface area (SSA) of the two-synthesized ye'elimite powders were studied (Table VII-1). The micrographs and the BET data show that Ye-chem powder presents a smaller average grain size (136 nm) and a higher specific surface area (2.2 m²/g), in comparison to Ye-sol powder, which has (2 μm) and (0.74 m²/g) as average grain size and specific surface area, respectively. On the contrary, the particle size distribution measured by laser diffraction reveals higher D₅₀ for Ye-chem powder (27.1 μm) than for Ye-sol (14.6 μm). This is due to the agglomeration state of Ye-chem powder as shown in SEM micrographs in Table VII-1.

CSA clinkers are generally blended with gypsum to prepared CSA cement powders. The quantity of the added gypsum ranges traditionally between 10 and 25 wt.% (wt.% refers to weight percentage of gypsum with respect to cement weight) [12]. In the present work, highly pure gypsum (> 99.0 wt.%) was used. It has the following characteristics: $4.19 \text{ m}^2/\text{g}$ as BET surface area, and particle size diameters equal to $d_{10} = 9.92 \text{ }\mu\text{m}$, $d_{50} = 23.08 \text{ }\mu\text{m}$ and $d_{90} = 45.32 \text{ }\mu\text{m}$.

Table VII-1: Physical and chemical characteristics of the ye'elinite powders (Ye-sol and Ye-chem).

		Ye-sol powder	Ye-chem powder
Synthesis method		Solid-state reactions	Sol-gel chemical route
Synthesis protocol details		Ref. [222]	Ref. [223]
Synthesis temperature (°C)		1300	1250
PSD	d10 (μm)	3.1	8.6
	d50 (μm)	14.6	27.1
	d90 (μm)	51.1	68.0
SSA _{BET} (m ² /g)		0.74	2.2
Quantitative Rietveld analysis	C ₄ A ₃ S̄ (wt.%)	99.2	98.3
	CA (wt.%)	-	1.7
	CA ₂ (wt.%)	0.8	-
Microstructure (SEM)			
Ye'elinite average grain size		$2 \pm 1.2 \text{ }\mu\text{m}$	$136 \pm 48 \text{ nm}$

VII.2. Effect of fineness and citric acid on ye'elinite dissolution

The dissolution rate of anhydrous cementitious phases is proportional to the slope of the ionic conductivity versus time curves during the first minutes of dissolution, if we assume no complex molecules can form. Figure VII-1 shows the ionic conductivity variations of the Ye-sol-0, Ye-sol-5, Ye-sol-10 and Ye-chem suspensions (W/Ye=1000). Provided the temperature remains constant, the ionic conductivity in these highly dilute situations depends mainly on two factors: concentration of ions and

ionic mobility. In the present situation, as soon as the powder is in contact with water, dissolution of ye'elinite grains starts and the ions go into solution. Since the concentration of ions starts increasing, the ionic conductivity also increases immediately. It reaches a plateau with Ye-chem after 25 min. The slope value (s) of the different ionic conductivity curves (Figure VII-1) during the first minutes of dissolution (~ 5 min) are in the following order: $s(\text{Ye-chem-0}) > s(\text{Ye-sol-0}) > s(\text{Ye-sol-5}) > s(\text{Ye-sol-10})$. In this later case, it looks as if there is no dissolution within 50 min since the ionic conductivity level remains constant. Thus, the corresponding dissolution rates (r) follow the following sequence as well: $r(\text{Ye-chem-0}) > r(\text{Ye-sol-0}) > r(\text{Ye-sol-5}) > r(\text{Ye-sol-10}) \approx 0$.

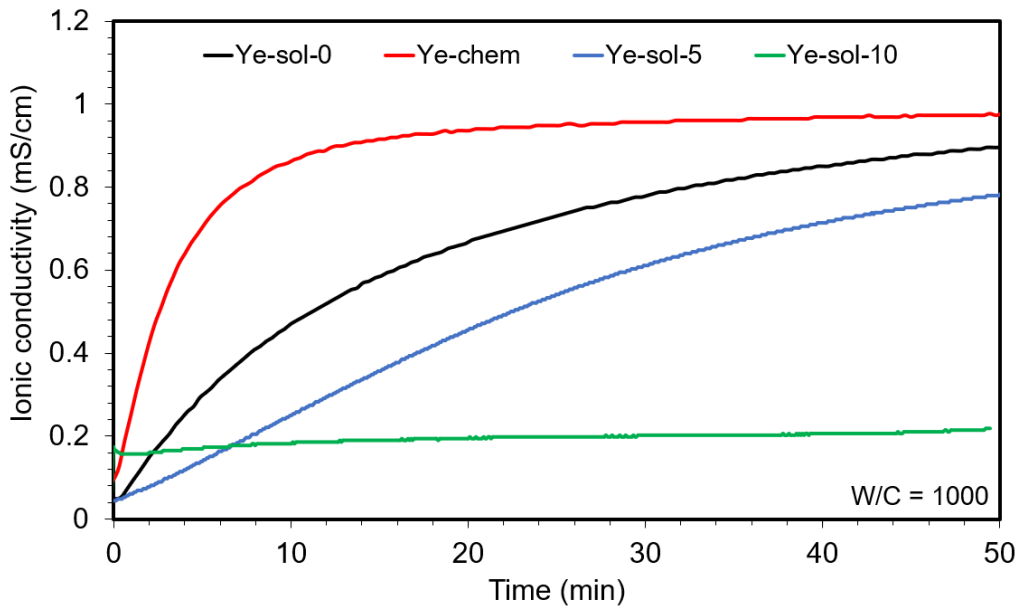


Figure VII-1: Ionic conductivity evolution of ye'elinite suspensions Ye-sol-0, Ye-chem, Ye-sol-5 and Ye-sol-10. All suspensions were prepared with $W/C = 1000$. $t = 0$ min in the graph's abscissa refers to the time when ye'elinite is added to the citric acid solution.

To investigate the morphological aspect of ye'elinite grains at early age dissolution stage, SEM micrographs of Ye-chem (Ye-chem-0) and that of Ye-sol powder immersed during 1 min in deionised water (Ye-sol-0), or in 10 wt.% citric acid solution (Ye-sol-10) are shown in Figure VII-2. The water to ye'elinite ratio was 1000. After only 1 min, ye'elinite grains immersed in deionised water (Ye-sol-0, Figure VII-2a, and Ye-chem-0, Figure VII-2c) show a severely corroded surface with the formation of several etch-pits (holes on the micrographs). In the case of ye'elinite which has been in contact with a citric acid solution (Ye-sol-10, Figure VII-2b), the ye'elinite grains surface appears smooth and much less attacked; moreover, the scarce etch-pits present characteristic geometries of crystal dissolution [35]. The SEM observations are in agreement with the (IC) measurements and confirm that the chemical nature of the solution in contact with ye'elinite plays an important role on its dissolution. The formation

of etch-pits during mineral dissolution has been evidenced in the literature for other cementitious anhydrous phases such as alite (tricalcium silicate, C_3S) and belite (dicalcium silicate, C_2S) [151,152,224,225] and other silicates like quartz [154,226,227]. In fact, the formation of such etch-pits was previously observed on the surface of alite phase grains, the major phase in ordinary Portland cements, by Juilland et al. [152], who stated that etch-pits formation depends on the over/under saturation state of solution, and also on the crystallographic defects density of anhydrous alite grains. Nicoleau et al. [151] confirmed the discussions of Juilland et al. concerning etch-pits formation during alite dissolution, by measuring the dissolution rate of alite according to the solution saturation state. The notion of etch-pits formation during mineral dissolution was identified and theorised early by Lasaga [153–155] who observed etch-pits formation during dissolution experiments of quartz and calcium carbonates.

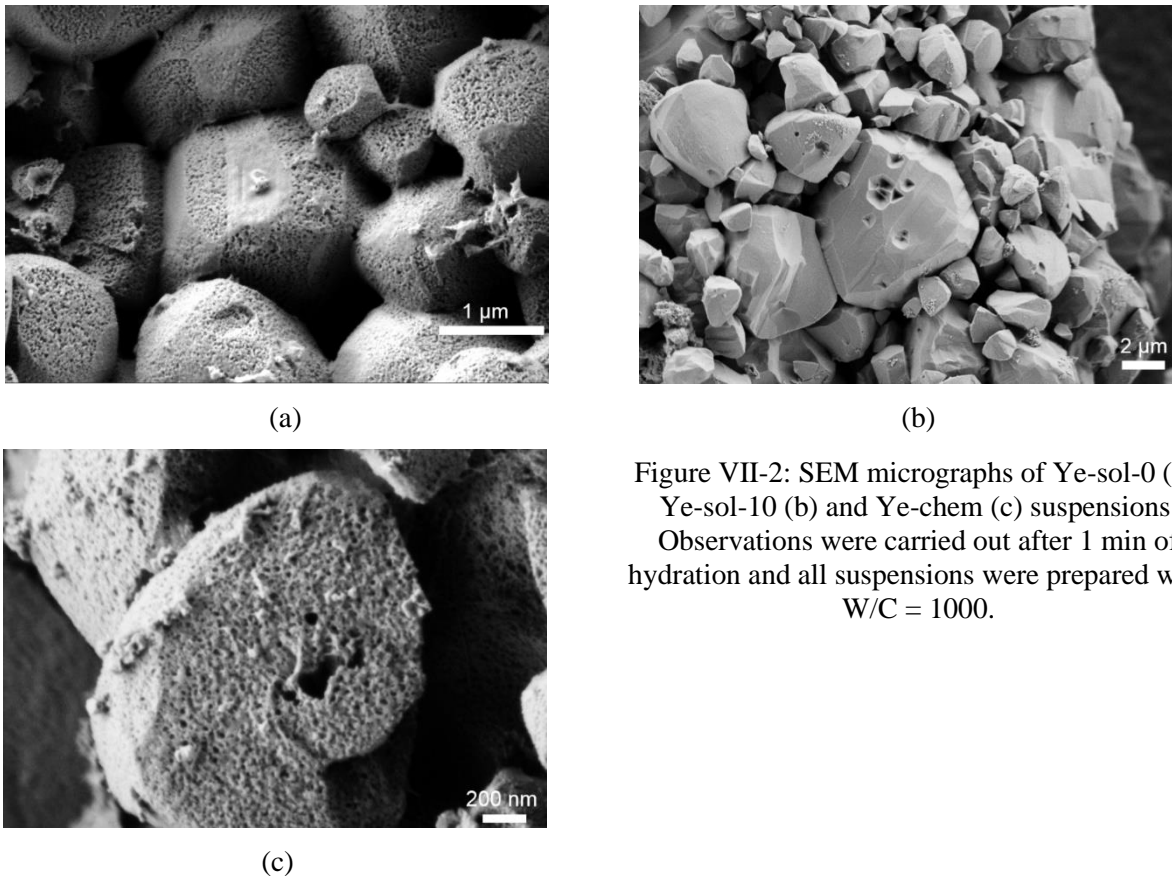


Figure VII-2: SEM micrographs of Ye-sol-0 (a), Ye-sol-10 (b) and Ye-chem (c) suspensions. Observations were carried out after 1 min of hydration and all suspensions were prepared with $W/C = 1000$.

The rapid reactivity of ye'elime powder synthesized by sol-gel method (Ye-chem) during the early dissolution step could be explained by its microstructure. In fact, Ye-chem powder shows very small ye'elime grains (136 ± 48 nm, Table VII-1) compared to Ye-sol powder which contains relatively larger ye'elime grains (2 ± 1.2 μm , Table VII-1). This morphological difference provides ye'elime surfaces with different reactivity to water.

To highlight the interaction between the added citric acid and ye'elimite powder, zeta potential measurements were carried out on the ye'elimite suspensions, Ye-sol-0, Ye-sol-5 and Ye-sol-10. The pH values of the corresponding acidic suspensions were 11.79, 10.84 and 10.80, respectively. Citric acid is normally considered to be a tri acid, with pKa values at 25°C, extrapolated to zero ionic strength, of 2.92, 4.28, and 5.21 [194]. Thereby, citrate is the dominant form of citric acid present in the prepared suspensions.

The results of zeta potential measurements are shown in Table VII-2. An increase in the citric acid concentration from 0 to 5 wt.% leads to a shift of the zeta potential from 7.7 ± 0.3 to -0.2 ± 0.1 mV, and the zeta potential turns to lower negative values (-10.9 ± 2.8 mV) for Ye-sol-10. The adsorption of citrate molecules at the surface of ye'elimite grains could explain this change of zeta potential values. In citrate, the distances between two oxygen atoms in two neighbouring carboxylate groups, are between 2.7 and 4.0 Å (Figure VII-3a) [46]. In ye'elimite, the $(13\bar{1})$ plane is a possible face for ye'elimite crystal [229]; the distances between two calcium atoms are between 3.0 and 4.0 Å (Figure VII-3b). Therefore, the citrate molecules can adsorb on the $(13\bar{1})$ faces via the oxygen of the carboxylate groups to form a complex. The remaining carboxylate functions of the adsorbed citrate molecules are negatively charged and can be responsible for the negative values of the zeta potential. This citrate adsorption can inhibit ye'elimite grains dissolution. In solution, calcium and citrate can form complex molecules too [230]. Therefore, two events can explain the slow setting of cement paste containing ye'elimite: the adsorption of citrate at the surface of ye'elimite grains can delay ye'elimite dissolution, and the formation of complex between calcium and citrate in the solution can prevent calcium ions to participate in the formation of hydrated phases. The concept of citrate adsorption on gypsum crystals was adopted by many authors [230–232] to explain the retarding effect on plaster setting.

Table VII-2: Zeta potential measurements of the prepared ye'elimite suspensions.

Ye'elimite suspension	ζ (mV)
Ye-sol-0	7.7 ± 0.3
Ye-sol-5	-0.2 ± 0.1
Ye-sol-10	-10.9 ± 2.8

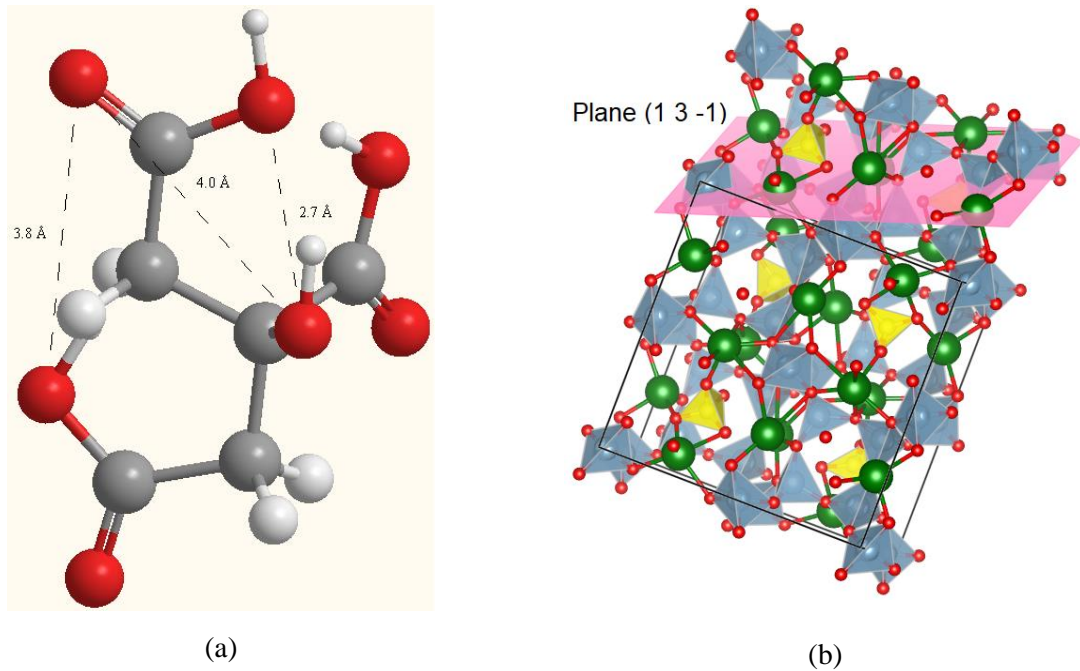


Figure VII-3: (a) Citric acid structure (CHEBI:30769) from the European Bioinformatics Institute Database [228], atoms are represented as spheres and are color coded as: carbon (grey), hydrogen (white) and oxygen (red). (b) Orthorhombic ye'elinite structure from Cuesta et al. [229] showing the $(1\bar{3}1)$ crystallographic plane, Ca denoted within dark-green spheres, Al within light blue tetrahedra, S within yellow tetrahedra, and O are red. For clarity CaO bonds are omitted in the represented structure.

Another possible way to explain the effect of citric acid addition in the shifting of the zeta potential from positive values to negative values, is to use Bombléd's approach [233]. This author estimated the surface charge of alite (C_3S) particles, and he showed that there are three times fewer positive sites than negative sites. Similarly, A. Smith et al. [234] applied Bombléd's approach to estimate the surface charge of krotite (calcium aluminate, CA) particles and they found that the negative sites are dominant. The approach is based on a statistical representation of the charges on the surface of grains. It can be expressed as follows:

$$\frac{\sigma^+}{\sigma^-} \text{ is proportional to } \frac{\sum_{\text{positive ions}} r_+^2}{\sum_{\text{negative ions}} r_-^2} \quad (\text{E.42})$$

where $\frac{\sigma^+}{\sigma^-}$ is the positive to negative surface charge ratio, r_+ is the ionic radius associated to positive ions and r_- is the ionic radius associated to negative ions.

The application of this approach to ye'elimite starts by knowing the ionic radius of each element: 1.35 Å for oxygen, 1.05 Å for calcium, 0.5 Å for aluminium and 0.43 Å for sulphur. $\frac{\sigma^+}{\sigma^-}$ (ye'elimite) can be calculated and is proportional to 0.2. This means that the negative sites are dominant and that the surface of the anhydrous $C_4A_3\bar{S}$ ($Ca_4Al_6O_{16}S$) particles is consequently negatively charged. Assuming that all of the calcium ions of the surface form complex molecules when citrate is present, the $\frac{\sigma^+}{\sigma^-}$ ratio becomes equal to 0.05. This means that negative sites become more dominant. Since zeta potential of a cement suspension is proportional to the surface charge of the cement grains present in this solution [234], the shift of (ζ) from positive to negative values could be explained by the high dominance of negative sites in the $C_4A_3\bar{S}$ particle surface in contact with citrate. Even though Bombléd's approach is somewhat simplistic because it assumes that all the surfaces have the same atomic arrangement and that the surface of the grains has the same chemical composition as the bulk, it gives an interesting insight into the surface charge.

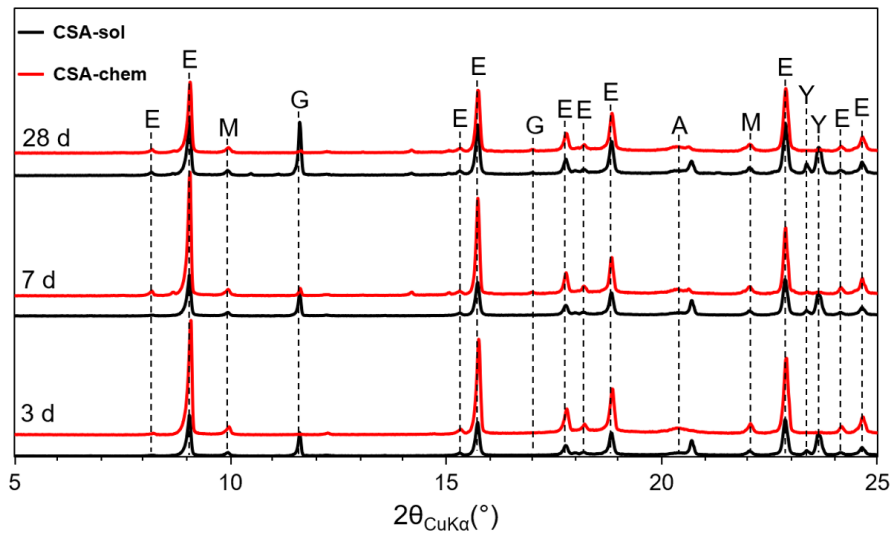
VII.3. Hydration of CSA model cements containing ye'elimite with two different grain sizes

The results of XRD analysis of the hydrated CSA model cements CSA-sol and CSA-chem at $t_0 = 0$ day, and after curing for 3 days, 7 days and 28 days are shown in Figure VII-4a. The corresponding Rietveld analysis results are given in Table VII-3. Since we consider that with Rietveld analysis it is somehow difficult to quantify accurately the remaining reactants (ye'elimite and gypsum) and formed hydrates, we will focus for clarity on the amount of remaining ye'elimite and on the total quantities of formed hydrates (mainly ettringite, followed by monosulfoaluminate and gibbsite). First of all, Figure VII-4b displays the calculated hydration degree, α given by equation (E.0), of CSA-sol and CSA-chem pastes. After 3 days, CSA-chem paste reaches more than 96.3 % while it is almost 72.4 % for the CSA-sol paste. After 7 days, the degree of reaction reached 97.6 % and 79.9 % for CSA-chem and CSA-sol, respectively. Finally, it was observed that at 28 days, the hydration of Ye-chem was nearly complete reaching almost 98 % hydration degree (mainly ettringite), while Ye-sol hydration degree attains only 88.7 %. Concerning the hydrates, the quantities are higher at any time in CSA-chem than in CSA-sol.

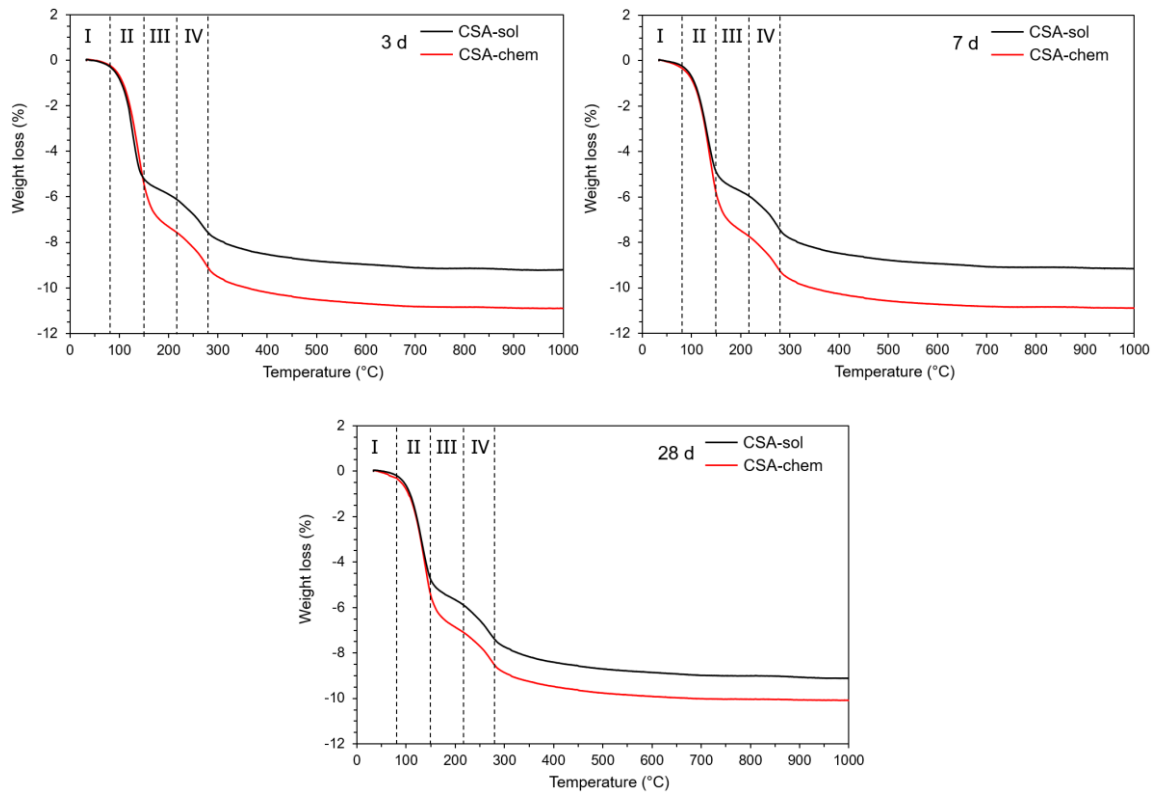
Table VII-3: Rietveld phase analysis results (wt.%) for model cements (CSA-sol) and (CSA-Chem) at different hydration ages. Rietveld agreement factors are also given (equations E.25, E.26 and E.27).

Phase	CSA-sol				CSA-chem			
	t ₀	3 d	7 d	28 d	t ₀	3 d	7 d	28 d
Ye'elimite $C_4A_3\bar{S}$	63.9	17.6	12.8	7.2	63.9	2.4	1.5	0.7
Gypsum $C\bar{S}H_2$	36.1	9.6	8.6	4.5	36.1	1.9	0.8	0.7
Ettringite $C_6A\bar{S}_3H_{32}$	-	58	65.9	45.0	-	74.1	52.2	83.0
Monosulfo -aluminate $C_4A\bar{S}H_{12}$	-	0.1	0.1	28.5	-	0.2	29.5	0.5
Gibbsite AH_3	-	14.7	12.6	14.8	-	21.4	16.0	15.1
Sum of hydrate amounts	-	72.8	78.6	88.3	-	95.7	97.7	98.6
R _{wp} (%)	-	19.9	18.5	16.8	-	23.1	18.8	21.8
R _{exp} (%)	-	2.8	3.6	2.9	-	2.6	2.7	2.6
GOF	-	7.1	5.1	5.8	-	8.7	6.9	8.3

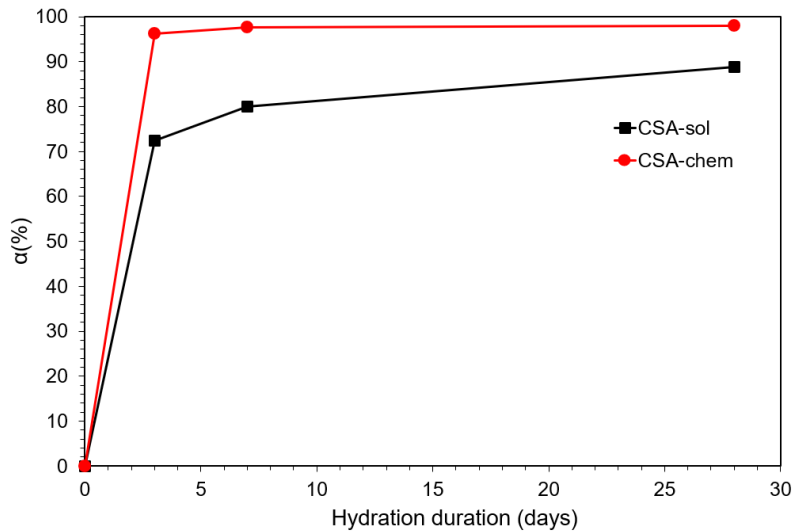
TGA curves are presented in Figure VII-4c. Weight loss between 80 and 150°C can be assigned to ettringite decomposition (Zone II, Figure VII-4c) [18,148]. Gypsum can decompose between 150 and 220°C (Zone III, Figure VII-4c) [18,148]. Weight loss between 100 and 800°C can originate from the decomposition of monosulfoaluminate (Zones II, III, and IV, Figure VII-4c), with a maximum decomposition at 200°C [18,146]. Lastly, between 200 and 300°C, the weight loss associated to the decomposition of gibbsite can be detected (Zone IV, Figure VII-4c) [18,148]. Despite an overlap between the decomposition of the different products with temperature, TGA results (Figure VII-4c) shows higher total weight loss for CSA-chem compared to CSA-sol, at all hydration durations, which comes mainly from the decomposition of hydrates. In conclusion, TGA and XRD results give similar trends: the finer the ye'elimite powder, the quicker the cement containing this powder hydrates.



(a)



(b)



(c)

Figure VII-4: XRD patterns (a), TGA curves (b), and calculated hydration degree (α) (c), for CSA model cements (CSA-sol-0) and (CSA-Chem) at different hydration ages. E: ettringite; G: Gypsum; M: monosulfate; Y: ye'elinite; A: Gibbsite, ($\alpha\%$) is given by equation (E.0).

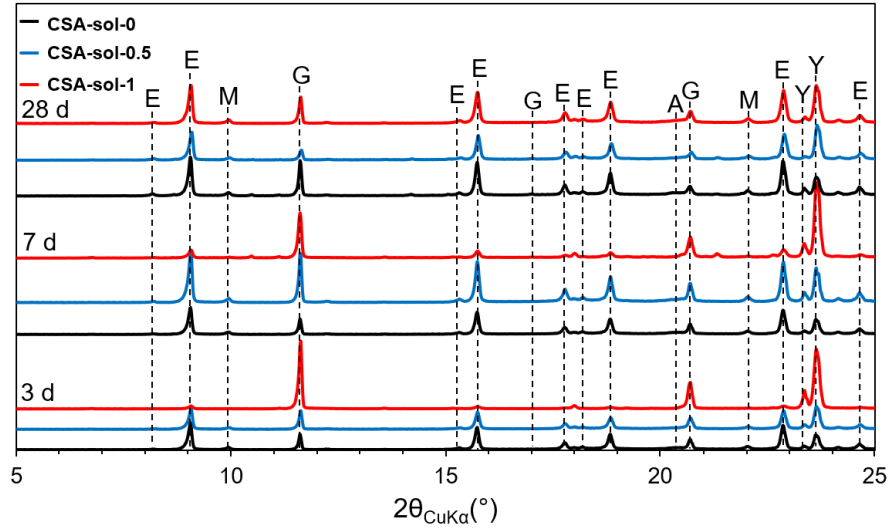
VII.4. Influence of citric acid on CSA model cements hydration

The composition evolution of the CSA-sol pastes, in the presence of different citric acid dosages (0 wt.%, 0.5 wt.% and 1 wt.%) for different curing ages (3 days, 7 days and 28 days), were followed by XRD (Figure VII-5a) with the corresponding Rietveld results (Table VII-4). Again, we will focus for clarity on the amount of remaining ye'elinite and on the total quantities of formed hydrates (mainly ettringite, followed by monosulfoaluminate and gibbsite). The variations of the calculated hydration degree, α given by equation (E.1), of CSA-sol pastes containing different citric acid dosages are presented in Figure VII-5b. The results show that citrate retards the hydration: CSA-sol-0 reacts at a faster pace after 3 days since the degree of hydration of ye'elinite is 72.4 %, while CSA-sol-0.5 and CSA-sol pastes reach only 66.6 % and 17.0 %, respectively. After 7 days, CSA-sol-0, CSA-sol-0.5 and CSA-sol-1 reach more than 79.9 %, almost 73.2 % and 26.4 % degree of hydration, respectively. Lastly, after 28 days of hydration, the figures are 88.7 %, almost 75.6 % and 65.2 % for CSA-sol-0, CSA-sol-0.5 and CSA-sol-respectively. Therefore, the major effect of citric acid addition on ye'elinite hydration is the slowing down of the hydration kinetics of the cement paste, suggesting an adsorption of citrate molecules on ye'elinite grains. In section (VII.2), it was explained how citric acid can delay ye'elinite

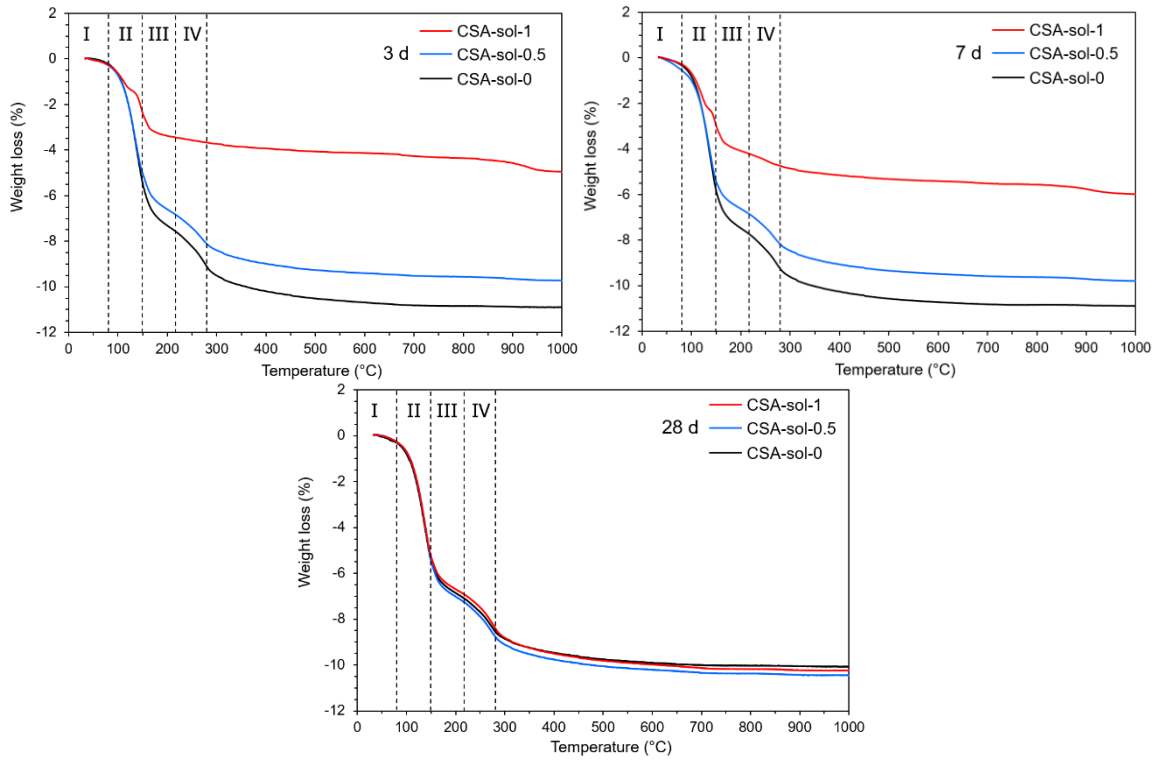
dissolution by the possible citrate adsorption on ye'elimite grains. An analysis of TGA results (Figure VII-5c) shows the same trend, i.e. a marked decrease of weight loss with the addition of citric acid, especially with 1 wt.%.

Table VII-4: Rietveld phase analysis results (wt.%) for model cements (CSA-sol-0), (CSA-sol-0.5) and (CSA-sol-1) at different hydration ages. Rietveld agreement factors are also given (equations E.25, E.26 and E.27).

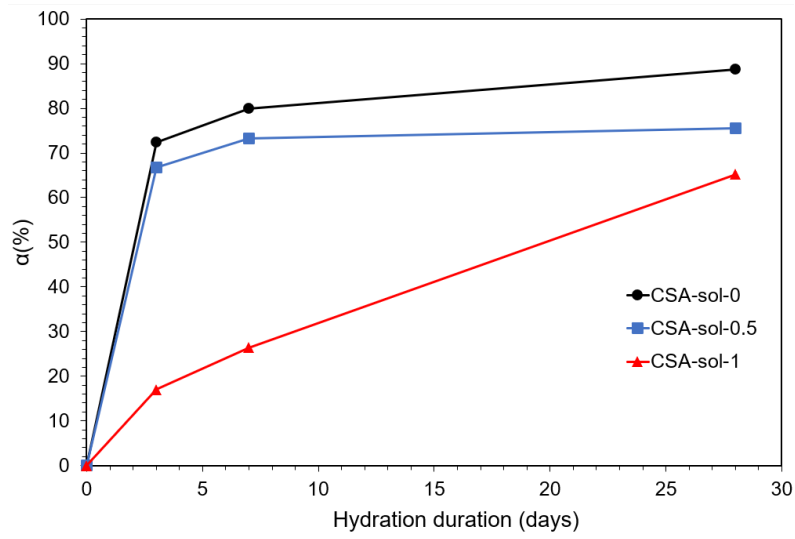
Phase	CSA-sol-0				CSA-sol-0.5				CSA-sol-1			
	t ₀	3 d	7 d	28 d	t ₀	3 d	7 d	28 d	t ₀	3 d	7 d	28 d
Ye'elimite $C_4A_3\bar{S}$	63.9	17.6	12.8	7.2	63.9	21.3	17.1	15.6	63.9	53.0	47.0	22.2
Gypsum $C\bar{S}H_2$	36.1	9.6	8.6	4.5	36.1	13.0	13.1	3.3	36.1	30.5	20.1	10.2
Ettringite $C_6A\bar{S}_3H_{32}$	-	58	65.9	45.0	-	54.2	60.2	39.9	-	8.4	17.1	54.4
Monosulfo -aluminate $C_4A\bar{S}H_{12}$	-	0.1	0.1	28.5	-	0.1	0.1	24.0	-	0.1	9.5	0.2
Gibbsite AH_3	-	14.7	12.6	14.8	-	11.4	9.5	17.2	-	8.0	6.3	13
Sum of hydrate amounts	-	72.8	78.6	88.3	-	65.7	69.8	81.1	-	16.5	32.9	67.6
R _{wp} (%)	-	19.9	18.5	16.8	-	18.1	21.4	15.9	-	21.2	17.2	20.4
R _{exp} (%)	-	2.8	3.6	2.9	-	3.7	2.7	3.0	-	4.0	3.2	2.8
GOF	-	7.1	5.1	5.8	-	4.9	7.8	5.3	-	5.4	5.4	7.2



(a)



(b)



(c)

Figure VII-5: XRD patterns (a), TGA curves (b), and calculated hydration degree (α) (c), for CSA model cements (CSA-sol-0), (CSA-sol-0.5) and (CSA-sol-1) at different hydration ages. E: ettringite; G: Gypsum; M: monosulfate; Y: ye'elinite; A: Gibbsite. ($\alpha\%$) is given by equation (E.0).

Important points to remember:

The purpose of these experiments was to investigate the effect of fineness on hydration of ye'elinite powder, prepared either by a solid-state method or by a chemical route, its effect on the hydration of two model CSA cements and finally the effect of citric acid addition on the hydration of a CSA model cement. The main conclusions can be summarized as follows.

The main difference found between the dissolution of ye'elinite powders prepared by chemical or solid state routes (Ye-chem or Ye-sol) is related to the reaction rate. The presence of fine grains (100 to 200 nm) of ye'elinite accelerates the dissolution. From an industrial point of view, the presence of a fine fraction of ye'elinite grains (of the order of 100 - 200 nm) in commercial CSA cements can considerably accelerate the hydration and therefore the expansion behavior.

The addition of citric acid to the mixing water leads to a retarding effect on the dissolution of ye'elinite grains. Also, the surface of the grains presents scarce etch pits when citric acid is present in the water, while the surface seems to be totally attacked when no citric acid is present. These results indicate that the hydration of CSA model cements prepared from the mixing of ye'elinite powder – prepared by solid state reaction - and gypsum is retarded in the presence of citric acid at concentrations of 0.5 wt.% and 1 wt.% with respect to ye'elinite. Citric acid may work efficiently as a retarding additive for CSA cements since it slows down the initial ye'elinite dissolution. In the present work, it was also shown that the addition of citric acid with CSA model cements delays the formation of hydrates, especially ettringite. Therefore, expansion behavior of commercial CSA cements could be controlled by the addition of citric acid, because it is well known that the fresh CSA concrete properties depend mainly on ettringite quantities in the hydrated cement pastes.

Therefore, it was concluded that ettringite formation and more generally hydrates could be accelerated by the addition of highly fine ye'elinite powder while the addition of small amounts of citric acid could delay the hydration. These two strategies could to be helpful for industrial CSA cement developers, because they constitute a practical key method to control the amount of formed ettringite, and hence the expansion behaviour of CSA cements.

The influence of ye'elinite powder finesse and citric acid addition on the dimensional stability, workability, mechanical properties and durability performances of CSA cements and concretes could be the subject of further studies.

Conclusions and perspectives

The first purpose of the present work is to investigate the synthesis of lab-made and highly pure ye'elimite powders, (i) by solid state reactions showing optimal synthesis conditions and identifying ye'elimite formation mechanisms, (ii) and by sol-gel method to synthesis ye'elimite powder with nano-size grains.

The second purpose of the present PhD thesis was to investigate the effect of fineness on hydration of lab-made ye'elimite powder, prepared either by a solid state method or by a chemical route, its effect on the hydration of two model CSA cements and finally the effect of citric acid addition on the hydration of a CSA model cement. The main conclusions of the present work can be summarized as follows.

The results of the present study have allowed us to clarify the effect of sintering conditions (temperature and duration) on the ye'elimite formation and microstructure of stoichiometric mixtures produced from pure commercial powders and with a thoroughly described protocol. Solid state formation of ye'elimite from the raw materials starts at 1000°C and continues to form from the reaction between minor calcium aluminate phases (CA, CA₂) and CaSO₄ until 1300°C. The optimal sintering condition to maximize the ye'elimite formation is about 1300°C for sintering temperature and 3 hours for sintering duration. Above 1300°C ye'elimite decomposes into calcium aluminate phases and SO₂ gas. Gas releases (CO₂ from calcite decomposition and SO₂ from unreacted anhydrite) are also observed during the ye'elimite formation which promote the dilatation of the fired pellets. It should also be noticed that to our knowledge, this is the first time a dilatometric study has been carried out on pure ye'elimite.

The reaction sequence by which ye'elimite forms through solid state reactions from pure raw materials (alumina, lime and gypsum) was studied. First, mineralogical development during ye'elimite formation from 1000 to 1300°C for 3 hours and from 15 to 180 min at 1300°C, shows that ye'elimite content increases with increasing sintering temperature and duration. These results were confirmed by microstructural observations using EDS mapping of BSE micrographs. The formation of thick ye'elimite region and the remanence of small alumina grains is explained qualitatively by the dependence of diffusion rate with sintering temperature, sintering duration and Al₂O₃ grains size. The microstructure forms in different layers going from Al₂O₃-rich region to C₄A₃ \bar{S} -rich region, where Ca²⁺ diffuses from CaO to Al₂O₃ through CA and CA₂, and S^{VI+} diffuse through C₄A₃ \bar{S} to calcium aluminate phases to form ye'elimite. It was concluded that CA and CA₂ are the main intermediate products during ye'elimite formation.

Fairly pure and fine ye'elimite particles were successfully obtained at 1250°C for 1 hour by means of the sol-gel method. Referring to X-ray diffraction results, CA and CA₂ are the only intermediate

crystalline phases detected. Upon increasing the heat treatment temperature, the amount of CA and CA₂ decreased being gradually transformed into the C₄A₃S̄ phase.

The main difference found between the dissolution of ye'elimite powders prepared by chemical or solid state routes (Ye-chem or Ye-sol) is related to the reaction rate. The presence of fine grains (100 to 200 nm) of ye'elimite accelerates the dissolution. From an industrial point of view, the presence of a fine fraction of ye'elimite grains (of the order of 100 – 200 nm) in commercial CSA cements can considerably accelerate the hydration and therefore the expansion behavior.

The addition of citric acid to the mixing water leads to a retarding effect on the dissolution of ye'elimite grains. Citric acid may work efficiently as a retarding additive for CSA cements since it slows down the initial ye'elimite dissolution. In the present work, it was also shown that the addition of citric acid with CSA model cements delays the formation of hydrates, especially ettringite. Consequently, expansion behavior of commercial CSA cements could be controlled by the addition of citric acid, because it is well known that the fresh CSA concrete properties depend mainly on ettringite quantities in the hydrated cement pastes.

Therefore, it was concluded that ettringite formation and more generally hydrates could be accelerated by the addition of highly fine ye'elimite powder while the addition of small amounts of citric acid could delay the hydration. These two levers could be helpful for industrial CSA cement developers, because they constitute a practical key method to control the amount of formed ettringite, and hence the expansion behaviour of CSA cements.

The influence of ye'elimite powder fineness and citric acid addition on the dimensional stability, workability, mechanical properties and durability performances of CSA cements and concretes could be the subject of further studies.

This work describes precisely protocols to prepare ye'elimite powders. It also offers perspectives for CSA cement producers by presenting solutions in order to better monitor their hydration, and therefore the expansion. On a more fundamental point of view, two ideas could be explored: (i) mixing pure ye'elimite with variable quantities of pure dicalcium silicate in order to study the hydration of binary systems. This could be helpful for the normalization issue; (ii) synthesis of ye'elimite containing specific dopants which can be present either in bauxite or alumina when these are used as raw materials. Again, a study of the hydration behavior could be of practical relevance for CSA cement producers.

References

- [1] E. Gartner, Industrially interesting approaches to “low-CO₂” cements, *Cem. Concr. Res.* 34 (2004) 1489–1498. doi:10.1016/j.cemconres.2004.01.021.
- [2] G.P. Hammond, C.I. Jones, Embodied energy and carbon in construction materials, *Proc. Inst. Civ. Eng. - Energy*. 161 (2008) 87–98. doi:10.1680/ener.2008.161.2.87.
- [3] G. Andersson, A. Ponzio, A. Gauffin, H. Axelsson, G. Nilson, Sustainable steel production—Swedish initiative to ‘close the loop,’ *Miner. Process. Extr. Metall.* 126 (2017) 81–88.
- [4] E.C.A. Cembureau, The role of cement in the 2050 low carbon economy, 2014. https://cembureau.eu/media/1500/cembureau_2050roadmap_lowcarboneyconomy_2013-09-01.pdf.
- [5] E. Gartner, H. Hirao, A review of alternative approaches to the reduction of CO₂ emissions associated with the manufacture of the binder phase in concrete, *Cem. Concr. Res.* 78 (2015) 126–142.
- [6] K.L. Scrivener, V.M. John, E.M. Gartner, Eco-efficient cements: Potential economically viable solutions for a low-CO₂ cement-based materials industry, *Cem. Concr. Res.* 114 (2018) 2–26.
- [7] Datasheet | CTS Cement, (n.d.). https://www.ctscement.com/datasheet/CTS_24-6_CONCRETE_MIX_Datasheet_DS_160_EN_8?c=PRODUCTS&t=Homeowners (accessed March 10, 2019).
- [8] F. Winnefeld, B. Lothenbach, Phase equilibria in the system Ca₄Al₆O₁₂SO₄–Ca₂SiO₄–CaSO₄–H₂O referring to the hydration of calcium sulfoaluminate cements, *RILEM Tech. Lett.* 1 (2016) 10–16.
- [9] Y. El Khessaimi, Y. El Hafiane, A. Smith, R. Trauchessec, C. Diliberto, A. Lecomte, Solid-state synthesis of pure ye’elimite, *J. Eur. Ceram. Soc.* (2018). doi:10.1016/j.jeurceramsoc.2018.03.018.
- [10] M.B. Haha, F. Winnefeld, A. Pisch, Advances in understanding ye’elimite-rich cements, *Cem. Concr. Res.* 123 (2019) 105778.
- [11] J.H. Sharp, C.D. Lawrence, R. Yang, Calcium sulfoaluminate cements—low-energy cements, special cements or what?, *Adv. Cem. Res.* 11 (1999) 3–13.
- [12] F. Winnefeld, B. Lothenbach, Hydration of calcium sulfoaluminate cements — Experimental findings and thermodynamic modelling, *Cem. Concr. Res.* 40 (2010) 1239–1247. doi:10.1016/j.cemconres.2009.08.014.
- [13] M.A.G. Aranda, A.G. De la Torre, Eco-efficient concrete: 18. Sulfoaluminate cement, Elsevier Inc. Chapters, 2013.
- [14] I. Janotka, L. Krajčí, An experimental study on the upgrade of sulfoaluminate—belite cement systems by blending with Portland cement, *Adv. Cem. Res.* 11 (1999) 35–41.
- [15] G. Sodoh, T. Ohta, H. Harada, High strength cement in the CaO–Al₂O₃–SiO₂–SO₃ system and its application, in: *Proc 7th Int Congr Chem Cem Paris, 1980*: pp. 152–157.
- [16] D. Jun-an, S. Muzhen, An investigation into cement CaO–SiO₂–Al₂O₃–Fe₂O₃–SO₃ system. *Proc. 8th Internat. Congr., Chem Cem Rio Jan. 2* (1986) 300–305.
- [17] A. Rungchet, P. Chindaprasirt, S. Wansom, K. Pimraksa, Hydrothermal synthesis of calcium sulfoaluminate–belite cement from industrial waste materials, *J. Clean. Prod.* 115 (2016) 273–283.
- [18] F. Winnefeld, S. Barlag, Calorimetric and thermogravimetric study on the influence of calcium sulfate on the hydration of ye’elimite, *J. Therm. Anal. Calorim.* 101 (2009) 949–957.

-
- [19] J.-B. Champenois, M. Dhoury, C. Cau Dit Coumes, C. Mercier, B. Revel, P. Le Bescop, D. Damidot, Influence of sodium borate on the early age hydration of calcium sulfoaluminate cement, *Cem. Concr. Res.* 70 (2015) 83–93. doi:10.1016/j.cemconres.2014.12.010.
- [20] S.C. Mojumdar, I. Janotka, Thermophysical properties of blends from Portland and sulfoaluminate-belite cements, *Acta Phys. Slovaca.* 52 (2002) 435–446.
- [21] S. Sahu, J. Majling, Preparation of sulphoaluminate belite cement from fly ash, *Cem. Concr. Res.* 24 (1994) 1065–1072.
- [22] K. Ikeda, Cements along the join $4\text{CaO}-3\text{Al}_2\text{O}_3 \cdot \text{SO}_3-2\text{CaO} \cdot \text{SO}_3$, in: *Proc 7th Int Congr Chem Cem. Paris 2 Theme*, 1980: p. 31.
- [23] P.K. Mehta, Investigations on energy-saving cements, *World Cem. Technol.* 11 (1980) 166–177.
- [24] N. Chitvoranund, F. Winnefeld, C.W. Hargis, B. Lothenbach, Synthesis and hydration of alite-calcium sulfoaluminate cement, *Adv Cem Res.* 29 (2017) 101–111.
- [25] E. Gartner, G. Li, High belite-containing sulfoaluminous clinker, method for the production and the use thereof for preparing hydraulic binders, 2010.
- [26] M.K. Sucu, T.H.D. Ba, Calcium sulphoaluminate cement with mayenite phase, EP3199500A1, 2017. <https://patents.google.com/patent/EP3199500A1/en?q=Patent+No.+EP3199500+A1>. (accessed March 4, 2019).
- [27] K. Alexander, Expansive and shrinkage-compensated cements, US3251701A, 1966. [https://patents.google.com/patent/US3251701A/en?q=Alexander%2c+K.+\(1966\).+U.S.+Patent+No.+3%2c251%2c701.+Washington%2c+DC:+U.S.+Patent+and+Trademark+Office](https://patents.google.com/patent/US3251701A/en?q=Alexander%2c+K.+(1966).+U.S.+Patent+No.+3%2c251%2c701.+Washington%2c+DC:+U.S.+Patent+and+Trademark+Office) (accessed March 4, 2019).
- [28] B. Classen, P. Colombet, Clinker sulfoalumineux sans fer et sans chaux libre, son procédé de préparation et son utilisation dans des liants blancs, EP1306356A1, 2003. <https://patents.google.com/patent/EP1306356A1/fr?q=EP1306356+A1>. (accessed March 5, 2019).
- [29] P.K. Mehta, High iron oxide hydraulic cement, US4036657A, 1977. <https://patents.google.com/patent/US4036657A/en?q=U.S.+Patent+No.+4%2c036%2c657> (accessed March 5, 2019).
- [30] B.W.A. Ost, B. Schiefelbein, J.M. Summerfield, Very high early strength cement, US3860433A, 1975. <https://patents.google.com/patent/US3860433A/en?q=Patent+No.+3%2c860%2c433>. (accessed March 5, 2019).
- [31] R.P. Ulibarri, W.L. Gonzalez, J. Torres, Hydraulic cement with accelerated high strength development, US6149724A, 2000. <https://patents.google.com/patent/US6149724A/en?q=Patent+No.+6%2c149%2c724>. (accessed March 5, 2019).
- [32] J.I. Tobón, C.G. Torres, A.B. Solarte, D.L. Zuluaga, Formulación de cemento en base a sulfatoaluminio con proporción particular de sistemas yelemíticos, WO2016088083A1, 2016. <https://patents.google.com/patent/WO2016088083A1/en?q=WO2016088083+A1>. (accessed March 5, 2019).
- [33] P.E. Halstead, A.E. Moore, The composition and crystallography of an anhydrous calcium aluminosulphate occurring in expanding cement, *J. Appl. Chem.* 12 (1962) 413–417.
- [34] R.K. Mehta, Investigation on the products in the system $\text{C}_4\text{A}_3\bar{\text{S}}-\text{CaSO}_4-\text{CaO}-\text{H}_2\text{O}$, in: *Annu. Meet. Highw. Res. Board Proc.*, 1965: pp. 328–352.
- [35] W. Kurdowski, A. Thiel, On the role of free calcium oxide in expansive cements, *Cem. Concr. Res.* 11 (1981) 29–40. doi:10.1016/0008-8846(81)90006-5.

- [36] M.D. Cohen, C.W. Richards, Effects of the particle sizes of expansive clinker on strength-expansion characteristics of type K expansive cements, *Cem. Concr. Res.* 12 (1982) 717–725. doi:10.1016/0008-8846(82)90034-5.
- [37] I. Teoreanu, M. Muntean, Expansive sulphate aluminate cements, *Cem. Concr. Res.* 13 (1983) 711–720. doi:10.1016/0008-8846(83)90062-5.
- [38] (3) The influence of anhydrite activity upon the hydration of calcium sulfoaluminate cement clinker | Request PDF, ResearchGate. (n.d.). https://www.researchgate.net/publication/256361418_The_influence_of_anhydrite_activity_upon_the_hydration_of_calcium_sulfoaluminate_cement_clinker (accessed March 5, 2019).
- [39] S. Sahu, J. Havlica, V. Tomková, J. Majling, Hydration behaviour of sulfoaluminate belite cement in the presence of various calcium sulphates, *Thermochim. Acta.* 175 (1991) 45–52. doi:10.1016/0040-6031(91)80244-D.
- [40] V. Kasselouri, P. Tsakiridis, Ch. Malami, B. Georgali, C. Alexandridou, A study on the hydration products of a non-expansive sulfoaluminate cement, *Cem. Concr. Res.* 25 (1995) 1726–1736. doi:10.1016/0008-8846(95)00168-9.
- [41] W. Lan, F.P. Glasser, Hydration of calcium sulfoaluminate cements, *Adv. Cem. Res.* 8 (1996) 127–134. doi:10.1680/adcr.1996.8.31.127.
- [42] J. Beretka, M. Marroccoli, N. Sherman, G.L. Valenti, The influence of $C_4A_3\bar{S}$ content and WS ratio on the performance of calcium sulfoaluminate-based cements, *Cem. Concr. Res.* 26 (1996) 1673–1681.
- [43] Sulfoaluminate-belite cement from low-calcium fly ash and sulfur-rich and other industrial by-products - ScienceDirect, (n.d.). <https://www.sciencedirect.com.ezproxy.unilim.fr/science/article/pii/S0008884699000721> (accessed March 6, 2019).
- [44] V. Živica, Properties of blended sulfoaluminate belite cement, *Constr. Build. Mater.* 14 (2000) 433–437. doi:10.1016/S0950-0618(00)00050-7.
- [45] C.D. Popescu, M. Muntean, J.H. Sharp, Industrial trial production of low energy belite cement, *Cem. Concr. Compos.* 25 (2003) 689–693. doi:10.1016/S0958-9465(02)00097-5.
- [46] E. Gartner, G. Li, Clinker sulfoalumineux a haute teneur en belite, procede de fabrication d'un tel clinker et son utilisation pour la preparation de liants hydrauliques, WO2006018569A2, 2006. <https://patents.google.com/patent/WO2006018569A2/en?q=high+belite+sulfoaluminate+clinker:fabrication+process+and+binder+preparation> (accessed March 6, 2019).
- [47] G. Bernardo, A. Telesca, G.L. Valenti, A porosimetric study of calcium sulfoaluminate cement pastes cured at early ages, *Cem. Concr. Res.* 36 (2006) 1042–1047. doi:10.1016/j.cemconres.2006.02.014.
- [48] Q. Zhou, N.B. Milestone, M. Hayes, An alternative to Portland cement for waste encapsulation—the calcium sulfoaluminate cement system, *J. Hazard. Mater.* 136 (2006) 120–129.
- [49] G.S. Li, G. Walenta, E.M. Gartner, Formation and hydration of low-CO₂ cements based on belite, calcium sulfoaluminate and calcium aluminoferrite, *Proc. 12th ICCM Montr. Can.* (2007) 9–12.
- [50] I. Janotka, L. Krajci, S.C. Mojumdar, Performance of sulfoaluminate-belite cement with high $C\sim 4A\sim 3S$ contents, *Ceram. Silik.* 51 (2007) 74.
- [51] M. Alesiani, I. Pirazzoli, B. Maraviglia, F. Canonico, NMR and XRD Study on Calcium Sulfoaluminate Cement, *Appl. Magn. Reson.* 35 (2008) 33–41. doi:10.1007/s00723-008-0152-2.
- [52] C. Cau Dit Coumes, S. Courtois, S. Peysson, J. Ambroise, J. Pera, Calcium sulfoaluminate cement blended with OPC: A potential binder to encapsulate low-level radioactive slurries of complex chemistry, *Cem. Concr. Res.* 39 (2009) 740–747. doi:10.1016/j.cemconres.2009.05.016.

-
- [53] G. Ellis, L. Guanshu, High-Belite-Containing Sulphoaluminous Clinker, Method for the Production and the Use Thereof for Preparing Hydraulic Binders, MY142505 (A), 2010. https://worldwide.espacenet.com/publicationDetails/biblio?FT=D&date=20101130&DB=EPODOC&locale=fr_EP&CC=MY&NR=142505A&KC=A&ND=4 (accessed March 4, 2019).
- [54] L. Pelletier, F. Winnefeld, B. Lothenbach, The ternary system Portland cement–calcium sulfoaluminate clinker–anhydrite: hydration mechanism and mortar properties, *Cem. Concr. Compos.* 32 (2010) 497–507.
- [55] Hydration mechanism of cements based on low-CO₂ clinkers containing belite, ye’elinite and calcium aluminoferrite, (n.d.). <http://ori.univ-lille1.fr/notice/view/univ-lille1-ori-17656> (accessed March 6, 2019).
- [56] S. Berger, C.C.D. Coumes, P. Le Bescop, D. Damidot, Influence of a thermal cycle at early age on the hydration of calcium sulfoaluminate cements with variable gypsum contents, *Cem. Concr. Res.* 41 (2011) 149–160. doi:10.1016/j.cemconres.2010.10.001.
- [57] Influence of the calcium sulphate source on the hydration mechanism of Portland cement–calcium sulfoaluminate clinker–calcium sulphate binders - ScienceDirect, (n.d.). <https://www.sciencedirect-com.ezproxy.unilim.fr/science/article/pii/S0958946511000473> (accessed March 6, 2019).
- [58] I.A. Chen, M.C.G. Juenger, Synthesis and hydration of calcium sulfoaluminate-belite cements with varied phase compositions, *J. Mater. Sci.* 46 (2011) 2568–2577. doi:10.1007/s10853-010-5109-9.
- [59] S. Berger, C. Cau Dit Coumes, J.-B. Champenois, T. Douillard, P. Le Bescop, G. Aouad, D. Damidot, Stabilization of ZnCl₂-containing wastes using calcium sulfoaluminate cement: Leaching behaviour of the solidified waste form, mechanisms of zinc retention, *J. Hazard. Mater.* 194 (2011) 268–276. doi:10.1016/j.jhazmat.2011.07.102.
- [60] Gartner: Hydration of a Belite-Calcium Sulfoaluminate-Ferrite Cement - Google Scholar, (n.d.). https://scholar.google.com/scholar_lookup?title=Hydration%20of%20a%20belite-calcium%20sulfoaluminate-ferrite%20cement%3A%20AetherTM&publication_year=2011&author=V.%20Morin&author=G.%20Walenta&author=E.%20Gartner&author=P.%20Termkhajornkit&author=I.%20Baco&author=J.%20Casabonne (accessed March 6, 2019).
- [61] N. Sun, W. Chang, L. Wang, J. Zhang, M. Pei, Effects of the Chemical Structure of Polycarboxy-Ether Superplasticizer on Its Performance in Sulfoaluminate Cement, *J. Dispers. Sci. Technol.* 32 (2011) 795–798. doi:10.1080/01932691.2010.488132.
- [62] I.A. Chen, C.W. Hargis, M.C.G. Juenger, Understanding expansion in calcium sulfoaluminate–belite cements, *Cem. Concr. Res.* 42 (2012) 51–60. doi:10.1016/j.cemconres.2011.07.010.
- [63] G. Álvarez-Pinazo, A. Cuesta, M. García-Maté, I. Santacruz, E.R. Losilla, A.G. De la Torre, L. León-Reina, M.A. Aranda, Rietveld quantitative phase analysis of Yeelinite-containing cements, *Cem. Concr. Res.* 42 (2012) 960–971.
- [64] B. Ma, X. Li, Y. Mao, X. Shen, Synthesis and characterization of high belite sulfoaluminate cement through rich alumina fly ash and desulfurization gypsum, *Ceram Silik.* 57 (2013) 7–13.
- [65] M. García-Maté, A.G. De la Torre, L. León-Reina, M.A.G. Aranda, I. Santacruz, Hydration studies of calcium sulfoaluminate cements blended with fly ash, *Cem. Concr. Res.* 54 (2013) 12–20. doi:10.1016/j.cemconres.2013.07.010.
- [66] F. Bullerjahn, D. Schmitt, M. Ben Haha, Effect of raw mix design and of clinkering process on the formation and mineralogical composition of (ternesite) belite calcium sulfoaluminate ferrite clinker, *Cem. Concr. Res.* 59 (2014) 87–95. doi:10.1016/j.cemconres.2014.02.004.

- [67]F. Bullerjahn, M. Zajac, M. Ben Haha, CSA raw mix design: effect on clinker formation and reactivity, *Mater. Struct.* 48 (2015) 3895–3911. doi:10.1617/s11527-014-0451-z.
- [68]R. Trauchessec, J.-M. Mechling, A. Lecomte, A. Roux, B. Le Rolland, Hydration of ordinary Portland cement and calcium sulfoaluminate cement blends, *Cem. Concr. Compos.* 56 (2015) 106–114. doi:10.1016/j.cemconcomp.2014.11.005.
- [69]M. Zajac, J. Skocek, F. Bullerjahn, M. Ben Haha, Effect of retarders on the early hydration of calcium-sulpho-aluminate (CSA) type cements, *Cem. Concr. Res.* 84 (2016) 62–75. doi:10.1016/j.cemconres.2016.02.014.
- [70]E.A. El-Alfi, R.A. Gado, Preparation of calcium sulfoaluminate-belite cement from marble sludge waste, *Constr. Build. Mater.* 113 (2016) 764–772. doi:10.1016/j.conbuildmat.2016.03.103.
- [71]W. Dienemann, K. Wortmann, 3d-druck von bauteilen und gebäuden mit bct-zement, WO2017050421A1, 2017.
<https://patents.google.com/patent/WO2017050421A1/fr?q=calcium+sulfoaluminate+cement> (accessed March 7, 2019).
- [72]A. Rungchet, C.S. Poon, P. Chindapasirt, K. Pimraksa, Synthesis of low-temperature calcium sulfoaluminate-belite cements from industrial wastes and their hydration: Comparative studies between lignite fly ash and bottom ash, *Cem. Concr. Compos.* 83 (2017) 10–19. doi:10.1016/j.cemconcomp.2017.06.013.
- [73]N. Khalil, G. Aouad, K. El Cheikh, S. Rémond, Use of calcium sulfoaluminate cements for setting control of 3D-printing mortars, *Constr. Build. Mater.* 157 (2017) 382–391. doi:10.1016/j.conbuildmat.2017.09.109.
- [74]P. Julphunthong, Synthesizing of calcium sulfoaluminate-belite (CSAB) cements from industrial waste materials, *Mater. Today Proc.* 5 (2018) 14933–14938. doi:10.1016/j.matpr.2018.04.033.
- [75]C.W. Hargis, B. Lothenbach, C.J. Müller, F. Winnefeld, Further insights into calcium sulfoaluminate cement expansion, *Adv. Cem. Res.* (2018) 1–18. doi:10.1680/jadcr.18.00124.
- [76]K.B. Addi, A. Diouri, N. Khachani, A. Boukhari, Mineralogical stabilization of Ternosite in Belite Sulfo-Aluminate Clinker elaborated from limestone, shale and phosphogypsum, *MATEC Web Conf.* 149 (2018) 01073. doi:10.1051/mateconf/201814901073.
- [77](2) (PDF) Progress in the development of Ternocem – a belite ye’elinite ferrite cement, ResearchGate. (n.d.).
https://www.researchgate.net/publication/327884384_Progress_in_the_development_of_Ternocem_-_a_belite_yeelinite_ferrite_cement (accessed March 10, 2019).
- [78]F. Bullerjahn, J. Skocek, M. Ben Haha, K. Scrivener, Chemical shrinkage of ye’elinite with and without gypsum addition, *Constr. Build. Mater.* 200 (2019) 770–780. doi:10.1016/j.conbuildmat.2018.12.170.
- [79]i.tech ALI PRE GREEN, (n.d.). <https://www.italcementi.it/it/itech-ALI-PRE-GREEN> (accessed March 6, 2019).
- [80]BluCem FSC, Bluey Technol. (n.d.). <http://www.bluey.com.au/products/blucem-fsc> (accessed March 10, 2019).
- [81]Calumex BeliCem (C.S.A) | Caltra Nederland B.V., (n.d.). <https://caltra.com/product/calumex-belicem/> (accessed March 10, 2019).
- [82]B. Unicem, The hydraulic binder based on calcium sulfoaluminate clinker, (n.d.) 2.
- [83]F. Bullerjahn, E. Boehm-Courjault, M. Zajac, M. Ben Haha, K. Scrivener, Hydration reactions and stages of clinker composed mainly of stoichiometric ye’elinite, *Cem. Concr. Res.* 116 (2019) 120–133. doi:10.1016/j.cemconres.2018.10.023.

-
- [84] Effect of crystal/amorphous ratio on mechanical properties in a $C_4A_3\bar{S}$ - C_2S hydration system with or without gypsum addition - ScienceDirect, (n.d.). <https://www.sciencedirect.com/science/article/abs/pii/S0950061819304775> (accessed March 9, 2019).
- [85] S. Gross, Occurrence of ye'elimite and ellestadite in an unusual cobble from the "pseudo-conglomerate" of the Hatrurim Basin, Israel, *Geol. Surv. Isr. Curr. Res.* 1983 (1984) 1–4.
- [86] Structural Investigation of Ye'elimite, $Ca_4Al_6O_{12}SO_4$, by ^{27}Al MAS and MQMAS NMR at Different Magnetic Fields - *The Journal of Physical Chemistry C* (ACS Publications), (n.d.). <https://pubs.acs.org/doi/10.1021/acs.jpcc.8b02497> (accessed March 8, 2019).
- [87] A. Cuesta, A.G. De la Torre, E.R. Losilla, V.K. Peterson, P. Rejmak, A. Ayuela, C. Frontera, M.A. Aranda, Structure, atomistic simulations, and phase transition of stoichiometric yeelimite, *Chem. Mater.* 25 (2013) 1680–1687.
- [88] S. Liu, X. Lu, J. Chen, S. Wang, Z. Ye, X. Cheng, Modulation of two ye'elimite phases via Ga^{3+} cation substitution, *CrystEngComm.* 20 (2018) 3755–3764. doi:10.1039/C8CE00405F.
- [89] B. Touzo, K.L. Scrivener, F.P. Glasser, Phase compositions and equilibria in the $CaO-Al_2O_3-Fe_2O_3-SO_3$ system, for assemblages containing ye'elimite and ferrite $Ca_2(Al,Fe)O_5$, *Cem. Concr. Res.* 54 (2013) 77–86.
- [90] A. Cuesta, A.G. De la Torre, E.R. Losilla, I. Santacruz, M.A. Aranda, Pseudocubic crystal structure and phase transition in doped ye'elimite, *Cryst. Growth Des.* 14 (2014) 5158–5163.
- [91] D. Kurokawa, S. Takeda, M. Colas, T. Asaka, P. Thomas, K. Fukuda, Phase transformation of $Ca_4[Al_6O_{12}]SO_4$ and its disordered crystal structure at 1073K, *J. Solid State Chem.* 215 (2014) 265–270. doi:10.1016/j.jssc.2014.03.040.
- [92] H. Banno, S. Ichikawa, S. Takeda, T. Asaka, M. Colas, P. Thomas, K. Fukuda, Crystal structures and polymorphism of $Sr_4[Al_6O_{12}]SO_4$, *J. Ceram. Soc. Jpn.* 125 (2017) 364–370. doi:10.2109/jcersj2.17008.
- [93] R. Kondo, The synthesis and crystallography of a group of new compounds belonging to the hauyne type structure, *J. Ceram. Soc. Jpn.* 73 (1965) 1–8.
- [94] H. Saalfeld, W. Depmeier, Silicon-Free Compounds with Sodalite Structure, *Krist. Tech.* 7 (1972) 229–233.
- [95] M.E. Brenchley, M.T. Weller, Synthesis and structure of sulfide aluminate sodalites, *J. Mater. Chem.* 2 (1992) 1003–1005.
- [96] I. Krstanović, A. Radaković, L. Karanović, X-Ray Powder Data for $Ca_4Al_6O_{12}SO_4$, *Powder Diffr.* 7 (1992) 47–48. doi:10.1017/S0885715600016092.
- [97] N.J. Calos, C.H.L. Kennard, A.K. Whittaker, R.L. Davis, Structure of calcium aluminate sulfate $Ca_4Al_6O_{16}S$, *J. Solid State Chem.* 119 (1995) 1–7. doi:10.1016/0022-4596(95)80002-7.
- [98] Z. Peixing, C. Yimin, S. Liping, Z. Guanying, H. Wenmei, W. Jianguo, The Crystal Structure of $C_4A_3\bar{S}$, New Delhi, *Proceedings of 9th ICCS*, 3, 1992, pp. 201–208. (n.d.).
- [99] K. Ikeda, K. Kishimoto, H. Shima, Structure refinement of calcium sulfoaluminate, $C_4A_3\bar{S}$ with emphasis to oxygen deficiency, *Cem. Concr. Res.* 26 (1996) 743–748.
- [100] J.-T. Song, J.F. Young, Direct synthesis and hydration of calcium aluminosulfate ($Ca_4Al_6O_{16}S$), *J. Am. Ceram. Soc.* 85 (2002) 535–539.
- [101] F. Hanic, J. Havlica, I. Kapralik, V. Ambruz, L. Galikova, O. Urbnova, Crystal Chemistry and Thermodynamics of the Sulphate Compounds $C_4A_3\sigma$ and $C_5S_2\bar{S}\sigma$, *Trans. J. Br. Ceram. Soc.* 85 (1986) 52–57.
-

-
- [102] M.M. Ali, S. Gopal, S.K. Handoo, Studies on the formation kinetics of calcium sulphoaluminate, *Cem. Concr. Res.* 24 (1994) 715–720.
- [103] O. Andac, F.P. Glasser, Polymorphism of calcium sulphoaluminate ($\text{Ca}_4\text{Al}_6\text{O}_{16}\text{SO}_3$) and its solid solutions, *Adv. Cem. Res.* 6 (1994) 57–60.
- [104] F. Puertas, M.B. Varela, S.G. Molina, Kinetics of the thermal decomposition of $\text{C}_4\text{A}_3\text{S}$ in air, *Cem. Concr. Res.* 25 (1995) 572–580.
- [105] E. Gartner, T. Sui, Alternative cement clinkers, *Cem. Concr. Res.* (2017). doi:10.1016/j.cemconres.2017.02.002.
- [106] F. Winnefeld, S. Barlag, Calorimetric and thermogravimetric study on the influence of calcium sulfate on the hydration of ye'elimite, *J. Therm. Anal. Calorim.* 101 (2009) 949–957.
- [107] F. Winnefeld, B. Lothenbach, Hydration of calcium sulfoaluminate cements—experimental findings and thermodynamic modelling, *Cem. Concr. Res.* 40 (2010) 1239–1247.
- [108] N. Chitvoranund, B. Lothenbach, F. Winnefeld, J. Skibsted, K. Scrivener, Comparison of different preparation methods for ye'elimite clinker synthesis, *Calcium Sulfoaluminate Cem.* (2018) 22.
- [109] C.W. Hargis, A.P. Kirchheim, P.J. Monteiro, E.M. Gartner, Early age hydration of calcium sulfoaluminate (synthetic ye'elimite, $\text{C}_4\text{A}_3\bar{\text{S}}$) in the presence of gypsum and varying amounts of calcium hydroxide, *Cem. Concr. Res.* 48 (2013) 105–115.
- [110] A. Cuesta, A.G. De la Torre, E.R. Losilla, V.K. Peterson, P. Rejmak, A. Ayuela, C. Frontera, M.A. Aranda, Structure, atomistic simulations, and phase transition of stoichiometric yeelimite, *Chem. Mater.* 25 (2013) 1680–1687.
- [111] A. Cuesta, A.G. De la Torre, E.R. Losilla, I. Santacruz, M.A. Aranda, Pseudocubic crystal structure and phase transition in doped ye'elimite, *Cryst. Growth Des.* 14 (2014) 5158–5163.
- [112] Y. El Khessaimi, Y. El Hafiane, A. Smith, Ye'elimite synthesis by chemical routes, *J. Eur. Ceram. Soc.* (2018). doi:10.1016/j.jeurceramsoc.2018.10.025.
- [113] X. Li, Y. Zhang, X. Shen, Q. Wang, Z. Pan, Kinetics of calcium sulfoaluminate formation from tricalcium aluminate, calcium sulfate and calcium oxide, *Cem. Concr. Res.* 55 (2014) 79–87.
- [114] S. Iftekhhar, J. Grins, G. Svensson, J. Löff, T. Jarmar, G.A. Botton, C.M. Andrei, H. akan Engqvist, Phase formation of CaAl_2O_4 from CaCO_3 – Al_2O_3 powder mixtures, *J. Eur. Ceram. Soc.* 28 (2008) 747–756.
- [115] A.N. Scian, J.P. Lopez, E. Pereira, High alumina cements. Study of $\text{CaO} \cdot \text{Al}_2\text{O}_3$ formation. I. Stoichiometric mechanism, *Cem. Concr. Res.* 17 (1987) 198–204.
- [116] B. Viswanath, N. Ravishankar, Interfacial reactions in hydroxyapatite/alumina nanocomposites, *Scr. Mater.* 55 (2006) 863–866.
- [117] E. de Bilbao, M. Dombrowski, H. Pilliere, J. Poirier, Time-resolved high-temperature X-ray diffraction for studying the kinetics of corrosion of high-alumina refractory by molten oxides, *Corros. Sci.* 139 (2018) 346–354. doi:10.1016/j.corsci.2018.05.003.
- [118] J.R. Mercury, A.H. De Aza, P. Pena, Synthesis of CaAl_2O_4 from powders: Particle size effect, *J. Eur. Ceram. Soc.* 25 (2005) 3269–3279.
- [119] A.N. Scian, J.P. López, E. Pereira, High alumina cements. Study of $\text{CaO} \cdot \text{Al}_2\text{O}_3$ formation II. Kinetics, *Cem. Concr. Res.* 17 (1987) 525–531.
- [120] B.M. Mohamed, J.H. Sharp, Kinetics and mechanism of formation of tricalcium aluminate, $\text{Ca}_3\text{Al}_2\text{O}_6$, *Thermochim. Acta.* 388 (2002) 105–114.

-
- [121] F. Hanic, I. Kaprálik, A. Gabrisová, Mechanism of hydration reactions in the system $C_4A_3\bar{S}$ -CS-CaO-H₂O referred to hydration of sulphoaluminate cements, *Cem. Concr. Res.* 19 (1989) 671–682.
- [122] J.-T. Song, J.F. Young, Direct synthesis and hydration of calcium aluminosulfate ($Ca_4Al_6O_{16}S$), *J. Am. Ceram. Soc.* 85 (2002) 535–539.
- [123] A. Cuesta, G. Álvarez-Pinazo, S.G. Sanfélix, I. Peral, M.A. Aranda, A.G. De la Torre, Hydration mechanisms of two polymorphs of synthetic ye'elimite, *Cem. Concr. Res.* 63 (2014) 127–136.
- [124] B. Raab, H. Pöllmann, 3. Synthesis of highly reactive pure cement phases, in: H. Pöllmann (Ed.), *Cem. Mater., De Gruyter, Berlin, Boston, 2017*: pp. 61–102. doi:10.1515/9783110473728-004.
- [125] Song Jong-Taek, Young J. Francis, Direct Synthesis and Hydration of Calcium Aluminosulfate ($Ca_4Al_6O_{16}S$), *J. Am. Ceram. Soc.* 85 (2004) 535–539. doi:10.1111/j.1151-2916.2002.tb00129.x.
- [126] S.-J. Lee, W.M. Kriven, Synthesis and hydration study of Portland cement components prepared by the organic steric entrapment method, *Mater. Struct.* 38 (2005) 87–92.
- [127] B. Raab, H. Pöllmann, Synthesis of pure cement phases by different synthesis methods, in: *Int. Conf. Calcium Aluminate Cem. Fr., 2008*.
- [128] J.J. Thomas, S. Ghazizadeh, E. Masoero, Kinetic mechanisms and activation energies for hydration of standard and highly reactive forms of β -dicalcium silicate (C_2S), *Cem. Concr. Res.* 100 (2017) 322–328.
- [129] S.-H. Hong, J.F. Young, Hydration kinetics and phase stability of dicalcium silicate synthesized by the Pechini process, *J. Am. Ceram. Soc.* 82 (1999) 1681–1686.
- [130] Y.-M. Kim, S.-H. Hong, Influence of minor ions on the stability and hydration rates of β -dicalcium silicate, *J. Am. Ceram. Soc.* 87 (2004) 900–905.
- [131] I. Nettleship, J.L. Shull, W.M. Kriven, Chemical preparation and phase stability of Ca_2SiO_4 and Sr_2SiO_4 powders, *J. Eur. Ceram. Soc.* 11 (1993) 291–298. doi:10.1016/0955-2219(93)90028-P.
- [132] A. Zapata, P. Bosch, Low temperature preparation of belitic cement clinker, *J. Eur. Ceram. Soc.* 29 (2009) 1879–1885.
- [133] D.A. Fumo, M.R. Morelli, A.M. Segadaes, Combustion synthesis of calcium aluminates, *Mater. Res. Bull.* 31 (1996) 1243–1255.
- [134] Tas A. Cüneyt, Chemical Preparation of the Binary Compounds in the Calcia-Alumina System by Self-Propagating Combustion Synthesis, *J. Am. Ceram. Soc.* 81 (2005) 2853–2863. doi:10.1111/j.1151-2916.1998.tb02706.x.
- [135] H.C. Yi, J.Y. Guigné, J.J. Moore, F.D. Schowengerdt, L.A. Robinson, A.R. Manerbino, Preparation of calcium aluminate matrix composites by combustion synthesis, *J. Mater. Sci.* 37 (2002) 4537–4543. doi:10.1023/A:1020671626797.
- [136] Z. He, W. Liang, L. Wang, J. Wang, Synthesis of C_3S by sol-gel technique and its features, *J. Wuhan Univ. Technol.-Mater Sci Ed.* 25 (2010) 138–141.
- [137] Gülğün Mehmet A., Popoola Oludele O., Kriven Waltraud M., Chemical Synthesis and Characterization of Calcium Aluminate Powders, *J. Am. Ceram. Soc.* 77 (2005) 531–539. doi:10.1111/j.1151-2916.1994.tb07026.x.
- [138] J.W. Bullard, H.M. Jennings, R.A. Livingston, A. Nonat, G.W. Scherer, J.S. Schweitzer, K.L. Scrivener, J.J. Thomas, Mechanisms of cement hydration, *Cem. Concr. Res.* 41 (2011) 1208–1223. doi:10.1016/j.cemconres.2010.09.011.
- [139] M.M. Costoya Fernández, Effect of particle size on the hydration kinetics and microstructural development of tricalcium silicate, (2008).

-
- [140] P.K. Mehta, Mechanism of expansion associated with ettringite formation, *Cem. Concr. Res.* 3 (1973) 1–6.
- [141] K. Ogawa, D.M. Roy, $C_4A_3\bar{S}$ hydration ettringite formation, and its expansion mechanism: I. expansion; Ettringite stability, *Cem. Concr. Res.* 11 (1981) 741–750.
- [142] H. Le Chatelier, *Recherches expérimentales sur la constitution des mortiers hydrauliques*, Dunod, 1904.
- [143] R. Trauchessec, J.-M. Mechling, A. Lecomte, A. Roux, B. Le Rolland, Impact of anhydrite proportion in a calcium sulfoaluminate cement and Portland cement blend, *Adv. Cem. Res.* 26 (2014) 325–333.
- [144] R. Trauchessec, J.-M. Mechling, A. Lecomte, A. Roux, B. Le Rolland, Hydration of ordinary Portland cement and calcium sulfoaluminate cement blends, *Cem. Concr. Compos.* 56 (2015) 106–114.
- [145] M. Zajac, J. Skocek, F. Bullerjahn, B. Lothenbach, K. Scrivener, M.B. Haha, Early hydration of ye’elimite: Insights from thermodynamic modelling, *Cem. Concr. Res.* 120 (2019) 152–163.
- [146] A. Cuesta, G. Álvarez-Pinazo, S.G. Sanfélix, I. Peral, M.A. Aranda, A.G. De la Torre, Hydration mechanisms of two polymorphs of synthetic ye’elimite, *Cem. Concr. Res.* 63 (2014) 127–136.
- [147] D. Jansen, A. Spies, J. Neubauer, D. Ectors, F. Goetz-Neunhoeffler, Studies on the early hydration of two modifications of ye’elimite with gypsum, *Cem. Concr. Res.* 91 (2017) 106–116.
- [148] F. Bullerjahn, M. Zajac, M.B. Haha, K.L. Scrivener, Factors influencing the hydration kinetics of ye’elimite; effect of mayenite, *Cem. Concr. Res.* 116 (2019) 113–119.
- [149] C.W. Hargis, A. Telesca, P.J.M. Monteiro, Calcium sulfoaluminate (Ye’elimite) hydration in the presence of gypsum, calcite, and vaterite, *Cem. Concr. Res.* 65 (2014) 15–20. doi:10.1016/j.cemconres.2014.07.004.
- [150] Studies on the early hydration of two modifications of ye’elimite with gypsum - ScienceDirect, (n.d.). <https://www.sciencedirect-com.ezproxy.unilim.fr/science/article/pii/S0008884615302246> (accessed March 11, 2019).
- [151] L. Nicoleau, A. Nonat, D. Perrey, The di- and tricalcium silicate dissolutions, *Cem. Concr. Res.* 47 (2013) 14–30. doi:10.1016/j.cemconres.2013.01.017.
- [152] P. Juilland, E. Gallucci, R. Flatt, K. Scrivener, Dissolution theory applied to the induction period in alite hydration, *Cem. Concr. Res.* 40 (2010) 831–844. doi:10.1016/j.cemconres.2010.01.012.
- [153] A.C. Lasaga, *Kinetic theory in the earth sciences*, Princeton university press, 2014.
- [154] A.C. Lasaga, A. Luttge, Variation of crystal dissolution rate based on a dissolution stepwave model, *Science*. 291 (2001) 2400–2404.
- [155] T.E. Burch, K.L. Nagy, A.C. Lasaga, Free energy dependence of albite dissolution kinetics at 80°C and pH 8.8, *Chem. Geol.* 105 (1993) 137–162. doi:10.1016/0009-2541(93)90123-Z.
- [156] L. Nicoleau, A. Nonat, A new view on the kinetics of tricalcium silicate hydration, *Cem. Concr. Res.* 86 (2016) 1–11.
- [157] S.L. Brantley, S.R. Crane, D.A. Crerar, R. Hellmann, R. Stallard, Dissolution at dislocation etch pits in quartz, *Geochim. Cosmochim. Acta.* 50 (1986) 2349–2361. doi:10.1016/0016-7037(86)90087-6.
- [158] J.P. Icenhower, B.P. McGrail, W.J. Shaw, E.M. Pierce, P. Nachimuthu, D.K. Shuh, E.A. Rodriguez, J.L. Steele, Experimentally determined dissolution kinetics of Na-rich borosilicate glass at far from equilibrium conditions: implications for transition state theory, *Geochim. Cosmochim. Acta.* 72 (2008) 2767–2788.

-
- [159] J.A. Davis, K.F. Hayes, Geochemical processes at mineral surfaces: an overview, in: *Geochem. Process. Miner. Surf.*, ACS Publications, 1986: pp. 2–19.
- [160] H. Eyring, The activated complex and the absolute rate of chemical reactions., *Chem. Rev.* 17 (1935) 65–77.
- [161] L. Lafferrere, Nucléation et transitions de phases en chimie pharmaceutique, PhD Thesis, Université Paul Cézanne-Aix-Marseille III, 2002.
- [162] H. Pöllmann, *Cementitious Materials: Composition, Properties, Application*, Walter de Gruyter GmbH & Co KG, 2017.
- [163] F. Sajedi, H.A. Razak, Effects of curing regimes and cement fineness on the compressive strength of ordinary Portland cement mortars, *Constr. Build. Mater.* 25 (2011) 2036–2045.
- [164] E.H. Kadri, S. Aggoun, G. De Schutter, K. Ezziane, Combined effect of chemical nature and fineness of mineral powders on Portland cement hydration, *Mater. Struct.* 43 (2010) 665–673.
- [165] L.E. Burris, K.E. Kurtis, Influence of set retarding admixtures on calcium sulfoaluminate cement hydration and property development, *Cem. Concr. Res.* 104 (2018) 105–113.
- [166] J. Tinnea, J.F. Young, Influence of Citric Acid on Reactions in the System $3\text{CaO}\cdot\text{Al}_2\text{O}_3\text{-CaSO}_4\cdot 2\text{H}_2\text{O-CaO-H}_2\text{O}$, *J. Am. Ceram. Soc.* 60 (1977) 387–389. doi:10.1111/j.1151-2916.1977.tb15518.x.
- [167] F. Winnefeld, S. Klemm, Influence of citric acid on the hydration kinetics of calcium sulfoaluminate cement, in: *Submitt. First Int. Conf. Sulphoaluminate Cem. Mater. Eng. Technol. Wuhan China, 2013*.
- [168] G. Zhang, G. Li, Y. Li, Effects of superplasticizers and retarders on the fluidity and strength of sulphoaluminate cement, *Constr. Build. Mater.* 126 (2016) 44–54.
- [169] A.K. Chatterjee, X-Ray Diffraction. IN RAMACHANDRAN, VS & BEAUDOIN, JJ (Eds.) *Handbook of Analytical Techniques in Concrete Science and Technology*, Noyes Publications, 2001.
- [170] M.A.G. Aranda, A.G. De la Torre, L. León-Reina, Rietveld quantitative phase analysis of cements, (2019).
- [171] W. Hörkner, Hk. Müller-Buschbaum, Zur kristallstruktur von CaAl_2O_4 , *J. Inorg. Nucl. Chem.* 38 (1976) 983–984. doi:10.1016/0022-1902(76)80011-5.
- [172] V.I. Ponomarev, D.M. Kheiker, N.V. Belov, Crystal structure of calcium dialuminate, CA_2 , *Sov. Phys. Crystallogr. USSR.* 15 (1971) 995–+.
- [173] E.N. Maslen, V.A. Streltsov, N.R. Streltsova, N. Ishizawa, Y. Satow, Synchrotron X-ray study of the electron density in $\alpha\text{-Al}_2\text{O}_3$, *Acta Crystallogr. B.* 49 (1993) 973–980.
- [174] D. Grier, G. McCarthy, North Dakota State University, Fargo, North Dakota, USA, ICDD Grant-in-Aid 1991, *Powder Diffr. File Int. Cent. Diffr. Data.* (1994).
- [175] G.C.H. Cheng, J. Zussman, The crystal structure of anhydrite (CaSO_4), *Acta Crystallogr.* 16 (1963) 767–769.
- [176] H. Boysen, M. Lerch, A. Stys, A. Senyshyn, Structure and oxygen mobility in mayenite ($\text{Ca}_{12}\text{Al}_4\text{O}_{33}$): a high-temperature neutron powder diffraction study, *Acta Crystallogr. B.* 63 (2007) 675–682.
- [177] F.A. Steele, W.P. Davey, The crystal structure of tricalcium aluminate, *J. Am. Chem. Soc.* 51 (1929) 2283–2293.
- [178] F. Goetz-Neunhoeffler, J. Neubauer, Refined ettringite ($\text{Ca}_6\text{Al}_2(\text{SO}_4)_3(\text{OH})_{12}\cdot 26\text{H}_2\text{O}$) structure for quantitative X-ray diffraction analysis, *Powder Diffr.* 21 (2006) 4–11.

-
- [179] R. Allmann, Refinement of the hybrid layer structure $[\text{Ca}_2\text{Al}(\text{OH})_6]^+ [\frac{1}{2}\text{SO}_4 \cdot 3\text{H}_2\text{O}]^-$, *Neues Jahrb. Für Mineral. Monatshefte*. 1977 (1977) 136–143.
- [180] H. Saalfeld, M. Wedde, Refinement of the crystal structure of gibbsite, $\text{Al}(\text{OH})_3$, *Z. Für Krist.-Cryst. Mater.* 139 (1974) 129–135.
- [181] G. Angeles, M.-G. López-Olmo, C. Alvarez-Rua, S. García-Granda, M.A. Aranda, Structure and microstructure of gypsum and its relevance to Rietveld quantitative phase analyses, *Powder Diffr.* 19 (2004) 240–246.
- [182] B.H. Toby, R factors in Rietveld analysis: how good is good enough?, *Powder Diffr.* 21 (2006) 67–70.
- [183] R. Trauchessec, *Mélanges de ciments sulfoalumineux et Portland*, PhD Thesis, Université de Lorraine, 2013.
- [184] S. Materazzi, S. Vecchio, S.D.A. Curtis, Thermal analysis and health safety, *J. Therm. Anal. Calorim.* 112 (2013) 529–533.
- [185] G. Eshel, G.J. Levy, U. Mingelgrin, M.J. Singer, Critical evaluation of the use of laser diffraction for particle-size distribution analysis, *Soil Sci. Soc. Am. J.* 68 (2004) 736–743.
- [186] R. Fisker, J.M. Carstensen, M.F. Hansen, F. Bødker, S. Mørup, Estimation of nanoparticle size distributions by image analysis, *J. Nanoparticle Res.* 2 (2000) 267–277.
- [187] G. Fagerlund, Determination of specific surface by the BET method, *Matér. Constr.* 6 (1973) 239–245.
- [188] Y. Liu, F. Sommer, E.J. Mittemeijer, Nature and kinetics of the massive austenite-ferrite phase transformations in steels, in: *Phase Transform. Steels*, Elsevier, 2012: pp. 311–381.
- [189] V.S. Ramachandran, J.J. Beaudoin, *Handbook of analytical techniques in concrete science and technology: principles, techniques and applications*, Elsevier, 2000.
- [190] H. Paqueton, J. Ruste, *Microscopie électronique à balayage: images, applications et développements*, *Tech. Ing. Anal. Caractér.* (2006).
- [191] F. Visconti, J.M. De Paz, J.L. Rubio, An empirical equation to calculate soil solution electrical conductivity at 25° C from major ion concentrations, *Eur. J. Soil Sci.* 61 (2010) 980–993.
- [192] Q. Chang, *Colloid and interface chemistry for water quality control*, Academic Press, 2016.
- [193] R.J. Hunter, *Zeta potential in colloid science: principles and applications*, Academic press, 2013.
- [194] R.N. Goldberg, N. Kishore, R.M. Lennen, Thermodynamic quantities for the ionization reactions of buffers, *J. Phys. Chem. Ref. Data.* 31 (2002) 231–370.
- [195] M.P. Pechini, Method of preparing lead and alkaline earth titanates and niobates and coating method using the same to form a capacitor, 1967.
- [196] T. Barbier, *Synthesis and characterization of new materials with colossal permittivity*, PhD Thesis, Tours, 2012.
- [197] X. Li, V. Agarwal, M. Liu, W.S. Rees, Investigation of the mechanism of sol-gel formation in the $\text{Sr}(\text{NO}_3)_2$ /citric acid/ethylene glycol system by solution state ^{87}Sr nuclear magnetic resonance spectroscopy, *J. Mater. Res.* 15 (2000) 2393–2399.
- [198] S.-J. Lee, E.A. Benson, W.M. Kriven, Preparation of Portland cement components by poly (vinyl alcohol) solution polymerization, *J. Am. Ceram. Soc.* 82 (1999) 2049–2055.
- [199] K.H. Wu, T.H. Ting, M.C. Li, W.D. Ho, Sol-gel auto-combustion synthesis of SiO_2 -doped NiZn ferrite by using various fuels, *J. Magn. Mater.* 298 (2006) 25–32.

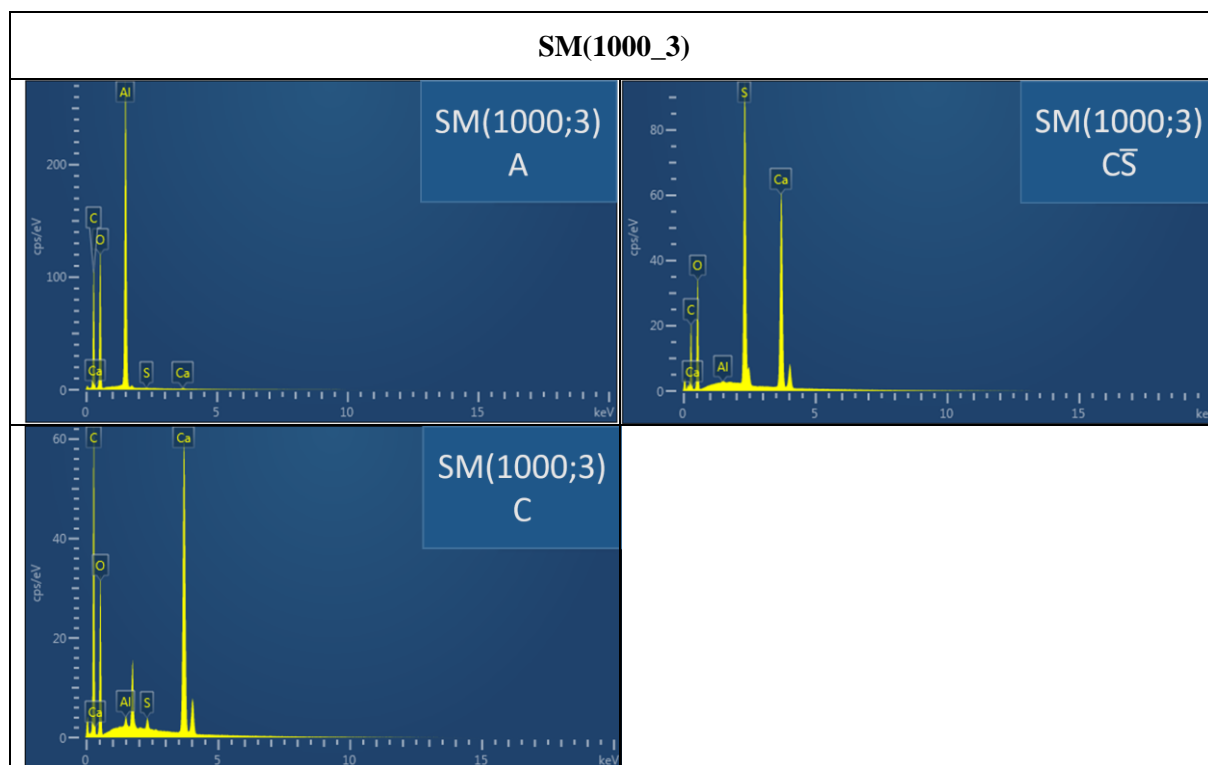
-
- [200] A.S. Mukasyan, P. Epstein, P. Dinka, Solution combustion synthesis of nanomaterials, *Proc. Combust. Inst.* 31 (2007) 1789–1795.
- [201] J.C. Restrepo, A. Chavarriaga, O.J. Restrepo, J.I. Tobón, Synthesis of Hydraulically Active Calcium Silicates Produced by Combustion Methods, *MRS Online Proc. Libr. Arch.* 1768 (2015). doi:10.1557/opl.2015.321.
- [202] A.S. Rogachev, A.S. Mukasyan, *Combustion for Material Synthesis*, CRC Press, 2014.
- [203] I. Halikia, L. Zoumpoulakis, E. Christodoulou, D. Prattis, Kinetic study of the thermal decomposition of calcium carbonate by isothermal methods of analysis., *Eur. J. Miner. Process. Environ. Prot.* 1 (2001) 89–102.
- [204] Z. Yan, Z. Wang, X. Wang, L.I.U. Hao, J. Qiu, Kinetic model for calcium sulfate decomposition at high temperature, *Trans. Nonferrous Met. Soc. China.* 25 (2015) 3490–3497.
- [205] Z. Yan, Z. Wang, H. Liu, Y. Tu, W. Yang, H. Zeng, J. Qiu, Decomposition and solid reactions of calcium sulfate doped with SiO₂, Fe₂O₃ and Al₂O₃, *J. Anal. Appl. Pyrolysis.* 113 (2015) 491–498.
- [206] R. Kuusik, P. Salkkonen, L. Niinistö, Thermal decomposition of calcium sulphate in carbon monoxide, *J. Therm. Anal.* 30 (1985) 187–193.
- [207] I. Gruncharov, Y. Pelovski, G. Bechev, I. Dombalov, P. Kirilov, Effects of some admixtures on the decomposition of calcium sulphate, *J. Therm. Anal.* 33 (1988) 597–602.
- [208] G.-S. Choi, F.P. Glasser, The sulphur cycle in cement kilns: vapour pressures and solid-phase stability of the sulphate phases, *Cem. Concr. Res.* 18 (1988) 367–374.
- [209] Á.G. De la Torre, A.J. Cuberos, G. Alvarez-Pinazo, A. Cuesta, M.A. Aranda, In situ powder diffraction study of belite sulfoaluminate clinkering, *J. Synchrotron Radiat.* 18 (2011) 506–514.
- [210] A.J. Cuberos, A.G. De la Torre, G. Alvarez-Pinazo, M.C. Martín-Sedeño, K. Schollbach, H. Pöllmann, M.A. Aranda, Active iron-rich belite sulfoaluminate cements: clinkering and hydration, *Environ. Sci. Technol.* 44 (2010) 6855–6862.
- [211] B.M. Mohamed, J.H. Sharp, Kinetics and mechanism of formation of monocalcium aluminate, CaAl₂O₄, *J. Mater. Chem.* 7 (1997) 1595–1599.
- [212] M. Aineto, A. Acosta, J.M. Rincon, M. Romero, Thermal expansion of slag and fly ash from coal gasification in IGCC power plant, *Fuel.* 85 (2006) 2352–2358.
- [213] D.A. Lange, H.M. Jennings, S.P. Shah, Image analysis techniques for characterization of pore structure of cement-based materials, *Cem. Concr. Res.* 24 (1994) 841–853.
- [214] J.W. Gilman, D.L. VanderHart, T. Kashiwagi, *Thermal Decomposition Chemistry of Poly (vinyl alcohol) Char Characterization and Reactions with Bismaleimides*, in: ACS Publications, 1995.
- [215] M. Wiśniewska, S. Chibowski, T. Urban, D. Sternik, Investigation of the alumina properties with adsorbed polyvinyl alcohol, *J. Therm. Anal. Calorim.* 103 (2011) 329–337.
- [216] P. Budrugaec, Kinetics of the complex process of thermo-oxidative degradation of poly (vinyl alcohol), *J. Therm. Anal. Calorim.* 92 (2008) 291–296.
- [217] V. Petrykin, M. Kakihana, *Chemistry and applications of polymeric gel precursors*, *Handb. Sol-Gel Sci. Technol. Process. Charact. Appl.* 1 (2005) 77–104.
- [218] M.H. Nguyen, S.-J. Lee, W.M. Kriven, Synthesis of oxide powders by way of a polymeric steric entrapment precursor route, *J. Mater. Res.* 14 (1999) 3417–3426.
- [219] H.F. Taylor, *Cement chemistry*, Thomas Telford, 1997.

-
- [220] A. Khawam, D.R. Flanagan, Solid-state kinetic models: basics and mathematical fundamentals, *J. Phys. Chem. B.* 110 (2006) 17315–17328.
- [221] W.D. Kingery, H.K. Bowen, D.R. Uhlmann, *Introduction to ceramics*, Wiley New York, 1976.
- [222] Y. El Khessaimi, Y. El Hafiane, A. Smith, R. Trauchessec, C. Diliberto, A. Lecomte, Solid-state synthesis of pure ye’elimite, *J. Eur. Ceram. Soc.* 38 (2018) 3401–3411.
- [223] Y. El Khessaimi, Y. El Hafiane, A. Smith, Ye’elimite synthesis by chemical routes, *J. Eur. Ceram. Soc.* 39 (2019) 1683–1695.
- [224] P. Juilland, E. Gallucci, Morpho-topological investigation of the mechanisms and kinetic regimes of alite dissolution, *Cem. Concr. Res.* 76 (2015) 180–191. doi:10.1016/j.cemconres.2015.06.001.
- [225] P. Barret, D. Ménétrier, Filter dissolution of C_3S as a function of the lime concentration in a limited amount of lime water, *Cem. Concr. Res.* 10 (1980) 521–534.
- [226] P.M. Dove, N. Han, Kinetics of mineral dissolution and growth as reciprocal microscopic surface processes across chemical driving force, in: *AIP Conf. Proc.*, AIP, 2007: pp. 215–234.
- [227] P.M. Dove, N. Han, J.J. De Yoreo, Mechanisms of classical crystal growth theory explain quartz and silicate dissolution behavior, *Proc. Natl. Acad. Sci.* 102 (2005) 15357–15362.
- [228] D.B. Emmert, P.J. Stoehr, G. Stoesser, G.N. Cameron, The European bioinformatics institute (EBI) databases, *Nucleic Acids Res.* 22 (1994) 3445–3449.
- [229] A. Cuesta, A.G. De la Torre, E.R. Losilla, V.K. Peterson, P. Rejmak, A. Ayuela, C. Frontera, M.A.G. Aranda, Structure, Atomistic Simulations, and Phase Transition of Stoichiometric Yeelimite, *Chem. Mater.* 25 (2013) 1680–1687. doi:10.1021/cm400129z.
- [230] J.-P. Boisvert, M. Domenech, A. Foissy, J. Persello, J.-C. Mutin, Hydration of calcium sulfate hemihydrate ($CaSO_4 \cdot \frac{1}{2}H_2O$) into gypsum ($CaSO_4 \cdot 2H_2O$). The influence of the sodium poly (acrylate)/surface interaction and molecular weight, *J. Cryst. Growth.* 220 (2000) 579–591.
- [231] A. Ersen, A. Smith, T. Chotard, Effect of malic and citric acid on the crystallisation of gypsum investigated by coupled acoustic emission and electrical conductivity techniques, *J. Mater. Sci.* 41 (2006) 7210–7217.
- [232] E. Badens, S. Veesler, R. Boistelle, Crystallization of gypsum from hemihydrate in presence of additives, *J. Cryst. Growth.* 198–199 (1999) 704–709. doi:10.1016/S0022-0248(98)01206-8.
- [233] J.P. Bomble, Rhéologie des mortiers et des bétons frais, influence du facteur ciment, in: *Proceeding RILEM Leeds Semin.*, 1973: pp. 1–169.
- [234] A. Smith, Y. El Hafiane, J.-P. Bonnet, P. Quintard, B. Tanouti, Role of a small addition of acetic acid on the setting behavior and on the microstructure of a calcium aluminate cement, *J. Am. Ceram. Soc.* 88 (2005) 2079–2084.

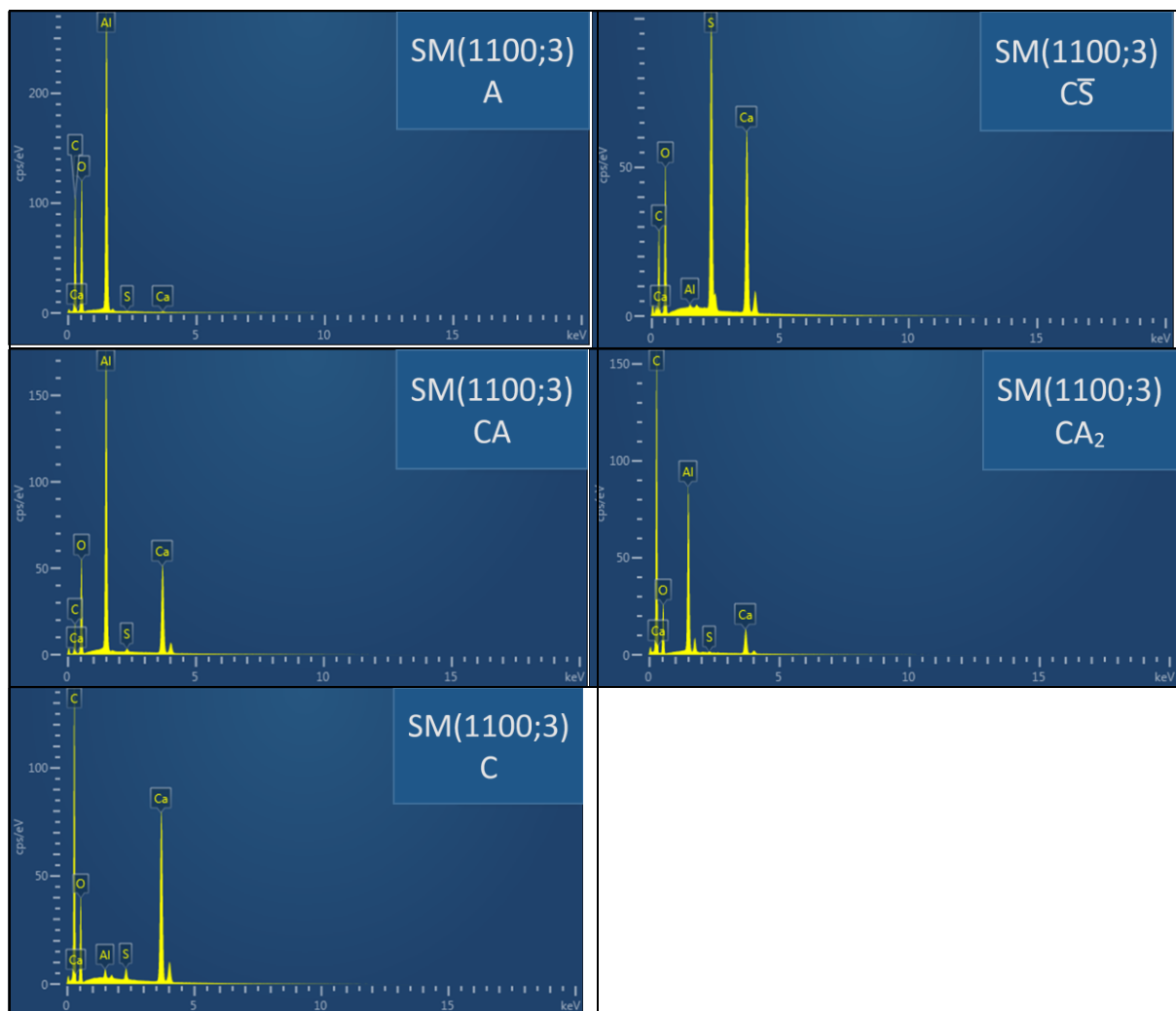
Appendixes

Appendix 1. EDS point analysis of Figure VI-3 and Figure VI-4	142
Appendix 2. Derivative curves of TGA analysis given in Figure VII-4b and Figure VII-5b.....	150
Appendix 3. All mathematical equations mentioned in the present thesis	151
Appendix 4. All chemical reactions mentioned in the present thesis	154
Appendix 5. Publications and communications.....	155

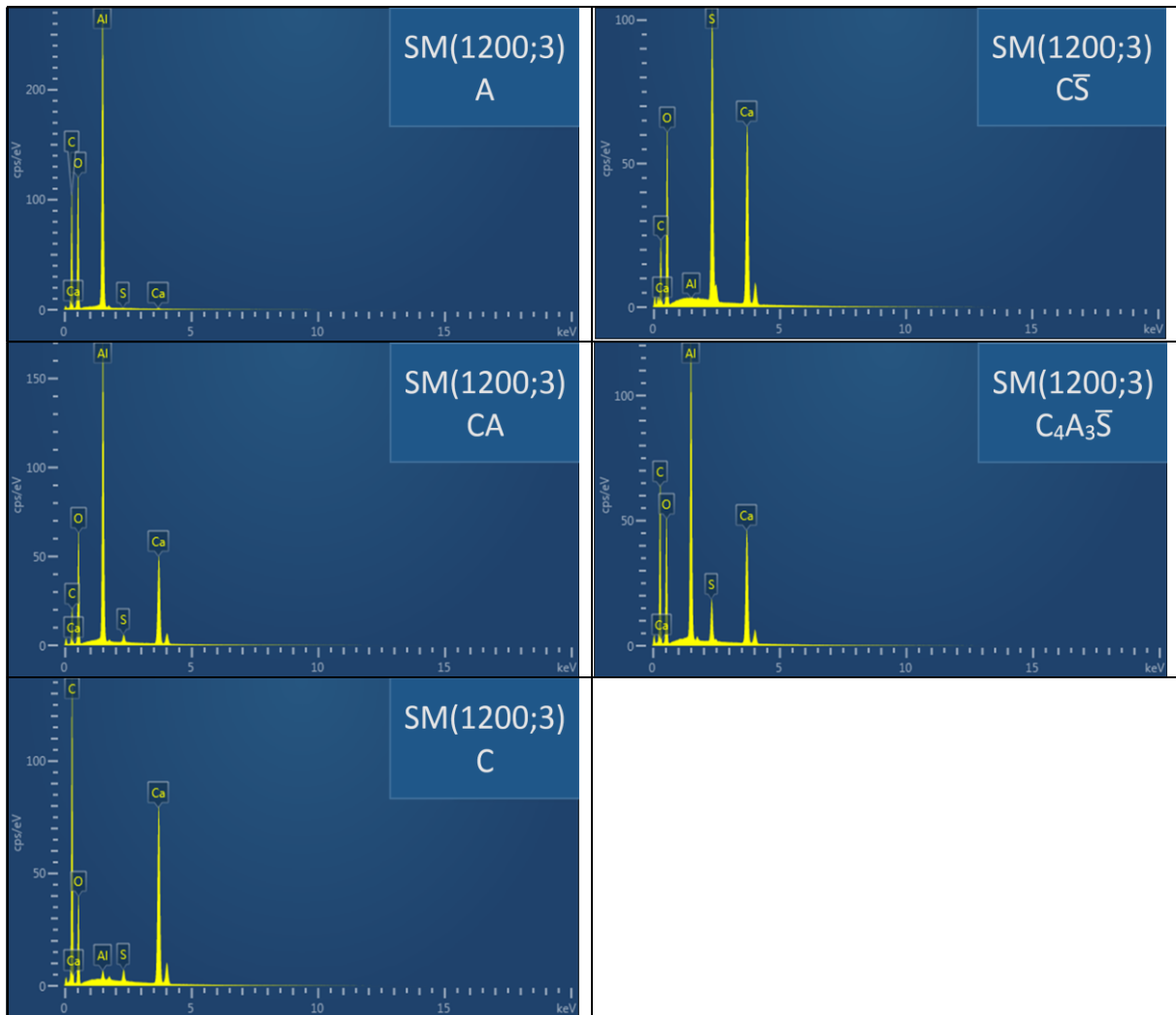
Appendix 1. EDS point analysis of Figure VI-3 and Figure VI-4



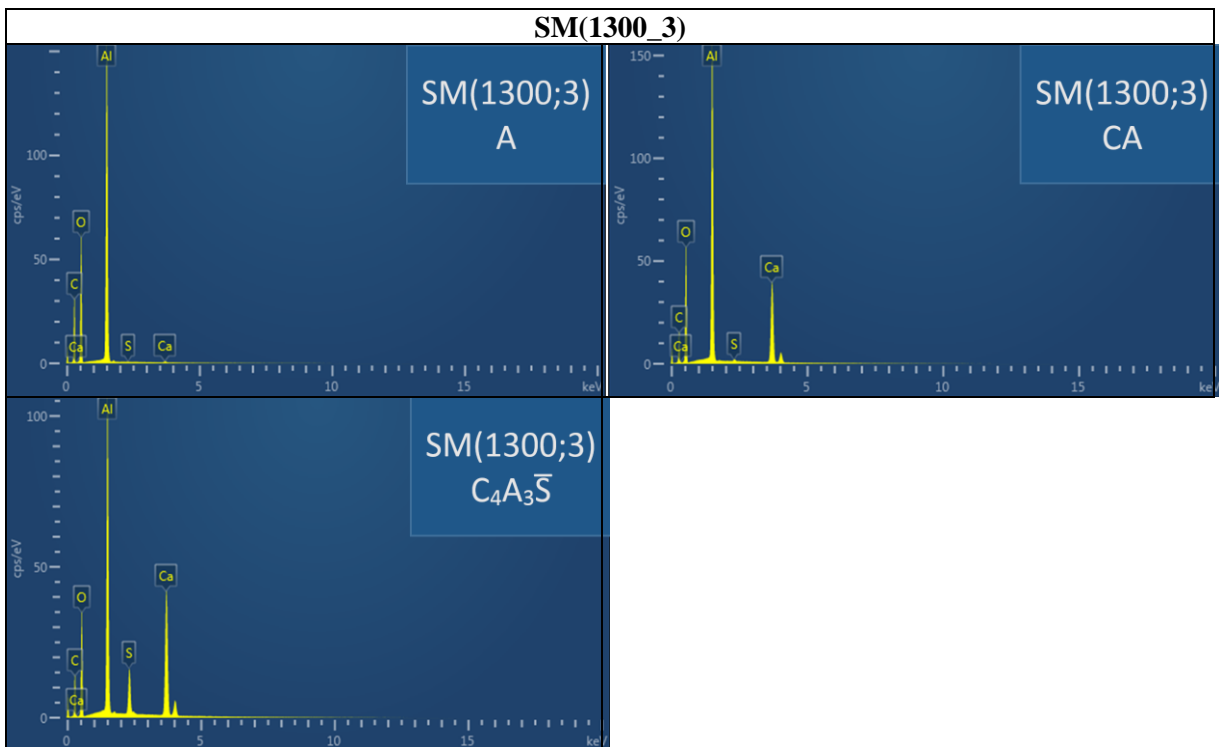
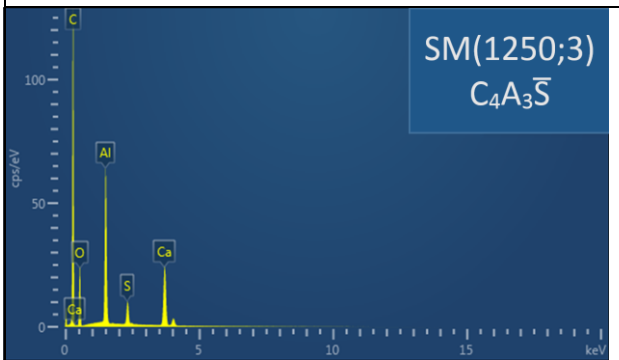
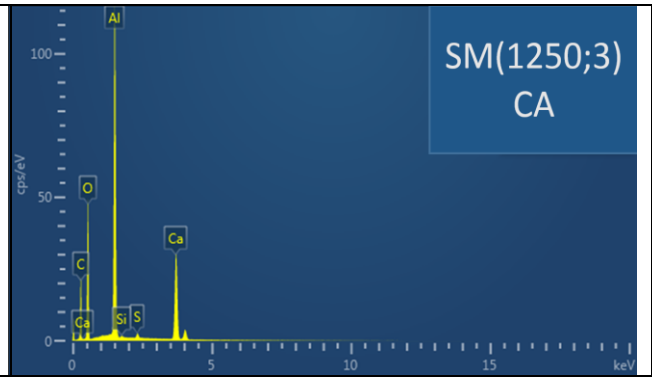
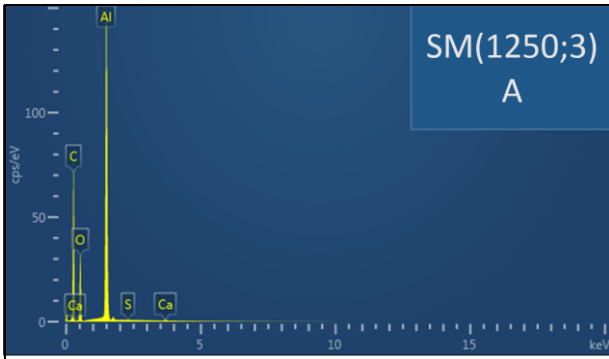
SM(1100_3)

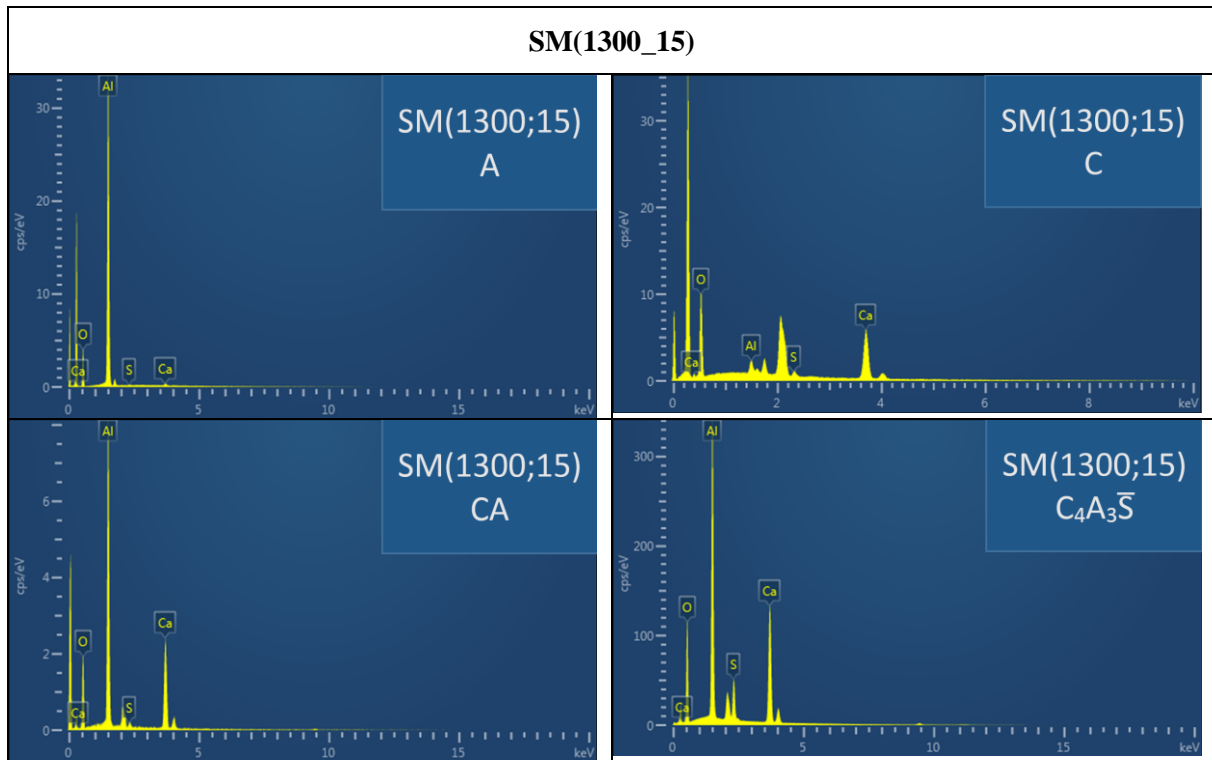


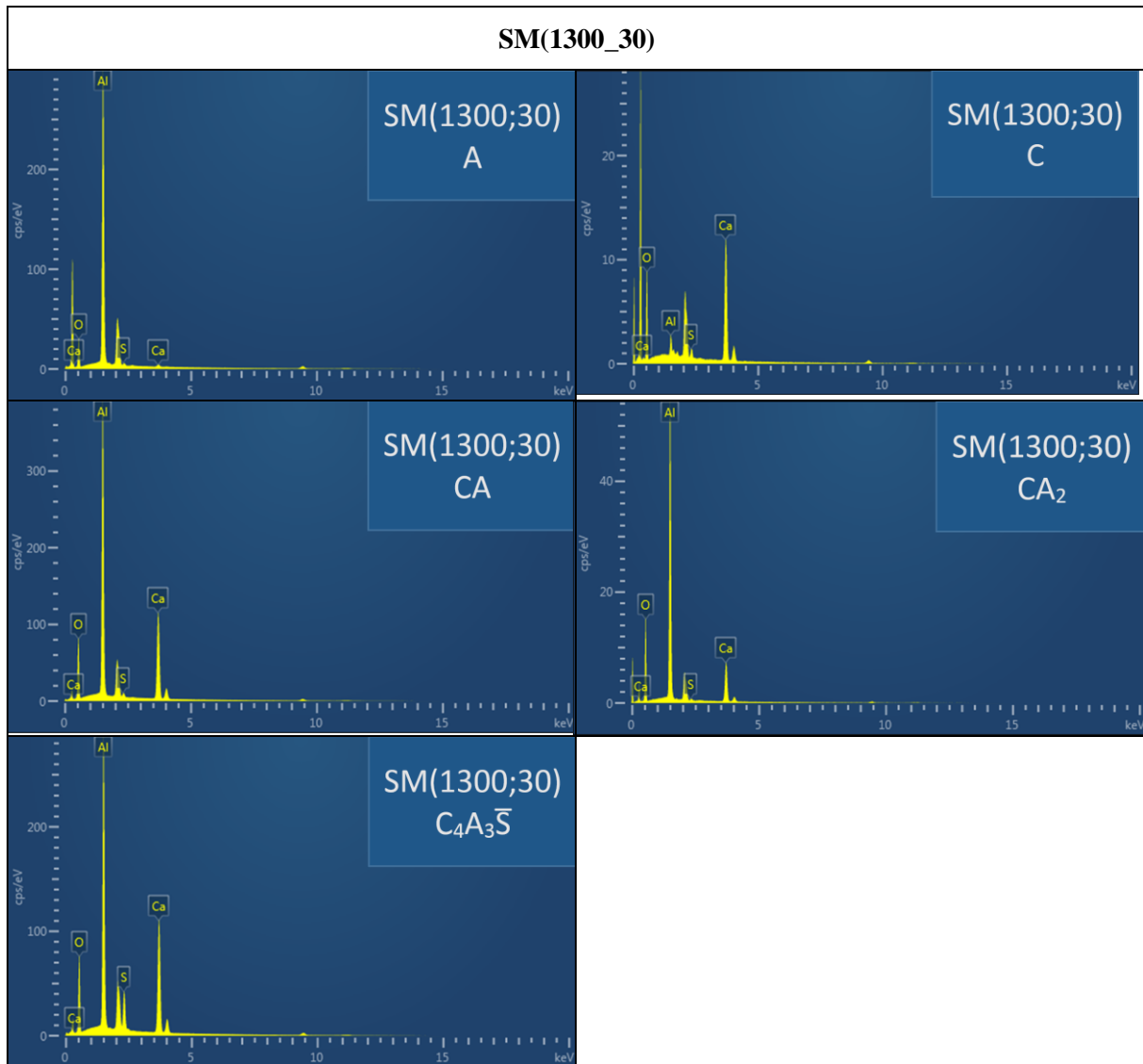
SM(1200_3)



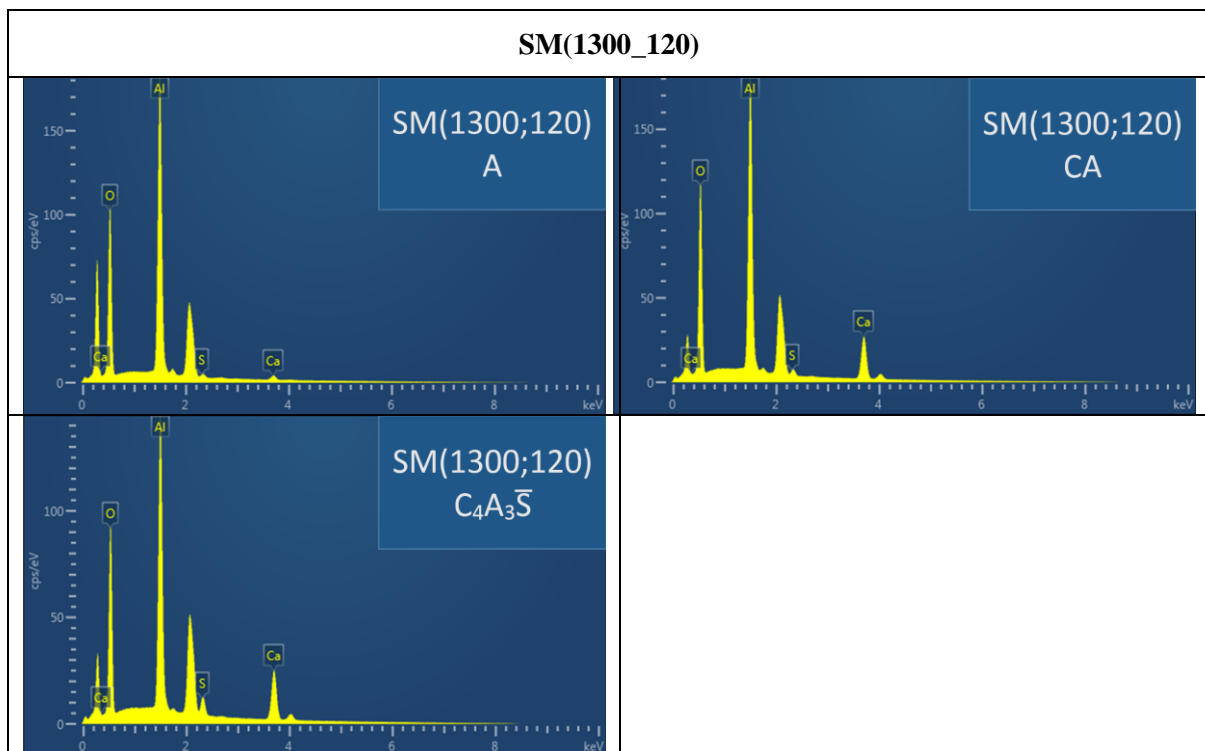
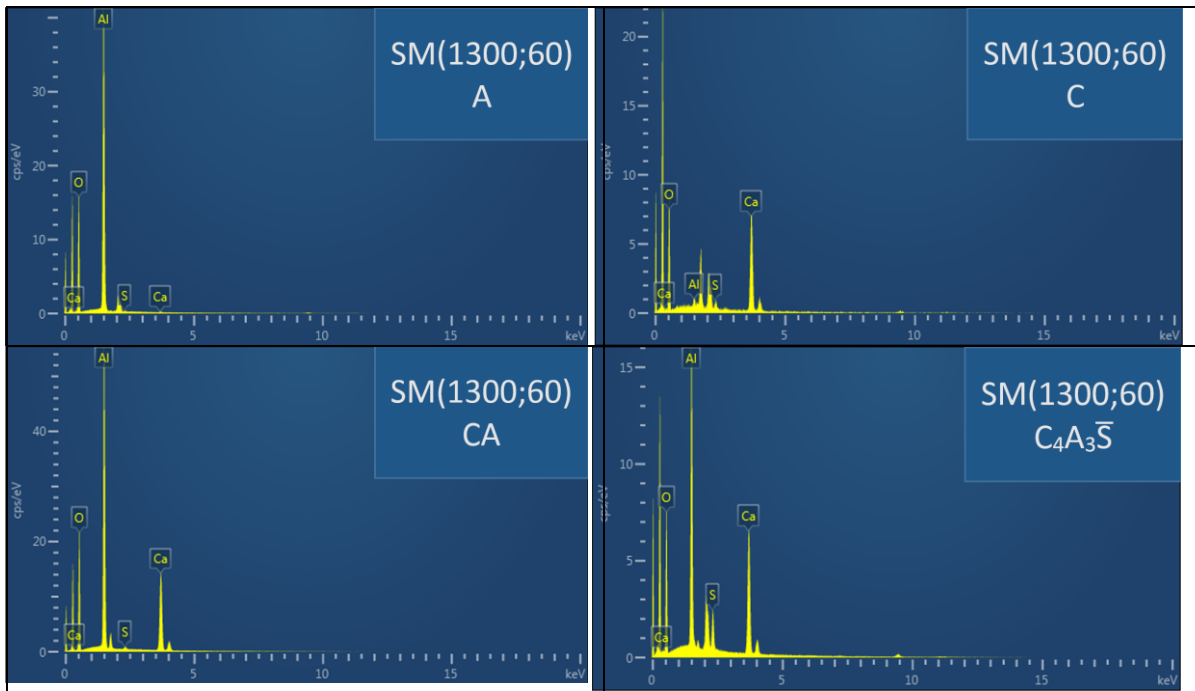
SM(1250_3)

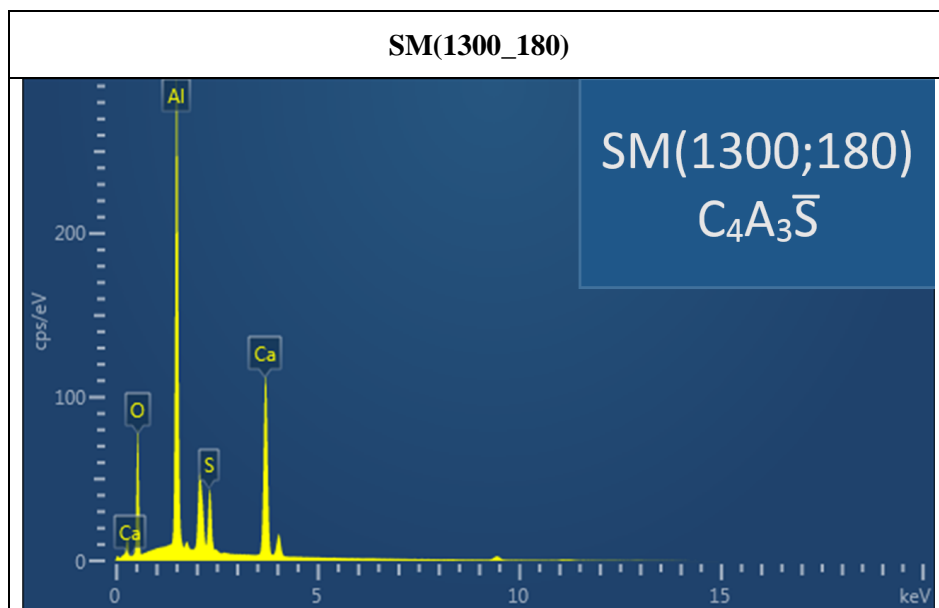




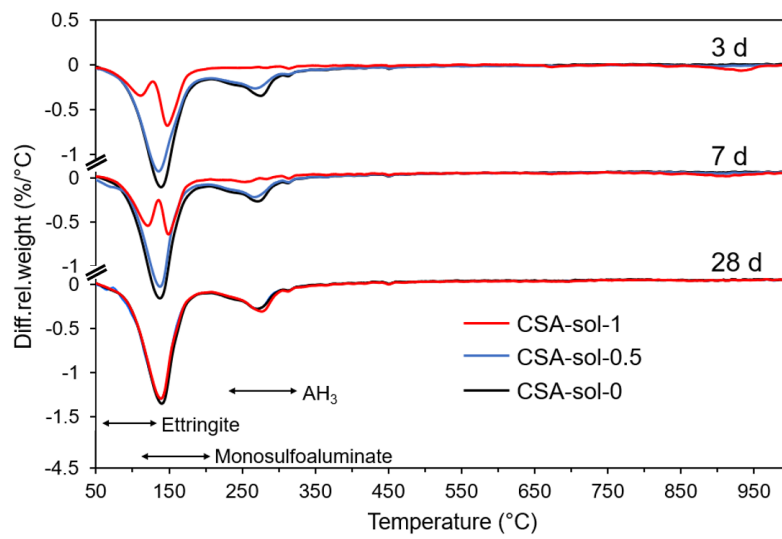
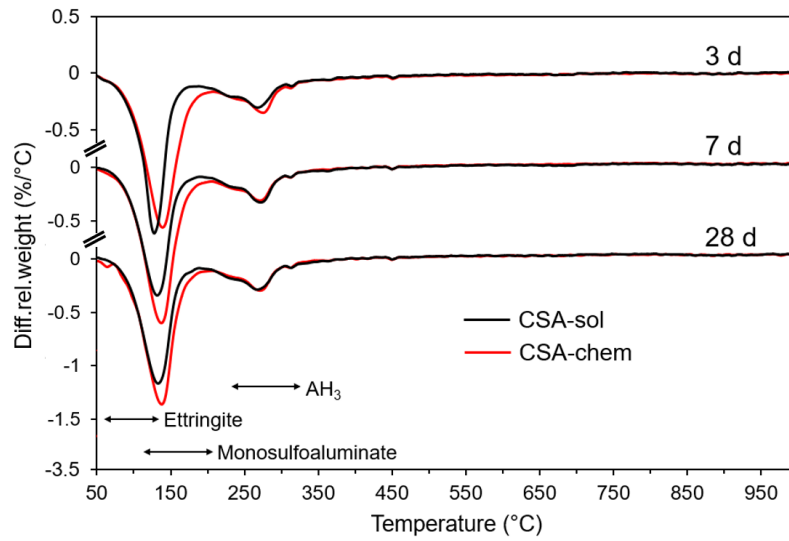


SM(1300_60)





Appendix 2. Derivative curves of TGA analysis given in Figure VII-4b and Figure VII-5b



Appendix 3. All mathematical equations mentioned in the present thesis

$$\alpha(\%) = \frac{\text{wt}\%_{\text{ye'elimité}}(t_0) - \text{wt}\%_{\text{ye'elimité}}(t)}{\text{wt}\%_{\text{ye'elimité}}(t_0)} \times 100 \quad \text{E.0}$$

$$\Delta G_r = \Delta G_r^0 + RT \ln[(a_A)^x (a_B)^y] \quad \text{E.1}$$

$$\Delta G_r = \Delta G_r^0 + RT \ln[(a_A)^x (a_B)^y] = 0 \quad \text{E.2}$$

$$\Delta G_r^0 = -RT \ln[(a_A)^x (a_B)^y]_{\text{éq}} = -RT \ln(k_{\text{sp}}) \quad \text{E.3}$$

$$\beta = \frac{[(a_A)^x (a_B)^y]}{[(a_A)^x (a_B)^y]_{\text{éq}}} = \frac{[(a_A)^x (a_B)^y]}{k_{\text{sp}}} \quad \text{E.4}$$

$$\Delta G_r = -RT \ln(k_{\text{sp}}) + RT \ln[(a_A)^x (a_B)^y] = RT \ln(\beta) \quad \text{E.5}$$

$$R_{\text{diss}} = k_0 \times S_{\text{reac}} \times e^{-E_a/RT} \times a_{\text{H}^+}^{\text{mH}^+} \times \prod_i a_i^{\text{mi}} \times g(1) \times f(\Delta G_r) \quad \text{E.6}$$

$$\Delta G_n^{\text{etch-pit}}(r) = \frac{\pi r^2 h}{V_m} [\Delta G_r] + 2\pi r h \sigma \quad \text{E.7}$$

$$\frac{d\Delta G_n^{\text{etch-pit}}(r)}{dr} = 0 \quad \text{E.8}$$

$$\frac{d\Delta G_n^{\text{etch-pit}}(r=r^*)}{dr} = \frac{2\pi r^* h}{V_m} [\Delta G_r] + 2\pi h \sigma = 0 \quad \text{E.9}$$

$$r^* = -\frac{\sigma \times V_m}{[\Delta G_r]} \quad \text{E.10}$$

$$\Delta G_n^* \text{etch-pit}(r = r^*) = \frac{-3\pi h V_m \sigma^2}{[\Delta G_r]} \quad \text{E.11}$$

$$\Delta G_n^* \text{etch-pit}(r = r^*) = \frac{3\pi h V_m \sigma^2}{[\Delta G_r]} \times \sqrt{1 - \omega} \quad \text{E.12}$$

$$\omega = \frac{N_a \times S \times b^2}{2\pi \sigma^2 V_m} \Delta G_r \quad \text{E.13}$$

$$f(\Delta G_r) = (1 - e^{\Delta G_r/RT}) \quad \text{E.14}$$

$$f(\Delta G_r) = \frac{\Delta G_r}{RT} \quad \text{E.15}$$

$$\Delta G_{\text{germ}} = \left\{ -\frac{4}{3} \pi r^3 \Delta G_v + 4\pi r^2 \gamma \right\} \left\{ \frac{1}{4} (2 + \cos \theta)(1 - \cos \theta)^2 \right\} \quad \text{E.16}$$

$$\Delta G_v = \frac{kT \ln \beta}{\Omega} \quad \text{E.17}$$

$$\Delta G_{\text{germ}} = \left\{ -\frac{4}{3} \pi r^3 \frac{kT \ln \beta}{\Omega} + 4\pi r^2 \gamma \right\} \left\{ \frac{1}{4} (2 + \cos \theta)(1 - \cos \theta)^2 \right\} \quad \text{E.18}$$

$$\frac{d\Delta G_{\text{germ}}}{dr} (r = r^*) = \left\{ -4\pi r^{*2} \frac{kT \ln \beta}{\Omega} + 8\pi r^* \gamma \right\} \left\{ \frac{1}{4} (2 + \cos \theta)(1 - \cos \theta)^2 \right\} = 0 \quad \text{E.19}$$

$$r^* = \frac{2\gamma\Omega}{kT \ln \beta} \quad \text{E.20}$$

$$\Delta G_{\text{germ}}^* (r = r^*) = \left(\frac{16\pi\Omega^2\gamma^3}{3(kT \ln \beta)^2} \right) \left\{ \frac{1}{4} (2 + \cos \theta)(1 - \cos \theta)^2 \right\} \quad \text{E.21}$$

$$\Delta G_{\text{germ}}^* (r = r^*) = \left(\frac{4}{3} \pi \gamma r^{*2} \right) \left\{ \frac{1}{4} (2 + \cos \theta)(1 - \cos \theta)^2 \right\} \quad \text{E.22}$$

$$n\lambda = 2d \sin \theta \quad \text{E.23}$$

$$D_{\text{crystallite}} = \frac{K \times \lambda}{\text{FWHM} \times \cos \theta} \quad \text{E.24}$$

$$\text{Rwp} = \sqrt{\frac{\sum_i w_i (I_{iM} - I_{iC})^2}{\sum_i w_i (I_{iM})^2}} \quad \text{E.25}$$

$$\text{Rexp} = \sqrt{\frac{N - P}{\sum_i w_i (I_{iM})^2}} \quad \text{E.26}$$

$$\text{GOF} = \left(\frac{\text{Rwp}}{\text{Rexp}} \right)^2 \quad \text{E.27}$$

$$D_{\text{particle}} = \frac{1}{N_{\text{total}}} \sum_{i=1}^{N_{\text{total}}} D_F \quad \text{E.28}$$

$$\sigma = \sqrt{\frac{1}{N_{\text{total}} - 1} \sum_{i=1}^{N_{\text{total}}} (D_F - D_{\text{particle}})^2} \quad \text{E.29}$$

$$\rho_s = \frac{m_1}{m_1 - m_2} \times \rho_L \quad \text{E.30}$$

$$P_o = \frac{m_3 - m_1}{m_3 - m_2} \times 100 \quad \text{E.31}$$

$$\sigma = \sum_i \lambda_i \times C_i \quad \text{E.32}$$

$$\%Rc = \frac{m_{\text{resin}}}{m_{\text{resin}} + m_{\text{oxide}}} \times 100 \quad \text{E.33}$$

$$\frac{d\sigma}{dt} = k f(\sigma) \quad \text{E.34}$$

$$\sigma = \frac{m_0 - m_t}{m_0 - m_\infty} \quad \text{E.35}$$

$$k = A \cdot e^{-Ea/RT} \quad \text{E.36}$$

$$r = r_0 - kt \quad \text{E.37}$$

$$\sigma = \frac{\frac{4}{3}\pi\rho r_0^3 - \frac{4}{3}\pi\rho r^3}{\frac{4}{3}\pi\rho r_0^3} \quad \text{E.38}$$

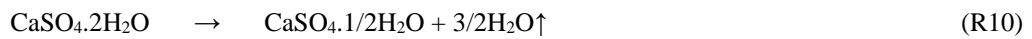
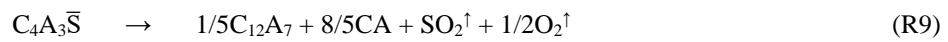
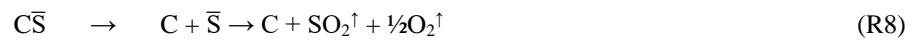
$$1 - \sigma = \frac{r^3}{r_0^3} \quad \text{E.39}$$

$$1 - (1 - \sigma)^{1/3} = \frac{k}{r_0} t = f(\sigma) \quad \text{E.40}$$

$$\frac{d\sigma}{dt} = A \cdot e^{\left(-\frac{Ea}{RT}\right)} \frac{t}{r_0} \quad \text{E.41}$$

$$\frac{\sigma^+}{\sigma^-} \text{ is proportional to } \frac{\sum_{\text{positive ions}} r_+^2}{\sum_{\text{negative ions}} r_-^2} \quad \text{E.42}$$

Appendix 4. All chemical reactions mentioned in the present thesis



Appendix 5. Publications and communications

List of publications

From PhD work

In international journals

Y. EL KHESSAIMI, Y. EL HAFIANE, A. SMITH, R. TRAUCHESSEC, C. DILIBERTO, A. LECOMTE
Solid state synthesis of pure Ye'elimite
Journal of the European Ceramic Society, 38 (2018), 3401-3411
<https://doi.org/10.1016/j.jeurceramsoc.2018.03.018>

Y. EL KHESSAIMI, Y. EL HAFIANE, A. SMITH
Ye'elemite synthesis by chemical routes
Journal of the European Ceramic Society, 39 (2019), 1683-1695
<https://doi.org/10.1016/j.jeurceramsoc.2018.10.025>

Y. EL KHESSAIMI, Y. EL HAFIANE, A. SMITH
Examination of ye'elimite formation mechanism
Journal of the European Ceramic Society 39 (15) (2019) 5086-5095
<https://doi.org/10.1016/j.jeurceramsoc.2019.07.042>

Y. EL KHESSAIMI, Y. EL HAFIANE, A. SMITH
Effect of fineness and citric acid addition on the hydration of ye'elimite
Submitted to the journal of Construction and Building materials (October 2019)

In a reviewed conference proceeding

Y. EL KHESSAIMI, Y. EL HAFIANE, A. SMITH
Synthesis and hydration of ye'elimite
Submitted as a reviewed proceeding for the American Ceramic Institute / RILEM international conference on cementitious materials and alternative binders for sustainable concrete to be held in 2020 in Toulouse (France)

In a conference proceeding

Y. EL KHESSAIMI, Y. EL HAFIANE, A. SMITH
Thermodynamic study of ye'elimite
Submitted as a proceeding of the Plumee 2019 conference

From a collaborative project

In an international journal

M. MOUIYA, A. BOUAZIZI, A. ABOURRICHE, Y. EL KHESSAIMI, A. BENHAMMOU, Y. EL HAFIANE, Y. TAHA, M. OUMAM, A. SMITH, H. HANNACHE
Effect of sintering temperature on the microstructure and mechanical behavior of porous ceramics made from clay and banana peel powder
Results in Materials, <https://doi.org/10.1016/j.rinma.2019.100028>

*From Master project*In international journals

Y. EL KHESSAIMI, N. TESSIER-DOYEN, A. SMITH
 Effects of microstructure on acoustical insulation of gypsum boards
 Journal of Building Engineering 2017, 14, 24–31
<http://dx.doi.org/10.1016/j.jobe.2017.09.011>

A. SMITH, Y. EL HAFIANE, Y. EL KHESSAIMI, A. FAURE
 Some examples of mineral eco-materials
 Journal of the European Ceramic Society 39 (2019) 3408-3415
<https://doi.org/10.1016/j.jeurceramsoc.2019.02.003>

List of communications

- | | | |
|---|---------------------|------------------|
| 16th European Ceramic Society Conference
<i>Sintering of ye'elimate</i>
Y. EL KHESSAIMI, <u>A. SMITH</u> , Y. EL HAFIANE
Oral presentation | Turin, Italy | 16-20 June 2019 |
| Symposium PLUMEE 2019
<i>Thermodynamic study of ye'elimate</i>
<u>Y. EL KHESSAIMI</u> , A. SMITH, Y. EL HAFIANE
Oral presentation | Limoges, France | 10-12 April 2019 |
| International Workshop on Calcium Sulfoaluminate
<i>Synthesis and characterization of ye'elimate</i>
<u>Y. EL KHESSAIMI</u> , A. SMITH, Y. EL HAFIANE
Poster presentation
Distinction: Best Poster Award | Murten, Switzerland | 04-06 June 2018 |
| Journées annuelles 2018 du Groupe Français de la Céramique.
<i>Chemical synthesis of ye'elimate</i>
<u>Y. EL KHESSAIMI</u> , A. SMITH, Y. EL HAFIANE
Oral presentation | Pessac, France | 21-23 March 2018 |
| International symposium « The Future of Cement »
<i>Synthesis of pure ye'elimate</i>
<u>Y. EL KHESSAIMI</u> , A. SMITH, Y. EL HAFIANE
Poster presentation | Paris, France | 6-8 June 2017 |

Synthèse et hydratation de la phase ye'elinite

Les ciments riches en ye'elinite ou les ciments sulfoalumineux (CSA) sont commercialisés pour la préparation des bétons à compensation de retrait. De plus, les ciments CSA présentent des caractéristiques écologiques associées à leur production, notamment une réduction de l'empreinte CO₂. Le comportement expansif des ciments CSA est principalement contrôlé par la quantité de la phase ettringite, cette dernière est produite lors de l'hydratation de la phase importante, la ye'elinite [Ca₄(Al₆O₁₂)SO₄]. Cette thèse présente, d'une part, les conditions optimales pour la synthèse de la phase ye'elinite la plus pure possible par des réactions à l'état solide, et d'autre part, une description fondamentale des mécanismes de formation de cette phase. Un autre aspect de ce travail vise à étudier l'influence de la finesse et de l'addition d'acide citrique sur la dissolution de la phase ye'elinite. Pour l'étude de l'effet de la finesse, une poudre fine et pure de ye'elinite a été synthétisée par des méthodes sol-gel, ces dernières méthodes de synthèse ont été développées d'une manière originale dans notre thèse. Plusieurs techniques expérimentales ont été réalisées pour mener à bien les différents aspects de la présente thèse, à savoir l'analyse quantitative par DRX (méthode Rietveld), l'analyse thermique (ATG, ATD, et dilatométrie), MEB (imagerie en rétrodiffusé et cartographie EDS), l'analyse BET, l'analyse granulométrique par diffraction laser, et l'analyse d'images (porosité 2D et analyse granulométrique 2D).

Mots-clés : ciment sulfoalumineux, dissolution, hydratation, analyse quantitative Rietveld, voie sol-gel, synthèse par réactions solides, ye'elinite

Synthesis and hydration of ye'elinite

Ye'elinite-rich cements or calcium sulfoaluminate (CSA) cements are commercialized to prepare shrinkage compensation and self-stressing concretes. Moreover, CSA cements show environmentally friendly characteristics associated to their production, which include reduced CO₂ footprint. The expansive behavior of CSA cements is mainly controlled by ettringite amount, produced upon hydration of the key-phase, ye'elinite [Ca₄(Al₆O₁₂)SO₄]. This work presents, on one hand, the optimal conditions for the synthesis highly pure ye'elinite by solid state reactions, and on the other hand, it shows a fundamental description of ye'elinite formation mechanisms. Another aspect of the study encompasses the influence of fineness and citric acid addition on ye'elinite phase dissolution, then on hydrates composition of lab made ye'elinite-rich cement. For the fineness effect study, a highly fine and pure ye'elinite was originally synthesized by sol-gel methods. Various experimental techniques were performed to conduct the different aspects of the present study, namely XRD-Quantitative Rietveld analysis, Thermal analysis (TGA, DTG, DTA and Dilatometry), SEM (BSE imaging and EDS mapping), BET analysis, PSD by laser diffraction, and Image analysis (2D porosity and 2D PSD).

Keywords: calcium sulfoaluminate cements, dissolution, hydration, quantitative Rietveld analysis, sol-gel synthesis, solid state synthesis, ye'elinite

